# IBRACON

## IBRACON Structures and Materials Journal
### Revista IBRACON de Estruturas e Materiais

# IBRACON Structures and Materials Journal
## Revista IBRACON de Estruturas e Materiais

# Contents

**Cover:** Parametric Tower

**Courtesy:** Marcela Noronha P. de O. e Sousa

# Aims and Scope

## Aims and Scope

The IBRACON Structures and Materials Journal (in Portuguese: Revista IBRACON de Estruturas e Materiais) is a technical and scientific divulgation vehicle of IBRACON (Brazilian Concrete Institute), published every two months. Each issue has 12 to 15 articles and, possibly, a technical note and/or a technical discussion regarding a previously published paper. All contributions are reviewed and approved by professionals with recognized scientific competence in the area. The IBRACON Structures and Materials Journal is an open access Journal, free of charges for authors and readers.

## Objectives

The IBRACON Structures and Materials Journal´s main objectives are:

- Present current developments and advances in concrete structures and materials.
- Make possible the better understanding of structural concrete behavior, supplying subsidies for a continuous interaction among researchers, producers, and users.
- Stimulate the development of scientific and technological research in the areas of concrete structures and materials, through papers peer-reviewed by a qualified Editorial Board.
- Promote the interaction among researchers, constructors and users of concrete structures and materials and the development of Civil Construction.
- Provide a vehicle of communication of high technical level for researchers and designers in the areas of concrete structures and materials.

## Submission Procedure

The procedure to submit and revise the contributions, as well as the formats, are detailed in the Journal Website (ismj.org).

The papers and the technical notes are revised by at least two reviewers indicated by the editors. Discussions and replies are accepted for publication after a review by the editors and at least one member of the Editorial Board. In case of disagreement between the reviewer and the authors, the contribution will be sent to a specialist in the area, not necessarily linked to the Editorial Board. Conflict of interests is carefully handled by the Editors.

## Contribution Types

The Journal will publish original papers, short technical notes, and paper discussions. Original papers will be accepted if they are in accordance with the objectives of the Journal and present quality of information and presentation. A technical note is a brief manuscript. It may present a new feature of research, development, or technological application in the areas of Concrete Structures and Materials, and Civil Construction. This is an opportunity to be used by industries, companies, universities, institutions of research, researchers, and professionals willing to promote their works and products under development.

A discussion is received no later than 3 months after the publication of the paper or technical note. The discussion must be limited to the topic addressed in the published paper and must not be offensive. The right of reply is granted to the Authors. The discussions and the replies are published in the subsequent issues of the Journal.

The submission file should be in accordance with the paper template available at the Journal Website. It is recommended that the length of the papers does not exceed 25 pages. Where available, URLs for the references should be provided.

The IBRACON Structures and Materials Journal will conduct the review process for manuscripts submitted in English. Titles, abstracts, and keywords are presented in English, and in Portuguese or Spanish. Articles and technical notes are peer-reviewed and only published after approval of the reviewers and the Editorial Board.

Once accepted, an article is typeset according to the journal layout. The author will be required to review and approve the galleys before publishing. At this stage only typesetting errors will be considered.

## Internet Access

The IBRACON Structures and Materials Journal Webpage is available at http://ismj.org.

## Sponsors

The funds for the maintenance of the Journal are currently obtained from the IBRACON. The Journal is not supposed to be maintained with funds from private sponsorship, which could diminish the credit of the publications.

## Photocopying

## Copyright

## IBRACON

## Disclaimer

Papers and other contributions and the statements made, or opinions expressed therein are published on the understanding that the authors of the contribution are the only responsible for the opinions expressed in them and that their publication does not necessarily reflect the views of IBRACON or of the Journal Editorial Board.

# Editorial Board

# Direction

# IBRACON Structures and Materials Journal
## Revista IBRACON de Estruturas e Materiais

ORIGINAL ARTICLE

# A climatology-based wind speed map for NBR 6123

*Mapa de isopletas para a NBR-6123 com base em abordagem climatológica*

Acir Mércio Loredo-Souza[a]
Michèle Schubert Pfeil[b]
Ernani de Lima Nascimento[c]
Jorge Daniel Riera[a]
Gilberto Fernando Fisch[d,e]
André Teófilo Beck[f]

[a]Universidade Federal do Rio Grande do Sul – UFRGS, Porto Alegre, RS, Brasil
[b]Universidade Federal do Rio de Janeiro – UFRJ, Rio de Janeiro, RJ, Brasil
[c]Universidade Federal de Santa Maria – UFSM, Santa Maria, RS, Brasil
[d]Universidade de Taubaté – UNITAU, Taubaté, SP, Brasil
[e]Instituto de Aeronáutica e Espaço – CTA, São José dos Campos, SP, Brasil
[f]Universidade de São Paulo – USP, Escola de Engenharia de São Carlos, São Carlos, SP, Brasil

**Abstract:** Updating the basic wind speed map of NBR 6123 –-Wind loading on buildings – is one of the duties of the committee responsible for the revision of this code. Traditionally such maps are elaborated by means of extreme value wind speed data collected at meteorological stations, use of statistical methods for data characterization, and application of mathematical regression to elaborate the territorial maps. However, the spatial distribution of the atmospheric phenomena responsible for strong winds cannot be disregarded. This work presents a proposal for a new wind speed map for NBR 6123 combining a climatological approach and wind speed data recently compiled from hundreds of meteorological stations. A climatological wind map was first produced considering the phenomena which cause strong winds, and used as a basis to draw the isopleths of the basic wind speed map, considering the measured wind speed data. The resulting map shows basic wind speeds ranging from 30 to 48m/s.

**Keywords:** extreme winds, basic wind speeds, climatology, Gumbel distribution, NBR 6123.

**Resumo:** A atualização do mapa de isopletas da norma NBR 6123 – Forças devidas ao vento em edificações – é um dos aspectos tratados no âmbito do trabalho da comissão encarregada da revisão da citada norma. Tradicionalmente estes mapas são elaborados por meio de análises de valores extremos das velocidades do vento registradas em estações meteorológicas, da aplicação de métodos estatísticos para caracterização dos dados, e de interpolação matemática para geração do mapa. Entretanto, a distribuição espacial dos fenômenos atmosféricos responsáveis por ventos fortes no Brasil não pode ser desconsiderada. Este trabalho apresenta uma proposta para um novo mapa de isopletas da velocidade básica do vento para a NBR 6123 elaborado com base em uma abordagem climatológica e em recente pesquisa incluindo novos dados de centenas de estações meteorológicas. Inicialmente foi desenvolvido um mapa de regiões climáticas associadas aos fenômenos que produzem ventos fortes, a partir do qual o mapa de isopletas foi traçado. Resultaram isopletas associadas a velocidades de vento variando entre 30 e 48m/s.

**Palavras-chave:** ventos extremos, isopletas, velocidade básica do vento, climatologia, distribuição de Gumbel, NBR 6123.

A. M. Loredo-Souza, M. S. Pfeil, E. L. Nascimento, J. D. Riera, G. F. Fisch, and A. T. Beck

# 1 INTRODUCTION

In NBR 6123 [1] the so-called "basic" wind speed $V_0$ is defined as the average speed over three seconds (wind gust), which is exceeded on average once every 50 years, measured 10m above ground in open and flat terrain. Based on annual maximum wind gusts obtained in 49 weather stations of Brazilian airports, a wind speed map was drawn [2], [3], [4], which served as a basis for the current basic wind speed map of NBR 6123 [1]. In this map (Figure 1), values between 30 and 50 m/s are observed, as well as a large, hatched region in central Brazil, for which data was not available at the time, and for which the "minimum" value of 30 m/s was adopted.
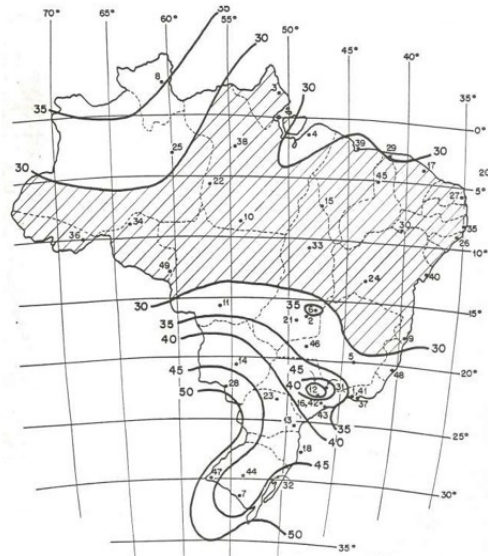


**Figure 1.** Isopleths map of current NBR 6123 [1]. $V_0$ values in m/s shown at tips of isocurves; numbers associated to dots identify the weather stations.

Recent research on the topic includes Almeida [5], Beck and Correa [6] and Vallis [7], who proposed maps based on mathematical regression. More recently, Kriging regression/interpolation was also proposed [8]. Vallis [7] also presented a $V_0$ map for Brazil in zone format. The author [7] developed algorithms to classify the events which cause strong winds in Brazil in synoptic and non-synoptic (definitions in Section 2). Vallis [7] concluded that non-synoptic winds dominate and define extreme winds in most parts of the Brazilian territory. Before that, other works pioneered identification and classification of winds in stationary synoptic and non-synoptic [9], [10].

The meteorological phenomena which produce extreme winds in Brazil have distinct characteristics in different parts of the country [11]–[14]. Recognizing this fact leads to the proposal of a climatological approach to the basic wind speed map, in opposition to purely mathematical regression. The purpose of this manuscript is to present and justify the proposal of a climatology-based basic wind speed map for NBR 6123. A climate zone map of Brazil is first proposed, focusing on the dominant atmospheric phenomena which typically cause strong winds. In the sequence, a literature review is conducted, addressing past literature proposing $V_0$ maps for Brazil. Finally, the climatology-based basic wind speed map for NBR 6123 is proposed and justified.

# 2 BRAZILIAN CLIMATOLOGY: SPATIAL DISTRIBUTION OF THE ATMOSPHERIC PHENOMENA RESPONSIBLE FOR STRONG WINDS

## 2.1 Types of atmospheric phenomena and their scales

Extreme winds in Brazil are generally caused by two types of meteorological phenomena which can also occur simultaneously: extratropical cyclones and local convective storms [12], [13], [15]. The winds originated in extratropical cyclones are better known and studied and serve as the basis for the design criteria and aerodynamic coefficients present in current wind codes worldwide.

*A. M. Loredo-Souza, M. S. Pfeil, E. L. Nascimento, J. D. Riera, G. F. Fisch, and A. T. Beck*

Extratropical cyclones belong to the synoptic scale of atmospheric phenomena, with horizontal dimensions of the order of hundreds of kilometers and duration of up to a few days. From this scale of motion originates the term 'synoptic wind' employed in wind engineering. Other extreme winds are associated to local convective storms, which belong to a different atmospheric scale, called mesoscale (or convective scale, more specifically) [15]. Local convective storms have a horizontal scale of the order of 10 km and duration of the order of one hour. In the convective scale are the winds known as TS (thunderstorm), as well as the general 'non-synoptic winds' of wind engineering. Among the most intense TS winds are those associated to strong downward currents (or downbursts) and tornadoes.

## 2.2 Characteristics of non-synoptic winds relevant to structural engineering

The term 'downburst' was coined by Fujita [16], and is understood as a dense column of cold air associated with which is a convective-scale downward current (or downdraft) that eventually reaches the earth´s surface, giving rise to a 'burst' of highly divergent winds. In terms of horizontal scale, a downburst can be classified as a microburst when the radius of the divergent motion spreads no more than 4 km from the central downdraft, and as a macroburst when this radius exceeds the 4 km threshold [17], [18].

Figure 2 shows photos of the leading edge of a 'supercell' storm (i.e., a convective storm that exhibits rotation) over the city of Porto Alegre, RS, in the 29th of January, 2016 from which strong downdrafts and accompanying gusts (non-synoptic winds) originated. The schematic illustration shows the short horizontal scale of the event. Due to their local character, many non-synoptic wind events are not adequately registered by operational surface weather stations, implying that the non-synoptic wind speeds, being poorly sampled, could be significantly stronger than those actually measured by the anemometers at weather stations.

The characteristics of the horizontal flow originating from the convective downdrafts are complex, and their detailed discussion is out of the scope of this manuscript. However, some aspects relevant to structural engineering should be discussed.

In terms of vertical structure, the mean velocity profiles of downbursts (as they spread laterally) are significantly different from those typically observed for winds originated from extratropical cyclones (atmospheric boundary layer profiles, or ABL), as illustrated in Figure 3 for profiles corresponding to $V_0$ equal to 40 m/s. The mean velocity profile illustrated for the downburst was obtained from Vicroy's model [20], considering maximum velocity at a height of 40 m, as in ref. [21]. In this case, the load effect on buildings with heights between 10 and 120 meters is more intense than for winds originated from extratropical cyclones, for the same value of $V_0$. The opposite occurs for buildings higher than 150 m. However, the height at which the maximum downburst wind speed occurs can be higher than 40 m (even reaching 120 m), increasing considerably the height of buildings for which the downburst profile would be more favorable than the ABL profile.



**Figure 2.** Schematic illustration of a convective-scale downward current (or downdraft), from which originates a type of intense non-synoptic winds, and photos of the leading edge of a microburst-producing supercell storm over the city of Porto Alegre, RS on 29th of January, 2016 [19].
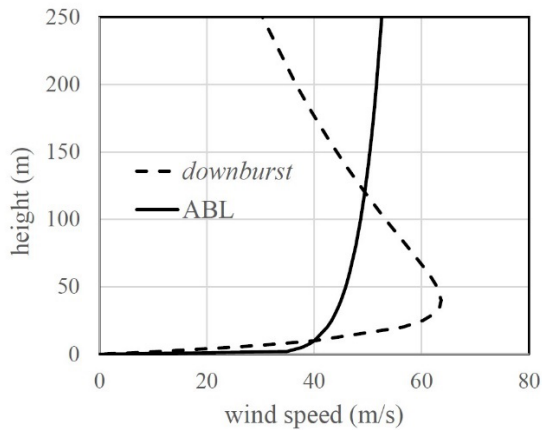
**Figure 3.** Mean wind profile corresponding to $V_0$ equal to 40 m/s for atmospheric boundary layer winds (full line) and downburst-like winds (dashed line, with maximum at height of 40 m) during its horizontal divergence at low-levels, based on Vicroy model [20].

Importantly, non-synoptic winds can occur simultaneously to synoptic winds. Such occurrences are quite frequent, for example, during the progression of a cold front, due to frontally-induced local convective storms. This combination of meteorological events changes wind flow patterns, as illustrated in Figure 4, leading to the classification of downbursts in stationary and non-stationary. Following Li et al. [22], non-stationary downbursts occur more often.

Figure 5 is a representation of horizontal flow patterns that arise from the combination of forcing mechanisms that belong to distinct scales of atmospheric motion (most notably, synoptic and sub-synoptic scales). The figure refers to the Northern Hemisphere and was elaborated by Fujita and Wakimoto [23] based on observed damage produced by the distinct wind types. Figure 5a) shows the flow associated with an anticyclone (synoptic winds) and also identifies the cold front zone. Figure 5b) provides a close-up view along a section of the cold front and illustrates the formation of the gust front associated with convective storms (TS) aligned with the cold front. Some of these storms can occasionally produce downburst winds. Figure 5c), which is a zoomed-in view of panel 5b), shows the flow patterns associated with a downburst. Finally, Figure 5d), on the 1 km scale, shows that inside a downburst there are more intense gust swaths, which lead to non-uniform wind patterns.
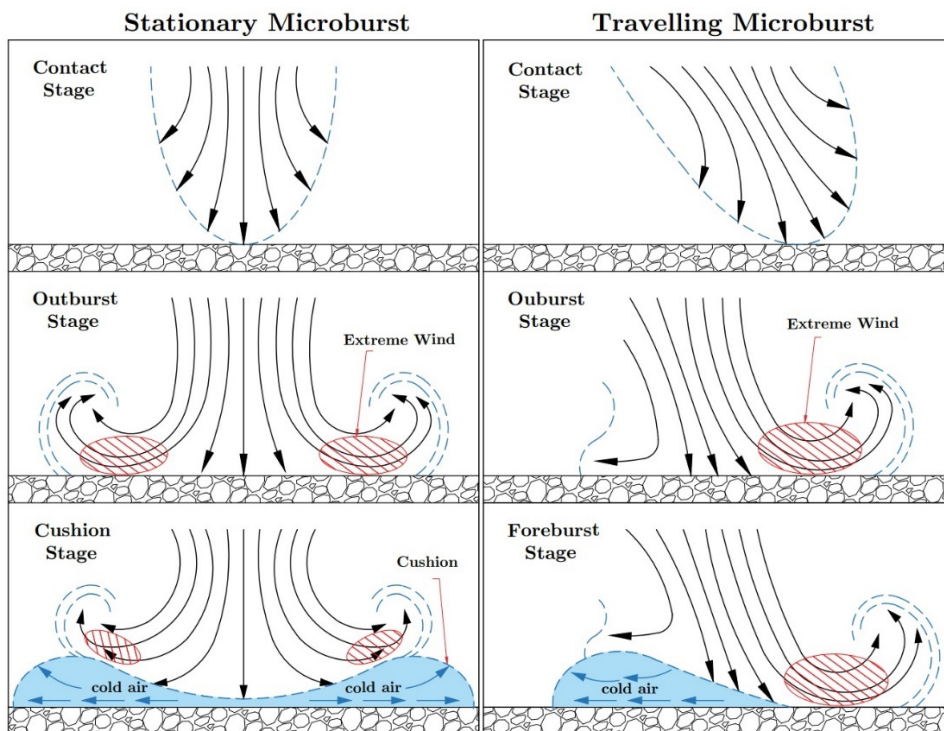


**Figure 4.** Schematic vertical cross-sections displaying the time evolution of the atmospheric flow across a stationary downburst (left column), and a typical moving or non-stationary downburst (right column) (based on Fujita [17]).
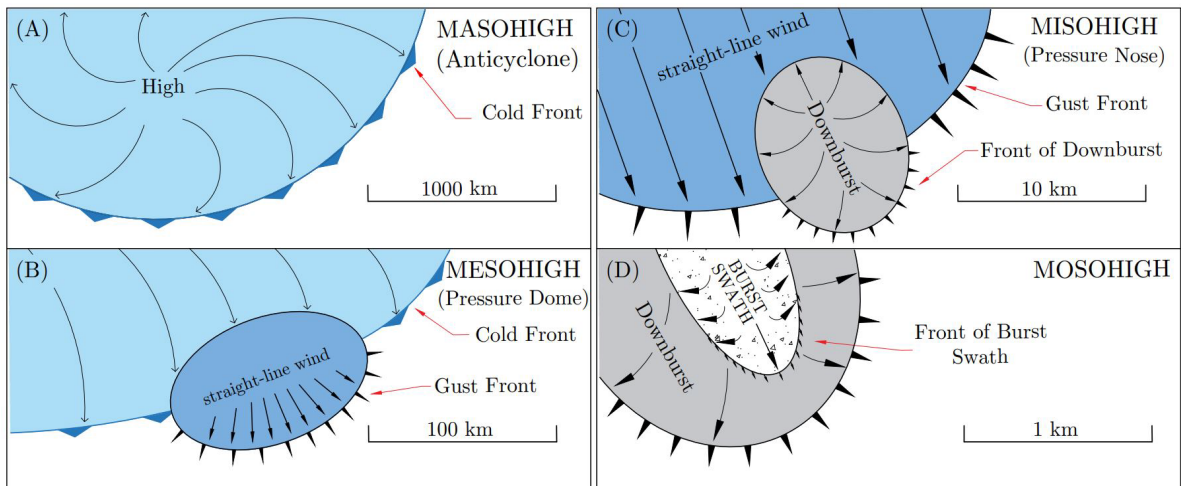
**Figure 5.** Schematic charts for the Northern Hemisphere displaying close up views of horizontal flow patterns originating from the combination of synoptic and non-synoptic winds forced by atmospheric processes belonging to different scales of motion. From (a) to (d), panels depict flow patterns at ever shorter horizontal scales (based on [17]).

Figure 6 illustrates, in a schematic way, the passage of a non-stationary downburst by a building [24]. It is evident that the building is subject to winds of different intensity and directions. This is one of the reasons why wind directionality cannot be used to reduce design wind speeds.
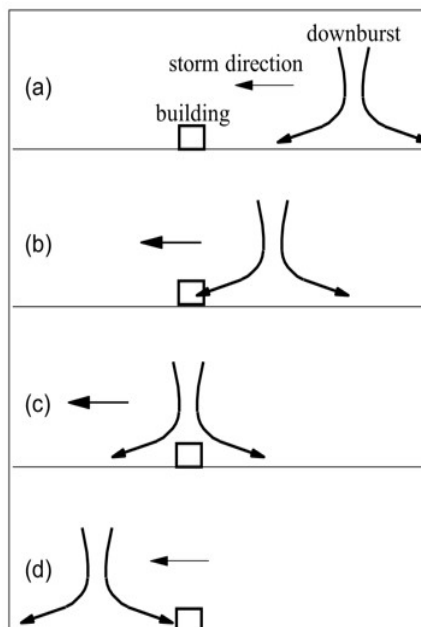


**Figure 6.** Schematic illustration of the passage of a non-stationary downburst by a building (based on Chay et al. [24]).

## 2.3 Climatology of non-synoptic winds

Figure 7 shows results of a recent study [25] that indicates the estimated frequency (in terms of the mean number of hours per year) of atmospheric conditions in South America which favor the occurrence of convective storms in general (left panel) and severe convective storms in particular (right panel); warm colors indicate higher frequencies. In this context, severe convective storms are the ones that generate hailstones with diameter greater than 2 cm, or tornadoes, or non-tornadic wind gusts above 50 kt (slightly over 90 km/h), representing, thus, characteristics that are

particularly relevant to wind engineering. The conditions conducive to general convective storms are more frequent in the Amazon Basin, especially over northwestern Brazil (Figure 7a). In contrast, the atmospheric conditions that lead to severe storms are more frequent over the La Plata Basin including subtropical Brazil (Figure 7b).

Even though the La Plata Basin is recognized as the South American hot spot for severe local storms, this does not exclude the potential for damaging TS winds in the Amazon River Basin. In fact, Figure 7b) does indicate that conditions for severe storms occur with reasonable frequency over far northwestern Brazil (see sector with yellow-orange colors). Second, there is physical evidence of destructive wind gusts of convective nature in the Amazon Basin. A number of studies report the sudden appearance of irregularly-shaped clearings in the rainforest, which are not related to human activity. These clearings are associated with intense wind gusts originated by local convective storms.

To illustrate that, Figure 8 highlights some key results from these studies, consisting of the identification of damage inflicted to the vegetation cover via high-resolution remote sensing using environmental satellite imagery [26]–[28]. Figure 8 shows that fall of large trees caused by natural factors are more frequent in the center-west and in the extreme east of the Amazon Basin. The fallen tree mapping in Figure 8 can be compared with the frequency map of convective storms over the Amazon Basin, Figure 4 of [28]. The color shading in Figure 4 of [28] indicates the frequency of convective storms based on the annual number of days with precipitation surpassing 20 mm (warm colors corresponding to greater frequency). A strong correlation can be identified between these independent sources of information, with a greater frequency of forest clearances occurring precisely where the convective activity is more frequent.

Going back to south-central Brazil, several studies using different methodologies confirm the frequent occurrence of severe storms in this region, including those generating strong winds. One example is shown in Figure 9, which illustrates a map of occurrences of wind gusts of convective nature greater than or equal to 25 m/s in southern Brazil (as measured by the operational network of automated weather stations maintained by INMET – National Institute of Meteorology) between 2005 and 2015 [29]. Figure 9 shows a general tendency for strong convective gusts to be more frequent in the south-west sector of southern Brazil, which matches reasonably well with the climatological map produced by Taszarek et al. [25] for the same sector (Figure 7b). Great part of the local storms producing destructive gusts in southern Brazil, such as supercells and severe quasi-linear convective systems, originate in northeastern Argentina or in southern Paraguay, before advancing to the east towards the Brazilian territory. This essentially accounts for the geographical distribution shown in Figures 7b and 9. With respect to Figure 9, it is important to point out that the density of INMET´s network of surface automated weather stations was not originally conceived to adequately detect wind gusts on the convective scale (i.e., of short duration and small horizontal extension). This means that one can safely state that the map shown Figure 9 provides an underestimation of the actual number of convective events that produced wind gusts equal to or larger than 25 m/s in southern Brazil.
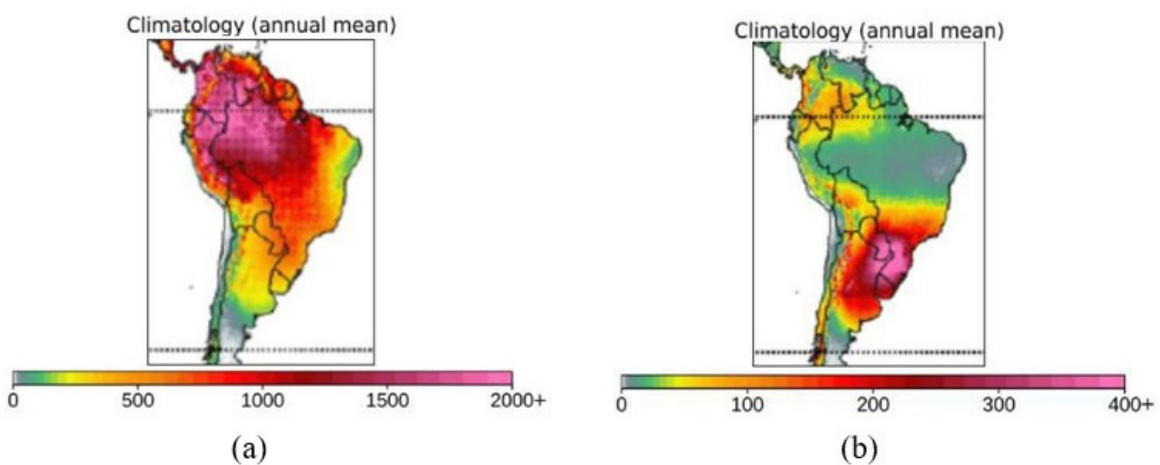


**Figure 7.** Annual frequency, in terms of the mean number of hours per year (see color convention), of atmospheric conditions that are favorable to the occurrence of (a) convective storms in general, and (b) severe convective storms, in South America. The climatology refers to the 1979 to 2019 period and is based on the 5th Generation of the European Center for Medium-Range Weather Forecasting reanalysis (ERA5) dataset. (Adapted from Taszarek et al. [25]).
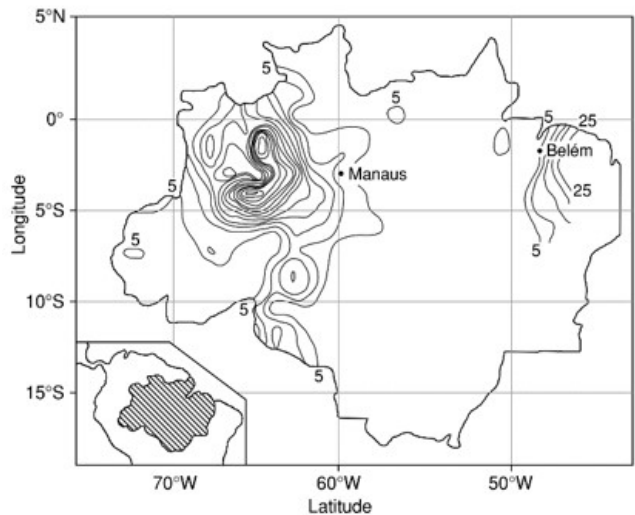
**Figure 8.** Distribution of large forest clearings due to natural causes in the Amazon region (adapted from [26]).
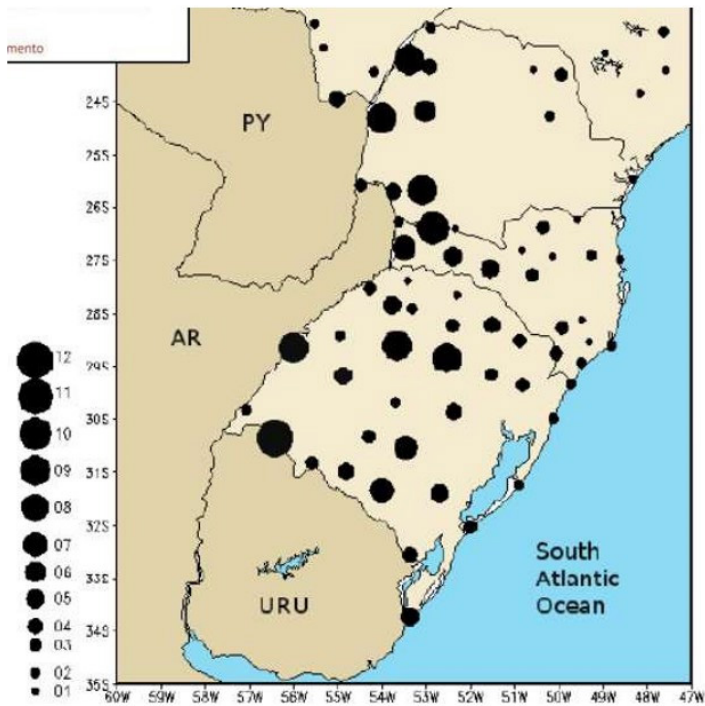


**Figure 9.** Climatology of wind gusts generated by severe storms in southern Brazil, based on measurements from the national network of INMET automated surface weather stations between 2005 and 2015. Diameters of the black circles are proportional to the number of occurrences of convectively-induced wind gusts equal to or greater than 25 m/s; see convention in ref. [29].

## 2.4 Climatology of synoptic winds

Apart from gusts produced by local convective events, synoptic scale winds can also occasionally reach destructive intensity in some regions of Brazil. Figure 10, taken from [30], shows the climatology of surface cyclogenesis over South America, in the period between 1979 and 2005. In the Brazilian context, cyclogenesis refers to formation of extratropical (and sometimes, subtropical) cyclones. These synoptic scale events, when formed over land or close to the shore, produce intense winds which typically last for at least a couple of hours, and which cover much wider areas when compared to local convective storms.

Among the three regions with frequent cyclogenesis in South America, two of them (RG1 and RG2 in Figure 10) affect coastal areas in southern Brazil. In South America, winds of destructive magnitude associated with synoptic-scale cyclones are observed in middle and subtropical latitudes; therefore, the northeast of Brazil is not shown in Figure 10.
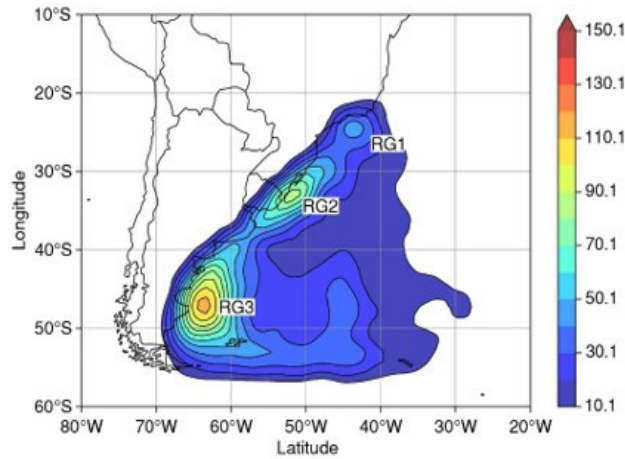


**Figure 10.** Mean annual density of surface cyclogenesis per km$^2$ (see color convention) detected between 1979 and 2015 based on the ERA-Interim reanalysis and the Climate Forecast System reanalysis. The three regions with more frequent cyclogenesis frequency are indicated as 'RG' (based on [30]).

## 2.5 Climate regions associated with strong winds in Brazil

The brief climatological description presented above serves as support to characterize the Brazilian regions which share common atmospheric conditions, leading to meteorological phenomena capable of producing wind gusts of destructive potential. Based on the above, the map of climate regions illustrated in Figure 11 is proposed by the authors to guide wind engineers. This climatological map, to be used in addition to the measured wind data (to be described later), is the basis for the technical sketch of isopleths of the basic wind speed map proposed for NBR 6123. Details of the climatology map are discussed in the sequence.
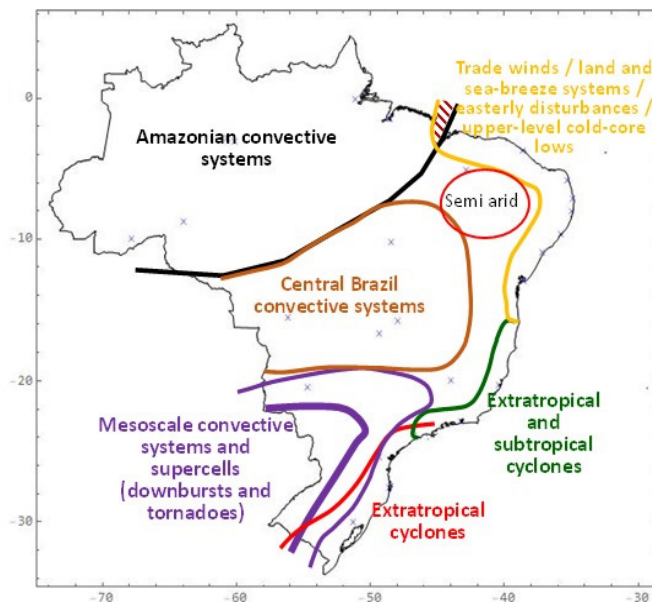


**Figure 11.** Geographical delineation of regions that share similar regimes of atmospheric phenomena that generate intense surface winds in Brazil.

The wind regions shown in Figure 11 are quite large and their delineation is not influenced by non-natural factors such as cities or administrative boundaries. This is in clear contrast with the exaggerated and artificial localized details of the current basic wind speed map [ref. [1], Figure 1], like the strong gradients (concentration of isopleths) over the cities of Brasília and Campinas. The large size of the climatology-based wind regions in Figure 11 is also evidence against some localized details of more recent maps, like the strong gradients over the west of Santa Catarina in [7], [8], and over other seemingly arbitrary small regions in [8]. Some regions, like the south of Brazil, can experience intense winds of synoptic-scale as well as from TS events

## 3 BASIC WIND SPEED FOR BRAZIL: PREVIOUS WORK

Pioneering work dedicated to identify and classify winds in synoptic and non-synoptic include Riera and Nanni [9], who studied annual maximum velocities registered at four towns in the state of Rio Grande do Sul. The authors have shown that, taken separately, winds originating in each type of storm can be better adjusted by a Gumbel or Type I extreme value distribution, than by a Type II or lognormal distribution. At the same time, a mixed series containing synoptic and non-synoptic winds does not adjust very well to Type I, but can be represented by a Type II (Frechet) distribution, as observed in the initial studies leading to the basic wind speed map of NBR 6123 [31].

More recent studies like Almeida [5], Beck and Correa [6], Vallis [7] and Pires et al. [8] employed the Gumbel distribution to adjust annual maximum velocities. Mixed wind series were considered in [5], [6] and [7]; classified and mixed wind series were considered in [7], [32]. In refs. [5]–[7], conventional mathematical regression was used to draw the $V_0$ isopleths map. Pires et al. [8] used Kriging, which is a powerful regression and interpolation tool, but which puts too much weight on the measured wind speed data.

The work of Vallis [7] is commended for the detailed analysis of the quality and homogeneity of the meteorological data [32], and for the large size of the database (a total of 692 weather stations were considered, as shown in Figure 12). One of the relevant results of [7], [32] was the classification of meteorological events into synoptic and non-synoptic. The authors found that, for a mean return period of 50 years, non-synoptic winds originated in TS storms dominate over the largest part of the Brazilian territory. After developing algorithms and criteria to identify and remove spurious data, to classify winds into synoptic and non-synoptic, and homogenize the wind speed time series, the author [7] performed the extreme value analysis for $V_0$ at each weather station. The extreme value analysis was performed for separated synoptic and non-synoptic winds, as well as for the mixed series. Figures 13 and 14 show examples of the Gumbel distribution fit for the mixed wind series in the cities of Florianópolis and Belém, respectively. In these figures, the vertical axis corresponds to wind velocities, and the horizontal axis is a transformed variable dependent on the return period T. For the 50-year return period (T=50), this variable equals 3.9 in the horizontal axis. The diamond markers indicate individual extreme events recorded; the continuous purple line shows the linear model corresponding to a Gumbel distribution fit to the mixed series; and the black line is an envelope of the distribution for the classified synoptic (blue line) and non- synoptic (red line) annual maximum winds. The data collected by Vallis [7], as well as the distribution fit for every weather station, can be checked at www.windytips.com.



Aerodrome (1996-2019)    INMET (2000-2019)
● International  ● Brazilian    ● Conventional  ● Automatic
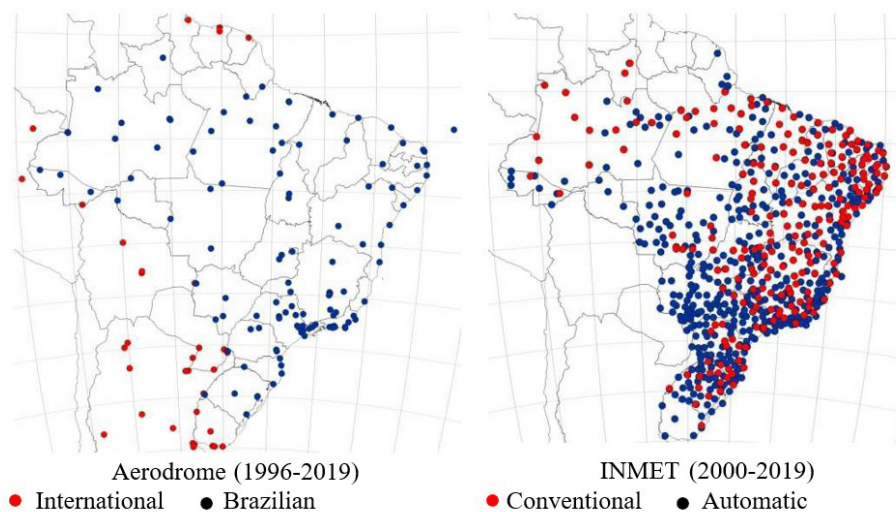
**Figure 12.** Network of meteorological weather stations with wind speed data processed by Vallis [7].
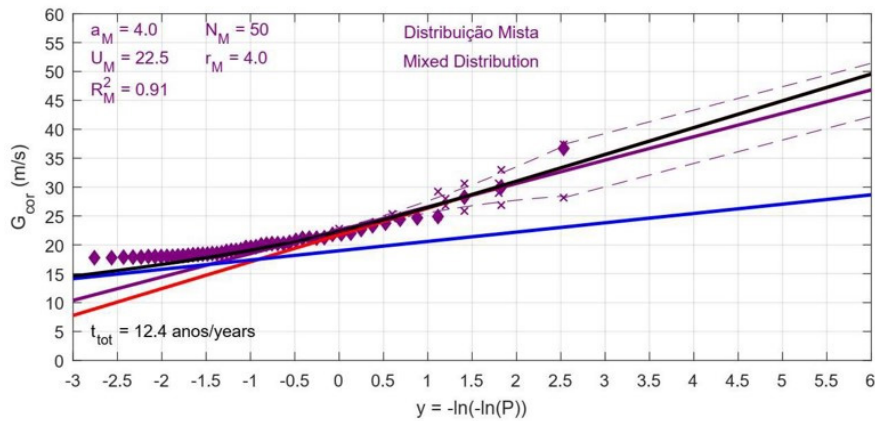
**Figure 13.** Distribution fit and data for maximum annual wind speeds at station A86 in Florianópolis, SC [7].
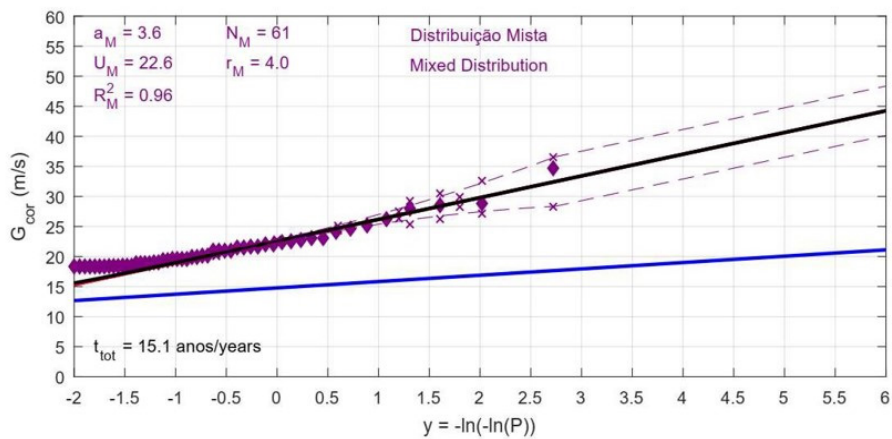


**Figure 14.** Distribution fit and data for maximum annual wind speeds at station SBBE in Belém, PA [7].

Figure 15 shows one of the proposals presented in [7] as basic wind speed map for NBR 6123, where the format of zones with the same basic wind speed is considered. However, the definition of these zones did not take into account the climatological aspects. Figure 16 shows the $V_0$ map proposed by Vallis [7], which was generated by mathematical regression from local mean V0 values determined at so-called dominant weather stations. Selection of these stations was done by a process of filtering, starting from a grid of nodes spaced roughly 50×50 km. The selection process begins with the eight stations closer to the node to be considered, by evaluation of the weighted mean of $V_0$ at these stations, with sample weight being the time-length of each time series. From the eight stations around each node, those with $V_0$ value lower than the local mean minus 3 m/s were removed.

In section 8.3 of his PhD thesis, Vallis [7] points some risks and shortcomings to be considered before adoption of the proposed the map in NBR 6123. The main points stated by the author are:

a) the elaborated map does not consider potential occurrence of tropical cyclones, like hurricane Catarina, which hit the coast of Santa Catarina in 2004, but which was not registered by the weather stations used by the author [7], [32], [33];

b) some weather stations produced $V_0$ values significantly larger than those of the proposed map (Figure 16); for instance, the stations with long time-series records SBBE in Belém (17 years of record) and SBEG in Manaus (19 years of record), with differences of 25 and 20%, respectively.

c) issues like the large differences between $V_0$ values of the current basic wind speed map [ref. [1], Figure 1] and the map elaborated by Vallis [ref. [7], Figure 16]; for instance, in the cities of Campinas, SP (reduction from 45 to 38 m/s) and the central region of Mato Grosso (increase from 30 to 38 m/s) which can also induce changes in the proposition.

In terms of data processing, the following limitations of the work of Vallis [7] can be identified:

i.   small length of the wind speed time series in several stations, which does not warrant reliability of the 50-year mean return wind speeds ($V_0$);
ii.  limitation of parameters to identify and separate synoptic and non-synoptic winds;
iii. several problems found in the database used and corrections implemented;
iv.  the Gumbel distribution used does not adjust itself very well to the data for several stations; for instance, that illustrated in Figure 13, as pointed out by Riera [31] and Riera and Nanni [9]. Typically, these stations are located at zones subject to mixed origin and/or combined (synoptic and non-synoptic) winds.



**Figure 15.** Zone map for non-synoptic winds proposed by Vallis [7].
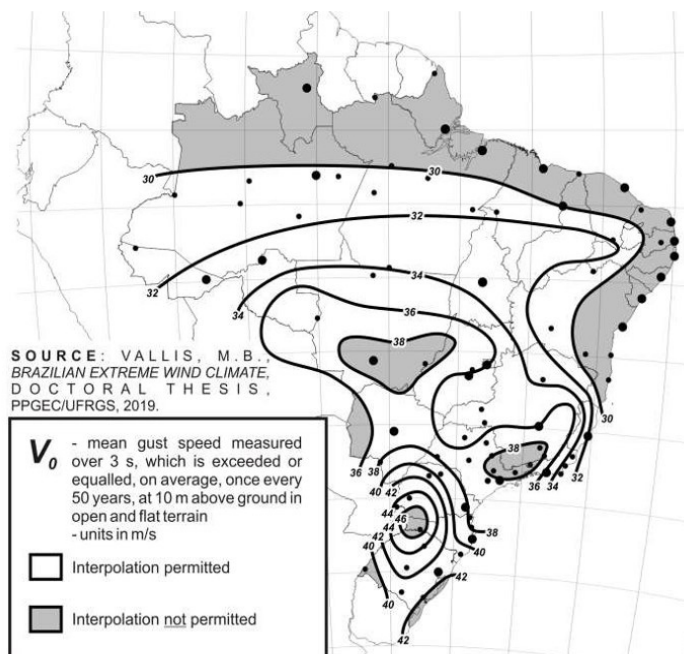


**Figure 16.** Basic wind speed map proposed by Vallis [7].

Despite the limitations mentioned above, the work of Vallis [7] is an important advancement of knowledge, within the research lines developed at Universidade Federal do Rio Grande do Sul (UFRGS) in partnership with Universidade Federal de Santa Maria (UFSM) and Instituto de Aeronáutica e Espaço / Departamento de Ciência e Tecnologia Espacial (IAE/DCTA).

# 4 PROPOSITION OF A CLIMATOLOGY-BASED BASIC WIND SPEED MAP FOR BRAZIL

## 4.1 Premises

From the observation that non-synoptic meteorological events determine extreme wind speeds in the majority of the Brazilian territory, and considering that design criteria and aerodynamic coefficients given in current wind codes were developed considering synoptic winds, a question arises about the possibility of establishing separate design procedures and maps for synoptic and non-synoptic winds. The specialized literature [34], [35], however, points to the impossibility of such division at present time, due to the lack of analytical models of universal acceptance which correctly represent the flow characteristics of non-synoptic events, and of their interactions with constructions. Moreover, as pointed out above, in the same meteorological event the mutual occurrence of synoptic and non-synoptic winds is possible, increasing the difficulty for separate consideration of these wind types. Another issue to be considered is the necessity to significantly increase the reliability of the wind speed data collected in the country before separate basic wind speed maps can be produced. The short length of wind time series at most weather stations [7], [32] also precludes, or reduces the reliability, of projecting the 140-year mean return wind, or the wind with 30% probability of occurrence in 50 years, as advocated by NBR 8681 [36].

Considering the above, the current proposition of a basic wind speed map for NBR 6123 is a 50-year return wind, without separation of meteorological events. We point out, however, that work is currently in progress, with the targets of separating these wind regimes in the future and adopting longer return periods. In this setting, the current proposition of a $V_0$ map for NBR 6123 is called 'transition code'.

The basic wind speed map proposed herein, to be adopted in the 'transition code', was build considering the climatic regions shown in Figure 11, and the $V_0$ values obtained and processed by Vallis [7]. Special attention was given to the possible occurrence of tropical cyclones in the coastal region of south Brazil, as hurricane Catarina registered in 27/03/2004 [37]. The proposed map uses the format of isopleths (a line on a map connecting points having equal incidence of a specified meteorological feature; in the present case, wind speeds).

In this work, subsets of weather stations and corresponding $V_0$ data were selected, among those processed by Vallis [7], to support drawing of the basic wind speed isopleths. These subsets are representative of the extreme winds to be expected at each climatological region (Figure 11). The selection of weather stations privileged those with higher $V_0$ values, and this is plainly justified by the localized characteristic of TS storms (see Figure 2), which leads to significant subsampling by the network of meteorological stations, as addressed in Section 2. In brief, non-synoptic winds may be captured by one station but not registered at a neighboring station, situated at a distance larger than the spatial scale of the phenomenon. Other events may not be registered at all. From this understanding, it can be concluded that Vallis's [7] procedure of taking the average of the $V_0$ values among neighboring stations, to obtain a representative value for one location, introduces a flagrant contradiction with the nature of the physical phenomena, particularly its reduced dimensions, with respect to the density of weather stations.

To compose the database of $V_0$ values to support drawing of the map, we selected weather stations which $V_0$ values are larger than a minimum for each climatologic region. These values, shown in Table 1, were defined by considering the current basic wind speed map (Figure 1).

**Table 1.** Range of $V_0$ values used in selecting weather stations to compose the database for the proposed map.

| Geographical Region* | Climate region (colors refer to Figure 11) | Basic velocity $V_0$ |
|---|---|---|
| Norte (Amazônia) | Amazonian Convective Systems | $V_0 > 30$m/s |
| Sul | Mesoscale Convective Systems / supercells (thick purple line), extra- tropical cyclones VS | $V_0 > 40$m/s |
| Centro-Oeste and Sudeste | Mesoscale convective systems (thin purple line) in MS and SP | $V_0 > 36$m/s |
| Centro-Oeste | Convective systems of central Brazil | $V_0 > 33$m/s |
| Sudeste (coast) | Extratropical / subtropical cyclones VS | $V_0 > 34$m/s |
| Nordeste | Trade winds / land and sea breeze systems / easterly disturbances | $V_0 > 30$m/s |
| Nordeste | Semi-arid | $V_0 > 33$m/s |

*Own names kept in Portuguese.

This procedure is also backed by the fact that $V_0$ values published by Vallis [7] were obtained from data selected using rigorous criteria with respect to the parameters of the homogenization phase. Hence, the data selected to support our map cannot be questioned for the single fact of being higher than the remaining ones. Moreover, due to the rigorous data processing, it is possible that non spurious values originated from real events have been excluded.

Figure 17 shows a panorama of the database used to support drawing of the map proposed herein. The $V_0$ values shown in the map refer to each weather station following Vallis [7].



**Figure 17.** Overview of selected weather stations and corresponding $V_0$ values (m/s) processed by Vallis [7].

## 4.2 Drawing of isopleths and final map

Having selected $V_0$ values to support drawing of the map, and looking at the climatic regions of Figure 11, we proceeded to draw the isopleths. The regions with well-defined atmospheric characteristics were considered first, leaving boundary regions with mixed climate for the last steps. We started by the Amazon region, following with the south and the northeast coast, concluding with the center and south-east. In general, the $V_0$ value for each curve was chosen based on more frequent (modal) values. For certain regions, in addition to the local climatology and $V_0$ values, other criteria were applied, such as physical evidence of destructive wind action, the possibility of occurrence of tropical cyclones and the imprecise fitting of the Gumbel distribution applied to the data. These will be explained for each region, as follows.

The analysis of few $V_0$ data in the Amazon region revealed an interesting correlation with the results shown in Figure 8. The cities of Coari (AM) and Belém (PA), highlighted by red circles in Figure 17, are found inside the contours shown in Figure 4 of [28] associated to higher frequency of intense storms and distribution of large areas of forest devastated by wind action (Figure 8). The $V_0$ values are 37.2 m/s and 36.7 m/s for the cities of Coari and Belém, respectively. The mentioned areas were associated to an isopleth of 36 m/s, whereas in the region between these, an isopleth of 33 m/s was drawn, as shown in Figure 18. Towards east, closing of the 33 and 36 m/s lines follows the boundaries of the Amazon climatic region, as shown in Figure 11.
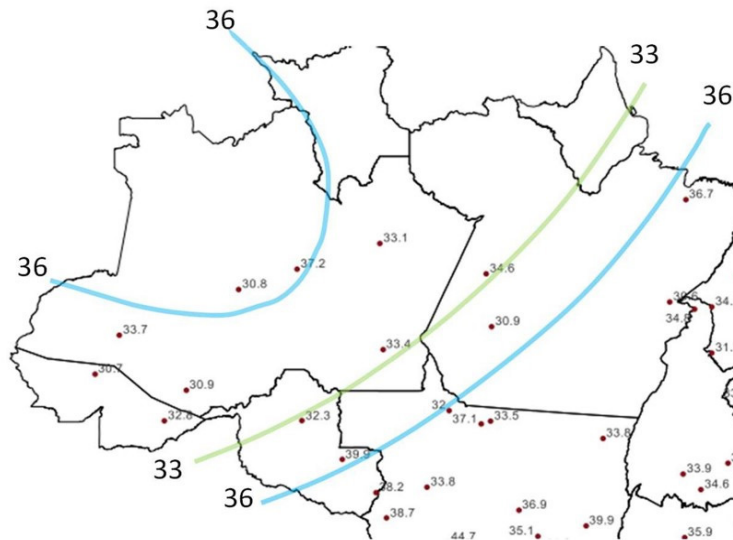


**Figure 18.** Amazon climate region and proposed isopleths, $V_0$ in m/s.

Figure 19a shows a detail of the south region of the map in Figure 11, where one observes the region of occurrence of severe TS storms, as described in Section 3. In this region, several stations show $V_0$ values in the range between 47 and 49 m/s, with the station of Chapecó (SC) showing $V_0$ =50.8 m/s. Hence, the $V_0$ value of 48 m/s was chosen for this region (Figure 19b). Progressing towards north and east, the $V_0$ values are reduced, and the isopleths of 45 and 42 m/s were drawn. This last line meets the coast near the boundaries between the states of São Paulo and Paraná, such that the coast of the states of Santa Catarina and Paraná have values between 42 and 45 m/s, also having in mind the known occurrence of tropical cyclones in this region, for which no measurements are available. Moreover, as a region subject to the simultaneous occurrence of synoptic and non-synoptic winds, the imprecise fit of the Gumbel distribution and the statistical treatment were also considered (see Section 3).

The northeast region presents the climate regions shown in detail in Figure 20a). In the coastal areas, almost all weather stations registered data leading to $V_0$ values lower than 30 m/s, such that the isoline of $V_0$ =30 m/s was drawn, following the boundary of the climate zone (see Figure 20b). In the semi-arid climate region, the $V_0$ values are higher, reaching 35 m/s, whereas at the Ouricuri station (PE) the value is 40.6 m/s.

The 'Centro-Oeste' climate region is characterized as shown in Figure 21a), and 'Sudeste' region shows large areas of transition between well characterized climate zones. As the last climate regions to be treated, a compatibility between previously drawn isopleths is sought. An extensive area including the states of MS and SP, and the south of the states of MT, GO and MG shows $V_0$ values between 38 and 42 m/s. In this region we inserted a 40 m/s isopleth following the thin purple line in Figure 21a) towards the west, and the curvature of this line towards the state of MG. More to the north, the isoline associated to 38 m/s and the adjacent 36 m/s line approach the northeast boundary of the region characterized as 'Central Brazil Convective systems' (Figure 11) and follow towards the coast of 'Sudeste' region. The three central lines associated to 36 m/s form a closed area with constant $V_0$.

With the methodology just described, the complete map shown in Figure 22 was obtained, and has been proposed for adoption in the next edition of NBR 6123. In the hatched areas interpolation is not permitted.

(a)       (b)
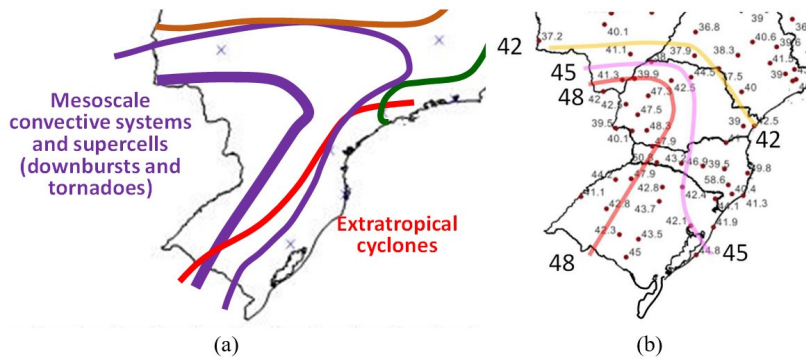
**Figure 19.** South region: a) climatic regions; b) proposed isopleths (V₀ in m/s).



(a)       (b)
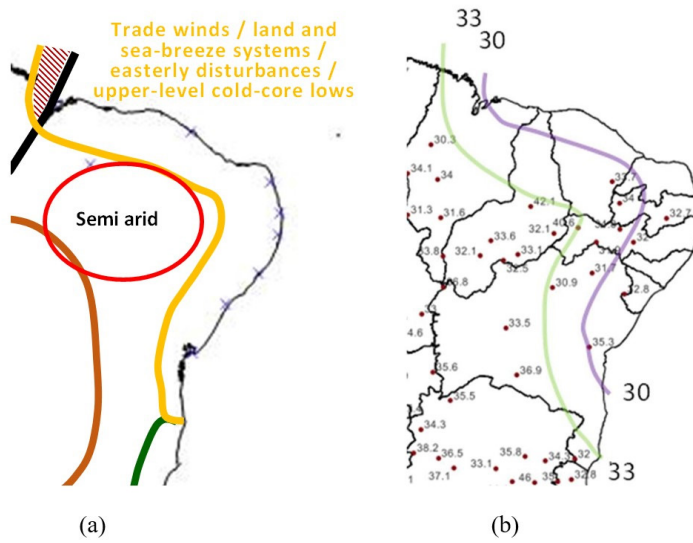
**Figure 20.** Northeast region: a) climatic regions; b) proposed isopleths (V₀ in m/s).



(a)       (b)
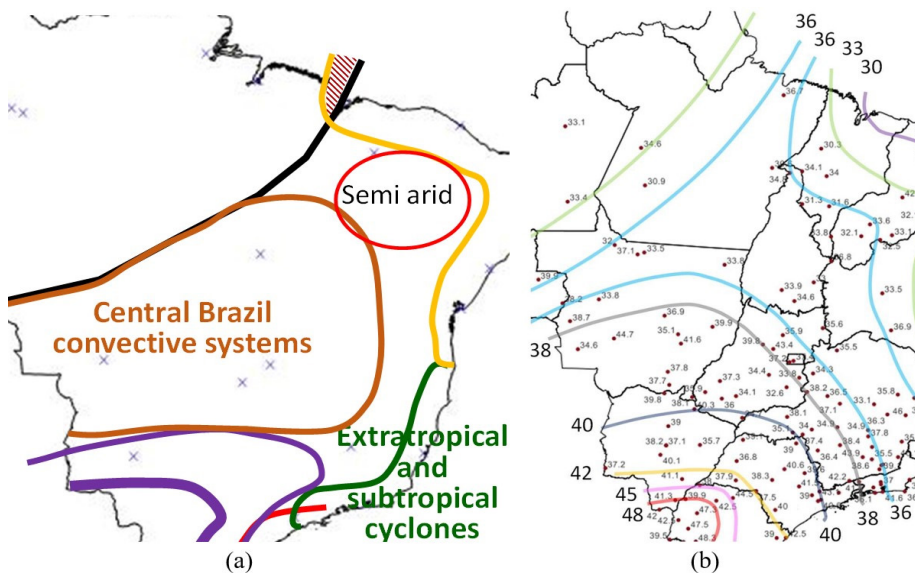
**Figure 21.** Center and southeast region: a) climatic regions; b) proposed isopleths (V₀ in m/s).

A. M. Loredo-Souza, M. S. Pfeil, E. L. Nascimento, J. D. Riera, G. F. Fisch, and A. T. Beck
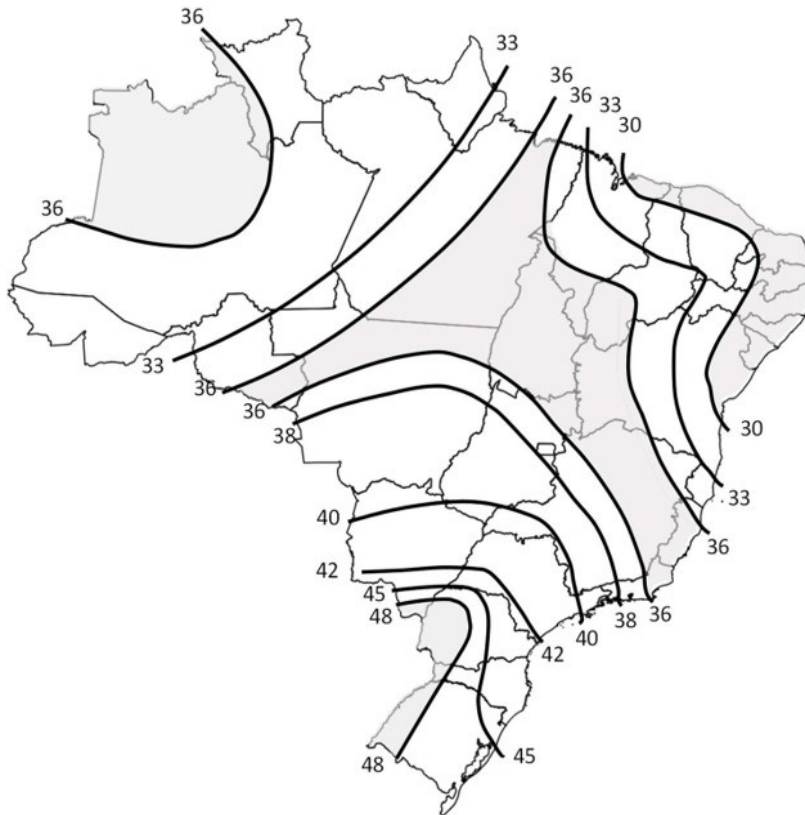


**Figure 22.** Final basic wind speed map proposed for NBR 6123 (isopleths with $V_0$ in m/s).

## 5 CONCLUDING REMARKS

In this manuscript a new basic wind speed ($V_0$) map, proposed for adoption in NBR 6123, is presented and justified. The novel approach to this map is the definition of characteristic climate zones producing strong winds in Brazil. These climate zones were used as a guide for the manual technical drawing of the wind speed isopleths. The $V_0$ values characterizing each climate zone and giving support to the isopleths were obtained from data categorized and processed by Vallis [7]. Unfortunately, due to limitations in the length of wind speed time series available in Brazil, the adoption of a return period longer than 50 years was not found possible at this time.

The proposed map, shown in Figure 22, has basic wind speeds ranging between 30 and 48 m/s. The climatological approach took into consideration the physical characteristics of the phenomena leading to strong winds in Brazil. This is in contrast with, and a significant improvement in comparison to, the pure mathematical regression approaches used in other maps. We expect that the adoption of the proposed map will increase the reliability of structural design in Brazil, with a proper balance between constructions and expected failure costs.

## ACKNOWLEDGEMENTS

## REFERENCES

[1]   Associação Brasileira de Normas Técnicas, *Forças devidas ao vento em edificações*, NBR-6123, 1988.

[2]   J. M. S. Vieira Fo., "Velocidades máximas do vento no Brasil," M.S. thesis, Esc. Eng., Univ. Fed. Rio Grd. Sul, Porto Alegre, Brasil, 1975.

[3]   J. Blessmann, *Tópicos de normas de vento* (2. ed., Série Engenharia Estrutural 6), Porto Alegre, RS: Editora da UFRGS, 1990.

[4]   I. J. Padaratz, "Velocidade básica do vento do Brasil," M.S. thesis, Esc. Eng., Univ. Fed. Rio Grd. Sul, Porto Alegre, RS, Porto Alegre, 1977.

[5] L. D. Almeida, "Estudo para atualização do mapa de ventos da NBR-612," Ph.D. dissertation, Engenharia de Infraestrutura Aeronáutica, Instituto Tecnológico de Aeronáutica, São José dos Campos, São Paulo, 2010.

[6] A. T. Beck and M. R. S. Correa, "New design chart for basic wind speeds in Brazil," *Lat. Am. J. Solids Struct.*, vol. 10, pp. 707–723, 2013, http://dx.doi.org/10.1590/S1679- 78252013000400003.

[7] M. B. Vallis, "Brazilian extreme wind climate," Ph.D. dissertation, Esc. Eng., Univ. Fed. Rio Grd. Sul, Porto Alegre, RS, 2019.

[8] A. V. Pires et al., "Updated design wind map for Brazil and impacts on the reliability of built structures," *ASCE J. Risk Uncertain. Part A.*, vol. 7, pp. 04021058, 2021, http://dx.doi.org/10.1061/AJRUA6.0001183.

[9] J. D. Riera and L. F. Nanni, "Pilot study of extreme wind velocities in a mixed climate," *J. Wind Eng. Ind. Aerodyn.*, vol. 32, pp. 11–20, 1989.

[10] J. D. Riera and M. M. Rocha, "Load definition for wind design and reliability assessments; extreme wind climate", in *Wind Effects on Buildings and Structures*, J. D. Riera, and A. G. Davenport, Ed., Rotterdam: A.A. Balkema, 1998.

[11] J. Ponte and J. D. Riera, "Simulation of extreme wind series caused by thunderstorms in temperate latitudes," *Struct. Saf.*, vol. 32, pp. 231–237, 2010, http://dx.doi.org/10.1016/j.strusafe.2010.02.002.

[12] J. Blessmann, *O Vento na Engenharia Estrutural*, 2. ed., Porto Alegre, RS, Brasil: Editora da UFRGS, 2013.

[13] A. M. Loredo-Souza, "Meteorological events causing extreme winds in Brazil," *Wind Struct Int. J.*, vol. 15, pp. 177–188, 2012, http://dx.doi.org/10.12989/was.2012.15.2.177.

[14] A. M. Loredo-Souza, E. G. Lima, M. B. Vallis, M. M. Rocha, A. R. Wittwer, and M. G. K. Oliveira, "Full-scale downburst damage versus boundary layer wind tunnel pressures: a survey analysis," in *Proc. 8th Int. Colloquium on Bluff Body Aerodynamics and Applications*, Northeastern University, Boston, Massachusetts, USA, June 2016.

[15] E. L. Nascimento, "Previsão de tempestades severas utilizando-se parâmetros convectivos e modelos de mesoescala: Uma Estratégia operacional adotável no Brasil," *Rev. Bras. Meteorol.*, vol. 20, pp. 121–140, 2005.

[16] T. T. Fujita, *Manual of Downburst Identification for Project NIMROD* (SMRP Research Paper 156). Chicago, IL, USA: Univ. of Chicago, 1978, 104 pp. [NTIS PB-286048].

[17] T. T. Fujita, "Tornadoes and downbursts in the context of generalized planetary scales," *J. Atmos. Sci.*, vol. 38, pp. 1511–1534, 1981.

[18] T. T. Fujita, *The Downburst: Microburst and MACROBURSt* (SMRP Research Paper 210), Chicago, IL, USA: Univ. of Chicago, 1985, 122 pp. [NTIS PB85-148880].

[19] Loredo-Souza, A.M., Lima, E.G., Vallis, M.B., Rocha, M.M., Wittwer, A.R., and M.G.K. Oliveira, "Downburst related damages in Brazilian buildings: are they avoidable," *J. Wind Eng. Ind. Aerodyn.*, vol. 185, pp. 33–40, 2019.

[20] D. D. Vicroy, "Assessment of microburst models for downdraft estimation," *J. Aircr.*, vol. 29, no. 6, pp. 1043–1048, 1992.

[21] L. F. F. Miguel, J. D. Riera, and L. F. F. Miguel, "Assessment of downburst wind loading on tall structures," *J. Wind Eng. Ind. Aerodyn.*, vol. 174, pp. 252–259, 2018, http://dx.doi.org/10.1016/j.jweia.2018.01.015.

[22] C. Li, Q. S. Li, Y. Q. Xiao, and J. P. Ou, "Simulations of moving downbursts using CFD," in *The Seventh Asia-Pacific Conf. Wind Engineering (APCWE-VII)*, Taipei, Taiwan, 2009 November 8-12.

[23] T. T. Fujita and R. M. Wakimoto, "Five scales of airflow associated with a series of downbursts on 16 July 1980," *Mon. Weather Rev.*, vol. 109, pp. 1438–1456, 1981.

[24] M. T. Chay, F. Albermani, and R. Wilson, "Numerical and analytical simulation of downburst wind loads," *Eng. Struct.*, vol. 28, no. 2, pp. 240–254, Jan 2006, http://dx.doi.org/10.1016/j.engstruct.2005.07.007.

[25] M. Taszarek, J. T. Allen, M. Marchio, and H. E. Brooks, "Global climatology and trends in convective environments from ERA5 and rawinsonde data," *npj Clim Atmos Sci.*, vol. 4, pp. 35, 2021, https://doi.org/10.1038/s41612-021-00190-x.

[26] M. Garstang, S. White, H. H. Shugart, and J. Halverson, "Convective clouds downdrafts as the cause of large blowdowns in the Amazon Rainforest," *Meteorol. Atmos. Phys.*, vol. 67, pp. 199–212, 1998.

[27] B. W. Nelson, V. Kapos, J. B. Adams, W. J. Oliveira, O. P. G. Braun, and I. L. Amaral, "Forest disturbance by large blowdowns in the Brazilian Amazon," *Ecology*, vol. 75, no. 3, pp. 853–858, 1994.

[28] F. D. B. Espírito-Santo, M. Keller, B. Braswell, B. W. Nelson, S. Frolking, and G. Vicente, "Storm intensity and old-growth forest disturbances in the Amazon region," *Geophys. Res. Lett.*, vol. 37, pp. L11403, 2010.

[29] V. Ferreira, "Um estudo observacional de rajadas de vento geradas por tempestades severas no sul do Brasil," M.S. thesis, Univ. Fed. Sta. Maria, Santa Maria, RS, Brasil, 2017.

[30] E. de Jesus, R. Rocha, N. Machado Crespo, M. Reboita, and L. Gozzo, "Multi-model climate projections of the main cyclogenesis hot-spots and associated winds over the eastern coast of South America," *Clim. Dyn.*, 2021, http://dx.doi.org/10.1007/s00382-020-05490-1.

[31] J. D. Riera, "Sobre a definição do vento para projeto estrutural na ABNT NBR-6123 (1989) e outras normas sul americanas," *Rev. Sul Amer. Eng. Estr.*, 2016, vol. 13, no. 3, pp. 1-27.

[32] M. B. Vallis, A. M. Loredo-Souza, and L. C. Watrin, "A review of Brazilian wind data," in *Proc.13th Americas Conf. Wind Eng. (13ACWE)*, Gainesville, Florida USA, 2017 May 21-24.

[33] A. J. Pereira Fo., A. B. Pezza, I. Simmonds, R. S. Lima, and M. Vianna, "New perspectives on the synoptic and mesoscale structure of Hurricane Catarina," *Atmos. Res.*, vol. 95, no. 2–3, pp. 157–171, 2010, http://dx.doi.org/10.1016/j.atmosres.2009.09.009.

[34] C. W. Letchford and F. T. Lombardo, "Is codification of non-synoptic wind loads possible? Invited Lecture," in *Proc. 14th Int. Conf. Wind Eng.*, Porto Alegre, RS, Brasil, June 2015.

[35] G. Solari, "Thunderstorm downbursts and wind loading of structures: progress and prospect," *Front. Built Environ.*, vol. 22, May 2020, http://dx.doi.org/10.3389/fbuil.2020.00063.

[36] Associação Brasileira de Normas Técnicas, *Ações e Segurança das Estruturas*, NBR-8681, 2003.

[37] Marcelino, I.P.V.O., Nascimento, E. L., Ferreira, N.J., *Tornadoes in Santa Catarina State (Southern Brazil): Event Documentation, Meteorological Analysis and Vulnerability Assessment*, São José dos Campos, SP, Brasil: INPE, 2005, pp. 1–15.

Rev. IBRACON Estrut. Mater., vol. 16, no. 4, e16401, 2023

18/18

# IBRACON Structures and Materials Journal
## Revista IBRACON de Estruturas e Materiais

ORIGINAL ARTICLE

# Cross-correlation for feature extraction applied to ultrasonic test for stress evaluation in concrete

*Correlação-cruzada para extração de características aplicada a ensaio ultrassônico para avaliação de tensão em concreto*

Rafaella Moreira Lima Gondim[a] 
Karen Fernanda Bompan[a] 
Vladimir Guilherme Haach[a] 

[a]Universidade de São Paulo – USP, Escola de Engenharia de São Carlos, Departamento de Engenharia de Estruturas, São Carlos, SP, Brasil

**Abstract:** Changes in the stress state of a solid medium cause small variations in wave propagation velocities. Cross-correlation (CC) is a tool used for similarity evaluations between two data series. This paper addresses the use of the CC function for the feature extraction of ultrasonic test data that evaluated the stress state in a concrete specimen subjected to compressive loads. The CC function was applied to waveforms, and an analysis of influential parameters (e.g., CC-Domain, time window, and center-time) assessed the differences between the various stress levels. The results showed the variations in $\Delta V/V_0$ vs. stress diagrams were lower in the elastic regime, whereas the analyzed parameters highly influenced the results. S-waves were more suitable for analyses of stress variation, since they were little influenced by time window and center-time.

**Keywords:** non-destructive tests; ultrasound; acoustoelasticity; direct waves; anisotropy.

**Resumo:** Mudanças no estado de tensões de um meio sólido causam pequenas variações nas velocidades de propagação de ondas mecânicas. A Correlação Cruzada (CC) é uma ferramenta utilizada para avaliação de similaridade entre dois conjuntos de dados. Este artigo aborda o uso da função CC para extração de características em dados de ensaios ultrassônicos que avaliam o estado de tensões em um corpo de prova de concreto submetido a carregamentos de compressão. A função CC foi aplicada aos sinais, e uma análise dos parâmetros relevantes (e.g., Domínio-CC, janela de tempo e tempo central) avaliou as diferenças entre os vários níveis de tensão. Os resultados mostraram que as variações nos diagramas $\Delta V/V_0$ *vs.* tensão foram menores no regime elástico, enquanto os parâmetros analisados tiveram grande influência sobre o resultado. Ondas secundárias foram mais adequadas para análises de variação de tensão por serem menos influenciadas por tamanho da janela e tempo central.

**Palavras-chave:** ensaios não destrutivos; ultrassom; acoustoelasticidade; ondas diretas; anisotropia.

# 1 INTRODUCTION

The emission of mechanical waves of above 20 kHz frequencies in a structural element is a nondestructive test, called ultrasonic pulse velocity (UPV) [1], usually applied for investigations of damages and material homogeneity and obtaining of mechanical properties [2]-[7]. Hughes and Kelly [8] demonstrated the stress state in a solid medium

influences the propagation velocity of mechanical waves. The phenomenon, called acoustoelastic effect, has been explored for evaluations of the stress state in several materials [9]-[11]. Lillamand et al. [12] verified this effect in concrete, analyzing the influence of stress level on the velocity of compression and transversal waves propagated in cylindric samples subjected to different compression loads. Authors concluded that longitudinal and transversal waves polarized along the direction of loading are more sensitive to the acoustoelastic effect, but the scattering caused by the material hindered ultrasonic velocity measurements [12]. Shokouhi et al. [13] evaluated the combination of damage and acoustoleastic effects in concrete prisms through compression tests with specimens and emission of ultrasonic waves during loading and unloading procedures and detected lower wave velocities in the unloading phase for a same stress level resulting from the mechanical damage caused to the concrete during loading. Bompan and Haach [14] performed ultrasonic tests in concrete prisms subjected to uniaxial compression and observed pre-loadings changed the acoustoelastic behavior due to the Kaiser effect related to the crack generated in concrete elements by the loading.

The propagation velocity of mechanical waves in a solid medium is not influenced by the stress state only in the elastic regime of the material behavior. Several researchers have extended the concepts of acoustoelasticity theory for evaluations of solids with plastic deformation and have called this interaction acoustoplasticity [15]-[17]. Belchenko et al. [18] studied the applicability of the acoustoelasticity method for the estimation of the strain-stress state of dilute aluminum manganese alloy specimens under cyclic loading in the presence of elastic and plastic strains and observed a dependence of stress state on the velocity measurements from the early stages of loading until the fracture of the sample. Mohammadi and Fesharaki [19] investigated the ability of the ultrasonic test to measure stress in both elastic and plastic limits in metal specimens using critically refracted longitudinal (LCR) waves and introducing acoustoplastic constants. LCR are bulk longitudinal waves that propagate parallel to the surface of the specimen.

Changes in the stress state of a solid lead to very small variations in the values of the propagated velocities, which requires an accurate feature extraction methodology. The simplest strategy involves an evaluation of the time-of-flight (TOF) of ultrasonic waves in unperturbed and perturbed media and calculation of the relative velocity variation with the use of path length. However, it may lead to some imprecise results due to difficulties in the definition of the exact time of arrival of compression and transversal waves.

Cross-correlation is a powerful tool widely used in several research areas (e.g., engineering, economics, statistics, medicine, etc.) for comparisons between two series. The cross-correlation function provides a measure of similarity between two signals (perturbed and unperturbed) through the translation of the first signal in the time axis. The coda wave interferometry (CWI), commonly used for evaluations of the acoustoelastic effect, is an example of the application of the CC function. CWI is based on a cross-correlation of two wave signals emitted in unperturbed (no stress) and perturbed (a stress state) media in the tail of the waveform [20]-[24]. Coda waves correspond to scattered waves of late arrival and longer travel-times [20]. According to Planès and Larose [25], the main advantage of the use of these waves is their very high sensitivity to weak perturbations in a medium. Two variations of the method, called doublet and stretching methods, are based on measurements of the time shift and stretching of the time axis of the perturbed signal, respectively [25], [26].

According to the doublet method, a *2T* time window is moved in the time axis by a time shift $t_s$ around a center-time $t_c$ of the perturbed signal. The cross-correlation function ($CC$) is calculated for each $t_s$. The value of time shift that maximizes $CC$, $t_{sMaxCC}$, corresponds to the time delay between unperturbed and perturbed signals. This procedure can be adopted for different values of $t_c$, therefore, the method evaluates the time shifts in consecutive time windows at different $t_c$. The normalized cross correlation function is applied according to Equation 1, where $u_{unp}$ and $u_{per}$ are unperturbed and perturbed signals, respectively [25], [27], [28], and its value ranges from -1 to 1, periodically, if the time shift is the only difference of the series.

$$CC(t_s) = \frac{\int_{t_c-T}^{t_c+T} u_{unp}(t) u_{pert}(t-t_s) dt}{\sqrt{\int_{t_c-T}^{t_c+T} u_{unp}^2(t) dt \int_{t_c-T}^{t_c+T} u_{pert}^2(t) dt}} \qquad (1)$$

Grêt et al. [28] reported the relative velocity variation ($\Delta V/V_0$) can be obtained by Equation 2, where $V_0$ is the wave velocity in the unperturbed medium.

$$\frac{\Delta V}{V_0} = -\frac{t_{sMaxCC}}{t_c} \qquad (2)$$

On the other hand, in the stretching method, the perturbed signal, $u_{pert}$, is stretched or compressed from $u_{pert}(t)$ to $u_{pert}[t(1+\tau)]$ according to a factor $\tau$ for simulating the velocity variation from $V$ to $V(1+\tau)$. The similarity between unperturbed and perturbed signals, $u_{unp}$ and $u_{pert}$, respectively, is evaluated by normalized cross correlation function $CC(\tau)$ within a $2T$ time window, as showed in Equation 3. The value of $\tau$ that maximizes $CC(\tau_{MaxCC})$ is the relative velocity variation, $\Delta V/V_0$, corresponding to the analysis conducted with the window central time, $t_c$.

$$CC(\tau) = \frac{\int_{t_c-T}^{t_c+T} u_{unp}(t)u_{pert}(t(1+\tau))dt}{\sqrt{\int_{t_c-T}^{t_c+T} u_{unp}^2(t)dt \int_{t_c-T}^{t_c+T} u_{pert}^2(t)dt}} \qquad (3)$$

Hadziioannou et al. [29] compared the use of doublet and stretching methods to verify small velocity changes in a medium with an agar-agar gel solution. The authors observed that, although demanding more computational costs, the stretching technique was more stable with respect to noise in the data. Authors also showed that cross-correlation techniques are valid to determine velocity variation even with low signal-to-noise ratios if there is a stable source signal.

Cross-correlation methods applied to time series are dependent on some variables, e.g., time window length, center-time of the window, and range of time shift. Payan et al. [30] employed the CWI doublet method and acoustoelasticity to obtain the coefficients defined by Murnaghan [31] in concrete samples. They applied a loading so as not to exceed 30% of the ultimate strength and remain in the elastic regime. The CWI analysis was performed with a center-time variation, and the results indicated a constant relative velocity variation for compressional waves. Niederleithinger et al. [32] compared relative velocity variation *vs.* stress obtained by TOF and CWI procedures and concluded CWI displays greater sensitivity to stress and damage in concrete cubes. However, they highlighted CWI and TOF results are not immediately comparable, since TOF is related to direct waves, whereas CWI evaluates a weighted average of different wave type velocities. As the authors used CWI, the cross-correlation procedure was only applied to waves of late arrival.

Although CWI is largely used in research on acoustoelastic and damage effects through ultrasonic tests, the literature lacks information on the application of cross-correlation methods for feature extraction in earlier parts of the signal, close to the arrival of longitudinal and transversal waves. Additionally, determination of parameters used for cross-correlation outside the elastic regime requires further investigation. Therefore, this paper discusses the parameters of cross correlation for feature extraction applied to longitudinal and transversal waves from ultrasonic tests to evaluate the stress state in concrete.

## 2 METHODOLOGY AND EXPERIMENTAL PROGRAM

This section describes the proposed methodology for the assessment of cross-correlation as a method for feature extraction applied to ultrasonic tests for stress evaluation in concrete. The main steps of this work are shown in Figure 1. Description of material properties and test specimens are found in Section 2.1 and Section 2.2, respectively. After characterization tests, ultrasonic tests were conducted in a prismatic specimen to evaluate the influence of stress level on the ultrasonic pulse velocity (UPV), as described in Section 2.3. The cross-correlation procedure was applied to the recorded ultrasonic waveforms and an analysis of the influential parameters assessed the differences between the applications of low and high stresses, as detailed in Section 2.4.
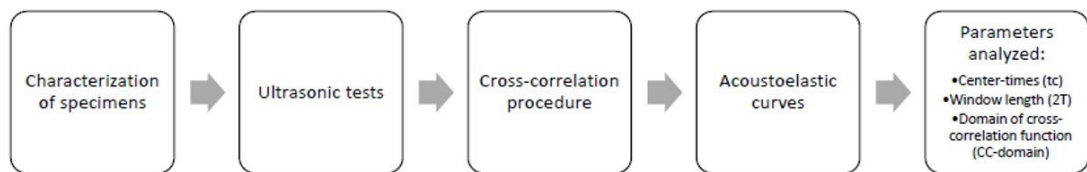


**Figure 1.** Methodology flowchart

## 2.1 Material properties

The materials applied to this research were chosen aiming to obtain a conventional concrete. The concrete mix used was composed of Type III Portland cement of high early strength, as specified by ASTM [33], sand of 2.36 mm maximum size and 2.00 fineness modulus, and gravel of 19 mm maximum size and 6.73 fineness modulus. Both maximum size and fineness modulus of the aggregates were in accordance with ABNT [34], and the proportions of

materials in mass for the production of the concrete were 1:1.30:2.20 (cement:sand:gravel). The water/cement ratio was 0.43 and the material had a 150 mm slump. The concrete composition reached a 30.62 MPa average compressive strength at 28 days, with a 13.45% coefficient of variation.

## 2.2 Test specimens

Four 150 mm x 150 mm x 500 mm prismatic specimens were molded and kept in laboratory for 24 h after casting. The molds were then removed, and the specimens were kept in a moist chamber for curing. At day 28, three prisms were tested under compression towards the definition of the average compressive strength ($f_{cm}$) of the samples. Ultrasonic tests were performed with the remaining sample at ages higher than 28 days.

## 2.3 Ultrasonic tests

Two 250 kHz transducers of 2.00 μs pulse width arranged in a through-transmission setting were used in the ultrasonic tests, and longitudinal and transversal waves were propagated to the tested specimens. A couplant paste specific for the transmission of normal incidence transversal waves was used in the sample-transducer interface. Pundit Lab+ and Pundit Link by Proceq® were, respectively, the ultrasound equipment and the software that obtained the ultrasound signals. The experimental values were recorded every 0.5 μs since the acquisition frequency of the equipment was 2 MHz. The UPV variation was analyzed in two directions, i.e., parallel and perpendicular to the loading direction, called axes 1 and 2, respectively (Figure 2a). The total recording times used in the ultrasonic tests were 360 μs (direction 1) and 120 μs (direction 2).

The ultrasonic tests were performed in a sample subjected to uniaxial compression (see Figure 2a for the experimental setup). A steel frame fixed to a reaction slab and equipped with a hydraulic jack applied the load. Two U-shaped steel plates were positioned above and under the sample (Figure 2b) for safely placing the transducers in an area not subjected to loading for the avoidance of damage to the equipment. Polystyrene pieces (Figure 2c) kept the transducers in contact with the prism surface when the waves were emitted in the direction of the loading, and in place by a rubber strip when the waves were emitted transversally to the loading direction. The transducers were positioned in the center of the corresponding surface of the sample, as shown in Figure 2c and Figure 2d.



(a)                                              (d)
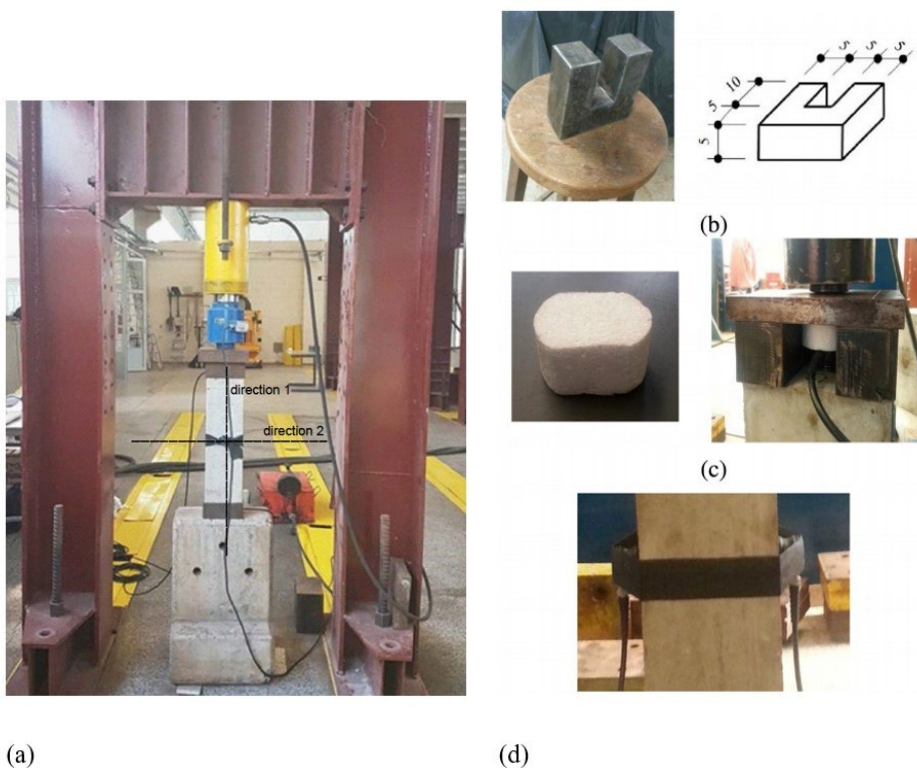
**Figure 2.** Test setup (dimensions in centimeters)

The longitudinal waves were called $LW_{ij}$, and the transversal waves were denoted by $TW_{ij}$, where i represents the axis of propagation of the wave and j is the polarization direction.

Twelve loading cycles were applied to the specimen. A maximum stress ($\sigma_{Max,UPV}$) was applied in each cycle, corresponding to approximately 60% of the compressive strength ($f_{cm}$) equivalent to a force of 440 kN. Bompan and Haach [14] demonstrated UPV variation due to the acoustoelastic effect shows high variability over the first loading cycles. However, there is a trend to a stable behavior as more loading cycles are applied. Towards avoiding this initial variation, the first ten cycles consisted only of pre-loading prior to the ultrasonic tests - no UPV measurements were recorded. The ultrasound test was performed in the unloading phases of the 11th and 12th cycles and the measurements were taken for every 20 kN decrement (22 decrements). According to Shokouhi et al. [13], new cracks are opened only when the applied load exceeds the maximum load of the previous step. Although some cracks propagate due to creep even if the applied load has not exceeded the maximum history load, the influence of new damage will be reduced in the results of the UPV tests performed during unloading. $LW_{11}$ and $TW_{12}$ were emitted in the 11th unloading phase, and $LW_{22}$ and $TW_{21}$ were analyzed in the 12th unloading cycle. The ultrasound signal for each load value was established by the average of ten pulses. The experimental program flowchart is shown on Figure 3.
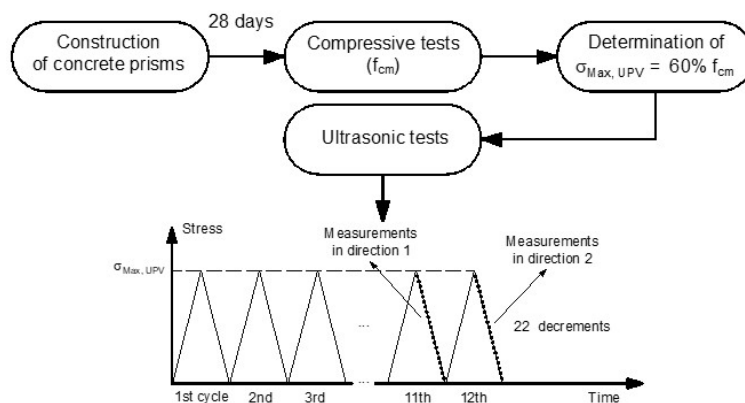


**Figure 3.** Experimental program flowchart

## 2.4 Procedures of feature extraction

Figure 4 shows the waveforms used as references in the UPV analyses. Longitudinal waves were the first to arrive, followed by transversal ones, indicated by an increase in the amplitudes. Arrival of these waves are indicated by grey circles in Figure 4. Cross-correlation was performed according to Equation 1 and the relative velocity variation was obtained by Equation 2.



| (a) | (b) |
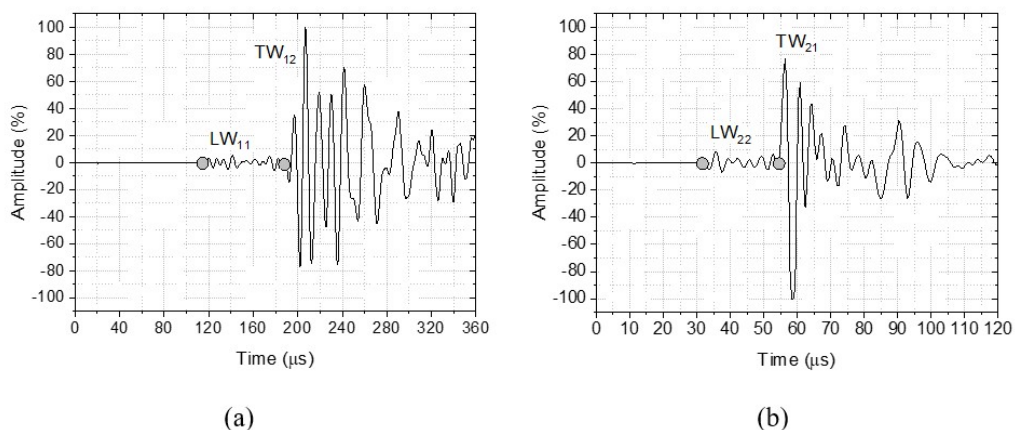
**Figure 4.** Reference waveforms obtained in UPV experiments: (a) direction 1 and (b) direction 2

The cross-correlation function was applied to parts of the waveform. These parts, named as time windows, are identified by a center-time, $t_c$, representing the middle time of the extracted time window; and by a window length, $2T$, that represents the size of the window defined between the points $[t_c - T, t_c + T]$, see Figure 5. In addition, the cross-correlation function was applied to a range of time-shift values ($t_s$) defining the CC-domain.
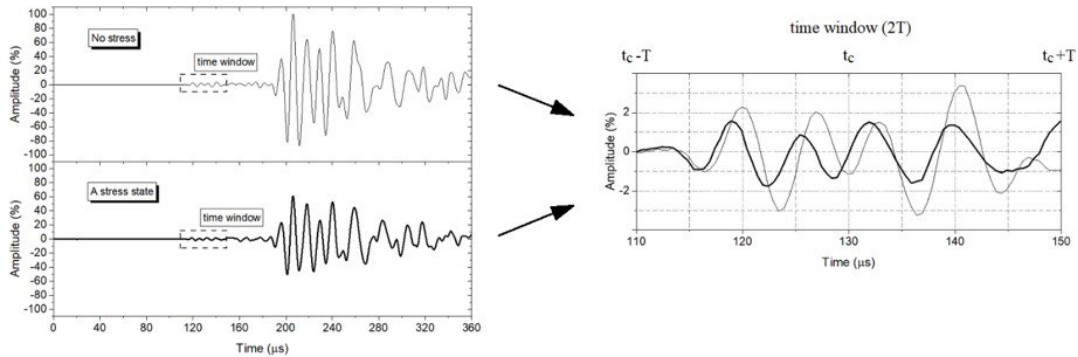


**Figure 5.** Typical time window variables in the feature extraction procedure.

Finally, the feature extraction analysis was performed following the sequence:
a) Construction of $\Delta V/V_0$ vs. $\sigma$ curves using direct waves,
b) Evaluation of the CC-Domain variation in the generation of the $\Delta V/V_0$ vs. $\sigma$ curves,
c) Evaluation of the $t_c$ variation in the generation of the $\Delta V/V_0$ vs. $\sigma$ curves,
d) Evaluation of the 2T variation in the generation of the $\Delta V/V_0$ vs. $\sigma$ curves,
    The range of values of $t_c$ and 2T used in the analyzes could not be standardized for all ultrasonic waves because they were chosen according to the respective waveform.

## 3 EXPERIMENTAL RESULTS

The experimental results show the evaluation of the relative velocity variation as a function of compressive stress for the studied prism. In case of prism with no stress, velocity values $LW_{11}$, $LW_{22}$, $TW_{12}$, and $TW_{21}$ were 4332 m/s, 4733 m/s, 2624 m/s, and 2736 m/s, respectively. All diagrams in Figure 6 show the effect of stress level on the relative velocity variation. According to Mehta and Monteiro [35], below approximately 30% of the compressive strength, the interfacial transition zone cracks remain stable; therefore, the stress vs. strain curve remains linear. This limit is commonly admitted for the elastic behavior of concrete - here, the value was 10.20 MPa. The dependence of UPV on the stress level may also be observed for stress levels over the elastic limit.
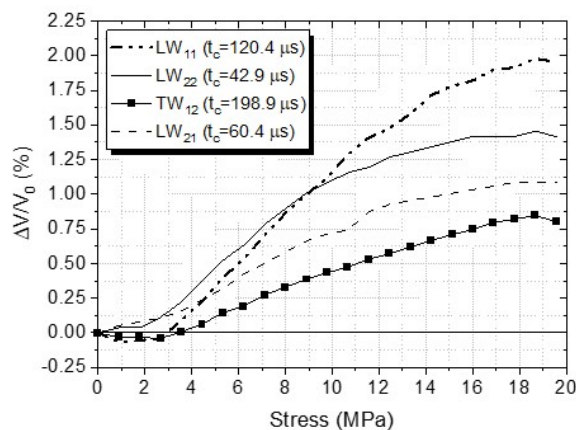


**Figure 6.** Relative velocity variation vs. stress (2T = 10 μs, CC-domain [-4 μs, 4 μs])

The diagrams in Figure 6 were obtained from specific center-times, window length, and *CC-domain*. Figure 7 displays the relative velocity variation *vs.* stress for longitudinal waves $LW_{11}$ with the same values of center-time and window length displayed in Figure 6, equal to 120.4 μs and 10 μs, respectively, but with different *CC-domain*. The change in the *CC-domain* in the analysis generated an abrupt increase in the relative velocity variation.
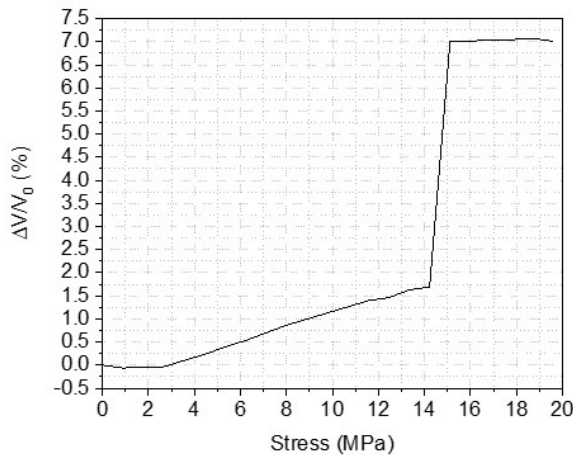


**Figure 7.** Relative velocity variation *vs.* stress for $LW_{11}$ ($t_c$ = 120.4 μs; 2T = 10 μs; CC-domain [-10 μs, 10 μs])

This sudden increase in $\Delta V/V_0$ values occurs because the cross-correlation function has several local maximums in domain [-10 μs, 10 μs], see Figure 8. For low stress levels, the argument of the global maximum in domain [-10 μs, 10 μs] is approximately 1 μs, which gradually increases with the stress level increase. However, once the stress reaches 13.3 MPa (≈ 43% of compressive strength), the argument of the global maximum value of *CC* in this domain abruptly changes to a value around 7 μs, causing the curve discontinuity showed in Figure 7. A smaller domain for the *CC* function provided the diagram in Figure 6, suggesting the analysis of the variation in UPV with stress level should evaluate the behavior of the same local maximum peak of the *CC* function as it changes with the stress increase.
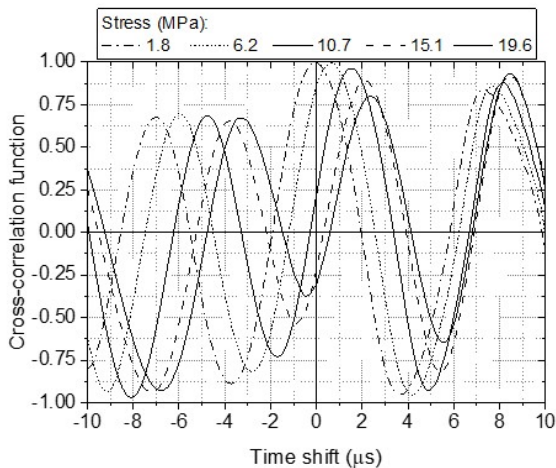


**Figure 8.** Cross-correlation function for $LW_{11}$ ($t_c$ = 120.4 μs; 2T = 10 μs)

Figure 9 displays the maximum value of the cross-correlation function and relative velocity variation for longitudinal and transversal waves, $LW_{11}$ and $TW_{12}$, respectively, considering different center-times $t_c$. Both waves were influenced by the center-time in the evaluated ranges; however, longitudinal waves showed the highest variations.

(a)                                                                      (b)
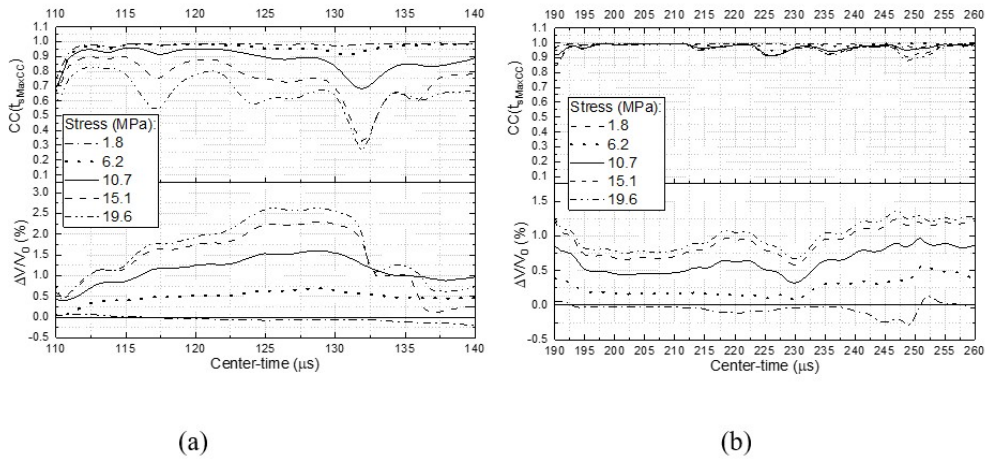
**Figure 9.** Maximum value of the Cross-correlation function and relative velocity variation *vs.* center-time (2T = 10 μs; CC-domain [-1 μs, 4 μs]): (a) LW$_{11}$ and (b) TW$_{12}$

The mean values of the relative velocity variation for LW$_{11}$ in the 110 μs and 140 μs range were 0.49% with a 30.97% coefficient of variation for 6.2 MPa stress, and 1.4% with a 50.82% coefficient of variation for 15.1 MPa stress. TW$_{12}$ were less influenced by the center-time variation. The mean value of the relative velocity variation in the 190 μs and 260 μs range for 6.2 MPa stress was 0.53% with 20.59% coefficient of variation. Differently from longitudinal waves, TW$_{12}$ showed small variations with the center-time even for high stress. The relative velocity variation was 0.89% with a 14.82% coefficient of variation for 15.1 MPa stress. A decrease in the maximum value of the cross-correlation function was observed as the compressive stress was applied. *CC* function is a measure of similarity between time series, and a decrease in its value denotes changes in waveforms with the stress application. Such changes are caused by the internal micro-cracking of the material, which produces a scatter of the ultrasonic waves.

Figure 10 shows the relative velocity variation *vs.* stress for longitudinal and transversal waves, LW$_{11}$ and TW$_{12}$, respectively, considering different center-times $t_c$. The center-time influence on the curves was smaller in the elastic behavior range; after this limit, the difference between the lowest and the highest $\Delta V/V_0$ for the same stress gradually increased, reaching very high values for LW$_{11}$.



(a)                                                                      (b)
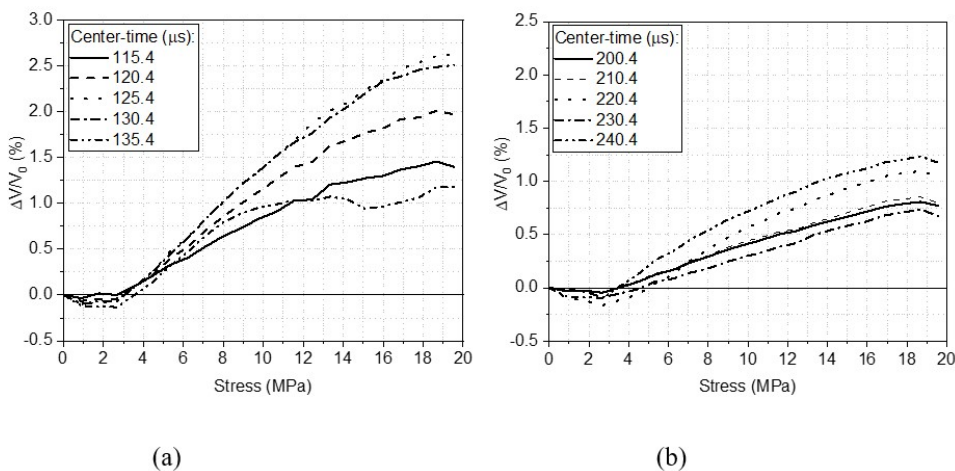
**Figure 10.** Relative velocity variation *vs.* stress (2T = 10 μs; CC-domain [-1 μs, 4 μs]): (a) LW$_{11}$ and (b) TW$_{12}$

In case of longitudinal waves LW$_{11}$, the relative velocity variation was not calculated for center-times higher than 140 μs because the same local maximum of the *CC* function was not observed in all stress levels, see Figure 11. The

*CC* local maximum clearly identified for low stresses could not be located for stresses higher than 8.0 MPa. Besides, the cross-correlation function values were very low in domain [-1 µs, 4 µs], indicating a weak similarity between the waveforms in this center-time range.
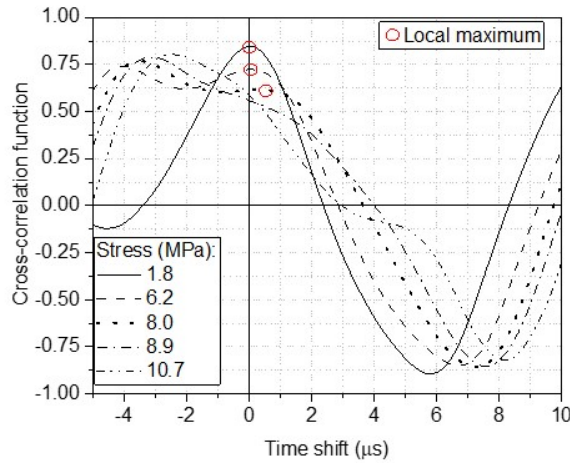


**Figure 11.** Cross-correlation function for $LW_{11}$ ($t_c$ = 154.4 µs, 2T = 10 µs)

Regarding transversal waves, $TW_{12}$, the relative velocity variation dependence on the stress continued to be verified for very high center-times such as 350.4 µs, and the analysis characterized Coda Wave Interferometry. However, the relative velocity variation values in such center-times were very different from those in center-times around 194.9 µs (see Figure 12).
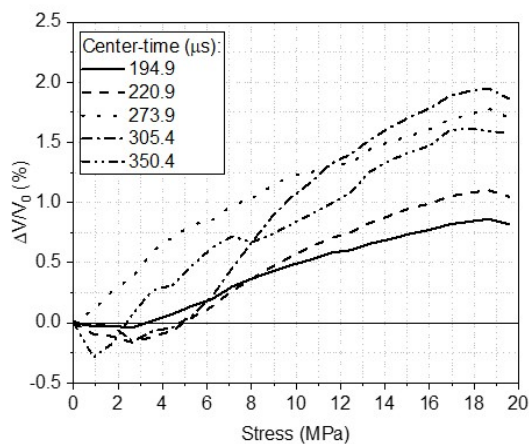


**Figure 12.** Relative velocity variation *vs.* stress for $TW_{12}$ (2T = 10 µs; CC-domain [-1 µs, 10 µs])

The center-time similarly influenced the results for ultrasonic waves propagated in direction 2 of the prism (Figure 13). However, a high variation in the $\Delta V/V_0$ *vs.* stress curve was observed for different center-times even in the elastic region for longitudinal waves $LW_{22}$ (Figure 14a). On the other hand, transversal waves $TW_{21}$ (Figure 14b) showed very small variations with 55.9 µs to 75.9 µs center-times.

Rev. IBRACON Estrut. Mater., vol. 16, no. 4, e16402, 2023

9/16
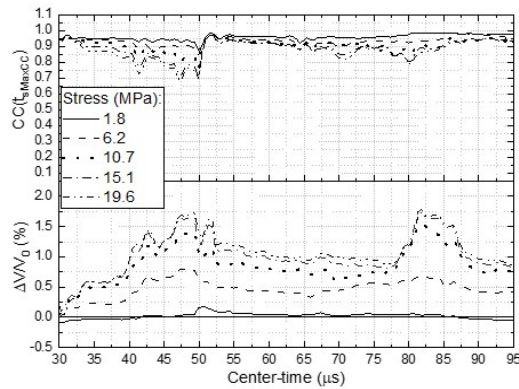
**Figure 13.** Maximum value of the Cross-correlation function and relative velocity variation *vs.* center-time for waves in the direction 2 (2T = 10 µs; CC-domain [-1 µs, 2 µs])



(a)                                                                 (b)
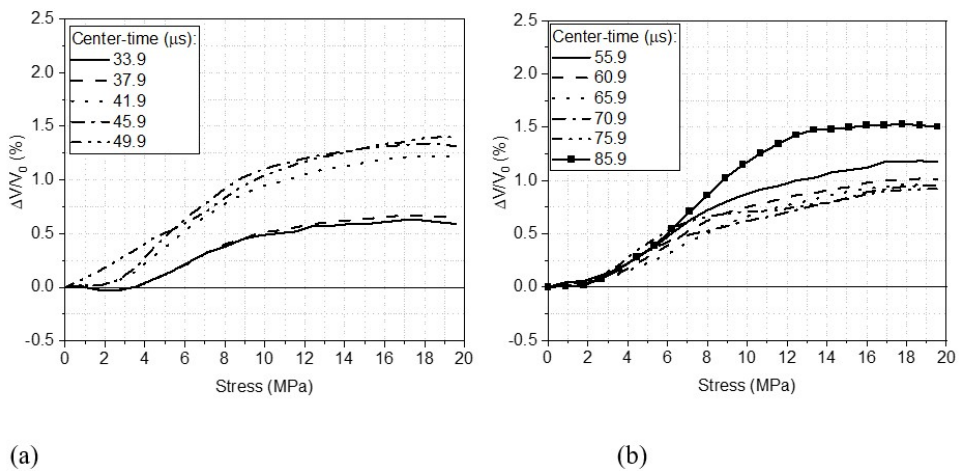
**Figure 14.** Relative velocity variation *vs.* stress (2T = 10 µs; CC-domain [-1 µs, 2 µs]): (a) $LW_{22}$ and (b) $TW_{21}$

Time window (*2T*) also influenced the results obtained from the cross-correlation function. Figures 15, 16 and 17 show high time-windows led to a decrease in the $\Delta V/V_0$ variation through different center-times.



(a)                                                                 (b)
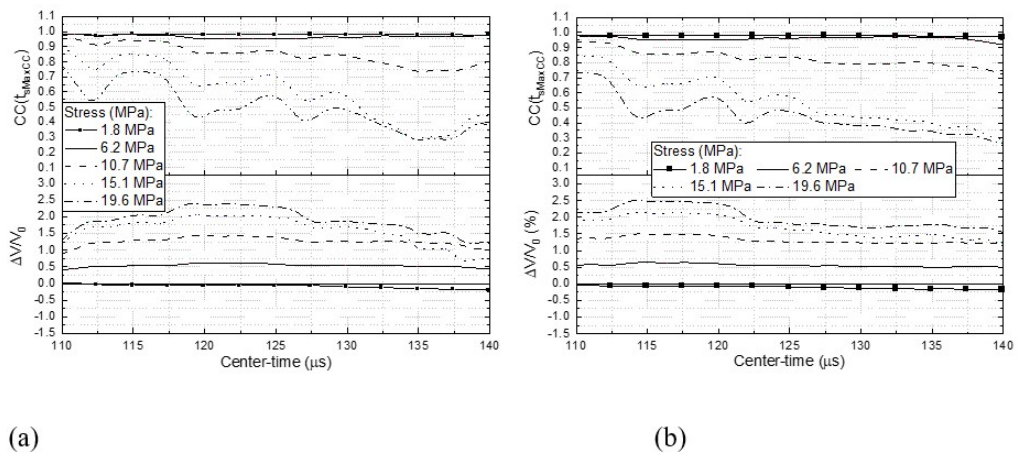
**Figure 15.** Maximum value of the Cross-correlation function and relative velocity variation *vs.* center-time for $LW_{11}$ (CC-domain [-1 µs, 4 µs]): (a) 2T = 20 µs and (b) 2T = 30 µs
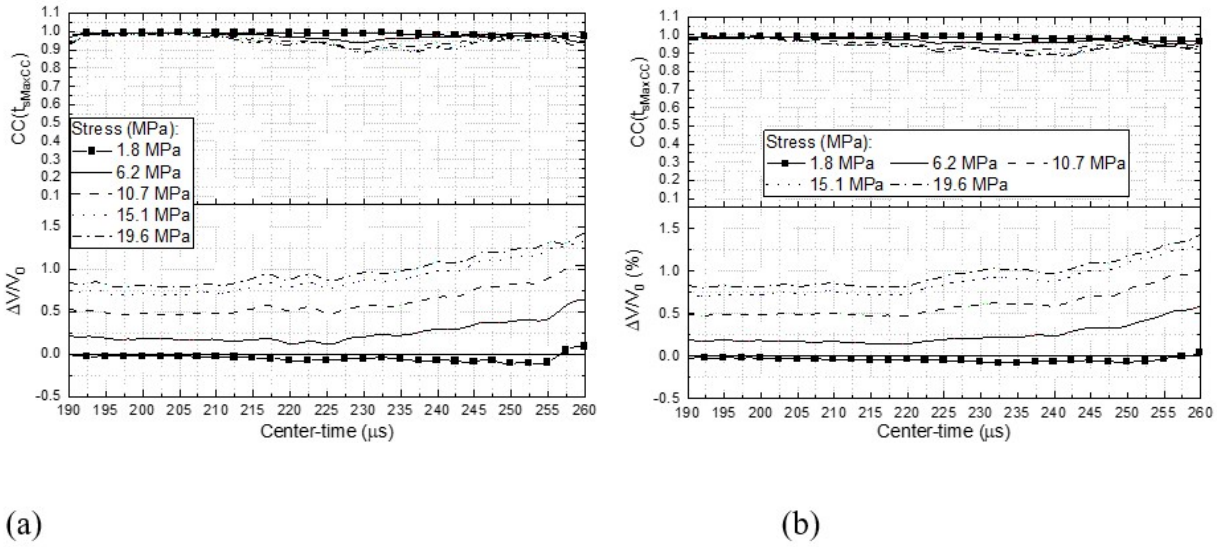
**Figure 16.** Maximum value of the Cross-correlation function and relative velocity variation *vs.* center-time for TW$_{12}$ (CC-domain [-1 μs, 4 μs]): (a) 2T = 20 μs and (b) 2T = 30 μs
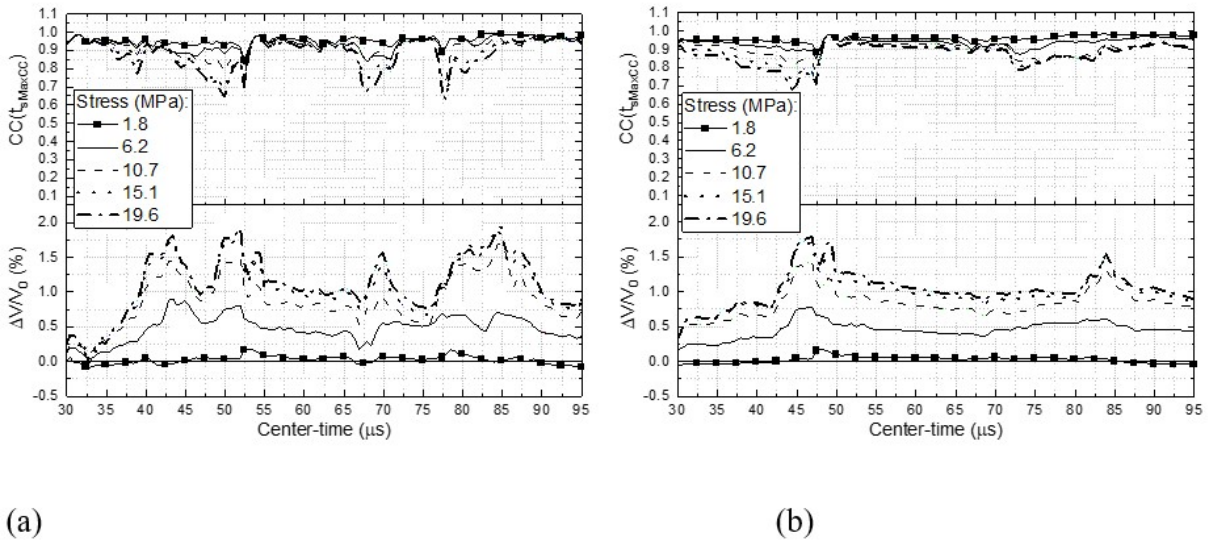


**Figure 17.** Maximum value of the Cross-correlation function and relative velocity variation *vs.* center-time for waves in the direction 2 (CC-domain [-1 μs, 2 μs]): (a) 2T = 5 μs and (b) 2T = 15 μs

The maximum value of the cross-correlation function was also reduced, indicating a lower similarity ratio between the waveforms inside that time window. This was expected, since a higher amount of data is evaluated due to the time window increase, becoming a more sensitive result to differences between the waveforms.

Figure 18 shows the relative velocity variation *vs.* stress for longitudinal and transversal waves for different time windows. Longitudinal waves were more influenced by the variation in time window in comparison to transversal waves. Regarding LW$_{11}$, expressive differences were observed for stresses higher than the nominal elastic limit, whereas high differences were observed for LW$_{22}$ even in the elastic region.

(a)

(b)

(c)

(d)
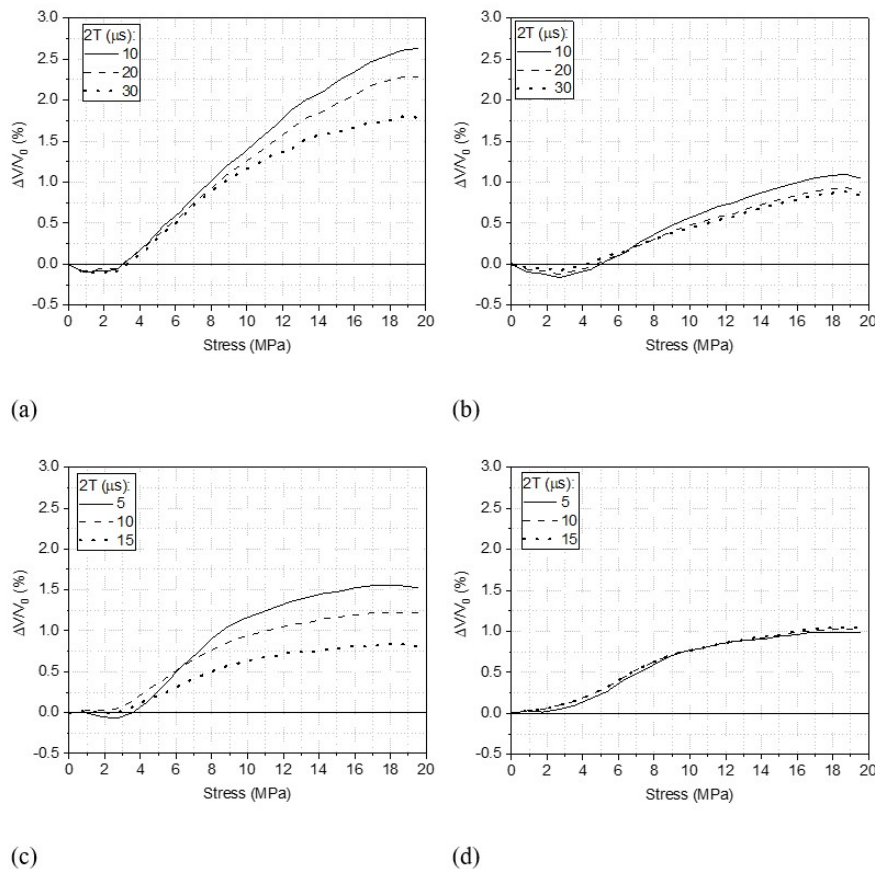
**Figure 18.** Relative velocity variation *vs.* stress (CC-domain [-1 μs, 4 μs]): (a) $LW_{11}$ ($t_c = 125.4$ μs), (b) $TW_{12}$ ($t_c = 220.4$ μs), (c) $LW_{22}$ ($t_c = 41.9$ μs) and (d) $TW_{21}$ ($t_c = 60.4$ μs)

## 4 DISCUSSIONS

The heterogeneity of concrete causes a scatter of the ultrasonic waves, which is increased when a stress level is applied to a concrete element, leading to the creation and extension of microcracks. This effect makes the ultrasonic waves travel along different trajectories inside the specimen from source to receiver. The waveform obtained from the ultrasonic tests in concrete specimens is a composition of the amplitudes of several scattered waves arriving at different times at the receiver. In the cross-correlation for feature extraction, the analysis uses a time window of the waveform, i.e., the relative velocity variation obtained is an average value of all waves arriving in time range. This average represents the exact value of the relative velocity variation in case of an isotropic material, which is constant for all paths. The velocities of compression and transversal waves for an isotropic material are independent of the propagation direction ($V_{11} = V_{22} = V_{33}$ and $V_{12} = V_{23} = V_{13}$). Therefore, in a scenario A where the prism showed in Figure 19 is composed of an isotropic material, velocities $V_A$, $V_B$, and $V_C$ related to paths $S_A$, $S_B$, and $S_C$, respectively, are equal, although the TOFs and the paths are different ($t_A \neq t_B \neq t_C$ and $S_A \neq S_B \neq S_C$, respectively). If the material remains isotropic after a stress state, the relative velocity variations ($\Delta V/V_o$) will be the same in all paths.
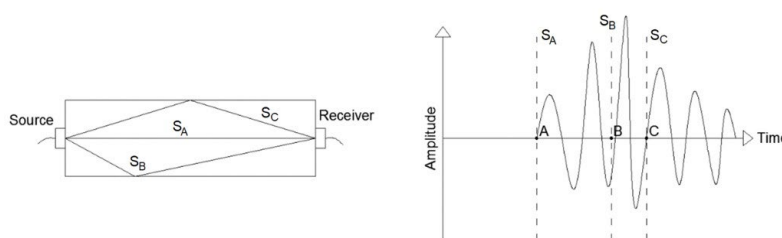


**Figure 19.** Scheme of wave paths in an ultrasonic waveform

Rev. IBRACON Estrut. Mater., vol. 16, no. 4, e16402, 2023

12/16

However, Hughes and Kelly [8] showed the stress state changes the constitutive matrix of a material, leading to a dependence of ultrasonic velocity on the stress level. The authors obtained expressions for the stress dependence of the velocities of direct waves using the finite strain formulation of Murnaghan [31], according to which an isotropic material becomes anisotropic due to the stress state. Regarding an anisotropic material, the wave velocities are dependent on the propagation direction ($V_{11} \neq V_{22}$ and $V_{12} \neq V_{21}$). In this scenario, called scenario B, velocities $V_A$, $V_B$ and $V_C$ (Figure 19) are completely different and dependent on the constitutive matrix of the material. Consequently, the relative velocity variation is not the same for different paths and the $\Delta V/V_o$ value from the cross-correlation function represents an average behavior of multiple waves travelling in distinct paths and arriving at the receiver in the evaluated time window.

The anisotropy level induced by the stress can be expressed as a fractional velocity difference. The more common expression from the literature relates the velocities of transverse ultrasonic waves polarized in mutually perpendicular directions [18], [36]. Here, this concept is extended by other velocities towards the definition of anisotropy dimensionless coefficients $\alpha$ and $\beta$ for longitudinal and transversal waves, respectively Equation 4 and Equation 5.

$$\alpha = \frac{V_{11}-V_{22}}{(V_{11}+V_{22})/2} \tag{4}$$

$$\beta = \frac{V_{12}-V_{21}}{(V_{12}+V_{21})/2} \tag{5}$$

Concrete displays some level of anisotropy even with no stress application [37]. The anisotropy dimensionless coefficients were 8.85% and 4.18% for longitudinal and transversal waves, respectively, for null stress, showing the anisotropy of the material affects the longitudinal velocity more intensively in the concrete specimen analyzed, and explaining the higher $\Delta V/V_o$ variability with time window or center-time for longitudinal waves in comparison to transversal ones (see section 5).

The anisotropy coefficients were calculated for all stress levels subtracting the coefficients at null stress ($\alpha_0$ and $\beta_0$) to facilitate the comparison between values of longitudinal and transversal waves. The stress application generates a small variation in anisotropy coefficients when compared with the initial values (Figure 20), showing the initial anisotropy of the concrete is the main contributing factor to scenario B, previously described.
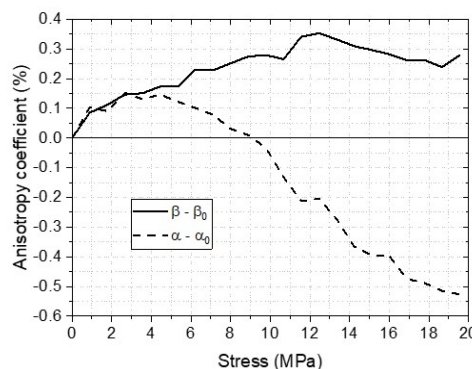


**Figure 20.** Variation of anisotropy coefficients with the stress level.

Although the $\Delta V/V_o$ value obtained by the cross-correlation function is influenced by the anisotropy of the material and represents the behavior of multiple waves, it remains dependent on the stress level for any center-time or time window, according to the results in section 5; however, it is neither constant with the change in the variables, nor the relative velocity variation of the direct waves - direct waves are those that arrived first at the receiver. Therefore, the time window should be small and the center-time should be closer to the time of arrival of the waves for the $\Delta V/V_o$ obtained by the cross-correlation function to represent direct waves.

## 5 CONCLUSIONS AND FINAL REMARKS

This study evaluated the influence of cross-correlation function parameters on the feature extraction of ultrasonic test results performed in a concrete prism. The specimen was subjected to different stress levels in/out of the elastic regime, and analyses were conducted for longitudinal and transversal waves emitted in two directions regarding time window length, center-time of the time window, and cross-correlation function domain. The influence of the stress level on the relative velocity variation was observed in all ultrasonic waves in and out the elastic regime. Discussions led to the following conclusions:

- The global maximum value of the *CC* function cannot be used for the calculation of the relative velocity variation in case of high stresses applied to concrete. The *CC* domain should be carefully selected, since the time-shift that represents the relative velocity variation is an argument of a local maximum value.
- Longitudinal waves were more sensitive to changes in time window and center-time than transversal waves, probably due to the anisotropic behavior of the concrete, since the anisotropic dimensionless coefficient for longitudinal waves was higher than that for transversal waves. This behavior made the transversal waves the most suitable for the analysis of stress variation since they are few influenced by the time window and center-time. Therefore, transversal waves, which are lightly influenced by time window and center-time, are the most suitable for analyses of stress variation.
- Variations in $\Delta V/V_0$ *vs.* stress diagrams caused by time window and center-time were lower for stresses in the elastic regime. Although the choice of the time window or center-time highly influences the results from the cross-correlation function, the relative velocity variation remains dependent on the stress level; however, this relation is not representative of direct waves, as the cross-correlation represents the average velocity variation between two time windows.
- The feature extraction procedure applied to the results of ultrasonic tests is a key point in the evaluation of the dependence of the propagation wave velocity on the stress level. The *CC*-function parameters should be carefully selected and kept constant in results that will be compared.

## LIST OF ACRONYMS AND SYMBOLS

2T: window length
$\alpha$: anisotropy dimensionless coefficient for longitudinal waves
$\beta$: anisotropy dimensionless coefficient for transversal waves
$\Delta V/V_0$: relative velocity variation
$\sigma$: applied compressive stress
$\sigma_{Max,UPV}$: maximum compressive stress applied during UPV tests
$\tau$: factor used to "stretch" or compress the signal in the stretching method
ABNT: Brazilian Association of Technical Standards
ASTM: American Society for Testing and Materials
CC: Cross-Correlation function
CC-domain: domain of cross-correlation function
CWI: Coda Wave Interferometry
$f_{cm}$: average compressive strength of concrete
LCR: Critically Refracted Longitudinal waves
$LW_{ij}$: longitudinal waves propagated in direction i and polarized in direction j
$S_A$, $S_B$, $S_C$: possible propagation paths
S-waves: secondary or transversal waves
$t_c$: center-time
TOF: Time of Flight
$t_s$: time shift used as argument of the cross-correlation function in the doublet method
$t_{sMaxCC}$: time shift that generates the maximum value of the cross-correlation function in the doublet method
$TW_{ij}$: transversal waves propagated in direction i and polarized in direction j
UPV: Ultrasonic Pulse Velocity
$u_{pert}$: signal recorded in the perturbed medium
$u_{unp}$: signal recorded in the unperturbed medium
$V_0$: propagation velocity in the unperturbed medium
$V_{ij}$: velocity of a wave propagated in direction i and polarized in direction j
$V_A$, $V_B$, $V_C$: velocity of waves traveling through paths $S_A$, $S_B$ and $S_C$, respectively

Rev. IBRACON Estrut. Mater., vol. 16, no. 4, e16402, 2023

14/16

## ACKNOWLEDGEMENTS

## REFERENCES

[1] V. M. Malhotra and N. J. Carino, *Handbook on Nondestructive Testing of Concrete*, 2nd ed, Boca Raton, Florida, USA: CRC Press, 2004.

[2] H. Chai, D. Aggelis, S. Momoki, Y. Kobayashi, and T. Shiotani, "Single-side access tomography for evaluating interior defect of concrete," *Constr. Build. Mater.*, vol. 24, no. 12, pp. 2411–2418, 2010, http://dx.doi.org/10.1016/j.conbuildmat.2010.03.003.

[3] F. Benmeddour, G. Villain, O. Abraham, and M. Choinska, "Development of an ultrasonic experimental device to characterise concrete for structural repair," *Constr. Build. Mater.*, vol. 37, pp. 934–942, 2012, http://dx.doi.org/10.1016/j.conbuildmat.2012.09.038.

[4] M. Benaicha, O. Jalbaud, X. Roguiez, A. H. Alaoui, and Y. Burtschell, "Prediction of Self-Compacting Concrete homogeneity by ultrasonic velocity," *Alexandria Eng. J.*, vol. 54, no. 4, pp. 1181–1191, 2015., http://dx.doi.org/10.1016/j.aej.2015.08.002.

[5] V. Haach, L. Juliani, and M. Ravanini, "Ultrasonic evaluation of mechanical properties of concretes produced with high early strength cement," *Constr. Build. Mater.*, vol. 96, pp. 1–10, 2015., http://dx.doi.org/10.1016/j.conbuildmat.2015.07.139.

[6] V. Haach and L. Juliani, "Possibilities of using ultrasound for the technological control of concrete of hollow-core slabs," *Constr. Build. Mater.*, vol. 133, pp. 409–415, 2017, http://dx.doi.org/10.1016/j.conbuildmat.2016.12.121.

[7] S. S. Kumar, J. Krishnamoorthi, B. Ravisankar, and V. Balusamy, "Assessing quality of diffusion bonded joints with interlayer using ultrasonic/ultrasound," *J. Mater. Process. Technol.*, vol. 242, pp. 139–146, 2017., http://dx.doi.org/10.1016/j.jmatprotec.2016.11.036.

[8] D. S. Hughes and J. L. Kelly, "Second-order elastic deformation of solids," *Phys. Rev.*, vol. 92, no. 5, pp. 1145–1149, 1953, http://dx.doi.org/10.1103/PhysRev.92.1145.

[9] C. L. Nogueira, "Ultrasonic evaluation of acoustoelastic parameters in aluminum," *J. Mater, Civ. Eng.*, vol. 29, no. 10, pp. 04017158-1-04017158-9, 2017, http://dx.doi.org/10.1061/(ASCE)MT.1943-5533.0002009.

[10] Q. Zhu, C. Burtin, and C. Binetruy, "The viscoelastic effect during acoustoelastic testing of polyethylene," *Polym. Test.*, vol. 69, pp. 286–292, 2018, http://dx.doi.org/10.1016/j.polymertesting.2018.05.032.

[11] S. Garstev and B. Köhler, "Direct measurements of Rayleigh wave acoustoelastic constants for shot-peened superalloys," *NDT Int.*, vol. 113, pp. 102279, 2020, http://dx.doi.org/10.1016/j.ndteint.2020.102279.

[12] I. Lillamand, J. F. Chaix, M. A. Ploix, and V. Garnier, "Acoustoelastic effect in concrete material under uni-axial compressive loading," *NDT Int.*, vol. 43, no. 8, pp. 655–660, 2010, http://dx.doi.org/10.1016/j.ndteint.2010.07.001.

[13] P. Shokouhi, A. Zoega, and H. Wiggenhauser, "Nondestructive investigation of stress-induced damage in concrete," *Adv. Civ. Eng.*, vol. 2010, pp. 740189, 2010, http://dx.doi.org/10.1155/2010/740189.

[14] K. F. Bompan and V. G. Haach, "Ultrasonic tests in the evaluation of the stress level in concrete prisms based on the acoustoelasticity," *Constr. Build. Mater.*, vol. 162, pp. 740–750, 2018, http://dx.doi.org/10.1016/j.conbuildmat.2017.11.153.

[15] M. Hirao and Y. H. Pao, "Dependence of acoustoelastic birefringence on plastic strains in a beam," *J. Acoust. Soc. Am.*, vol. 77, no. 5, pp. 1659–1664, 1985, http://dx.doi.org/10.1121/1.391964.

[16] Y. H. Pao, "Theory of acoustoelasticity and acoustoplasticity", in *Solid mechanics Research for Quantitative Non-Destructive Evaluation*, J. D. Achenbach, and Y. Rajapakse, Ed., Dordrecht, Netherlands: Martinus Nijhoff Publishers, 1987, ch. 8.1, sec. 8, pp. 257–273.

[17] M. Kobayashi, "Acoustoelastic theory for plastically deformed solids", *JSME Int J.*, vol. 33, no. 3, pp. 310–318, 1990.

[18] V. K. Belchenko, A. M. Lobachev, V. S. Modestov, D. A. Tretyakov and L. V. Shtukin, "An estimation of the strain-stress state under cyclic loading by the acoustoelasticity method", *St. Petersburg Polytechnical Univ. J. Phys. Math.*, vol. 3, no. 1, pp. 71–76, 2017.

[19] M. Mohammadi and J. J. Fesharaki, "Determination of acoustoelastic/acoustoplastic constants to measure stress in elastic/plastic limits by using LCR wave," *NDT Int.*, vol. 104, pp. 69–76, 2019., http://dx.doi.org/10.1016/j.ndteint.2019.04.003.

[20] S. C. Stähler, C. Sens-Schönfelder, and E. Niederleithinger, "Monitoring stress changes in a concrete bridge with coda wave interferometry," *J. Acoust. Soc. Am.*, vol. 129, no. 4, pp. 1945–1952, 2011., http://dx.doi.org/10.1121/1.3553226.

[21] Y. Zhang et al., "Study of stress-induced velocity variation in concrete under direct tensile force and monitoring of the damage level by using thermally-compensated coda wave interferometry," *Ultrasonics*, vol. 52, no. 8, pp. 1038–1045, 2012., http://dx.doi.org/10.1016/j.ultras.2012.08.011.

[22] P. Shokouhi, J. Rivière, C. R. Lake, P. Y. Le Bas, and T. J. Ulrich, "Dynamic acousto-elastic testing of concrete with a coda-wave probe: comparison with standard linear and nonlinear ultrasonic techniques," *Ultrasonics*, vol. 81, pp. 59–65, 2017, http://dx.doi.org/10.1016/j.ultras.2017.05.010.

[23] E. Niederleithinger, X. Wang, M. Herbrand, and M. Muller, "Processing Ultrasonic data by coda wave interferometry to monitor load tests of concrete beams," *Sensors (Basel)*, vol. 18, no. 6, pp. 1971, 2018., http://dx.doi.org/10.3390/s18061971.

[24] H. Zhan, H. Jiang, C. Zhuang, J. Zhang, and R. Jiang, "Estimation of stresses in concrete by using coda wave interferometry to establish an acoustoelastic modulus database," *Sensors (Basel)*, vol. 20, no. 14, pp. 4031, 2020., http://dx.doi.org/10.3390/s20144031.

[25] T. Planès and E. Larose, "A review of ultrasonic Coda Wave Interferometry in concrete," *Cement Concr. Res.*, vol. 53, pp. 248–255, 2013, http://dx.doi.org/10.1016/j.cemconres.2013.07.009.

[26] A. Grêt, R. Snieder, and J. Scales, "Time-lapse monitoring of rock properties with coda wave interferometry," *J. Geophys. Res.*, vol. 111, pp. B03305, 2006, http://dx.doi.org/10.1029/2004JB003354.

[27] R. Snieder, A. Grêt, H. Douma, and J. Scales, "Coda Wave Interferometry for estimating nonlinear behavior in Seismic Velocity," *Science*, vol. 295, no. 5563, pp. 2253–2255, 2002, http://dx.doi.org/10.1126/science.1070015.

[28] A. Grêt, R. Snieder, and U. Ozbay, "Monitoring in situ stress changes in a mining environment with coda wave interferometry," *Geophys. J. Int.*, vol. 167, no. 2, pp. 504–508, 2006, http://dx.doi.org/10.1111/j.1365-246X.2006.03097.x.

[29] C. Hadziioannou, E. Larose, O. Coutant, P. Roux, and M. Campillo, "Stability of monitoring weak changes in multiply scattering media with ambient noise correlation: laboratory experiments," *J. Acoust. Soc. Am.*, vol. 125, no. 6, pp. 3688–3695, 2009, http://dx.doi.org/10.1121/1.3125345.

[30] C. Payan, V. Garnier, J. Moysan, and P. A. Johnson, "Determination of third order elastic constants in a complex solid applying coda wave interferometry," *Appl. Phys. Lett.*, vol. 94, no. 1, 2009, http://dx.doi.org/10.1063/1.3064129.

[31] F. D. Murnaghan, *Finite deformation of an elastic solid*, New York, NY, USA: John Wiley and Sons, Inc., 1951.

[32] E. Niederleithinger, P. Shokouhi, S. Stahler, and T. R. Nowak, "Detection of subtle changes in materials by coda wave interferometry", in *Proc 10th European Conf. Non-Destructive Testing*, Moscow, June 7-11 2020, 2010.

[33] American Society for Testing and Materials, *Standard Specification for Portland Cement*, C150/C150M – 07, 2007.

[34] Associação Brasileira de Normas Técnicas, *Aggregates – Sieve analysis of fine and coarse aggregates*, NBR NM 248, 2003.

[35] P. K. Mehta and P. J. M. Monteiro, *Concrete: microstructure, properties and materials*, 3rd ed. New York, New York, USA: McGraw-Hill, 2006.

[36] P. A. Smith, "Stress-induced anisotropy in solids - the acousto-elastic effect," *Ultrasonics*, vol. 94, pp. 135–147, 1963.

[37] V. G. Haach, R. Carrazedo, P. O. Ribeiro, L. P. A. Ferreira, and I. P. Abe, "Evaluation of elastic anisotropic relations for plain concrete using ultrasound and impact acoustic tests," *J. Mater. Civ. Eng.*, vol. 33, pp. 1–14, 2020, http://dx.doi.org/10.1061/(ASCE)MT.1943-5533.0003562.

**IBRACON Structures and Materials Journal**
Revista IBRACON de Estruturas e Materiais

REVIEW ARTICLE

# Flexural design of concrete beams reinforced with FRP rebars

## Dimensionamento à flexão de vigas em concreto armado com barras de FRP

Felipe Augusto da Silva Barbosa[a] (iD)
Túlio Nogueira Bittencourt[a] (iD)
Gustavo Rodovalho Boriolo[a] (iD)
Fellipe Rodrigues André[b] (iD)
Marcos Massao Futai[a] (iD)

[a]Universidade de São Paulo – USP, Department of Structural and Geotechnical Engineering, São Paulo, SP, Brasil
[b]Universidade São Judas Tadeu – USJT, Department of Civil Engineering, São Paulo, SP, Brasil

**Abstract:** The corrosion of steel rebars is the main cause of reinforced concrete degradation, which results in increasing costs with structural rehabilitation and repairs. As a solution, corrosion resistant rebars, such as those of FRP – Fiber-reinforced polymer –, have been used to replace conventional steel. This paper describes the development of a design program that calculates the flexural FRP reinforcement of T-shape beams. The possibilities as regards the neutral axis position, failure mode and concrete linear or non-linear behavior define the design scenarios for which their respective equations were deduced. The flexural strengths computed using the deduced equations showed agreement with experimental results for 125 beams, validating the proposed methodology. Since FRP rebars are vulnerable to creep rupture, the sustained stresses must be lower than the maximum allowed by ACI 440.1R-15, which may require increases in areas, modifying the flexural strength. Therefore, the equations to compute the new neutral axis depth and flexural strength based on the adjusted area were deduced and implemented in the computational program. Subsequently, this paper presents design examples considering all scenarios for which the equations were deduced. The design of one T-section considering different FRP rebars combined to normal and high-performance concretes is also reported. The results showed that beams reinforced with aramid and glass FRP required large areas to avoid creep rupture, whereas the areas of those reinforced by carbon FRP rebars were considerably small; however, they exhibited small curvatures and fragile failure when under-reinforced.

**Keywords:** reinforced concrete, FRP rebars, T-sections, non-metallic reinforcement, design program.

**Resumo:** A corrosão do aço é a principal causa de degradação do concreto estrutural, implicando elevados custos com reabilitação e reparos. Diante disto, barras de FRP – Polímeros Reforçados por Fibras – constituem uma alternativa ao aço convencional em virtude de sua excelente resistência à corrosão. Este trabalho descreve o desenvolvimento de um programa para dimensionamento da armadura de FRP à flexão em vigas de seção T. As diferentes possibilidades referentes à posição da linha neutra, modo de falha e comportamento linear ou não-linear do concreto definem os cenários de dimensionamento para os quais se aplicam as formulações desenvolvidas. Os momentos resistentes calculados apresentaram concordância com valores obtidos experimentalmente, validando a metodologia proposta. Uma vez que as barras de FRP são suscetíveis à ruptura por fluência, tensões devido a cargas permanentes devem se manter inferiores ao limite estabelecido pelo ACI 440.1R-15, ajustando-se as áreas de armadura quando necessário. Desta maneira, foram implementadas no programa, as equações para cálculo da linha neutra e momento resistente baseadas nas áreas ajustadas. Subsequentemente, são apresentados exemplos de dimensionamento considerando os diversos cenários para os quais desenvolveram-se as formulações, combinando-se diferentes tipos de FRP a variadas classes de concreto. Os resultados mostraram que vigas T armadas com FRP de aramida e vidro exigiram elevadas áreas de armadura para atender ao estado limite de ruptura por fluência. Em contrapartida, seções armadas com FRP de carbono exigiram áreas menores, porém exibindo ruptura frágil e curvaturas reduzidas quando sub-armadas.

**Palavras-chave:** concreto armado, barras de FRP, seções T, armadura não-metálica, programa de dimensionamento.

F. A. S. Barbosa, T. N. Bittencourt, G. R. Boriolo, F. R. André, and M. M. Frutai

# 1 INTRODUCTION

During the past century, the focus on obtaining high strength concretes entailed certain unconcern regarding durability issues. Somehow, the use of materials with excellent mechanical properties contributed to negligence as regards quality control at construction sites [1]. However, the degradation of structures subjected to aggressive environments as well as the increasing costs in repairs raised the discussion on how to avoid steel corrosion and preserve structural integrity [2]. Therefore, the use of different types of fiber-reinforced polymer (FRP) reinforcements in place of steel has gained space, especially in structures located in aggressive environments [3].

FRP rebars are constituted by a tangle of high strength and stiffness fibers impregnated in a low modulus resin, which characterizes them as anisotropic materials. The fibers contribute to the material tensile strength and modulus, whereas the polymeric matrix governs the overall stress-strain relationship and protects the fibers against the concrete environment [4]. Moreover, the resin low modulus entails very large strains, which ensures that the maximum load is transferred to the fibers [5].

FRP is also a lightweight material. Its specific weight varies from 20 to 25% of that of steel, which facilitates the handling process. This property allows using FRP rebars in slender columns, where steel congestion is very common [3]. Moreover, FRP has been utilized as internal reinforcement for tunnels, retaining walls, bridges, highway pavements and sea walls. It also constitutes an economic solution for repairing existing bridges, replacing the conventional steel of the decks [6].

The most popular polymeric rebars are defined according to their respective types of fiber: aramid (AFRP), carbon (CFRP) and glass (GFRP). Among all FRP categories, CFRP has the highest tensile strength and elasticity modulus; however, the raw materials necessary for its production are difficult to find, and the production of carbon fibers requires high energy consumption, which makes the utilization of CFRP very costly [6]. AFRP bars, in turn, are characterized by their high tensile strength and toughness, in addition to possessing the highest strength-to-weight ratio [4].

Nonetheless, losses in strength due to sustained stresses and exposition to UV radiation have limited the AFRP use in the civil construction [5]. In contrast, GFRP became the most popular non-metallic reinforcement due to its low cost and environmental resistance [6]. Some of GFRP properties include excellent response to cyclic loads, high strength-to-weight ratio, non-conductivity and coefficient of thermal expansion close to that of concrete [7].

Despite the corrosion resistance, non-conductivity and lightweight, FRP rebars behave linearly up to failure, not exhibiting a yield plateau as steel does. The cross-sections fail due to either concrete crushing or FRP rupture. Both failure modes are fragile; yet, previous versions of ACI 440.1R-15 [3] recommended over-reinforcing the cross-sections since concrete exhibits some plateau before failure.

# 2 RESEARCH SIGNIFICANCE

As previously mentioned, the costs with structural repairs have considerably increased, which suggests the gradual replacement of steel by non-metallic reinforcements such as FRP. However, there is no code approaching the design of FRP flexural members, which means the responsibility for structural safety and functionality is entirely attributed to the designer [6]. Furthermore, in spite of the excellent design examples presented by ACI 440.1R-15, this guideline does not address the design of T-shape sections. All examples refer to rectangular sections, with priority to compression-controlled members.

T-shape beams often occur in practice, given the need to consider the slab contribution to the flexural strength. Their design with FRP rebars is not as simple as that of steel, especially for under reinforced cross-sections where the parameters $\alpha$ and $\lambda$ of the concrete simplified stress block are unknown. There are several design approaches that depend on the neutral axis position associated to FRP and concrete simultaneous failure, as well as that related to the initiation of the concrete non-linear behavior at the most compressed fiber [8].

Therefore, the development of computational programs incorporating the FRP constitutive models and safety factors to a particular reinforced concrete code has the potential to familiarize students and engineers with the design of T-shape beams reinforced with FRP, given the need to replace steel by durable and sustainable materials. Furthermore, they are able to calculate the same cross-section for different FRP types and concrete strength grades, electing the design that combines structural safety and functionality to economic solutions.

# 3 SCOPE

This paper incorporates the FRP parameters provided by ACI 440.1R-15 [3] to the Brazilian code NBR 6118:2014 [9], deducing the formulations to calculate the FRP longitudinal reinforcement of tension and compression-controlled T-shape sections. The design assumptions accounted for failure due to concrete crushing and FRP rupture, neutral axes on the flange or web and concrete exhibiting linear or non-linear behavior. Additionally, considering that the reinforcement areas

may be adjusted to avoid creep rupture, the assumptions and formulations to compute the final flexural strength are also described. Those formulations are validated by comparing the flexural capacities obtained experimentally to those predicted by the proposed procedures.

The primordial objective was to computationally implement those formulations, developing a design program that calculates the longitudinal FRP reinforcement of T-sections under different scenarios of failure mode, neutral axis position and concrete linear or non-linear behavior. The objective was to identify effective combinations of FRP and concrete strengths resulting in balanced sections, ductility and proper use of materials' mechanical properties. Furthermore, this research aimed to evaluate changes in failure modes, flexural strengths and curvatures caused by adjustments in the FRP areas to avoid creep rupture.

## 4 DESIGN FOR THE ULTIMATE LIMIT STATE FOR FLEXURE

In order to develop the formulations for the design, the concrete constitutive model of NBR 6118:2014 [9] as well as its parameters were utilized. Figure 1 illustrates the parabola-rectangle model defined by Equations 1 and 2.
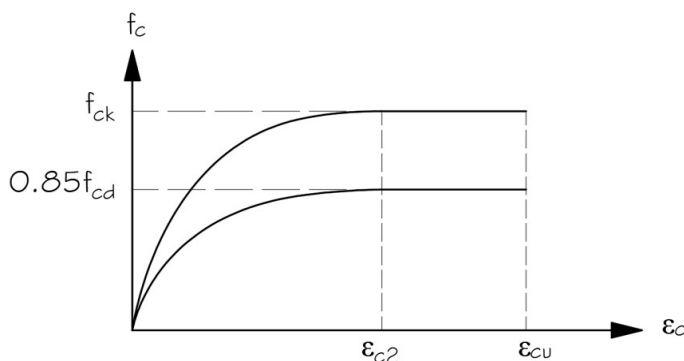


**Figure 1.** Concrete constitutive model for compression, for which $0.85f_{cd}$ and $f_{ck}$ correspond to the design and characteristic strength, respectively [9]

$$\sigma_{cd} = 0.85f_{cd}\left[1-\left(1-\frac{\varepsilon_c}{\varepsilon_{c2}}\right)^n\right] \text{ if } 0 \leq \varepsilon_c < \varepsilon_{c2} \tag{1}$$

$$\sigma_{cd} = 0.85f_{cd} \text{ if } \varepsilon_{c2} \leq \varepsilon_c < \varepsilon_{cu} \tag{2}$$

The FRP RC cross-sections fail due to concrete crushing or reinforcement rupture. ACI 440.1R-15 [3] introduces the concept of balanced reinforcement ratio, for which both failure modes occur simultaneously. The balanced area $A_b$ is associated to the neutral axis position $x_b$ and to the balanced moment $M_b$. Unlike ACI 440.1R-15, Barbosa [8] compares the design moment $M_d$ to $M_b$ to define the failure mode. If $M_d < M_b$, the cross-section is tension-controlled, whereas $M_d \geq M_b$ indicates compression-control. Since concrete and FRP reaches their ultimate strains $\varepsilon_{cu}$ and $\varepsilon_{fud}$ simultaneously, $x_b$ is obtained through compatibility as:

$$x_b = \left(\frac{\varepsilon_{cu}}{\varepsilon_{cu} + \varepsilon_{fud}}\right) d \tag{3}$$

Table 4.2.1 of ACI 440.1R-15 [3] establishes intervals of tensile strengths $f_{fu}*$ and elasticity moduli $E_f$ for the three types of FRP rebars. The strengths are reduced by the environmental coefficients specified in Table 6.2 of this guideline. Unlike NBR 6118:2014 [9], ACI 440.1R-15 imposes safety factors to the cross-section flexural strength and not to the FRP tensile strength. Thus, to incorporate the FRP parameters to NBR 6118:2014 [9] design procedures, the adjusted strength for environmental conditions still needs another factor. As indicated by the Brazilian Recommended Practice for FRP RC structures CT 303 [10], the value of 1.30 was adopted. Thus, the design tensile strength $f_{fud}$ accounts for the environment and eventual uncertainties covered by this factor.

Figures 2 and 3 illustrate balanced sections for which the concrete simplified stress block reaches the flange and web, respectively, resulting in two different approaches to calculate $M_b$. If $\lambda_u x_b < h_f$, the calculation of the balanced moment accounts only for the flange compressed area. Otherwise, if $\lambda_u x_b \geq h_f$, both flange and web compressed areas are considered. Equations 4 and 5 define the balanced moments for both scenarios, following the order they were mentioned:

$$M_b = \alpha_u \lambda_u f_{cd} b_f x_b (d - 0.5\lambda_u x_b) \qquad (4)$$

$$M_b = \alpha_u f_{cd}[\lambda_u x_b b_w (d - 0.5\lambda_u x_b) + h_f(b_f - b_w)(d - 0.5h_f)] \qquad (5)$$
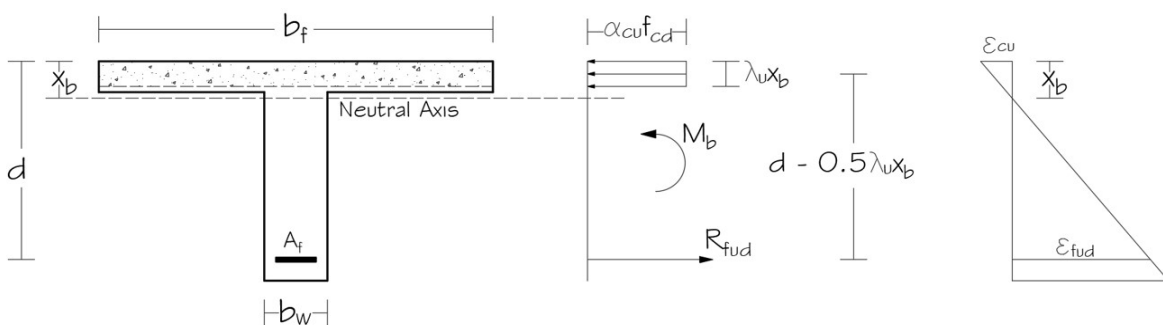


**Figure 2.** Equilibrium and compatibility of a balanced cross-section with the simplified stress block located on the flange [8]
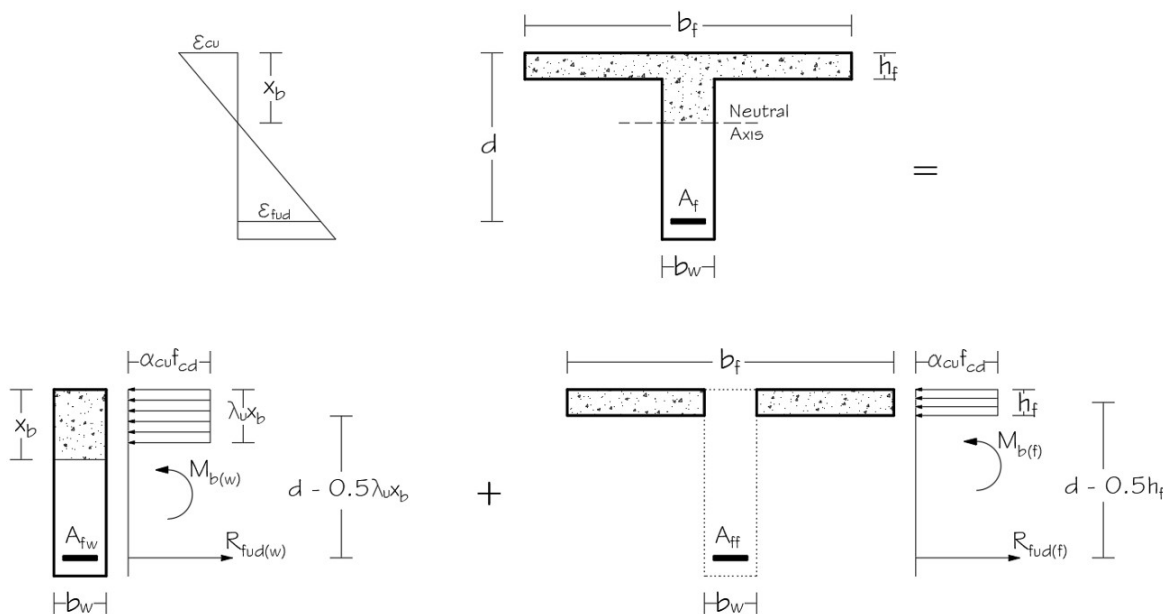


**Figure 3.** Compatibility and equilibrium of a balanced cross-section with the simplified stress block reaching the web [8]

If the balanced block depth $\lambda_u x_b$ does not reach the web and the design bending moment is lower than the balanced one, the cross-section is tension-controlled and the actual stress block $\lambda_u x$ associated to $M_d$ is smaller than the flange thickness [7]. Moreover, if the cross-section is too under-reinforced, the FRP rebars may fail before the concrete exhibits non-linear behavior. As a result, the values of $\alpha_u$ and $\lambda_u$ no longer applies, which suggests a linear constitutive model for concrete [3]. Therefore, this scenario results in two design approaches distinguished by the concrete behavior. In contrast, if $M_d \geq M_b$, the actual stress block may reach the web or not, leading to other two approaches [8].

Conversely, if the balanced stress block $\lambda_u x_b$ reaches the web and $M_d < M_b$, there are two possibilities as regards the stress block associated to the design moment: $\lambda_u x < h_f$ or $\lambda_u x \geq h_f$. Furthermore, for each of these two possibilities, concrete may behave linearly or not, resulting in other four design approaches. However, if $M_d \geq M_b$, the actual stress block reaches the web [8]. Therefore, there are nine different design approaches considering only the ultimate limit state for flexure. All formulations are deduced as follows:

### 4.1 Scenario 1 – Balanced block on the flange and tension-controlled section

This scenario is characterized by $\lambda_u x_b < h_f$ and $M_d < M_b$, which implies that $\lambda_u x < h_f$. However, given the assumption of concrete behaving linearly, it is necessary to define the neutral axis position and the bending moment from which linearity no longer applies. NBR 6118:2014 [9] allows considering the linear stress-strain relationship for stresses under 50% of the concrete compressive strength. Accordingly, this research adopted the maximum stress of $0.5(0.85f_{cd})$, which provides the strain $\varepsilon_{clin}$ from Equation 1 as $\varepsilon_{c2}(1-0.5^{1/n})$. Therefore, the neutral axis $x_{lin}$ related to the linearity limit and obtained through strain compatibility is:

$$x_{lin} = \left( \frac{\varepsilon_{clin}}{\varepsilon_{clin} + \varepsilon_{fud}} \right) d \tag{6}$$

Since the balanced block lies on the flange and the section is tension-controlled, $x_{lin}$ is smaller than the flange thickness [8]. Figure 4 illustrates the equilibrium and compatibility conditions to calculate the moment $M_{lin}$ associated to $x_{lin}$ considering the linear stress-strain relationship for concrete. Thus, if the design moment $M_d$ is lower than the reference moment $M_{lin}$ provided by Equation 7, the linear constitutive model applies [8].
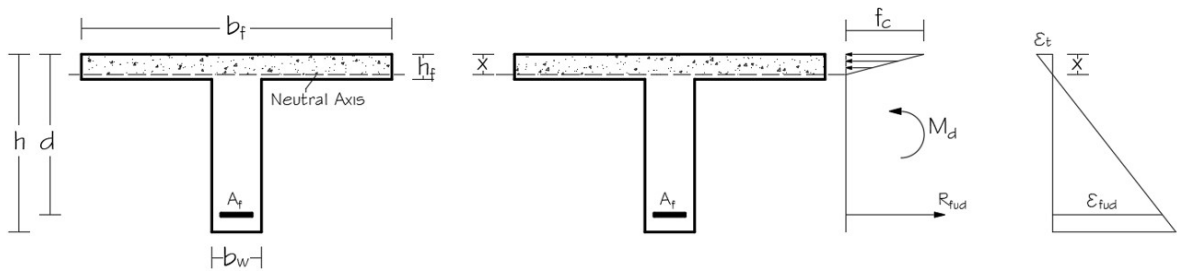


**Figure 4.** Equilibrium and compatibility conditions of a tension-controlled section with neutral axis on the flange and concrete exhibiting linear behavior [8].

$$M_{lin} = \left( \frac{0.425f_{cd}x_{lin}b_f}{2} \right) \left( d - \frac{x_{lin}}{3} \right) \tag{7}$$

The secant elasticity modulus $E_{lin}$ adopted for the linear approach corresponds to the slope of the line connecting the origin to the point ($\varepsilon_{clin}$, $0.425f_{cd}$). In order to find the unknown neutral axis depth $x$, the values of $M_{lin}$ and $x_{lin}$ in Equation 7 are replaced by $M_d$ and $x$, respectively. The stress $0.425f_{cd}$, in turn, is replaced by the product of the secant modulus $E_{lin}$ and the most compressed fiber strain $\varepsilon_t$, written as a function of $x$. As a result, there is a cubic equation whose solution within the interval $0 < x < h_f$ corresponds to the neutral axis depth:

$$x^3 - 3dx^2 + \left( \frac{6M_d}{E_{lin}\varepsilon_{fud}b_f} \right) (d - x) = 0 \tag{8}$$

Equation 8 is solved through the Newton-Raphson Method, initially assuming that $x = 1.5x_b$. The iterative process ends once the error $|x_{i+1} - x_i|$ reaches $10^{-5}$, which means the neutral axis depth has been found. Negative roots or values exceeding $x_{lin}$ are computationally disregarded. By imposing equilibrium, the required area $A_f$ to resist $M_d$ is found through:

$$A_f = \frac{M_d}{f_{fud}\left(d - \frac{x}{3}\right)} \tag{9}$$

Conversely, if the design moment $M_d$ is higher than $M_{lin}$, the linear approach no longer applies seeing that the stress in the most compressed fiber exceeds 50% of $0.85 f_{cd}$. Although concrete does not fail, ACI 440.1R-15 recommends using, as a conservative approach, the simplified stress block associated to the crushing of the concrete. In this scenario, the parameters $\alpha_{cu}$ and $\lambda_u$ are calculated as follows, in consonance with NBR 6118:2014 [9]:

$$\alpha_{cu} = 0.85$$

$$\lambda_u = 0.8 \text{ if } f_{ck} \leq 50 \text{ MPa} \tag{10}$$

$$\alpha_{cu} = 0.85[1 - (f_{ck} - 50)/200]$$

$$\lambda_u = 0.8 - (f_{ck} - 50)/400 \text{ if } 50 < f_{ck} \leq 90 \text{ MPa} \tag{11}$$

By imposing the equilibrium conditions illustrated in Figure 5, the neutral axis and the required FRP area are computed as follows:

$$x = \frac{d}{\lambda_u}\left(1 - \sqrt{1 - \frac{2M_d}{\alpha_{cu} f_{cd} b_f d^2}}\right) \tag{12}$$

$$A_f = \frac{M_d}{f_{fud}(d - 0.5\lambda_u x)} \tag{13}$$

Regardless on the concrete behavior, the strain at the most concrete compressed fiber $\varepsilon_t$ is computed through compatibility as:

$$\varepsilon_t = \varepsilon_{fud}\left(\frac{x}{d - x}\right) \tag{14}$$
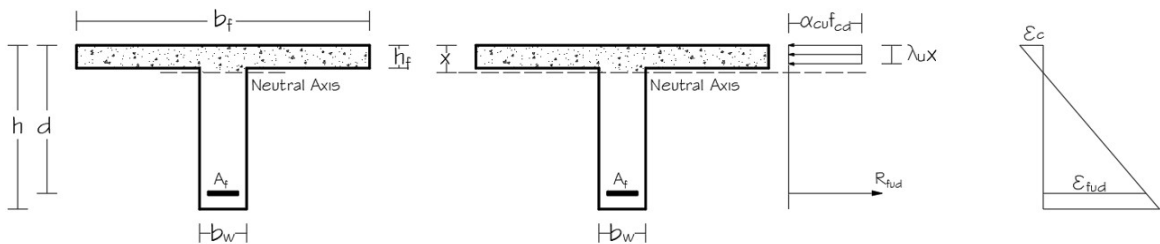


**Figure 5.** Equilibrium and compatibility conditions of a tension-controlled section for which concrete behaves non-linearly [8].

## 4.2 Scenario 2 – Balanced block on the web and tension-controlled section

If the balanced stress block reaches the web and the cross-section is tension-controlled, there are four possibilities: first, the actual stress block is on the flange and the concrete linear approach applies; second, the stress block remains on the flange but concrete exhibits non-linear behavior; third, the stress block reaches the web while concrete behaves linearly and fourth, the linear approach no longer applies for the stress block on the web [8].

Furthermore, the reference neutral axis $x_{lin}$ may be either on the flange or web, which results in two different methods to compute the reference moment $M_{lin}$. If $x_{lin} < h_f$, $M_{lin}$ is determined from Equation 7; otherwise, the compressive stresses on the flange and web must be considered as shown in Figure 6. First, it is necessary to determine the resulting

Rev. IBRACON Estrut. Mater., vol. 16, no. 4, e16403, 2023

6/20

compressive force $F_{lin}$ from Equation 15 and its center $\bar{y}_{lin}$ from Equation 16. Therefore, the reference moment $M_{lin}$ is computed as the product of $F_{lin}$ and the moment arm d - $\bar{y}_{lin}$.

$$F_{lin} = \frac{1}{2} E_{lin} \varepsilon_{clin} \left[ \left(2 - \frac{h_f}{x_{lin}}\right)(b_f - b_w)h_f + b_w x_{lin} \right] \tag{15}$$

$$\bar{y}_{lin} = \frac{\frac{b_w x_{lin}^2}{3} + h_f^2\left(1 - \frac{2h_f}{3x_{lin}}\right)(b_f - b_w)}{b_w x_{lin} + h_f\left(2 - \frac{h_f}{x_{lin}}\right)(b_f - b_w)} \tag{16}$$

If $x_{lin} < h_f$ and $M_d < M_{lin}$, the neutral axis $x$ and the reinforcement area $A_f$ are computed through Equations 8 and 9, the same as for scenario 1. Conversely, if $x_{lin} \geq h_f$ and $M_d < M_{lin}$, the neutral axis $x$ associated to $M_d$ may be on the flange or web. Initially, it is assumed that $x < h_f$, for which Equation 8 applies. If the value found for $x$ is smaller than the flange thickness, the assumption is correct, and the required area is computed through Equation 9. Nonetheless, if $x \geq h_f$, the assumption is incorrect, and the value of $x$ is not valid. Consequently, the calculation of the neutral axis depth and the required FRP area must account for the compressive stresses on the flange and web as shown in Figure 6.
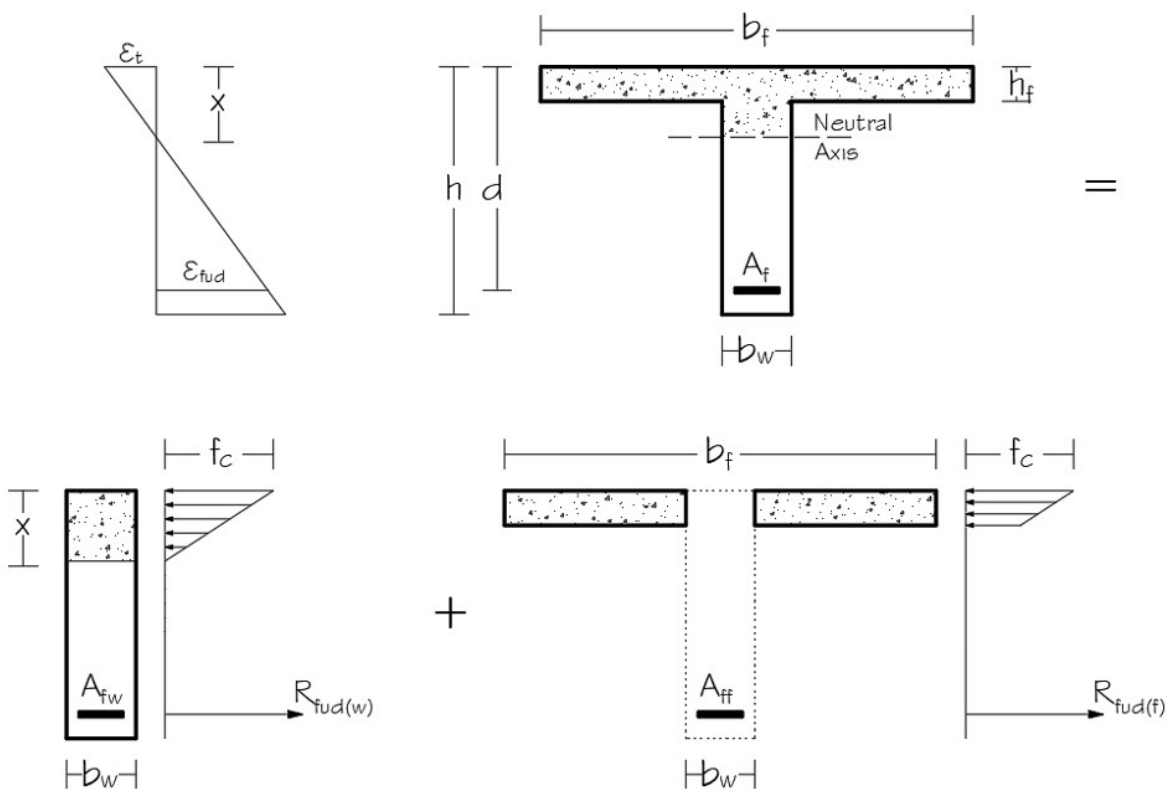


**Figure 6.** Compatibility and equilibrium of a tension-controlled cross-section for which the concrete linear stress-strain relationship applies [8].

Thus, the variables $x_{lin}$ and $\varepsilon_{clin}$ in Equations 15 and 16 are replaced by the neutral axis depth $x$ and the strain at the most compressed fiber $\varepsilon_t$, respectively. Since the strain $\varepsilon_t$ can be written as a function of $x$, the neutral axis depth becomes the only unknown variable. As a result, the expression $F_c (d - \bar{y}_c) = M_d$ results in a third-degree equation described as follows:

$$a_1 = \frac{6h_f(d - 0.5h_f)(b_f - b_w)}{b_w} \tag{17}$$

Rev. IBRACON Estrut. Mater., vol. 16, no. 4, e16403, 2023

7/20

$$a_2 = \frac{3h_f^2[d - (h_f/3)](b_f - b_w)}{b_w} \tag{18}$$

$$a_3 = \frac{6M_d}{E_{lin}\varepsilon_{fud}b_w} \tag{19}$$

$$x^3 - 3dx^2 - (a_1 + a_3)x + (a_3d + a_1h_f - a_2) = 0 \tag{20}$$

Equation 20 is solved exactly as Equation 8, through the Newton-Raphson Method, initially arbitrating $x$ as $1.5x_b$ and ceasing the iterative process once the error becomes smaller than $10^{-3}$. Entering the value of $x$ in $F_c$ leads to the resulting compressive and tensile forces, which allows determining the required FRP area as:

$$A_f = \frac{F_c}{f_{fud}} \tag{21}$$

However, if $x_{lin} < h_f$ and $M_d \geq M_{lin}$, concrete behaves non-linearly and the simplified stress block related to $M_d$ may reach either only the flange or the web. First, it is assumed that $\lambda_u x < h_f$ so that $x$ is computed through Equation 12. If the found neutral axis depth is smaller than $h_f/\lambda_u$, the assumption is confirmed, and the reinforcement area computed through Equation 13. In contrast, if $x \geq h_f/\lambda_u$, the assumption is incorrect, and the calculation of $x$ needs to account for both flange and web compressed areas.

Figure 7 illustrates the cross-section analysis for two bending moments: $M_{dw}$ and $M_{df}$, accounting for the areas $b_w x$ and $(b_f-b_w)h_f$, respectively. They are directly determined as:

$$M_{df} = \alpha_{cu}f_{cd}h_f(b_f - b_w)(d - 0.5h_f) \tag{22}$$

$$M_{dw} = M_d - M_{df} \tag{23}$$

Since the neutral axis position relies on the compressed area $b_w x$ and the moment $M_{dw}$, its depth $x$ is computed as follows:

$$x = \frac{d}{\lambda_u}\left(1 - \sqrt{1 - \frac{2M_{dw}}{\alpha_{cu}f_{cd}b_w d^2}}\right) \tag{24}$$

The areas $A_{fw}$ and $A_{ff}$ illustrated in Figure 7 are calculated to resist the moments $M_{dw}$ and $M_{df}$, respectively. Thus, the total reinforcement area $A_f$ corresponds to:

$$A_f = \frac{1}{f_{fud}}\left(\frac{M_{dw}}{d - 0.5\lambda_u x} + \frac{M_{df}}{d - 0.5h_f}\right) \tag{25}$$

This approach is also valid if $x_{lin} \geq h_f$ and $M_d \geq M_{lin}$ considering that concrete exhibits non-linear behavior and the stress block $\lambda_u x$ associated to $M_d$ reaches the web. For all these possibilities, the concrete most compressed fiber $\varepsilon_t$ is determined in the same manner as for the scenario 1, through Equation 14.

Rev. IBRACON Estrut. Mater., vol. 16, no. 4, e16403, 2023

8/20
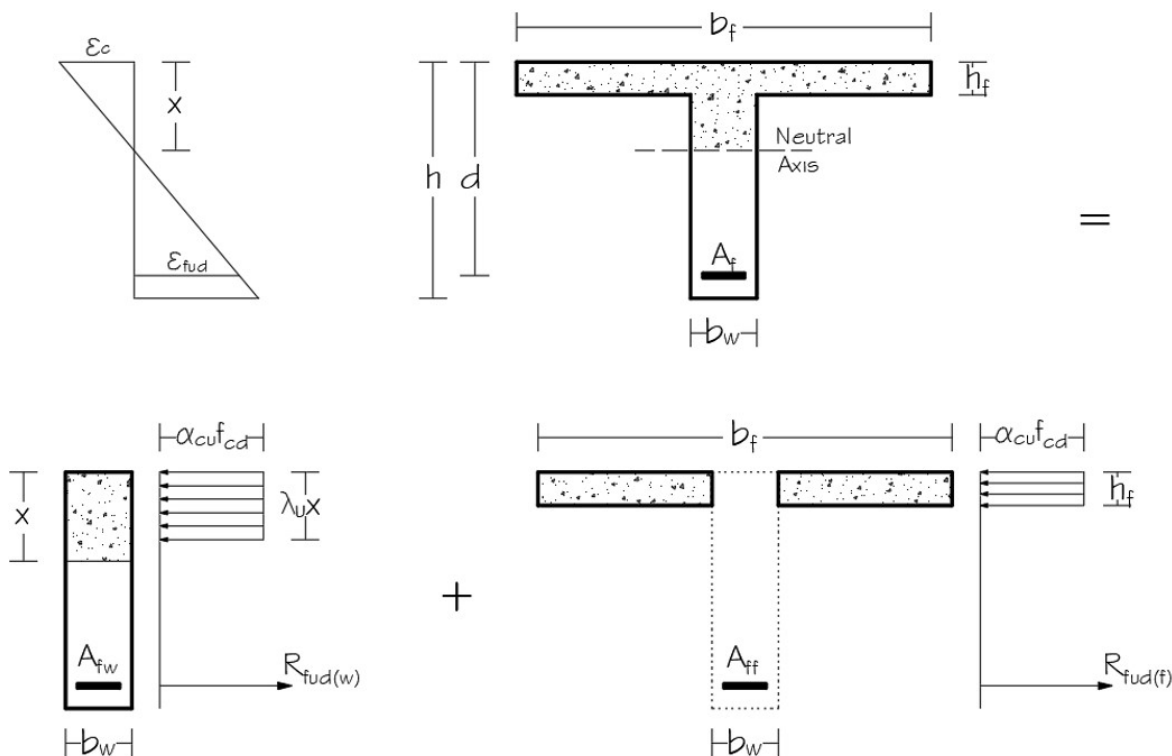
**Figure 7.** Compatibility and equilibrium of a tension-controlled section for which the concrete behaves non-linearly [8].

## 4.3 Scenario 3 - Balanced block on the flange and compression-controlled section

If the balanced stress block lies on the flange and the design moment is higher than the balanced one, the cross-section is over-reinforced and the stress block $\lambda_u x$ can reach the web or not. First, it is assumed that $\lambda_u x < h_f$, with $x$ obtained from Equation 12. If the value found for $x$ confirms this assumption, the next step consists of computing the reinforcement stress $f_f$. Since FRP exhibits linear elastic behavior, the compatibility conditions illustrated in Figure 8 allows determining $f_f$ directly from its strain as:

$$f_f = E_f \varepsilon_{cu} \left( \frac{d - x}{x} \right) \tag{26}$$

The required area $A_f$ found through equilibrium is calculated as follows:

$$A_f = \frac{M_d}{f_f(d - 0.5\lambda_u x)} \tag{27}$$

However, if the neutral axis depth obtained from Equation 12 is equal to or higher than $h_f/\lambda_u$, the assumption is incorrect, and the stress block reaches the web. Figure 9 depicts the cross-section analysis for the calculation of the neutral axis depth and reinforcement area.

Rev. IBRACON Estrut. Mater., vol. 16, no. 4, e16403, 2023

9/20
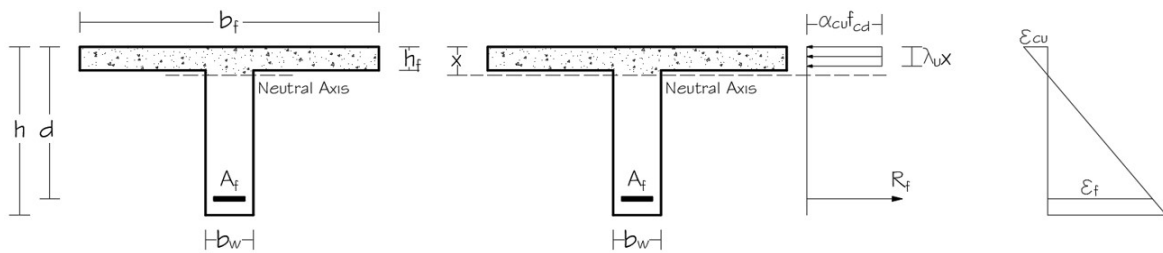
**Figure 8.** Equilibrium and compatibility of a compression-controlled section with stress block on the flange [8].
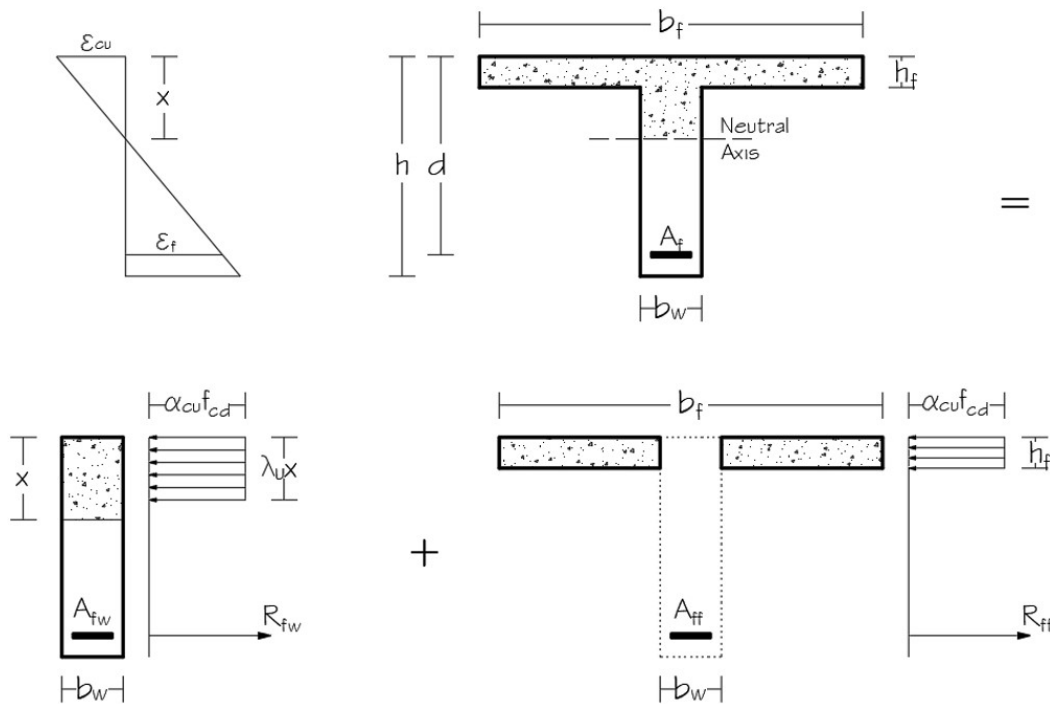


**Figure 9.** Equilibrium and compatibility of a compression-controlled section whose stress block reaches the web [8].

The moments $M_{df}$, $M_{dw}$ as well as the neutral axis depth $x$ are obtained from Equations 22, 23 and 24. This approach is the same as that of tension-controlled sections with stress block reaching the web and concrete behaving non-linearly. Nonetheless, the reinforcement stress is not equal to $f_{fud}$ since the FRP rebars do not fail. Therefore, the stress in the FRP layer is obtained from Equation 26, and the total reinforcement area $A_f$ from:

$$A_f = \frac{1}{f_f}\left(\frac{M_{dw}}{d - 0.5\lambda_u x} + \frac{M_{df}}{d - 0.5h_f}\right) \tag{28}$$

### 4.4 Scenario 4 - Balanced block on the web and compression-controlled section

Unlike the scenario 3, $\lambda_u x_b \geq h_f$ and $M_d \geq M_b$, which ensures that the stress block depth $\lambda_u x$ is equal to or larger than the flange thickness. Therefore, the compatibility and equilibrium conditions for this scenario are also illustrated in Figure 9. The neutral axis depth $x$ and the reinforcement area $A_f$, in turn, are computed through Equations 24 and 28, respectively.

## 5 CHECKING FOR FRP CREEP RUPTURE

The required area $A_f$ to meet the ultimate limit state for flexure may not be enough to avoid creep rupture due to sustained stresses [8]. ACI 440.1R-15 establishes that such stresses must not exceed 20, 30 and 55% of the tensile

strength $f_{fu}$ for GFRP, AFRP and CFRP, respectively. Accordingly, the tensile strength $f_{fu}$ for this verification accounts only for the environmental conditions, not incorporating other safety factors.

To determine the sustained stresses $f_{fs}$, the load combination defined as almost permanent by NBR 6118:2014 [9] was implemented. Additionally, Equations 29 to 31 developed by Ghali and Favre [11] were used to calculate the neutral axis depths $x_{cr}$ under service conditions as shown in Figure 10. The parameter $\eta_f$, in turn, refers to the modular ratio $E_f/E_{cs}$.

$$a_1 = \frac{b_w}{2} \tag{29}$$

$$a_2 = h_f(b_f - b_w) + \eta_f A_f \tag{30}$$

$$a_3 = -d\eta_f A_f - \frac{h_f^2}{2}(b_f - b_w) \tag{31}$$

$$x_{cr} = \frac{-a_2 + \sqrt{a_2^2 - 4a_1 a_3}}{2a_1} \tag{32}$$

The cracking moment of inertia $I_{cr}$ depends on the neutral axis position. Equations 33 and 34 apply for $x_{cr} < h_f$ and $x_{cr} \geq h_f$, respectively [12]. To find the sustained stress $f_{fs}$, ACI 440.1R-15 and NBR 6118:2014 [9] adopt the linear approach defined in Equation 35. The moment $M_{apc}$ refers to the almost permanent load combination.

$$I_{cr} = \frac{b_f x_{cr}^3}{3} + \eta_f A_f(x_{cr} - d)^2 \tag{33}$$

$$I_{cr} = \frac{(b_f - b_w)h_f^3}{12} + \frac{b_w x_{cr}^3}{3} + (b_f - b_w)\left(x_{cr} - \frac{h_f}{2}\right)^2 + \eta_f A_f(x_{cr} - d)^2 \tag{34}$$

$$f_{fs} = M_{apc}\eta_f \frac{(d - x_{cr})}{I_{cr}} \tag{35}$$
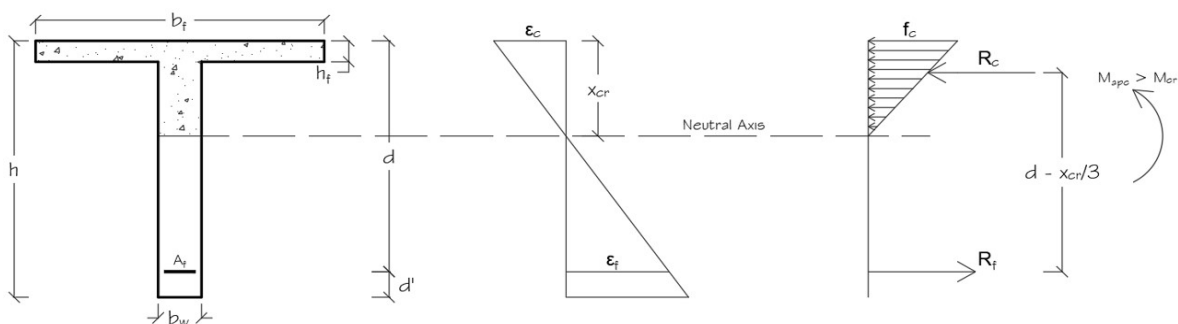


**Figure 10.** Compatibility and equilibrium to compute the sustained stress considering the almost permanent load combination [12].

If the sustained stress exceeds the maximum allowed by ACI 440.1R-15, areas of 0.001 cm$^2$ are progressively incremented to $A_f$, for which Equations 29 to 35 are computationally solved for each adjustment. The sustained stress decreases continuously, and the final adjusted area $A_{adj}$ is that making the sustained stress equal to or slightly lower than the maximum allowed. Thus, the area $A_{adj}$ meets both limit states for flexure and creep rupture.

# 6 DETERMINATION OF THE FLEXURAL STRENGTH

Because of increments in FRP areas to meet both limit states, the flexural strengths and the neutral axis depths increase. Consequently, the simplified stress block previously located on the flange may reach the web, the failure mode may switch from tension to compression-controlled and for the cross-sections that remain tension-controlled, the concrete linear behavior may no longer apply [8].

In order to determine the failure mode, the adjusted area is compared to the balanced one $A_b$ and, in case of tension-control, $A_{adj}$ is compared to $A_{lin}$, the area from which the concrete linear approach no longer applies. There are four scenarios as regards the determination of the flexural strength, explained as follows:

## 6.1 Tension-Control and balanced block on the flange

If $A_{adj} < A_b$, the cross-section is under-reinforced with failure characterized by the FRP rupture. Additionally, if the balanced block depth is smaller than the flange thickness, the stress block associated to the adjusted area $\lambda_u x_{adj}$ does not reach the web. Furthermore, if $A_{adj} < A_{lin}$, the concrete stress-strain relationship can be considered as linear [8].

By imposing equilibrium in Figure 4, the area $A_{lin}$ for which the stress in the most compressed fiber corresponds to 50% of $0.85f_{cd}$ is:

$$A_{lin} = \frac{E_{lin}\varepsilon_{lin}x_{lin}b_f}{2f_{fud}} \tag{36}$$

If $A_{adj} < A_{lin}$, the adjusted neutral axis depth $x_{adj}$ associated to $A_{adj}$ is computed by imposing the equilibrium and compatibility conditions illustrated in Figure 4, which leads to Equations 37 and 38. Once $x_{adj}$ is found, the flexural strength $M_r$ is, thus, obtained from Equation 39.

$$a = \frac{E_{lin}b_f}{2E_fA_{adj}} \tag{37}$$

$$x_{adj} = \frac{\sqrt{1 + 4ad} - 1}{2a} \tag{38}$$

$$M_r = A_{adj}f_{fud}\left(d - x_{adj}/3\right) \tag{39}$$

Conversely, if $A_{adj} \geq A_{lin}$, the simplified stress block represents the concrete constitutive model seeing that the linear approach no longer applies. By imposing the equilibrium conditions shown in Figure 5, the adjusted neutral axis and the flexural strength are determined as follows:

$$x_{adj} = \frac{A_{adj}f_{fud}}{\alpha_{cu}\lambda_uf_{cd}b_f} \tag{40}$$

$$M_r = A_{adj}f_{fud}\left(d - 0.5\lambda_ux_{adj}\right) \tag{41}$$

## 6.2 Tension-control and balanced block on the web

If $A_{adj} < A_b$ and the balanced stress block reaches the web, the block associated to the adjusted area as well as the reference neutral axis $x_{lin}$ can be located either on the flange or web. If $x_{lin} < h_f$ and $A_{adj} < A_{lin}$, the neutral axis associated to $A_{adj}$ is on the flange [8]. Therefore, the adjusted neutral axis and the flexural strength are obtained from Equations 37, 38 and 39.

However, if $x_{lin} < h_f$ and $A_{adj} \geq A_{lin}$, concrete exhibits non-linear behavior and the adjusted stress block may be located either on the flange or web. First, it is assumed that $\lambda_u x_{adj} < h_f$, which allows computing the adjusted neutral axis and flexural strength through Equations 40 and 41, respectively. However, if the value found for $x_{adj}$ is equal to or higher than $h_f/\lambda_u$, the assumption is incorrect; the stress block reaches the web [8]. Therefore, both flange and web compressed areas must be considered. Imposing equilibrium and compatibility for the cross-section illustrated in Figure 7 leads to the correct values of $x_{adj}$ and $M_r$, computed as follows:

$$x_{adj} = \frac{A_{adj}f_{fud} - \alpha_{cu}f_{cd}h_f(b_f - b_w)}{\alpha_{cu}\lambda_u f_{cd}b_w} \tag{42}$$

$$M_r = \alpha_{cu}f_{cd}\left[\lambda_u b_w x_{adj}\left(d - 0.5\lambda_u x_{adj}\right) + h_f(b_f - b_w)(d - 0.5h_f)\right] \tag{43}$$

In contrast, if $x_{lin} \geq h_f$, Equation 36 no longer applies to compute $A_{lin}$ since the linear distribution of the compressive stresses extends to the web, as shown in Figure 6. Therefore, $A_{lin}$ corresponds to the ratio between $F_{lin}$, defined in Equation 15, and the FRP design tensile strength $f_{fud}$. If $A_{adj} < A_{lin}$, the adjusted neutral axis may be on the flange or web. The cross-section analysis illustrated in Figure 4 as well as Equations 37 and 38 determine $x_{adj}$ for the assumption $x_{adj} < h_f$. However, if the solution of such equations provides $x_{adj} \geq h_f$, the assumption is invalid and the correct value of $x_{adj}$ is obtained considering the cross-section analysis shown in Figure 6.

Subsequently, by imposing that the compressive force $F_{adj}$ equals to the ultimate reinforcement load $A_{adj}f_{fud}$, the adjusted neutral axis depth is computed as follows:

$$a_1 = \frac{2}{b_w}\left[(b_f - b_w)h_f + 2A_{adj}\frac{E_f}{E_{lin}}\right] \tag{44}$$

$$a_2 = \frac{1}{b_w}\left[(b_w - b_f)h_f^2 - 2A_{adj}d\frac{E_f}{E_{lin}}\right] \tag{45}$$

$$x_{adj} = a_1\left(\sqrt{\frac{1}{4} - \frac{a_2}{a_1^2}} - \frac{1}{2}\right) \tag{46}$$

The compressive force center $\bar{y}_{adj}$ associated to $x_{adj}$ is obtained from Equation 16, replacing $x_{lin}$ by $x_{adj}$. Therefore, the adjusted flexural strength corresponds to:

$$M_r = A_{adj}f_{fud}\left(d - \bar{y}_{adj}\right) \tag{47}$$

Finally, if $x_{lin} \geq h_f$ and $A_{adj} \geq A_{lin}$, the stress block associated to $A_{adj}$ reaches the web and the concrete exhibits non-linear behavior. Thus, the adjusted neutral axis depth and the flexural strength are obtained from Equations 42 and 43, according to the cross-section analysis illustrated in Figure 7.

## 6.3 Compression-control and balanced block on the flange

If the balanced block is located on the flange and the section is compressed-controlled, the stress block associated to $A_{adj}$ may reach the web or not. First, it is assumed that $\lambda_u x_{adj} < h_f$, corresponding to the analysis illustrated in Figure 8. Since the reinforcement does not fail, its strain is unknown, written as a function of $x_{adj}$ [8]. Therefore, since the resulting compression and tension forces are equal, the adjusted neutral axis is obtained as follows:

$$a = \frac{\alpha_{cu}\lambda_u f_{cd}b_f}{E_f\varepsilon_{cu}A_{adj}} \tag{48}$$

$$x_{adj} = \frac{\sqrt{4ad+1}-1}{2a} \tag{49}$$

If the value found for $x_{adj}$ confirms the assumption that $\lambda_u x_{adj} < h_f$, the flexural strength is:

$$M_r = \alpha_{cu}\lambda_u f_{cd}b_f x_{adj}\left(d - 0.5\lambda_u x_{adj}\right) \tag{50}$$

Rev. IBRACON Estrut. Mater., vol. 16, no. 4, e16403, 2023

13/20

Conversely, if $x_{adj} \geq h_f/\lambda_u$, the assumption is incorrect and Equations 49 and 50 do not apply. It is necessary to consider the compressive stresses on the flange and web as shown in Figure 9, establishing equilibrium of forces and strain compatibility. Thus, $x_{adj}$ is computed as:

$$a_1 = \frac{\alpha_{cu}\lambda_u f_{cd} b_w}{E_f \varepsilon_{cu} A_{adj}} \tag{51}$$

$$a_2 = 1 + \frac{\alpha_{cu} f_{cd}(b_f - b_w)h_f}{E_f \varepsilon_{cu} A_{adj}} \tag{52}$$

$$x_{adj} = \frac{a_2}{a_1}\left(\sqrt{\frac{1}{4} + \frac{a_1}{a_2^2}d} - \frac{1}{2}\right) \tag{53}$$

The flexural strength is obtained from Equation 43, the same as for tension-controlled sections whose neutral axis is on the web and concrete behaves non-linearly [8].

## 6.4 Compression-control and balanced block on the web

If the balanced block reaches the web and the cross-section is compression-controlled, the adjusted neutral axis depth is larger than the balanced one, which means that $\lambda_u x_{adj} \geq h_f$ as well. Therefore, $x_{adj}$ is computed through Equations 51, 52 and 53 while the flexural strength through Equation 43. The only difference from the previous scenario is that the designer knows for sure that the stress block reaches the web.

## 7 EXPERIMENTAL VALIDATION

To validate the proposed methodology, the design equations were used to inversely compute the flexural capacities of 125 beams to posteriorly compare with experimental results. The details of all specimens are shown in Table 1, where the reference in brackets indicates the experimental program related to a group of specimens. The T-section dimensions are given as $b_w/b_f$ and $h/h_f$ in the fields corresponding to *b* and *h*, respectively. The abbreviations **TC** and **CC** refer to the tension and compression-controlled failure modes, respectively.

The concrete compressive strengths were obtained experimentally, mostly from testing cylinders in uniaxial compression after 28 days. The majority of experimental programs obtained the FRP mechanical properties from direct tensile tests; others provided only the manufacturer data, as indicated with a * in Table 1. The majority of the beams were tested under four-point bending, with the load applied at a steady rate of 0.8 to 1.2 mm/min or at steps of 2 to 5 kN. Those from [25] and [20], in turn, were tested under three-point loading. All specimens exhibited flexural failure either due to FRP rupture or crushing of the concrete.

Since the experimental flexural capacities are influenced by the actual mechanical properties of materials, the reduction factors for the concrete compressive and FRP tensile strengths were not included in the analytical analysis. The term 0.85 in $\alpha_{cu}$ was also suppressed to account for the short-term loading inherent to the experimental programs. Moreover, since some beams had multiple reinforcement layers, the compatibility and equilibrium equations were adapted to account for different reinforcement distributions. The theoretical and experimental ultimate moments were plotted along with the identity line, and the accuracy of the analytical model assessed through the coefficient of determination $R^2$.

## 8 RESULTS AND DISCUSSION

This section addresses two aspects of the results: the experimental validation of the proposed methodology and the application of the design program, considering different examples for each scenario described in Section 4.

## 8.1 Comparison to Experimental Results

Table 1 summarizes this comparison for each group of beams, considering different concrete grades and FRP types, as well as beams of rectangular and T-sections. The average ratio between theoretical and experimental moments $M_{th}/M_{exp}$ corresponds to 1.0006, with mean deviation of 0.10 and coefficient of determination $R^2 = 0.962$, which suggests agreement of the analytical methods with respect to experimental results. Figure 11 illustrates the scattering of the data in relation to the identity line.

Rev. IBRACON Estrut. Mater., vol. 16, no. 4, e16403, 2023

14/20
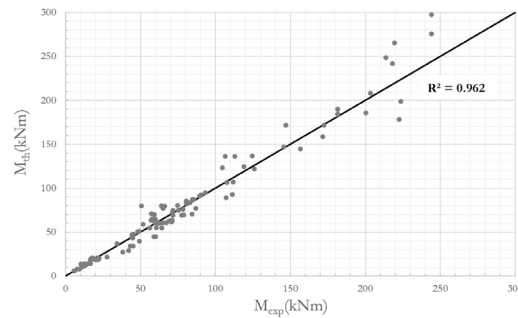
**Figure 11** – Correlation scatter plot for the experimental $M_{exp.}$ and theoretical $M_{th}$ flexural capacities

## 8.2 Program Interface

Using the developed design program, Figure 12 illustrates the calculation of a T-shape section reinforced with AFRP rebars. The user chooses the FRP type and inserts its mechanical properties. Yet, they are not able to define tensile strengths and elasticity moduli out of the intervals defined by Table 4.2.1 of ACI 440.1R-15 for each FRP type. For this example, in particular, the design bending moment corresponds to 98% of the balanced one, which indicates proper use of AFRP and concrete mechanical properties. Nonetheless, since the sustained stress due to the almost permanent load combination is higher than the maximum allowed by ACI 440.1R-15, the required area was increased by 1% to avoid creep rupture. This increment in the FRP area was not enough to switch the failure mode from tension to compression-controlled, resulting in a flexural strength 0.8% higher. This slight increase was not enough to characterize waste of the AFRP rebars' mechanical properties.

If a high-performance concrete with $f_{ck} = 90$ MPa is used, the cross-section becomes too under-reinforced, with flexural strength corresponding to 38% of the balanced moment. As a result, there is waste of the concrete's mechanical properties since the strain at the top corresponds to only 29% of the ultimate strain $\varepsilon_{cu}$. In conclusion, the grade that best fits the reinforcement type for this particular load condition is the grade C20, which allows taking advantage of both concrete and FRP mechanical properties.
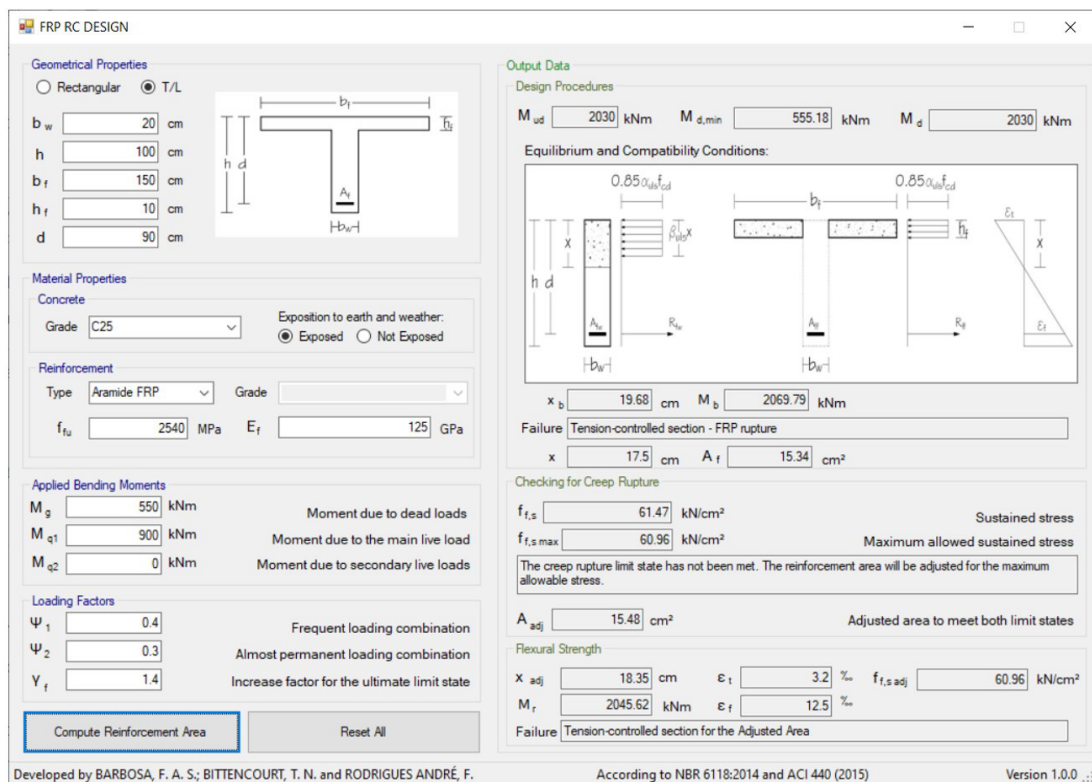


**Figure 12.** Computation of the AFRP reinforcement area using the developed design program.

**Table 1 -** Comparison between experimental and predicted flexural capacities

| Ref. | Beam | Geometrical features | | | Materials (MPa) | | | Ultimate Moments (kNm) | | | Failure |
|------|------|--------|--------|--------|------|------|--------|-------|------|-------------------|------|
| | | b (cm) | h (cm) | $\rho_f$ (%) | $f'_c$ | $f_{fu}$ | $10^{-3} E_f$ | $M_{exp}$ | $M_{th}$ | $M_{th}/M_{exp}$ | |
| [13] | C1-4 | 20 | 30 | 0.47 | 40.4 | 1368.0 | 114.0 | 71.20 | 71.72 | 1.01 | TC |
| | C1-4b | 20 | 30 | 0.47 | 40.4 | 1368.0 | 114.0 | 74.58 | 80.20 | 1.08 | CC |
| | C1-6 | 20 | 30 | 0.71 | 39.3 | 1368.0 | 114.0 | 83.13 | 83.53 | 1.00 | CC |
| | C1-8 | 20 | 30 | 0.95 | 39.3 | 1368.0 | 114.0 | 90.39 | 92.43 | 1.02 | CC |
| | C2-4 | 20 | 30 | 0.43 | 39.9 | 1904.0 | 112.0 | 78.75 | 69.38 | 0.88 | CC |
| | C2-4b | 20 | 30 | 0.43 | 39.9 | 1904.0 | 112.0 | 78.18 | 76.16 | 0.97 | CC |
| | C2-6 | 20 | 30 | 0.64 | 40.8 | 1904.0 | 112.0 | 80.89 | 82.09 | 1.01 | CC |
| | C2-8 | 20 | 30 | 0.85 | 40.8 | 1904.0 | 112.0 | 89.39 | 91.09 | 1.02 | CC |
| | G1-6 | 20 | 30 | 1.29 | 39.1 | 600.0 | 40.0 | 77.47 | 68.86 | 0.89 | CC |
| | G1-8 | 20 | 30 | 1.72 | 39.1 | 600.0 | 40.0 | 86.76 | 76.77 | 0.88 | CC |
| | G2-6 | 20 | 30 | 1.13 | 39.1 | 648.0 | 36.0 | 71.00 | 63.03 | 0.89 | CC |
| | G2-8 | 20 | 30 | 1.51 | 39.1 | 648.0 | 36.0 | 84.54 | 70.52 | 0.83 | CC |
| | AR-6 | 20 | 30 | 0.71 | 39.1 | 1716.0 | 52.0 | 70.85 | 61.62 | 0.87 | CC |
| | AR-8 | 20 | 30 | 0.95 | 39.1 | 1716.0 | 52.0 | 71.75 | 69.04 | 0.96 | CC |
| [14] | BC4NA | 13 | 18 | 2.03 | 46.2 | 772.9 | 38.0 | 22.40 | 20.13 | 0.90 | CC |
| | BC4NB | 13 | 18 | 2.03 | 46.2 | 772.9 | 38.0 | 20.60 | 20.13 | 0.98 | CC |
| | BC4HA | 13 | 18 | 2.03 | 53.9 | 772.9 | 38.0 | 21.00 | 20.63 | 0.98 | CC |
| | BC4HB | 13 | 18 | 2.03 | 53.9 | 772.9 | 38.0 | 21.40 | 20.63 | 0.96 | CC |
| | BC2NA | 13 | 18 | 1.02 | 53.1 | 772.9 | 38.0 | 21.90 | 18.89 | 0.86 | CC |
| | BC2NB | 13 | 18 | 1.02 | 53.1 | 772.9 | 38.0 | 20.00 | 18.89 | 0.94 | CC |
| | BC2HA | 13 | 18 | 1.02 | 57.2 | 772.9 | 38.0 | 19.70 | 18.48 | 0.94 | CC |
| | BC4HB | 13 | 18 | 1.02 | 57.2 | 772.9 | 38.0 | 20.60 | 18.48 | 0.90 | CC |
| [15] | CB2B-1 | 20 | 30 | 0.58 | 52.0 | 779.0 | 38.0 | 57.90 | 65.04 | 1.12 | TC |
| | CB2B-2 | 20 | 30 | 0.58 | 52.0 | 779.0 | 38.0 | 59.80 | 65.04 | 1.09 | TC |
| | CB3B-1 | 20 | 30 | 0.87 | 52.0 | 779.0 | 38.0 | 66.00 | 79.30 | 1.20 | CC |
| | CB3B-2 | 20 | 30 | 0.87 | 52.0 | 779.0 | 38.0 | 64.80 | 79.30 | 1.22 | CC |
| | CB4B-1 | 20 | 30 | 1.16 | 45.0 | 779.0 | 38.0 | 75.40 | 74.63 | 0.99 | CC |
| | CB4B-2 | 20 | 30 | 1.16 | 45.0 | 779.0 | 38.0 | 71.70 | 74.63 | 1.04 | CC |
| | CB6B-1 | 20 | 30 | 1.74 | 45.0 | 779.0 | 38.0 | 84.80 | 87.48 | 1.03 | CC |
| | CB6B-2 | 20 | 30 | 1.74 | 45.0 | 779.0 | 38.0 | 85.40 | 87.48 | 1.02 | CC |
| [16] | FB-2 | 30 | 40 | 0.22 | 30.0 | 690.0 | 41.0 | 68.94 | 62.75 | 0.91 | TC |
| | FB-3 | 30 | 40 | 0.33 | 30.0 | 690.0 | 41.0 | 111.18 | 93.04 | 0.84 | TC |
| | FB-4 | 30 | 40 | 0.44 | 30.0 | 690.0 | 41.0 | 125.88 | 121.91 | 0.97 | TC |
| | FB-6 | 30 | 40 | 0.66 | 30.0 | 690.0 | 41.0 | 171.54 | 158.56 | 0.92 | CC |
| | FB-8 | 30 | 40 | 0.88 | 30.0 | 690.0 | 41.0 | 222.60 | 178.05 | 0.80 | CC |
| | HFB-3 | 30 | 40 | 0.33 | 50.0 | 690.0 | 41.0 | 93.24 | 94.89 | 1.02 | TC |
| | HFB-4 | 30 | 40 | 0.44 | 50.0 | 690.0 | 41.0 | 119.04 | 124.63 | 1.05 | TC |
| | HFB-6 | 30 | 40 | 0.66 | 60.0 | 690.2 | 41.0 | 200.46 | 185.69 | 0.93 | TC |
| | HFB-8 | 30 | 40 | 0.88 | 50.0 | 690.0 | 41.0 | 218.04 | 241.47 | 1.11 | TC |
| | HFB-10 | 30 | 40 | 1.11 | 50.0 | 690.0 | 41.0 | 219.36 | 265.55 | 1.21 | CC |
| [17]* | ISO30-2 | 20 | 30 | 0.95 | 44.0 | 688.8 | 42.0 | 80.40 | 85.18 | 1.06 | CC |
| | KD30-1 | 20 | 30 | 0.95 | 44.0 | 640.9 | 49.0 | 50.60 | 79.79 | 1.58 | CC |
| | KD30-2 | 20 | 30 | 0.95 | 44.0 | 640.9 | 49.0 | 63.80 | 79.79 | 1.25 | CC |
| | KD45-1 | 20 | 45 | 0.64 | 55.0 | 640.9 | 49.0 | 106.60 | 136.16 | 1.28 | TC |
| | KD45-2 | 20 | 45 | 0.64 | 55.0 | 640.9 | 49.0 | 113.00 | 136.16 | 1.20 | TC |
| | ISO55-1 | 20 | 55 | 0.52 | 43.0 | 688.8 | 42.0 | 181.50 | 184.17 | 1.01 | TC |
| | ISO55-2 | 20 | 55 | 0.52 | 43.0 | 688.8 | 42.0 | 181.50 | 184.17 | 1.01 | TC |
| | KD55-1 | 20 | 55 | 0.52 | 43.0 | 640.9 | 49.0 | 146.90 | 171.48 | 1.17 | TC |
| | KD55-2 | 20 | 55 | 0.52 | 43.0 | 640.9 | 49.0 | 172.50 | 171.48 | 0.99 | TC |
| [18]* | ISO2 | 20 | 30 | 0.95 | 43.0 | 688.5 | 45.0 | 80.40 | 83.26 | 1.04 | CC |
| | ISO3 | 20 | 55 | 0.52 | 43.0 | 688.5 | 45.0 | 181.70 | 189.95 | 1.05 | TC |
| | ISO4 | 20 | 55 | 0.52 | 43.0 | 688.5 | 45.0 | 181.70 | 189.95 | 1.05 | TC |
| [19] | Beam 2 | 15 | 20 | 0.19 | 27.7 | 650.0 | 38.0 | 5.89 | 5.84 | 0.99 | TC |
| | Beam 4 | 15 | 25 | 0.15 | 27.7 | 650.0 | 38.0 | 7.85 | 7.94 | 1.01 | TC |
| | Beam 6 | 15 | 30 | 0.13 | 27.7 | 650.0 | 38.0 | 10.79 | 9.77 | 0.91 | TC |
| | Beam 8 | 15 | 20 | 0.19 | 50.1 | 650.0 | 38.0 | 5.89 | 5.90 | 1.00 | TC |
| | Beam 10 | 15 | 25 | 0.15 | 50.1 | 650.0 | 38.0 | 9.48 | 8.00 | 0.84 | TC |
| | Beam 12 | 15 | 30 | 0.25 | 50.1 | 650.0 | 38.0 | 16.75 | 19.46 | 1.16 | TC |

Rev. IBRACON Estrut. Mater., vol. 16, no. 4, e16403, 2023

16/20

**Table 1 –** Continued…

| Ref. | Beam | Geometrical features | | | Materials (MPa) | | | Ultimate Moments (kNm) | | | Failure |
|------|------|------|------|------|------|------|------|------|------|------|------|
| | | b (cm) | h(cm) | $\rho_f$ (%) | f'$_c$ | f$_{fu}$ | $10^{-3}$ E$_f$ | M$_{exp}$ | M$_{th}$ | M$_{th}$/M$_{exp}$ | |
| [20]* | 1FRP1 | 38 .1 | 20.3 | 0.10 | 27.6 | 829.7 | 41.4 | 11.49 | 11.60 | 1.01 | TC |
| | 1FRP2 | 38.1 | 20.3 | 0.10 | 27.6 | 829.7 | 41.4 | 12.67 | 11.60 | 0.92 | TC |
| | 1FRP3 | 38.1 | 20.3 | 0.10 | 27.6 | 829.7 | 41.4 | 11.49 | 11.60 | 1.01 | TC |
| | 2FRP1 | 31.8 | 21.6 | 0.12 | 27.6 | 829.7 | 41.4 | 13.62 | 12.46 | 0.91 | TC |
| | 2FRP2 | 31.8 | 21.6 | 0.12 | 27.6 | 829.7 | 41.4 | 13.26 | 12.46 | 0.94 | TC |
| | 2FRP3 | 31.8 | 21.6 | 0.12 | 27.6 | 829.7 | 41.4 | 13.06 | 12.46 | 0.95 | TC |
| | 4FRP1 | 20.3 | 15.2 | 1.04 | 27.6 | 829.7 | 41.4 | 15.78 | 14.68 | 0.93 | TC |
| | 4FRP2 | 20.3 | 15.2 | 1.04 | 27.6 | 829.7 | 41.4 | 15.58 | 14.68 | 0.94 | TC |
| | 4FRP3 | 20.3 | 15.2 | 1.04 | 27.6 | 829.7 | 41.4 | 16.29 | 14.68 | 0.90 | TC |
| | 5FRP1 | 19.1 | 15.2 | 1.10 | 27.6 | 829.7 | 41.4 | 16.37 | 14.14 | 0.86 | CC |
| | 5FRP2 | 19.1 | 15.2 | 1.10 | 27.6 | 829.7 | 41.4 | 16.65 | 14.14 | 0.85 | CC |
| | 5FRP3 | 19.1 | 15.2 | 1.10 | 27.6 | 829.7 | 41.4 | 15.78 | 14.14 | 0.90 | CC |
| [21] | C-S-1 | 20 | 30 | 0.75 | 26.9 | 1000.0 | 200.0 | 64.11 | 54.50 | 0.85 | TC |
| | C-S-2 | 20 | 30 | 0.29 | 27.5 | 2000.0 | 200.0 | 44.28 | 43.68 | 0.99 | TC |
| | C-C-3 | 20 | 30 | 0.52 | 23.6 | 2000.0 | 200.0 | 44.76 | 43.30 | 0.97 | TC |
| | C-C-4 | 20 | 30 | 0.52 | 27.2 | 1000.0 | 200.0 | 60.66 | 54.87 | 0.90 | TC |
| | C-C-5 | 20 | 30 | 0.75 | 28.0 | 1000.0 | 200.0 | 56.03 | 54.64 | 0.98 | TC |
| [22] | T/C150-2 | 20/70 | 70/15 | 0.36 | 37.5 | 1060.0 | 200.0 | 64.89 | 76.77 | 1.18 | TC |
| | T/C150-4 | 20/70 | 70/15 | 0.52 | 37.5 | 1060.0 | 200.0 | 145.69 | 146.89 | 1.01 | TC |
| | T/C100-4 | 20/70 | 70/10 | 0.63 | 37.5 | 1060.0 | 200.0 | 104.63 | 123.23 | 1.18 | TC |
| | R/C-2 | 20 | 35 | 0.47 | 40.5 | 1060.0 | 200.0 | 57.33 | 71.05 | 1.24 | TC |
| | R/C-4 | 20 | 35 | 0.79 | 40.5 | 1060.0 | 200.0 | 124.60 | 136.60 | 1.10 | TC |
| [23] | II | 20 | 21 | 2.70 | 31.3 | 700.0 | 35.6 | 34.19 | 36.84 | 1.08 | CC |
| | III | 20 | 26 | 0.98 | 31.3 | 886.0 | 43.4 | 45.13 | 47.67 | 1.06 | CC |
| | IV | 20 | 30 | 0.95 | 40.7 | 700.0 | 35.6 | 59.19 | 69.84 | 1.18 | CC |
| | V | 20 | 25 | 2.27 | 40.7 | 700.0 | 35.6 | 57.00 | 63.54 | 1.11 | CC |
| [24] | C-212-D1 | 14 | 19 | 0.85 | 59.8 | 1353.0 | 63.3 | 38.20 | 27.13 | 0.71 | CC |
| | C-216-D1 | 14 | 19 | 1.51 | 56.3 | 995.0 | 64.2 | 45.06 | 34.09 | 0.76 | CC |
| | C-316-D1 | 14 | 19 | 2.27 | 55.2 | 995.0 | 64.2 | 49.38 | 39.75 | 0.80 | CC |
| | C-212-D2 | 16 | 19 | 0.74 | 39.6 | 1353.0 | 63.3 | 27.69 | 21.64 | 0.78 | CC |
| | C-216-D2 | 16 | 19 | 1.32 | 61.7 | 995.0 | 64.2 | 42.15 | 29.17 | 0.69 | CC |
| | C-316-D2 | 16 | 19 | 1.98 | 60.1 | 995.0 | 64.2 | 43.20 | 34.07 | 0.79 | CC |
| [25] | GS1 | 20 | 30 | 1.65 | 28.0 | 736.0 | 46.0 | 60.20 | 62.59 | 1.04 | CC |
| | GS2 | 20 | 30 | 1.65 | 26.0 | 736.0 | 46.0 | 49.00 | 50.70 | 1.03 | CC |
| | CS1 | 20 | 30 | 0.59 | 26.0 | 1392.0 | 116.0 | 51.80 | 58.99 | 1.14 | CC |
| [26]* | B4 | 15.24 | 15.24 | 0.27 | 51.7 | 1899.9 | 140.0 | 12.60 | 13.84 | 1.10 | TC |
| | B5 | 15.24 | 15.24 | 0.27 | 48.0 | 1899.9 | 140.0 | 10.15 | 13.76 | 1.36 | TC |
| | B6 | 15.24 | 15.24 | 0.27 | 45.9 | 1899.9 | 140.0 | 12.87 | 13.73 | 1.07 | TC |
| | B7 | 15.24 | 15.24 | 0.43 | 49.3 | 1899.9 | 140.0 | 17.10 | 18.49 | 1.08 | CC |
| | B8 | 15.24 | 15.24 | 0.43 | 51.1 | 1899.9 | 140.0 | 16.92 | 18.45 | 1.09 | CC |
| | B9 | 15.24 | 15.24 | 0.43 | 53.3 | 1899.9 | 140.0 | 16.58 | 18.21 | 1.10 | CC |
| | B10 | 15.24 | 15.24 | 0.61 | 53.4 | 1899.9 | 140.0 | 17.85 | 20.74 | 1.16 | CC |
| | B11 | 15.24 | 15.24 | 0.61 | 55.0 | 1899.9 | 140.0 | 17.61 | 20.59 | 1.17 | CC |
| | B12 | 15.24 | 15.24 | 0.61 | 43.9 | 1899.9 | 140.0 | 17.51 | 19.52 | 1.12 | CC |
| [27] | AF2T1 | 15 | 30 | 0.35 | 42.8 | 1759.6 | 53.0 | 44.17 | 46.58 | 1.05 | CC |
| | BF3T1 | 15 | 30 | 0.52 | 85.8 | 1759.6 | 53.0 | 59.46 | 60.81 | 1.02 | CC |
| | CF3T1 | 15 | 30 | 0.52 | 85.6 | 1759.6 | 53.0 | 67.21 | 60.75 | 0.90 | CC |
| | DF2T1 | 15 | 30 | 0.35 | 84.5 | 1759.6 | 53.0 | 48.06 | 50.28 | 1.05 | CC |
| | DF3T1 | 15 | 30 | 0.52 | 84.5 | 1759.6 | 53.0 | 62.77 | 60.40 | 0.96 | CC |
| | DF4T1 | 15 | 30 | 0.70 | 84.5 | 1759.6 | 53.0 | 60.02 | 62.06 | 1.03 | CC |
| | DF3T2 | 15 | 30 | 0.52 | 84.5 | 1759.6 | 53.0 | 62.41 | 60.40 | 0.97 | CC |
| | DF3T3 | 15 | 30 | 0.52 | 84.5 | 1759.6 | 53.0 | 60.80 | 60.40 | 0.99 | CC |
| | DS4T2 | 15 | 30 | 1.79 | 84.5 | 1759.6 | 53.0 | 107.20 | 89.01 | 0.83 | CC |
| [28]* | B1T1 | 15/91 | 46/7.6 | 1.07 | 38.6 | 620.0 | 40.0 | 111.85 | 106.63 | 0.95 | TC |
| | B2T1 | 15/76 | 46/7.6 | 1.17 | 35.2 | 620.0 | 40.0 | 107.79 | 106.58 | 0.99 | TC |
| | B3C1 | 15/46 | 45/6.4 | 4.31 | 21.4 | 620.0 | 40.0 | 203.37 | 208.13 | 1.02 | CC |
| | B4T1 | 15/107 | 45/6.4 | 1.27 | 18.6 | 620.0 | 40.0 | 156.60 | 144.44 | 0.92 | TC |
| | B3C2 | 15/61 | 37/6.4 | 3.73 | 21.4 | 620.0 | 40.0 | 223.71 | 198.51 | 0.89 | CC |
| | B1T2 | 15/91 | 38/7.6 | 1.83 | 38.6 | 620.0 | 40.0 | 213.54 | 248.59 | 1.16 | TC |
| | B2C1 | 15/76 | 38/7.6 | 2.57 | 35.2 | 620.0 | 40.0 | 244.05 | 297.66 | 1.22 | CC |
| | B4C1 | 15/107 | 37/6.4 | 3.31 | 18.6 | 620.0 | 40.0 | 244.05 | 275.70 | 1.13 | CC |

Rev. IBRACON Estrut. Mater., vol. 16, no. 4, e16403, 2023

17/20

**Table 1** – Continued…

| Ref. | Beam | Geometrical features | | | Materials (MPa) | | | Ultimate Moments (kNm) | | | Failure |
|------|------|------|------|------|------|------|------|------|------|------|------|
| | | b (cm) | h(cm) | $\rho_f$ (%) | f'$_c$ | f$_{fu}$ | $10^{-3}$ E$_f$ | M$_{exp}$ | M$_{th}$ | M$_{th}$/M$_{exp}$ | |
| [29] | GB1-1 | 18 | 30 | 0.47 | 35.0 | 695.0 | 40.0 | 60.00 | 44.82 | 0.75 | TC |
| | GB1-2 | 18 | 30 | 0.47 | 35.0 | 695.0 | 40.0 | 59.00 | 44.82 | 0.76 | TC |
| | GB2-1 | 18 | 30 | 0.71 | 35.0 | 695.0 | 40.0 | 65.00 | 60.69 | 0.93 | CC |
| | GB2-2 | 18 | 30 | 0.71 | 35.0 | 695.0 | 40.0 | 64.30 | 60.69 | 0.94 | CC |
| | GB3-1 | 18 | 30 | 0.94 | 35.0 | 695.0 | 40.0 | 71.00 | 63.27 | 0.89 | CC |
| | GB3-2 | 18 | 30 | 0.94 | 35.0 | 695.0 | 40.0 | 70.50 | 63.27 | 0.90 | CC |

*Direct tensile tests not performed by the authors, FRP properties provided by the manufacturer, TC = Tension-controlled; CC = Compression-controlled

## 8.3 Examples considering different design scenarios

Since there are several approaches to compute the required FRP area, Table 2 describes the design of the same T-shape section illustrated in Figure 12, considering all the possibilities presented in Section 4. The approach 1A and 1B refer to the first scenario, considering the concrete linear and non-linear behavior, respectively. In turn, 2A indicates concrete linearity and $x < h_f$, whereas 2B, non-linearity. Additionally, both 2C and 2D refer to $x \geq h_f$ with concrete behaving linear and non-linear, respectively. Regarding the third scenario, the approaches 3A and 3B refer to $\lambda_u x < h_f$ and $\lambda_u x \geq h_f$, respectively; whereas the only possibility for the fourth scenario, 4A, corresponds to $\lambda_u x_b \geq h_f$ and $M_d \geq M_b$.

**Table 2.** Definition of the failure mode corresponding to all design approaches previously described

| Case | FRP | f$_{fu}$* (MPa) | Exposition | E$_f$ (GPa) | f$_{ck}$ (MPa) | M$_d$ (kNm) | x$_b$ (cm) | M$_b$ (kNm) | Failure Mode |
|------|-----|------|------|------|------|------|------|------|------|
| 1A | Aramid | 2540 | No | 125 | 80 | 2100 | 14.1 | 5276.5 | TC |
| 1B | Carbon | 3690 | No | 150 | 60 | 1820 | 11.9 | 4088.2 | TC |
| 2A | Glass | 683 | Yes | 51 | 65 | 962.7 | 24.8 | 5144.1 | TC |
| 2B | Glass | 600 | No | 51 | 40 | 759.4 | 29.3 | 3575.6 | TC |
| 2C | Carbon | 1300 | Yes | 145 | 90 | 1820 | 26.6 | 6142.7 | TC |
| 2D | Aramid | 2300 | Yes | 100 | 20 | 1582 | 17.8 | 1629.0 | TC |
| 3A | Carbon | 3000 | No | 120 | 80 | 4340 | 10.7 | 4149.0 | CC |
| 3B | Carbon | 3690 | Yes | 180 | 90 | 5670 | 13.9 | 5444.6 | CC |
| 4A | Aramid | 1800 | Yes | 70 | 20 | 1820 | 16.3 | 1606.2 | CC |

Regarding the cases 1A and 1B, the results showed that the balanced block is located on the flange when high-performance concretes are used in conjunction with FRP rebars exhibiting large ultimate strains. If the cross-section is tension-controlled, the concrete linear stress-strain relationship is more likely to apply if the applied bending moment is considerably lower than the balanced one, especially if high-performance concretes are used.

In contrast, the second scenario is characterized by the use of FRP with low deformability compared to first scenario. As a result, the balanced block reached the web. However, since the design bending moments regarding 2A and 2B are significantly lower than the balanced ones, their respective stress blocks fell on the flange. Even though the design moments corresponding to 2C and 2D are lower than the balanced ones, their respective neutral axes are positioned on the web. However, the linear approach applied only for 2B.

Alike the possibilities 1A and 1B, the association of high-performance concretes with large deformability FRP caused the balanced block to reach only the flange for cases 3A and 3B. In contrast, the applied moments are higher than the balanced ones, making stresses blocks fall on the flange and web, respectively. Regarding 4A, the association of concrete and FRP is similar to that of scenario 2, with the balanced block reaching the web.

The design for the ultimate limit state and verification for creep rupture are described in Table 3. The adjustments in AFRP and GFRP areas for 1A, 2A and 2B resulted in deeper neutral axes $x_{adj}$ and increased top concrete strains $\varepsilon_c$, not reducing the reinforcement strains $\varepsilon_f$. As a result, the cross-section curvatures $\varphi$ slightly increased, improving ductility. The CFRP RC compression-controlled sections 3A and 3B, in turn, exhibited the largest curvatures while the tension-controlled 2C, the smallest.

Since the cross-sections 2A, 2B and 2C are tensile-controlled with small curvatures, the designer may either increase the amount of reinforcement up to the balanced area $A_b$ or decrease the compressive strength $f_{ck}$, which would lead to larger curvatures. However, if the section becomes compression-controlled, a further increase in A$_f$ or decrease in f$_{ck}$ would deepen the neutral axis and reduce the FRP strain, leading to smaller curvatures.

Rev. IBRACON Estrut. Mater., vol. 16, no. 4, e16403, 2023

18/20

**Table 3.** Design for the ultimate limit state and checking for creep rupture for all approaches

| Case | $x$ (cm) | $A_f$ (cm$^2$) | $M_{apc}$ (kNm) | $f_{fs}$ (MPa) | $A_{adj}$ (cm$^2$) | $A_b$ (cm$^2$) | Failure | $x_{adj}$ (cm) | $\varepsilon_c$ (‰) | $\varepsilon_f$ (‰) | $M_r$ (kNm) | $10^3\varphi$ (rad/m) |
|---|---|---|---|---|---|---|---|---|---|---|---|---|
| 1A | 5.3 | 13.0 | 1010 | 841.4 | 16.7 | 35.3 | TC | 6.8 | 1.10 | 14.1 | 2678.3 | 0.17 |
| 1B | 5.1 | 7.3 | 810 | 1244 | 7.3 | 16.9 | TC | 5.1 | 1.15 | 18.9 | 1820.0 | 0.22 |
| 2A | 8.6 | 30.0 | 325 | 122 | 38.7 | 166.5 | TC | 9.7 | 0.87 | 7.21 | 1233.4 | 0.09 |
| 2B | 2.9 | 23.2 | 360 | 175.5 | 43 | 116.4 | TC | 5.5 | 0.47 | 7.24 | 1394.4 | 0.09 |
| 2C | 11.6 | 23.5 | 880 | 431 | 23.5 | 81.2 | TC | 11.6 | 0.92 | 6.21 | 1820.0 | 0.08 |
| 2D | 14.7 | 13.2 | 549 | 477 | 13.2 | 13.6 | TC | 14.7 | 2.76 | 14.15 | 1582.0 | 0.19 |
| 3A | 11.3 | 23.1 | 1700 | 841.9 | 23.1 | 20.9 | CC | 11.3 | 2.60 | 18.22 | 4340.0 | 0.23 |
| 3B | 16.3 | 31.5 | 3350 | 1307.4 | 31.5 | 25.0 | CC | 16.3 | 2.6 | 11.78 | 5670.0 | 0.16 |
| 4A | 31.9 | 49.2 | 1090 | 279 | 49.2 | 17.1 | CC | 31.9 | 3.5 | 6.39 | 1820.0 | 0.11 |

## 9 CONCLUSIONS

This paper implemented the FRP mechanical properties provided by ACI 440.1R-15 [3] to the Brazilian code NBR 6118:2014 [9], developing the equations for the design of T-shape sections reinforced by FRP rebars. The deduced formulations accounted for all possibilities of neutral axis position, failure mode and concrete behavior, which resulted in a design applet that calculates the FRP area based on the ultimate limit state for flexure and creep rupture.

The design procedures were validated by comparing the predicted flexural capacities with experimental results available in the literature for 125 beams. The average ratio between computed and experimental ultimate moments corresponds to 1.0006 with mean deviation of 0.10 and $R^2 = 0.962$, which suggests efficacy of the proposed methodology to compute the required amount of flexural FRP reinforcement given a design bending moment.

In conclusion, since there is no guideline deeply addressing the design of T-shape beams reinforced by FRP rebars, the presented design approaches can help students and engineers to understand how these members behave, considering different combinations of FRP and concrete grades. Therefore, they are able to elect the ones that provide the best results in terms of ductility, flexural strength and economical solutions.

## ACKNOWLEDGEMENTS

## REFERENCES

[1]   A. M. Neville, "Consideration of durability of concrete structures: past, present and future," *Mater. Struct.*, vol. 34, pp. 114–118, 2001.

[2]   L. Bertolini, "Steel corrosion and service life of reinforced concrete structures," *Struct. Infrastruct. Eng.*, vol. 4, no. 2, pp. 123–137, 2008.

[3]   American Concrete Institute, *Guide for the Design and Construction of Structural Concrete Reinforced with Fiber-Reinforced Polymer (FRP) Bars*, ACI 440.1R-15, 2015, 83 p.

[4]   *fib* International Federation for Structural Concrete, *FRP Reinforcement in RC Structures* (Bulletin 40). Lausanne: *fib* Task-Group 9.3, Federal Institute of Technology, 2007, 147 p.

[5]   C. Tuakta, "Use of fiber-reinforced polymer composite in bridge structures," M.S. thesis, Massachusetts Inst. Technol., Cambridge, 2005, 50 p.

[6]   E. Gudonis, E. Timinskas, V. Gribniak, G. Kaklauskas, A. K. Arnautov, and V. Tamulènas, "FRP reinforcement for concrete structures: state-of-the-art review of application and design," *Eng. Struct. Technol.*, vol. 5, no. 4, pp. 147–158, 2013.

[7]   D. H. Tavares, J. S. Giongo, and P. Paultre, "Behavior of reinforced concrete beams reinforced with GFRP bars," *Ibracon Struct. Mater. J.*, vol. 1, no. 3, pp. 285–295, 2008.

[8]   F. A. S. Barbosa, "Numerical assessment of concrete flexural members reinforced by FRP rebars," M.S. thesis, Univ. São Paulo, São Paulo, 2020.

[9]   Associação Brasileira de Normas Técnicas, *Projeto de Estruturas de Concreto,* ABNT NBR 6118, 3ª ed., 2014, 238 p.

[10] Comitê IBRACON/ABECE, *Prática Recomendada CT 303 – Estruturas de Concreto Armado com Barras de Polímero Reforçado com Fibras (FRP)*, 1ª ed. São Paulo: IBRACON, 2021, 63 p.

[11] A. Ghali and R. Favre, *Concrete Structures: Stresses and Deformations*, 1st ed. London, UK: Chapman & Hall, 1986, 352 p.

[12] R. C. Carvalho and J. R. Figueiredo Fo., *Cálculo e Detalhamento de Estruturas Usuais de Concreto Armado: Segundo a NBR 6118:2014*, 4ª ed. São Carlos: Edufscar, 2014, 415 p.

[13] C. Kassem, A. S. Farghaly, and B. Benmokrane, "Evaluation of flexural behavior and serviceability performance of concrete beams reinforced with FRP bars," *J. Compos. Constr.*, vol. 5, no. 11, pp. 682–695, 2011.

[14] M. Thériault and B. Benmokrane, "Effects of FRP reinforcement ratio and concrete strength on flexural behavior of concrete beams," *J. Compos. Constr.*, vol. 2, no. 1, pp. 7–16, 1998.

[15] R. Masmoudi, M. Thériault, and B. Benmokrane, "Flexural behavior of concrete beams reinforced with deformed fiber reinforced plastic reinforcing rods," *ACI Struct. J.*, vol. 5, no. 6, pp. 665–675, 1998.

[16] Ridwan and D. T. Putri, "Flexural capacity of concrete beam reinforced with GFRP bars," *J. Phys. Conf. Ser.*, vol. 2049, no. 1, pp. 012075, 2021.

[17] B. Benmokrane, O. Chaallal, and R. Masmoudi, "Glass Fibre Reinforced Plastic (GFRP) rebars for concrete structures," *Constr. Build. Mater.*, vol. 9, no. 6, pp. 353–364, 1995.

[18] B. Benmokrane, O. Chaallal, and R. Masmoudi, "Flexural response of concrete beams reinforced with FRP reinforcing bars," *ACI Struct. J.*, vol. 91, no. 2, pp. 46–55, 1996.

[19] A. F. Ashour, "Flexural and shear capacities of concrete beams reinforced with GFRP bars," *Constr. Build. Mater.*, vol. 20, pp. 1005–1015, 2006.

[20] J. R. Yost, C. H. Goodspeed, and E. R. Schmeckpeper, "Flexural performance of concrete beams reinforced with FRP grids," *J. Compos. Constr.*, vol. 5, no. 1, pp. 18–25, 2005.

[21] A. F. Ashour and M. N. Habeeb, "Continuous concrete beams reinforced with CFRP bars," *ICE Proc. Struct. Build.*, vol. 161, no. 6, pp. 349–357, 2008.

[22] A. F. Ashour, and M. Family, "Tests of concrete flanged beams reinforced with CFRP bars," *Mag. Concr. Res.*, vol. 58, no. 9, pp. 627–639, 2006.

[23] S. H. Alsayed, Y. A. Al-Salloum, and T. H. Almusallam, "Performance of glass fiber reinforced plastic bars as a reinforcing material for concrete structures," *Compos., Part B Eng.*, vol. 31, pp. 555–567, 2000.

[24] C. Barris, L. Torres, A. Turom, M. Baena, and A. Catalan, "An experimental study of the flexural behavior of GFRP RC beams and comparison with predicted models," *Compos. Struct.*, vol. 91, pp. 286–295, 2009.

[25] M. El-Mogy, A. El-Ragaby, and E. El-Salakawy, "Flexural behavior of continuous FRP-reinforced concrete beams," *J. Compos. Constr.*, vol. 14, no. 6, pp. 669–680, 2010.

[26] G. Thiagarajan, "Experimental and Analytical Behavior of Carbon Fiber-based rods as Flexural Reinforcement," *J. Compos. Constr.*, vol. 7, no. 1, pp. 64–72, 2003.

[27] M. A. Rashid, M. A. Mansur, and P. Paramasivam, "Behavior of aramid fiber-reinforced polymer reinforced high strength concrete beams under bending," *J. Compos. Constr.*, vol. 9, no. 2, pp. 117–127, 2005.

[28] R. K. Kalluri, "Bending behavior of concrete T-beams reinforced with glass-fiber reinforced polymer bars," Ph.D. dissertation, West Virginia Univ., Morgantown, 1999, 112 p.

[29] H. A. Toutanji and M. Saafi, "Flexural behavior of concrete beams reinforced with glass fiber-reinforced polymer (GFRP) bars," *ACI Struct. J.*, vol. 97, no. 5, pp. 712–719, 2000.

**Editors:** Rebecca Gravina, Guilherme Aris Parsekian.

ORIGINAL ARTICLE

# Steel-concrete composite highway bridges dynamic structural behaviour assessment considering the pavement progressive deterioration effect

*Avaliação do comportamento estrutural dinâmico de pontes rodoviárias mistas (aço-concreto) considerando o efeito da deterioração progressiva do pavimento*

Ana Célia Soares da Silva[a]  iD

Vencislau Manuel Quissanga[a]  iD

José Guilherme Santos da Silva[a]  iD

[a]Universidade do Estado do Rio de Janeiro – UERJ, Faculdade de Engenharia – FEN, Programa de Pós-graduação em Engenharia Civil – PGECIV,
 Rio de Janeiro, RJ, Brasil

**Abstract:** Highway bridges are usually subjected to random dynamic actions of variable magnitude due to vehicles convoys crossing on the bridge pavement deck along their service life. In this context, the asphalt pavement deteriorated road surface condition represents a key issue to assess the bridge displacement and stress values. This way, this research work aims to develop an analysis methodology in order to assess the dynamic structural behaviour of steel-concrete composite highway bridges including the vehicles convoys dynamic actions and the pavement progressive deterioration effect. The conclusions of this investigation have indicated that the displacements and stresses values are considerably higher, with relevant amplifications up to four times, when the road pavement deterioration effect is considered in the bridge dynamic analysis.

**Keywords:** steel-concrete highway bridges, dynamic structural analysis, pavement progressive deterioration effect, finite element modelling.

**Resumo:** As pontes rodoviárias geralmente estão sujeitas a ações dinâmicas aleatórias de magnitude variável devido aos comboios de veículos que cruzam o tabuleiro da ponte ao longo de sua vida útil. Diante deste contexto, a condição de deterioração da superfície do pavimento asfáltico da estrutura torna-se relevante para avaliar os valores de deslocamentos e tensões. Deste modo, este trabalho de pesquisa tem como objetivo desenvolver uma metodologia de análise para avaliação da resposta estrutural dinâmica de pontes rodoviárias mistas (aço-concreto), considerando-se as ações dinâmicas oriundas do tráfego de comboios de veículos sobre a superfície irregular, além do efeito da deterioração progressiva da superfície do pavimento. As conclusões desta investigação indicam que os valores de deslocamentos e tensões são consideravelmente superiores, com amplificações de até quatro vezes, quando o efeito da deterioração do pavimento da pista é considerado na análise dinâmica da ponte.

**Palavras-chave:** pontes rodoviárias mistas (aço-concreto), análise estrutural dinâmica, efeito da deterioração progressiva do pavimento, modelagem em elementos finitos.

# 1 INTRODUCTION

During the life cycle of a bridge, dynamic impacts related to random traffic loads and deteriorated road surfaces can induce significant increase of the displacements and stress values. These dynamic actions can generate the nucleation of fractures or even their propagation on the bridge deck. This is a relevant problem, especially in regions where road maintenance is not effective, causing premature deterioration of the bridge's superstructure and pavement [1]. Considering the relevance of this scenario, the scientific community has initiated a continuous effort since the middle 80's, associated to the assessment of the dynamic effects due to vehicles traffic on bridge irregular pavement surfaces.

Several research works have been developed [1]–[4] and it was made evident that the effects due to the dynamic interaction between the vehicle's wheels and the irregular pavement surface can be much more important than those produced by the vehicle's smooth movement [2]. The poor road-roughness levels could lead to high amplifications and in some cases, these effects are even larger than those due to the vehicle's static presence, increasing drastically with the decrease of the pavement surface quality [2].

Thus, approaches based on the use of a unique road-roughness level for the entire bridge life cycle can lead to unrealistic results or over-conservative life process whether an excellent or poor roughness level is adopted, respectively. It is necessary and more realistic to consider the influence of the progressive degradation of the road surface roughness based on the use of a vehicle-bridge interaction model. This influence was considered in the research works developed by Zhang and Cai [3], [5] conducting to more realistic estimations.

This way, having these thoughts in mind, in this paper an analysis methodology is developed in order to assess the steel-concrete composite highway bridge decks dynamic structural behaviour due to the vehicles crossing on the rough pavement surfaces, defined by a probabilistic model, considering the dynamic actions of vehicles convoys and also the progressive pavement surface deterioration effect [1].

Therefore, the studied structural model corresponds to a typical steel-concrete composite highway bridge deck, with straight axis, simple supported and spanning 13.0 m by 40.0 m [6]. The developed numerical model adopted the usual mesh refinement techniques present in Finite Element Method (FEM) simulations implemented in the ANSYS [7] program.

Initially, the investigated bridge road surface roughness was defined based on the use of the Power Spectral Density (PSD) function, as an expression of the road surface random irregularities. The road surface roughness was assumed as a zero-mean stationary Gaussian random process [2]. After that, a complete mathematical formulation associated to the bridge road pavement progressive deterioration effect, along the time, was investigated [1].

This way, the bridge dynamic structural response is obtained by the integration of its equations of motion, in the time domain, considering the excitation produced by the vehicles traffic on the bridge deck irregular pavement surface, incorporating the pavement progressive deterioration effect [1], [2].

The bridge dynamic structural response was investigated through an extensive parametric study based on the calculated displacements and stresses values. This way, response spectra were generated considering the vehicles convoys velocities between 20 km/h and 80 km/h, and the increases on different levels of vehicles traffic on the deck structure along of a period of 15 years, aiming to investigate the road pavement progressive deterioration effect on the bridge dynamic response.

The main conclusions of this this research work focused on alerting structural engineers to the possible distortions associated with the steel-concrete composite bridge dynamic structural response, when subjected to dynamic actions due to vehicle convoys on the irregular pavement surface. The results have indicated that the displacements and stresses values were considerably higher, with relevant amplifications up to four times, when the road pavement deterioration effect was considered in the bridge dynamic analysis.

# 2 VEHICLES MATHEMATICAL MODELLING

The truck adopted in this work is presented in Figure 1a, and is one of the most common vehicles used in Brazilian roads [8], but other types are available [9]. The developed two-axle truck structural-mechanical mathematical model is shown in Figure 1b. The vehicle dynamic properties were determined based on experimental tests [10], and the vehicle mathematical model presents four degrees of freedom: three translations and one rotation. The dynamic properties (mass, damping and stiffness), including the truck tires and suspensions are listed in Table 1.

(a) Truck geometry: 2C vehicle.  (b) Modelling of the rigid body, springs and dampers.
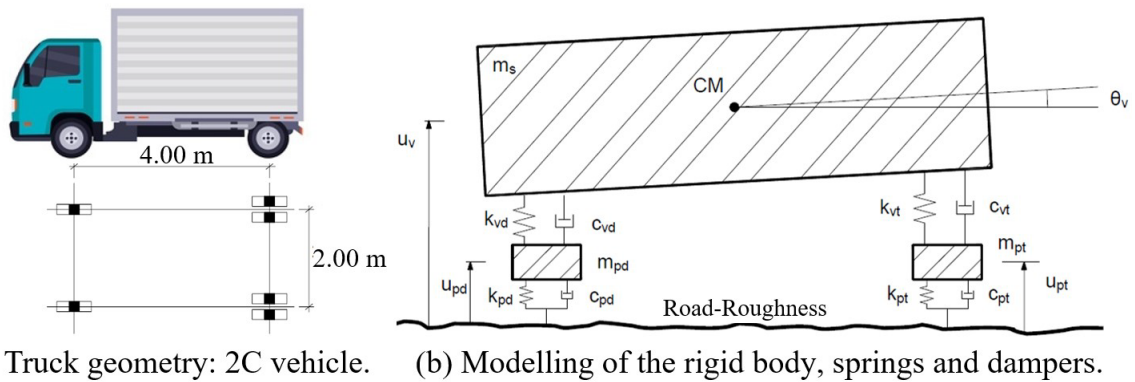
**Figure 1.** Model of the two-axle truck prototype.

**Table 1.** Dynamic properties of the vehicle (2C vehicle: 2 axles).

| Parameter | 1st Axle | 2nd Axle | Units |
|---|---|---|---|
| Suspension spring stiffness ($k_v$) | 864 | 2,340 | kN/m |
| Tire spring stiffness ($k_p$) | 1,620 | 6,720 | kN/m |
| Suspension mass ($m_p$) | 635 | 1,066 | kg |
| Total mass (m) | 20.3 | | t |
| Truck body mass ($m_s$) | 18,599 | | kg |
| Natural frequencies (f) | [1.17 ; 2.08 ; 10.00 ; 14.73] | | Hz |

## 3 MODELLING OF THE ROAD SURFACE ROUGHNESS

The road surface roughness is generally defined as an expression of road surface irregularities and it is the primary factor affecting the dynamic response of both vehicles and bridges [2], [10]. Based on the studies carried out by Dodds and Robson [11], the road surface roughness was assumed as a zero-mean stationary Gaussian random process and it can be generated through an inverse Fourier transformation as shown in Equation 1.

$$r(x) = \sum_{i=1}^{N} \sqrt{2\ \Delta\Omega\ G_d(\Omega_i)}\ \cos\left(2\pi\ \Omega_i\ x + \theta_i\right) \tag{1}$$

where $\theta_i$ = random phase-angle uniformly distributed from 0 to $2\pi$; $G_d(\Omega)$ = Power Spectral Density (PSD) function (cm$^3$/cycle); and $\Omega_i$ = wave number (cycles/m).

The PSD function for road surface roughness was developed by Dodds and Robson [11] as presented in Equation 2.

$$G_d(\Omega_i) = G_d(\Omega_0) \left[\frac{\Omega}{\Omega_0}\right]^{-2} \tag{2}$$

where $\Omega$ = spatial frequency of the pavement harmonic i (cycles/m); $\Omega_0$ = discontinuity frequency of $1/2\pi$ (equal to 1 rad/m); and $G_d(\Omega_0)$ = road roughness coefficient (m$^3$/cycle), also called RRC, whose value is chosen depending on the road class presented in Table 2, EN 1991-2 (Annex B) [12].

**Table 2.** Average values of $G_d(\Omega_0)$ for different levels of road quality (in cm$^3$) [12].

| Road class | Road quality level | $G_d(\Omega_0)$: lower | $G_d(\Omega_0)$: mean | $G_d(\Omega_0)$: upper |
|---|---|---|---|---|
| A | Excellent | - | 1 | 2 |
| B | Good | 2 | 4 | 8 |
| C | Average | 8 | 16 | 32 |
| D | Poor | 32 | 64 | 128 |
| E | Very poor | 128 | 256 | 512 |

# 4 PAVEMENT PROGRESSIVE DETERIORATION EFFECT MODELLING

In this work a mathematical formulation associated to the bridge road pavement progressive deterioration effect was investigated. This way, in order to consider the road surface damages from loads or corrosions, a progressive deterioration model for the road-roughness is necessary when generating the random road profiles. Thus, Paterson and Attoh-Okine [13] have developed a model considering the International Roughness Index (IRI) with the values at any time after the service of the road surface being calculated, see Equation 3.

$$IRI_t = 1.04e^{\eta t} [\, IRI_0 + 263 \,(1+ SNC)^{-5} \,(CESAL)_t] \tag{3}$$

where $IRI_t$ = IRI value at time t; $IRI_0$ = initial roughness value directly after completing the construction and before opening to traffic; t = time in years; $\eta$ = environmental coefficient; SNC = structural number; and $(CESAL)_t$ = estimated number of traffic in terms of AASHTO 80-kN (18-kip) cumulative equivalent single axle load at time t, in millions.

The initial $IRI_0$ is modified from one region to another depending on the specifications adopted in each country for road constructions. In this work the adopted values was equal to 0.90 m/km. The environmental coefficient, $\eta$, varies from 0.01 to 0.7 and depends on dry/wet, freezing/non-freezing conditions. The value usually adopted is equal to 0.10 for bridges exposed in general environment conditions. Structural number, SNC, is associated to a parameter that is calculated from data on the strength and thickness of each layer in the pavement, adopted equal to 4 in this analysis. To estimate the traffic number in terms of AASHTO 80-kN (18-kip), the Equation 4 was used.

$$(CESAL)_t = f_d \, n_{tr}(t) \, F_{Ei} \, 10^{-6} \tag{4}$$

where $f_d$ = design lane factor; $n_{tr}(t)$ = cumulated number of truck passages for the future year t, estimated using Equation 5; and $F_{Ei}$ = load equivalency factor for axle category i, calculated following the rules of AASHTO Guide for Design of Pavement Structures [14].

Due to the yearly traffic increase, the CESAL parameter is modified resulting in a change of the progressive deterioration function. Kwon and Frangopol [15], based on the Average Daily Truck Traffics (ADTTs) and traffic increase rate per year, also estimated the cumulated number of truck passages for the future year t using Equation 5.

$$n_{tr}(t) = N_{obs} \left[ \frac{(1+\alpha)^t - 1}{\ln(1+\alpha)} \right] \tag{5}$$

where subscript "tr" means trucks only; t = number of years; $N_{obs}$ = total number of vehicles at first year, considered equal to 50,000, due to the localization of the bridge within a local road with a low traffic of trucks [12]; and $\alpha$ = traffic increase rate per year. In this research work the traffic increase rate per year was adopted equal to 0%, 3% and 5%.

The IRI formulation was developed in 1986 and is used to define the longitudinal profile of a travelled wheel track [16]. This coefficient (IRI) is based on the average rectified inclination (ARS), which is a filtered ratio of the accumulated movement of the standard vehicle suspension divided by the distance travelled by the vehicle during the measurement. According to Sayers et al. [17], since the World Bank published a technical report for conducting and calibrating the roughness measurements, IRI started to be used as a worldwide standard method for analysing the road longitudinal profile [1], [4].

Alternatively, the International Organization for Standardization [18] used RRC to define the road-roughness classification, and the ranges are listed in Table 3. This coefficient (RRC) was created to relate the tire characteristics to the road rolling resistance. Several correlations have been developed between the IRI and RRC indexes [19], [20]. Based on the corresponding ranges of the road-roughness coefficient and the IRI value [20], a relationship between IRI and RRC is used in the present study as shown in Equation 6.

$$RRC_t = G_d(\Omega_0)_t = 6.1972 \times 10^{-9} \times \exp[\, IRI_t \,/\, 0.42808] + 2 \times 10^{-6} \tag{6}$$

**Table 3.** RRC Values for road-roughness classification [18].

| Road-roughness classification | Ranges for RRCs |
|---|---|
| Very good | $2\times10^{-6}$ to $8\times10^{-6}$ |
| Good | $8\times10^{-6}$ to $32\times10^{-6}$ |
| Average | $32\times10^{-6}$ to $128\times10^{-6}$ |
| Poor | $128\times10^{-6}$ to $512\times10^{-6}$ |
| Very poor | $512\times10^{-6}$ to $2048\times10^{-6}$ |

In sequence, Figure 2 presents a general flowchart for the pavement progressive deterioration mathematical modelling investigated in this research work, indicating the used equations and a logical sequence of application.

## 5 INVESTIGATED HIGHWAY BRIDGE

In this work, a typical simply supported steel-concrete composite highway bridge designed in accordance with AASHTO LRFD [21] and NBR 16694 [22] design specifications was investigated. The selected case study is a good representative of real simply-supported highway bridges with straight axis and spanning 13 m by 40 m [6]. The structural system is constituted by four composite girders and a 0.225 m thick concrete slab. In order to prevent web buckling, steel plate stiffeners are welded along the steel girders with 1880 mm spacing at the span-sections and 1200 mm spacing at the support-sections. Steel plate stiffeners were also adopted above the girder supports. Two different cross sections were adopted along the longitudinal composite beams, designated as support cross-section and span cross-section. The bridge structural system comprises cross diaphragms like steel trusses. The diaphragms are made of equal angle profiles with 10 mm wall thickness, see Figures 3 to 5.
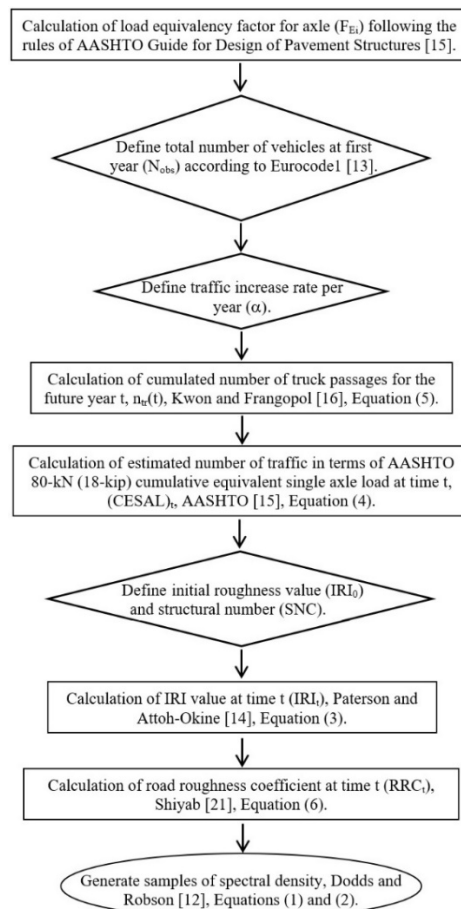


**Figure 2.** General flowchart used for the pavement progressive deterioration modelling.

Rev. IBRACON Estrut. Mater., vol. 16, no. 4, e16404, 2023

5/14
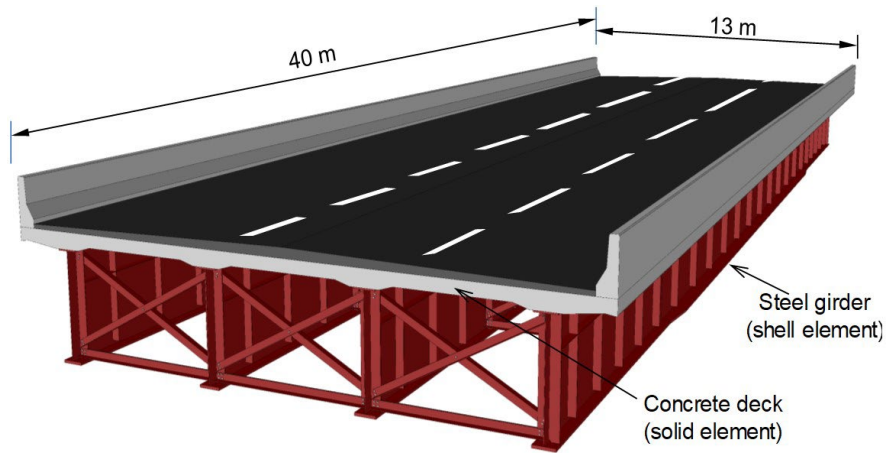
**Figure 3.** Simply supported steel-concrete roadway bridge: overall view.
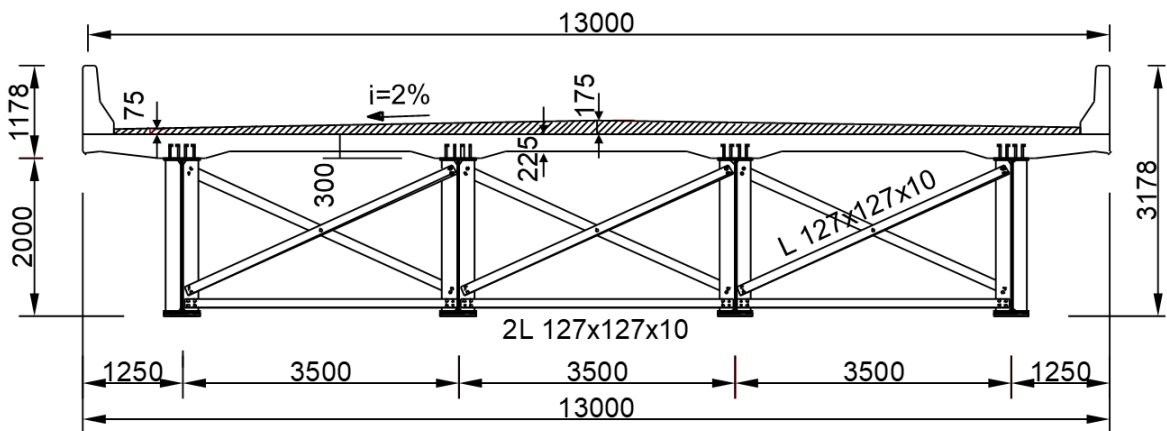


**Figure 4.** Bridge section at the support: units in millimetres [6].

The steel sections are composed by welded wide flanges made with A588 steel with 350 MPa yield strength and 485 MPa ultimate tensile strength. A $2.05 \times 10^5$ MPa Young's modulus with 0.3 Poisson's ratio and 7,850 kg/m³ material density was adopted for the steel girders. The concrete slab has a density of 2,500 kg/m³, 25 MPa compression strength and $3.05 \times 10^4$ MPa of Young's modulus, with 0.2 Poisson's ratio.
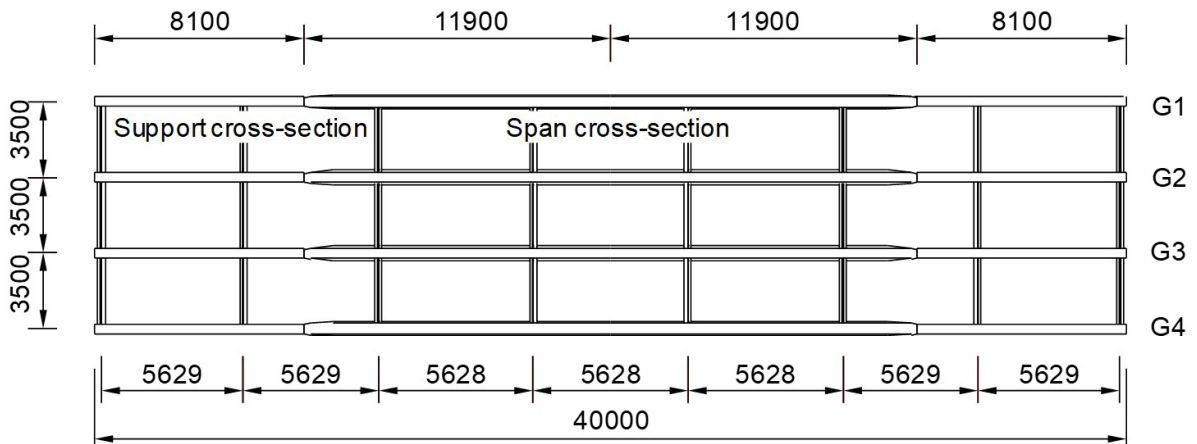


**Figure 5.** Bridge steel girder's top view: units in millimetres [6].

Rev. IBRACON Estrut. Mater., vol. 16, no. 4, e16404, 2023

6/14

# 6 STEEL-CONCRETE COMPOSITE BRIDGE FINITE ELEMENT MODELLING

The numerical model developed for the steel-concrete composite bridge dynamic analysis adopted the usual mesh refinement techniques present in finite element method simulations implemented in the ANSYS [7] computational program, see Figure 6. The bridge girders top and bottom flanges, the girders web and the longitudinal and vertical stiffeners were represented based on the use of shell finite elements (SHELL63). The bridge concrete slab was simulated by solid finite elements (SOLID45). The transverse steel bracing systems were simulated by beam finite elements (BEAM44). The developed bridge finite element model used 17,542 nodes, 16,112 elements, which resulted in a numeric model with 105,252 degrees of freedom.

The strain compatibility between the solid elements (concrete slab) and the shell elements (steel plate girders) was guaranteed by coupling the corresponding degrees of freedom, simulating the composite bridge decks' full interaction. The damping ratio was assumed to be 0.005 ($\xi = 0.5\%$), as stated by EN 1991-2 [12] for steel and steel-concrete composite bridges. In sequence, Figure 6 illustrates the investigated highway bridge finite element model. The investigated steel-concrete composite bridge natural frequencies (eigenvalues) and vibration modes (eigenvectors) have been determined based on numerical methods of extraction (modal analysis), through a free vibration analysis and using the ANSYS program [7]. The associated bridge main global vibration modes are shown in Figure 7.



Nodes: 17,542
Elements: 16,112
DOF: 105,252

Transverse steel bracing system (BEAM 44)

Steel girders (SHELL 63)

Concrete Deck (SOLID 45)
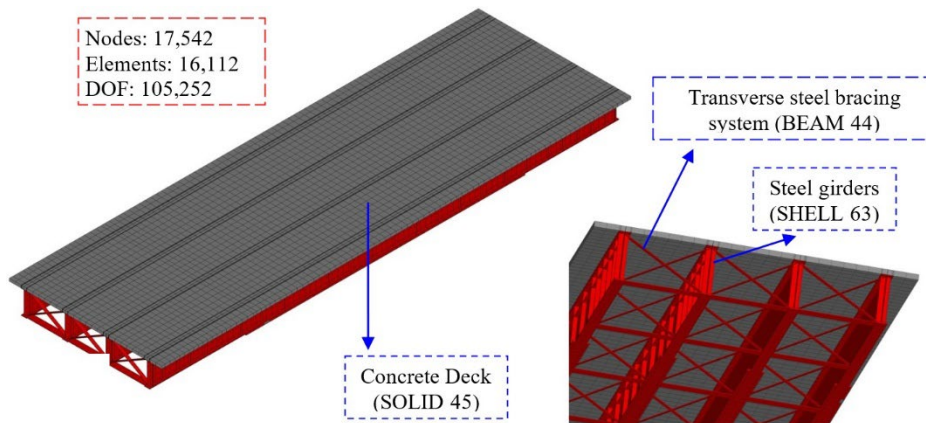
**Figure 6.** Finite element model of the roadway bridge.



(a) $f_{01} = 2.97$ Hz: longitudinal bending.

(b) $f_{02} = 3.67$ Hz: axial torsion.

(c) $f_{03} = 6.28$ Hz: beam's lateral bending.

(d) $f_{04} = 9.67$ Hz: longitudinal bending.
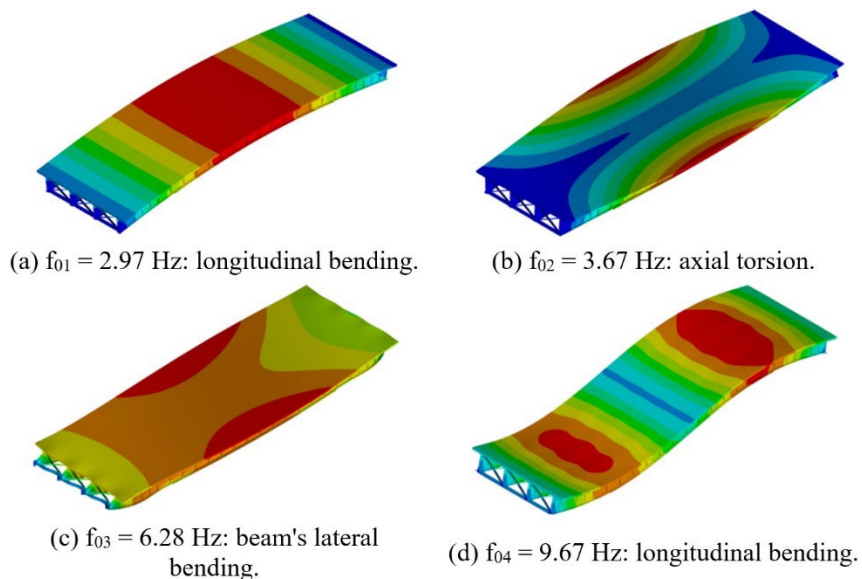
**Figure 7.** Investigated bridge global vibration modes.

Rev. IBRACON Estrut. Mater., vol. 16, no. 4, e16404, 2023

7/14

# 7 MODELLING OF THE VEHICLE-BRIDGE DYNAMIC INTERACTION

The moving load is modelled by an infinite series of equal vehicles, regularly spaced, and running at constant velocity, $\upsilon$. If "L" is the distance between two successive vehicles and if these cars enter the bridge deck one by one, a time repeated movement variation governed by the frequency, $f = \upsilon/L$, is created, and is associated with the vehicle movement on the bridge [2]. After a certain time period, $t_1$, named "crossing period", the first convoy vehicle reaches the far end of the bridge and from this instant on the total mass of the vehicles on the bridge remains practically constant, considering the condition that the distance L is sufficiently small. Under these conditions the bridge will soon reach a steady-state response situation, which includes the repetition of the maximum values [2].

The mathematical model simulates the bridge structure and the vehicle series as a system, the "vehicle-bridge system". In this system, the vehicle series and the bridge deck form just one system. Consequently, its frequencies are modified by the vehicle properties and the vehicle-bridge dynamic interaction force incorporates the bridge flexibility influence. The effect of the pavement roughness is introduced in the vehicle-bridge system equations of motion as a load vector analogous to what would be considered if the vehicle was subjected to a base movement equal to the irregular pavement profile [2].

The bridge dynamic response was obtained by the integration of its equations of motion, in the time domain, considering the excitation produced by the vehicles convoys' traffic on the bridge deck irregular pavement surface, taking into account the pavement progressive deterioration effect [1], [2]. The interaction force vector, F(t), is modified throughout time and, for each time interval (or "steps"), a dynamic force is applied on the bridge deck. The dynamic loading position changes according to the positions of the vehicles on the bridge deck, and the generated time function has a space and time description. This procedure encompasses the actual bridge structural response, where the dynamic loads can induce displacements and stresses greater than the maximum bridge response values.

# 8 PAVEMENT PROGRESSIVE DETERIORATION ANALYSIS

The road-roughness classification is defined in accordance with ISO 8608 [18] (Table 3) and Figure 8 illustrates RRC values calculated from Equation 6. The presented results are classified as very good for the first 10 years, as the RRC value is less than $8 \times 10^{-6}$ (see Table 3). After 11 and 12 years of the pavement deterioration, the roughness is classified as good for the three investigated scenarios. The roughness after 13 years is classified as average for all studied traffic increase values, and also for $\alpha = 0\%$ and $\alpha = 3\%$ after a 14 years period. However, considering the age of 14 years onwards, the pavement is considered poor for a 5% increase in traffic and, after 15 years, the roughness rating is poor for all analysed scenarios.
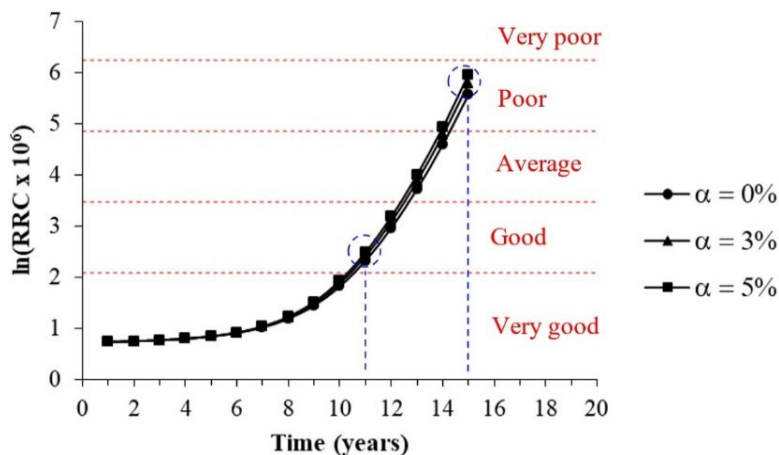


**Figure 8.** Deterioration of road-roughness condition in terms of $\ln(\mathrm{RRC}\times10^6)$.

# 9 DYNAMIC LOADINGS APPLICATION STRATEGY

In this study, the dynamic actions on the bridge are considered due to vehicle convoy's traffic on the irregular pavement surface and the effect of the pavement progressive deterioration, taking into account the road surface

damages. The vehicles passage on the bridge deck may have different velocities and can be randomly or simultaneously located in different traffic lanes.

The dynamic loads on the bridge deck can be assumed as a series of identical vehicles [1]–[5] or even the passage of one vehicle at time and different vehicle configurations [10], [23]. In this research work it must be emphasized that the adopted dynamic loads application strategy, based on the use of a series of identical vehicles positioned in one bridge deck traffic lane, is relevant to allow the highway bridge decks steady-state response assessment. This way, the bridge deck width was divided in three equal lanes adopted for the vehicles traffic simulation, discounting the two New Jersey barriers widths, see Figure 9.

Moreover, the vehicles were positioned at the centre of the traffic lanes, having in mind each studied loading situation. Thus, the vehicle convoys are crossing the bridge deck with constant velocity up to a specified number of crossings (defined as $t/t_1$), which assumed in this work to be 10 ($t/t_1 = 10$). The spacing between the single axle and the double wheel single axle of two consecutive vehicles was limited by the bridge length and by a minimum space between consecutive vehicles (L = 11 m), as presented in Figure 10.
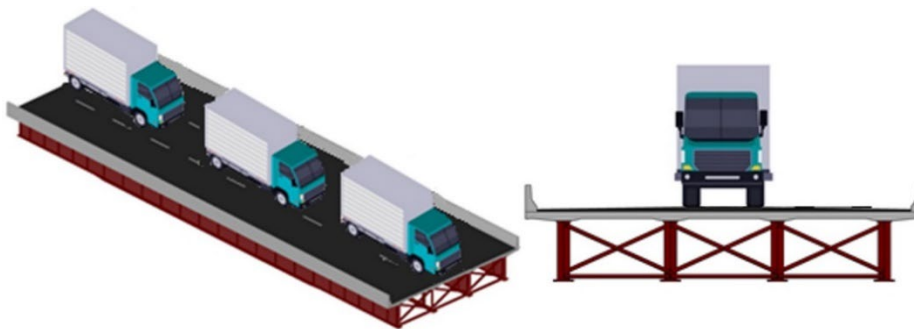


**Figure 9.** Vehicle convoys on the bridge deck: central traffic lane.
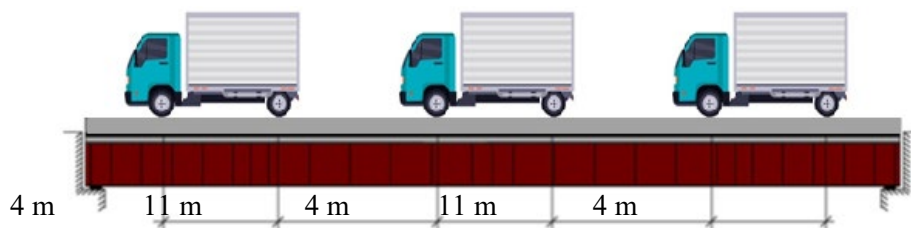


**Figure 10.** Vehicle convoys spacing: three vehicles.

## 10 BRIDGE RESPONSE SPECTRA ASSESSMENT

Aiming to assess the steel-concrete composite bridge dynamic structural behaviour, several response spectra were generated for each traffic condition (Figures 10 to 12). To do this, the vehicles velocities vary from 20 km/h to 80 km/h (intervals of 10 km/h), resulting in seven different velocities in each spectrum. Furthermore, for each considered vehicle velocity three different traffic increase levels were analysed in this study. This way, response spectra were generated to study the global bridge dynamic structural response, as presented in Figure 11.

Therefore, first of all, it is noteworthy that along the bridge dynamic analysis (forced vibration analysis) the following results considered the situation without the bridge deck pavement deterioration (t = 0), and also for t = 11 years and t = 15 years, that characterize the change in RRC (see Table 3), to a road-roughness classification from very good to good and from average to poor, respectively, as shown in Figure 8.

(a) Without deterioration (t=0).

(b) t = 11 years.

(c) t = 15 years.
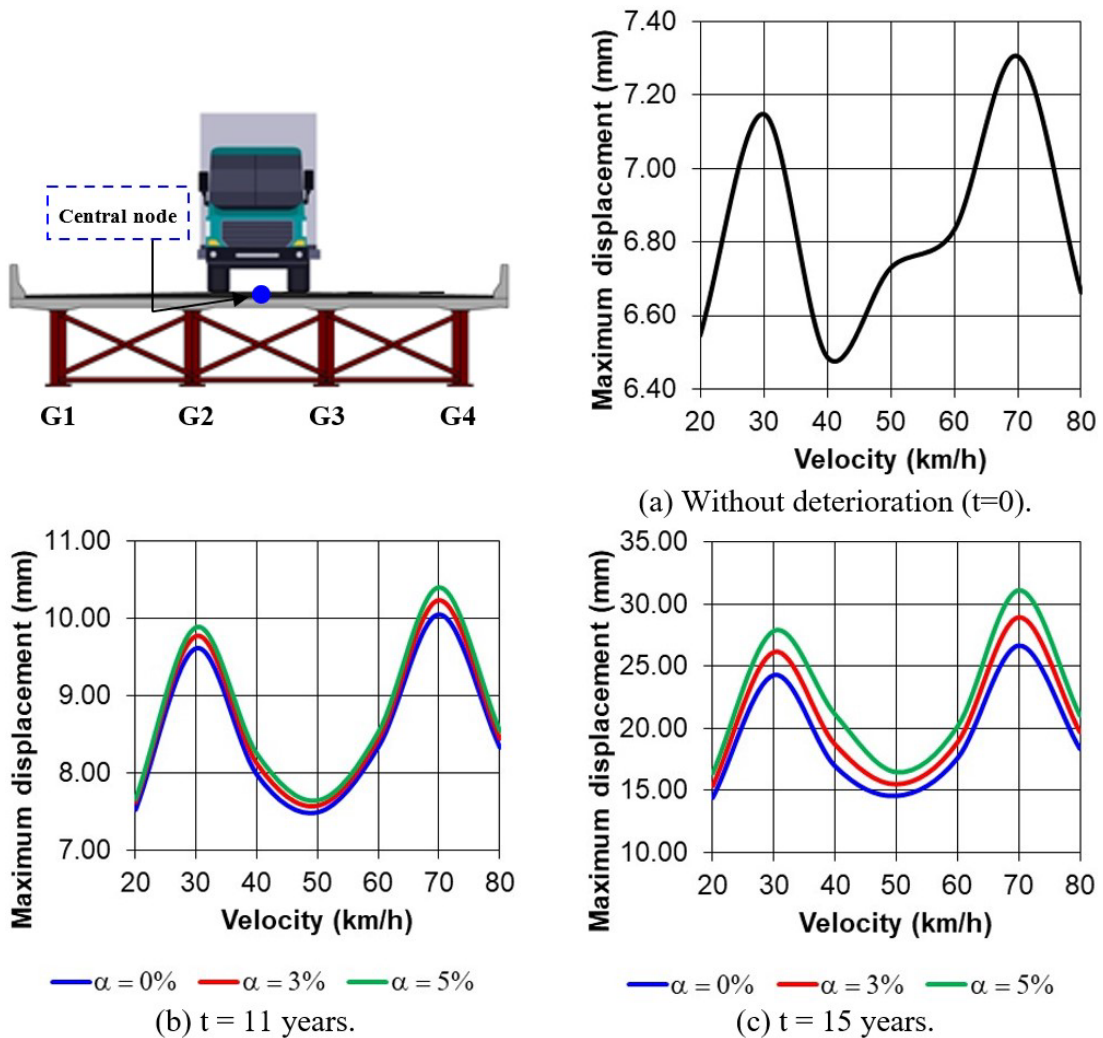
**Figure 11.** Response spectra: translational vertical displacements (see **Figure 9).**

The bridge response spectra illustrated in Figure 11 presents two main energy transfer peaks: the first peak of greater magnitude is associated with the vehicles traffic velocity of 70 km/h, and the other one is related to the velocity of 30 km/h. The most important peak ($\upsilon$ = 70 km/h) is associated with the dynamic excitation frequency (vehicles convoy crossing frequency on the bridge deck) equal to 1.30 Hz (f = $\upsilon$/L = 70/3.6/15 = 1.30 Hz), due to the mobility between two single axles spaced by 15 m and corresponding to consecutive vehicles (see Figure 10). This way, this dynamic excitation frequency mobilizes the second harmonic (2.60 Hz), associated to the bridge fundamental frequency ($f_{01}$ = 2.97 Hz), close to the structure resonance frequency range.

On the other hand, the energy peak transfer ($\upsilon$ = 30 km/h), see Figure 11, is related to the dynamic excitation frequency (vehicles convoy crossing frequency on the bridge deck) equal to 0.76 Hz (f = $\upsilon$/L = 30/3.6/11 = 0.76 Hz), due to the mobility between the vehicles single directional axis and the double wheels single axis associated to two consecutive vehicles spaced by 11 m (see Figure 10). This way, this dynamic excitation frequency mobilizes only the fourth harmonic (3.04 Hz), associated to the bridge fundamental frequency ($f_{01}$ = 2.97 Hz), close to the bridge resonance frequency range. For this reason, the peak associated with the velocity of 30 km/h is smaller than the one associated with the velocity of 70 km/h.

It must be emphasized that all the response spectra resonance peaks, presented in Figure 11, are related to the proximity of the excitation frequency produced by the vehicles convoy passage on the bridge deck and the natural frequencies of the system (vehicle-pavement-bridge system), having in mind the investigated traffic conditions, see Figure 9. In sequence, the investigated steel-concrete composite bridge maximum vertical translational displacements values are presented in Table 4.

Rev. IBRACON Estrut. Mater., vol. 16, no. 4, e16404, 2023

10/14

**Table 4.** Translational vertical displacement values (see Figure 9).

| Velocity | Without | α = 0% | | α = 3% | | α = 5% | |
|---|---|---|---|---|---|---|---|
| (km/h) | deterioration | t = 11 | t = 15 | t = 11 | t = 15 | t = 11 | t = 15 |
| 20 | 6.54 | 7.53 | 14.40 | 7.63 | 15.40 | 7.66 | 16.37 |
| 30 | 7.15 | 9.62 | 24.25 | 9.78 | 26.19 | 9.89 | 27.88 |
| 40 | 6.49 | 7.98 | 16.92 | 8.12 | 18.72 | 8.25 | 21.12 |
| 50 | 6.73 | 7.5 | 14.54 | 7.58 | 15.54 | 7.65 | 16.46 |
| 60 | 6.83 | 8.35 | 17.58 | 8.45 | 18.92 | 8.53 | 20.15 |
| **70** | **7.3** | **10.05** | **26.62** | **10.24** | **28.97** | **10.4** | **31.15** |
| 80 | 6.66 | 8.33 | 18.32 | 8.45 | 19.73 | 8.54 | 21.04 |

## 11 STUDY OF THE PAVEMENT PROGRESSIVE DETERIORATION EFFECT

In this section, aiming to study the bridge general global behaviour, based on the pavement progressive deterioration progressive mathematical model, it was adopted the loading case considering the vehicles convoys positioned on the traffic central lane (Figure 9). This way, based on the bridge response spectra results (Figure 11), two velocities are considered in this analysis: 30 km/h and 70 km/h.

On the other hand, three scenarios of traffic increase (α = 0%, 3% and% 5%) are studied for a 15-year period, resulting in 90 different situations. Thus, Figures 12 and 13 present the progressive deterioration progressive effect, based on the displacements and stresses values analysis related to the investigated bridge central section.



(a) Vertical displacements (central section).

(b) Stresses in Girder 1.

(c) Stresses in Girder 2.
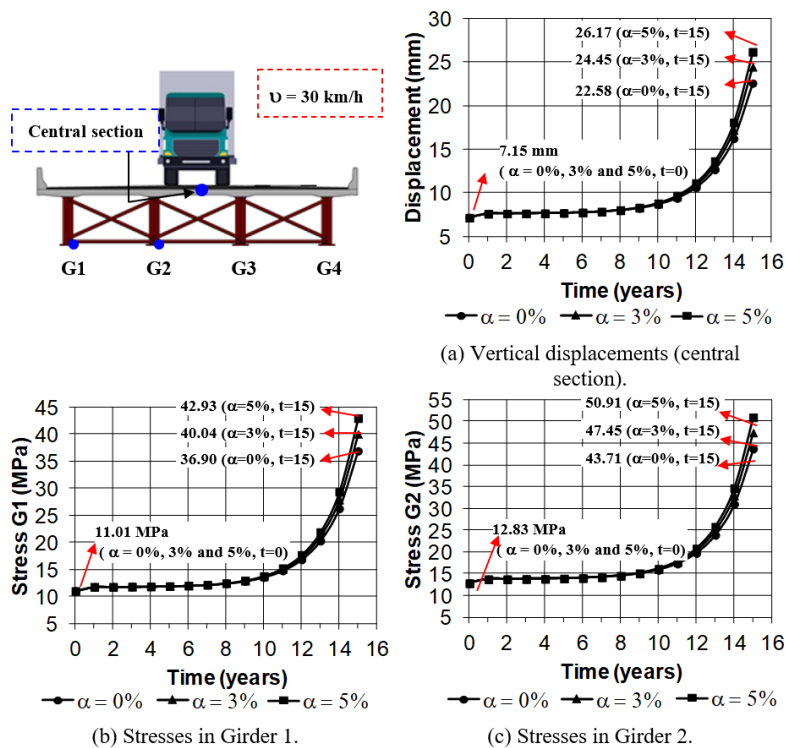
**Figure 12.** Pavement progressive deterioration effect: υ = 30 km/h (traffic central lane).

Rev. IBRACON Estrut. Mater., vol. 16, no. 4, e16404, 2023

11/14

(a) Vertical displacements (central section).

(b) Stresses in Girder 1.

(c) Stresses in Girder 2.
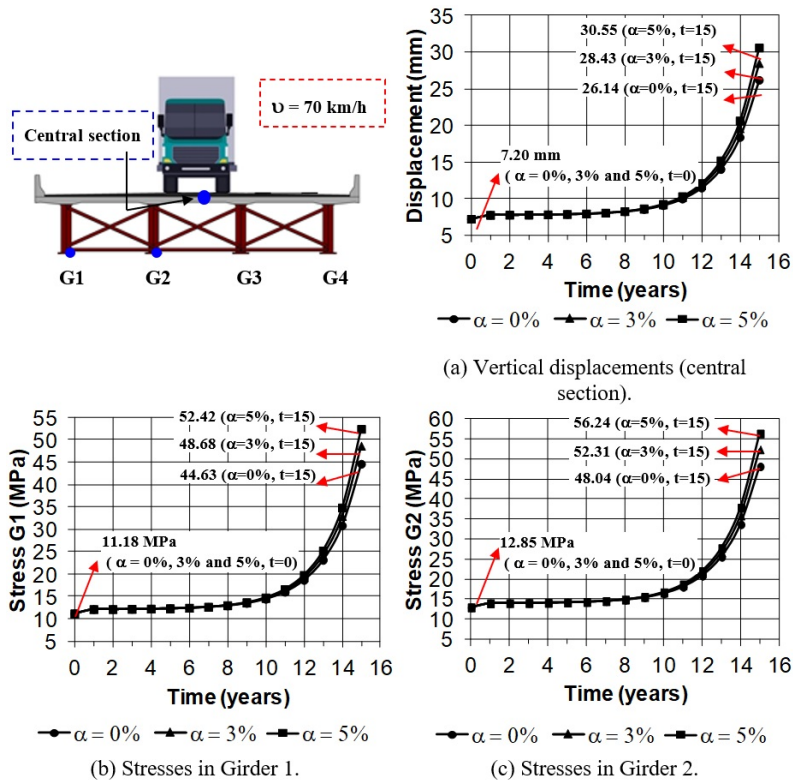
**Figure 13.** Pavement progressive deterioration effect: $\upsilon = 70$ km/h (traffic central lane).

Based on the Figures 12 and 13 results, it must be emphasized that over time, as the bridge deck pavement deterioration process increases, the calculated vertical translational displacements and stresses are higher. Considering the vehicle velocity of 30 km/h ($\upsilon = 30$ km/h), after 15 years of deterioration, the displacement values exceed more than three times when compared to those associated to the pavement without deterioration (t = 0). On the other hand, when the velocity of 70 km/h ($\upsilon = 70$ km/h) is investigated this value is up to four times higher, see Figure 12a and Figure 13a.

The same scenario can be observed when the stresses values are analysed, based on the bridge dynamic response and having in mind the pavement deterioration process. Over the years, the stresses values in the bridge G1 and G2 girders are up to three times higher than those obtained without deterioration (t = 0), when the vehicles velocity is equal to 30 km/h ($\upsilon = 30$ km/h), and up to four times higher for 70 km/h ($\upsilon = 70$ km/h), than those found without deterioration (t = 0), see Figures 12b and 12c and also Figures 13b and 13c.

Finally, based on the response spectra investigation, the bridge dynamic response maximum effects (displacements and stresses) occurs when the vehicles velocity is equal to 70 km/h ($\upsilon = 70$ km/h), and the displacements and stresses values, after 15 years of pavement deterioration, are up to four times higher than those found without deterioration (t = 0). These results clearly indicate the relevance of considering the pavement deterioration effect, when the highway bridges structural behaviour subjected to dynamic loads is investigated.

## CONCLUSIONS

In this research work an assessment of steel-concrete composite highway bridge decks dynamic structural behaviour is presented, considering the road surface roughness pavement progressive degradation effect, and based on the use of a vehicle-bridge-pavement interaction model.

The main objective was to determine the displacements and stresses values considering the vehicles convoys' traffic on the bridge deck taking to account the irregular pavement surface progressive deterioration up to 15 years of the structure service life. This way, having in mind the steady-state response assessment, in this research work the dynamic loads on the bridge deck were assumed as series of three 2C vehicles, regularly spaced and moving at constant velocity, and three different scenarios of traffic increase ($\alpha = 0\%$, 3% and 5%) were considered in this investigation.

The main conclusions of this work focused on alerting structural engineers to the possible distortions associated with the steel-concrete composite bridge dynamic structural response, when subjected to dynamic actions due to vehicle convoys traffic on the irregular pavement surface, considering the progressive deterioration along the time. This way, the following conclusions can be drawn from the results presented in this study:

1. The vehicles velocities affect the bridge dynamic structural response (displacements and stresses values). In all investigated loading situations, the structure dynamic response was modified when the vehicle velocity was changed.

2. The vehicles traffic configurations present significant influence on the bridge displacements and stresses values. These positions vary according to the vehicles transverse location and spacing between vehicles on the bridge deck. It must be emphasized that these vehicles convoy's configurations are directly related to the dynamic excitation frequency (vehicles convoy passage on the bridge), which can induce a resonance condition.

3. The road-roughness condition directly influences the investigated steel-concrete composite highway bridge dynamic structural response. It must be emphasized that over time, as the bridge deck pavement deterioration process increases, the calculated vertical translational displacements and stresses values are higher than the bridge pavement is found without deterioration (t = 0).

4. Based on the traffic rates increase ($\alpha = 0\%$ to $\alpha = 5\%$), after 15 years of the bridge road pavement deterioration, the displacement and stresses values exceed up to four times when compared to those calculated when the bridge pavement is assumed without deterioration (t = 0). The results obtained in this paper clearly indicate the relevance of considering the bridge pavement progressive deterioration effect, when the dynamic structural behaviour is investigated.

Finally, it must be emphasized that the results obtained in the present investigation are associated mainly for vehicles convoys moving over irregular pavement surfaces of steel-concrete composite highway bridge decks, considering the pavement progressive deterioration effect. However, the analysis methodology presented in this paper is completely general and is the author's intention to sophisticate the vehicles convoy mathematical modelling, based on the use of different vehicles models with different dynamic properties, and apply this solution strategy considering other highway bridge structural systems.

## ACKNOWLEDGEMENTS

## REFERENCES

[1] A. C. S. Silva, "Study of the dynamic behaviour of highway bridges based on the assessment of the pavement progressive deterioration," M.S. thesis, State Univ. Rio de Janeiro (UERJ), Rio de Janeiro, 2020. [in Portuguese].

[2] J. G. S. Silva, "Dynamical performance of highway bridge decks with irregular pavement surface," *Comput. Struc.*, vol. 82, no. 11–12, pp. 871–881, 2004, http://dx.doi.org/10.1016/j.compstruc.2004.02.016.

[3] W. Zhang and C. S. Cai, "Fatigue reliability assessment for existing bridges considering vehicle speed and road surface conditions," *J. Bridge Eng.*, vol. 17, no. 3, pp. 443–453, 2012, http://dx.doi.org/10.1061/(ASCE)BE.1943-5592.0000272.

[4] G. S. Alencar, "Dynamic analysis and fatigue evaluation of steel-concrete composite highway bridges subjected to vehicles traffic on the irregular pavement surface," M.S. thesis, State Univ. Rio de Janeiro (UERJ), Rio de Janeiro, 2015. [in Portuguese].

[5] W. Zhang and C. S. Cai, "Reliability-based dynamic amplification factor on stress ranges for fatigue design of existing bridges," *J. Bridge Eng.*, vol. 18, no. 6, pp. 538–552, 2013, http://dx.doi.org/10.1061/(ASCE)BE.1943-5592.0000387.

[6] F. O. Pinho and I. H. Bellei, *Manual de Pontes e Viadutos em Vigas Mistas*, 2ª ed. Rio de Janeiro: CBCA, 2020.

[7] ANSYS Swanson Analysis Systems Inc., Theory Reference (R-12.1). USA, 2010.

[8] C. E. Rossigali, "Probabilistic studies for mobile load models on road bridges in Brazil," M.S. thesis, Fed. Univ. Rio de Janeiro (UFRJ), Rio de Janeiro, 2006. [in Portuguese].

[9] Agência Nacional de Transporte Terrestres, *Manual de Procedimentos e Fiscalização: Fiscalização em Postos de Pesagem Veicular*, 2ª ed. Brasília: ANTT, 2017.

[10] R. C. Battista, M. S. Pfeil, and E. M. L. Carvalho, "Fatigue life estimates for a slender orthotropic steel deck," *J. Construct. Steel Res.*, vol. 64, no. 1, pp. 134–143, 2008, http://dx.doi.org/10.1016/j.jcsr.2007.03.002.

[11] C. J. Dodds and J. D. Robson, "The description of road surface roughness," *J. Sound Vibrat.*, vol. 31, no. 2, pp. 175–183, 1973, http://dx.doi.org/10.1016/S0022-460X(73)80373-6.

[12] European Committee for Standardization, *EUROCODE 1: Actions on Structures - Part 2: Traffic Loads on Bridges*, EN 1991-2, 2003.

[13] W. D. O. Paterson and B. Attoh-Okine, "Simplified models of paved road deterioration based on HDM-III," *Transp. Res. Rec.*, vol. 1344, pp. 99–105, 1992.

[14] American Association of State Highway and Transportation Officials, *AASHTO Guide for Design of Pavement Structures.* Washington, DC, USA: AASHTO, 1993.

[15] K. Kwon and D. M. Frangopol, "Bridge fatigue reliability assessment using probability density functions of equivalent stress range based on field monitoring data," *Int. J. Fatigue*, vol. 32, no. 8, pp. 1221–1232, 2010, http://dx.doi.org/10.1016/j.ijfatigue.2010.01.002.

[16] M. W. Sayers and S. M. Karamihas, *The Little Book of Profiling: Basic Information About Measuring and Interpreting Road Profiles*. Ann Arbor, USA: Univ. Michigan, 1998.

[17] M. W. Sayers, T. D. Gillespi, and W. D. O. Paterson, *Guidelines for Conducting and Calibrating Road Roughness Measurements* (World Bank Technical Report WTP 46). Washington, DC, USA: World Bank, 1986.

[18] International Standard Organization, *Mechanical Vibration-Road Surface Profiles-Reporting of Measured Data*, ISO 8608, 1995.

[19] W. D. O. Paterson, "International roughness index: relationship to other measures of roughness and riding quality," *Transp. Res. Rec.*, vol. 1084, pp. 49–58, 1986.

[20] A. Shiyab, "Optimum use of the flexible pavement condition indicators in pavement management system," Ph.D. dissertation, Curtin Univ. Technol., Perth, Australia, 2007.

[21] American Association of State Highway and Transportation Officials, *AASHTO LRFD Bridge Design Specifications*. Washington, DC, USA: AASHTO, 2012.

[22] Associação Brasileira de Normas Técnicas, *Projeto de Pontes Rodoviárias de Aço e Mistas de Aço e Concreto*, ABNT NBR 16694, 2020.

[23] J. G. S. Silva and J. L. P. Roehl, "Probabilistic formulation for the analysis of highway bridge decks with irregular pavement surface," *J. Braz. Soc. Mech. Sci.*, vol. 21, no. 3, pp. 433–445, 1999, http://dx.doi.org/10.1590/S0100-73861999000300006.

Rev. IBRACON Estrut. Mater., vol. 16, no. 4, e16404, 2023

14/14

ORIGINAL ARTICLE

# Machine learning models to predict the punching shear strength of reinforced concrete flat slabs

*Modelos de aprendizado de máquina para previsão da resistência à punção de lajes lisas de concreto armado*

Francisco Eudázio Suriano da Silva Júnior[a] 
Wellison José de Santana Gomes[a] 

[a]Universidade Federal de Santa Catarina – UFSC, Department of Civil Engineering, Florianópolis, SC, Brasil

**Abstract:** Punching shear failure is caused by shear stress concentration in the slab-column connection of reinforced concrete flat slabs. As it is a brittle failure, it is crucial to understand how this mechanism works and to correctly predict the resistance of slabs subjected to it. In this paper, machine learning-based models were developed and compared to predict the punching shear resistance of reinforced concrete interior slabs without shear reinforcement. The models were based on 373 experimental data of interior slabs. Artificial neural network, decision tree, random forest and extreme gradient boosting algorithms were employed. The input variables considered herein were the effective depth of the slabs, flexural reinforcement ratio, effective width of the columns, concrete compressive strength and steel yield strength, and the target variable was the punching shear strength. The results for the punching shear resistances obtained by the developed models, as well as those obtained by employing models presented in five reinforced concrete design codes, were compared to the experimental data. All machine learning models showed coefficient of determination above 0.95 for test data. As for the design code models, large discrepancies were observed between them, with the Brazilian code showing more accuracy than the others in predicting the failure load of the slabs.

**Keywords:** predictive models, structural safety, design provisions, computational modeling, XGBoost.

**Resumo:** A ruptura por punção é causada pela concentração de tensões de cisalhamento na ligação laje-pilar de lajes lisas de concreto armado. Por se tratar de uma ruptura frágil, é fundamental entender como esse mecanismo funciona e prever corretamente a resistência das lajes submetidas a ele. Neste artigo, modelos baseados em aprendizado de máquina foram desenvolvidos e comparados para prever a resistência à punção de lajes internas de concreto armado sem armadura de cisalhamento. Os modelos foram baseados em 373 resultados experimentais de lajes apoiadas sobre pilar intermediário. Os algoritmos de rede neural artificial, árvore de decisão, floresta aleatória e *extreme gradient boosting* foram empregados. As variáveis de entrada aqui consideradas foram a altura útil das lajes, taxa de armadura de flexão, largura efetiva dos pilares, resistência à compressão do concreto e tensão de escoamento do aço, e a variável alvo foi a resistência à punção. Os resultados das resistências ao cisalhamento obtidos pelos modelos desenvolvidos, bem como aqueles obtidos pelo emprego de modelos apresentados em cinco códigos de projeto de concreto armado, foram comparados com os dados experimentais. Todos os modelos de aprendizado de máquina apresentaram coeficiente de determinação acima de 0,95 para dados de teste. Quanto aos modelos de normas de projeto, foram observadas grandes discrepâncias entre eles, com a norma brasileira apresentando maior precisão que as demais na previsão da carga de ruptura das lajes.

**Palavras-chave:** modelos preditivos, segurança estrutural, disposições de projeto, modelagem computacional, XGBoost.

# 1 INTRODUCTION

Flat slabs are systems where the slabs are supported directly on the columns. Although simple in appearance, the flat slab system presents a complex behavior, especially in the slab-column connection, since punching failure develops in a brittle manner and with limited deflections, and is followed by an almost complete loss of the load carrying capacity [1].

According to Muttoni [2], the design of flat slabs is mostly governed by serviceability conditions (with relatively large deflections in service) and by the ultimate limit state of punching shear (also called two-way shear). The design standards for concrete structures present models to try to predict the shear resistance of flat slabs. However, several studies in the literature suggest that the standards differ significantly in predicting punching shear strength.

In the paper by Sanabria et al. [3] two slabs were studied and it was found that the results obtained using the formulations presented in the Brazilian, European and North American standards varied by up to 70% for the same slab, with most of the results being far from the experimental data. Avagyan [4] studied the punching shear resistance of four slabs with shear reinforcement according to the European, North American, Armenian and Russian design models, and found that the strength of the slabs varied by up to 35% between the design provisions. Silva et al. [5] observed significant differences between the North American, Brazilian and European standards regarding the prediction of the punching shear strength of four flat slabs, with results varying by up to 75% for the same slab. Issa and Ismail [6] studied the punching shear strength of 257 slabs using the European, North American, British, Egyptian, Japanese and European design formulas. The authors observed large discrepancies between the models, and the European standards were the most accurate in predicting the punching shear resistance of the slabs, while the North American and Japanese were the less accurate.

Experimental tests and numerical simulations can be used to better understand the mechanical behavior of structural elements. As a complement of these two approaches, models based on machine learning (ML) are increasingly employed. In Xu and Saleh [7] the state of the art and trends for the use of ML in structural engineering problems are presented. The authors stated that the areas of structural reliability and safety will, in the near future, be profoundly changed by the incorporation of ML. According to the authors, this is being made possible in part by the advent of big data, the collection and storage of large amounts of data and the development of powerful algorithms to probe it.

By using self-learning features, ML extracts the complicated relationship between input and output data and then uses this relationship to make predictions, without being explicitly programmed to do so [8]. ML is actually a "black box" that maps the relationship between inputs and outputs, so it can be used for classification and regression, without complicated mathematical derivations. It usually has better performance compared to traditional models, making it a good complement to traditional structural mechanics approaches [9]. As disadvantages, ML-based models require many observational data to be built and are dependent on the quality and distribution of the data. Furthermore, they can be slow to train and they usually lack the extrapolation capacity and the physical meaning or interpretability that traditional numerical models usually have.

Some recent studies that employed ML in structural engineering problems can be highlighted. Nguyen et al. [10] used the extreme gradient boosting algorithm (XGBoost or XGB) to predict the punching shear strength of interior slabs, using data from 497 slabs available in the literature. The XGB model was compared to models based in artificial neural networks (ANN) and random forest (RF), as well as design code models, showing superior accuracy and with coefficient of determination ($R^2$) around 0.96 for test data. It was also observed that the effective depth of the slab was the variable with the greatest impact on the resistance.

Mangalathu et al. [11] used 380 experimental results and the models were based on linear regression techniques and ML methods. These models were compared with each other and with design models. The XGB-based model was the most accurate in predicting punching shear, with $R^2$ around 0.85 for test data. However, in conflict with the conclusions of Nguyen et al. [10], it was observed that the material properties had more influence on the punching shear strength than the geometric properties of the slab.

Lu et al. [12] studied some approaches for the feature selection step to determine the best way to estimate the punching shear strength of RC slabs reinforced with SFRC (steel fibers). For this, the authors used 140 experimental results to build models based on trees, obtaining models with $R^2$ between 0.95 and 0.98. Ly et al. [13] developed two hybrid models that combined ANN and optimization techniques to predict the shear strength of reinforced concrete beams reinforced with SFRC, where 463 experimental results were used and models with $R^2$ of the order of 0.95 were obtained. Gomes [14] used a structural reliability approach to compare shallow and deep ANNs in the solution of four reliability problems, showing that while both types of ANN produce good results, deep networks usually outperform shallow ones. Feng et al. [9] used ensemble learning and developed a model capable of predicting the resistance and failure mode of circular columns subjected to cyclic loading, which is both a regression and classification problem. In their paper, 254 experimental results were used and the model based on the adaptive boosting (AdaBoost) algorithm was the one with the highest $R^2$ (0.98).

The results were compared to design code predictions, showing superior accuracy. In the literature, other papers regarding application of ML to structural problems are available, including [15]–[20].

Despite usually providing more accurate models than those present in design codes, the use of ML in structural engineering problems is still in a maturing process and needs to be further investigated, which is one of the reasons for this study. Another reason is that, as already mentioned, some references in the literature show that the design standards for punching shear in RC slabs have large discrepancies between them. Thus, in the present paper, the ABNT NBR 6118 [21], ACI 318 [22], Eurocode 2 [23], BS 8110 [24] and DIN 1045-1 [25] design models were compared. In particular, no comparisons involving ML models for punching shear and the NBR 6118 [21] model were found in the literature so far, so that the present paper expands the discussion about previously studied models and includes the model presented in the Brazilian standard.

The present paper is organized as follows. A summary of the ML algorithms employed in this study is presented in section 2; a brief background of the structural problem is presented along with design provisions in section 3; the experimental dataset used herein is discussed in section 4, along with data cleaning and preprocessing; the development of the ML models is presented in section 5; the results of the developed ML models are presented in section 6; discussions about design standard models and comparisons are made in section 7; and the conclusions are drawn in section 8.

## 2 MACHINE LEARNING ALGORITHMS OVERVIEW

Four regression algorithms are used in this research: ANN, decision tree (DT), RF and XGBoost. The basic concepts behind each technique are presented below.

### 2.1 Artificial Neural Network – ANN

Artificial neural networks emerged from the idea of mathematically modeling the functioning of biological neurons, whose discussions began in the 1940s. In a generic way, neural networks are the implementation of connections between inputs, mathematical functions and outputs in computer code [26]. For Albon [27], neural networks can be visualized as a series of connected layers that form a network that connects features at one end to target values at the other. At the heart of neural networks is the unit (also called a neuron). The unit takes one or more inputs, multiplies each input by a parameter (also called a weight), adds these values to a constant (bias), and feeds them to an activation function. The output is then passed on to the next layers in the network, if any, or presented as the output of the ANN if no more deeper layers are present.

Aggarwal [28] explains that the most basic architecture of a neural network is known as perceptron. The perceptron contains two layers of nodes (neurons), one corresponding to inputs and one to output, with a single node in the latter. The number of nodes in the input layer depends on the dimensionality of the problem. Each input node is connected to the output and for each connection a weight is assigned. Just as learning in biological systems is done by modifying the intensity of synapses, learning in the perceptron is done by adjusting the weights of connections between inputs and outputs whenever an incorrect prediction is made. The function employed by the perceptron at each node is called an activation function. Arbitrary functions like logistic, sigmoid, hyperbolic tangent or rectified linear unit (ReLU) can be used.

The perceptron algorithm cycles through all the training samples and iteratively adjusts the weights until convergence is reached. Each cycle is called an epoch. During the learning process, a loss function (or cost function) is employed to evaluate how poorly the model is performing at each epoch. Mohri et al. [29] explain that a loss function measures the difference between a predicted label and a true one. Examples of loss functions are the mean absolute error (MAE) and the root mean squared error (RMSE). According to Aggarwal [28], the perceptron algorithm starts with a random vector of weights. The algorithm then performs the initial predictions and updates the weight vector using optimization algorithms (such as gradient descent) and a learning rate to minimize the error defined by the loss function.

In practice, one or more hidden layers are used between the inputs and the output. In this case, the network is a multilayer perceptron. Neural networks with many hidden layers are considered deep networks and their application is called deep learning [27]. In networks with hidden layers, the gradient descent algorithm cannot be used to calculate the error gradient for hidden neurons [30]. Consequently, the contribution of each neuron to the overall error of the network must be calculated by using a backpropagation algorithm.

Examples of single and multilayer perceptrons are shown in Figure 1.
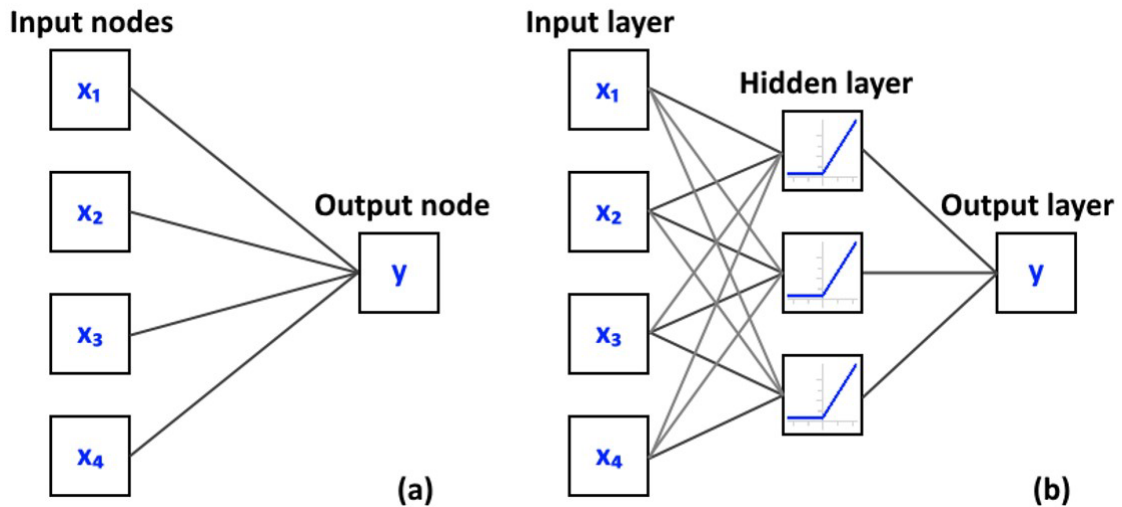
**Figure 1.** Illustration of single layer (a) and multilayer perceptron (b).

ANNs have been widely used in civil and structural engineering problems, as in [8]–[10], [13], [14] and [31]–[33].

## 2.2 Decision Tree – DT

Decision trees are models based on a tree-like structure where a series of decisions are connected [27]. One of the reasons for their popularization is that, unlike ANNs, they are more interpretable, intuitive and faster to train.

According to Aggarwal [28], the algorithm for building a decision tree has two types of nodes, called internal and leaf nodes. Each leaf is labeled with the dominant class at that node. A special internal node is the root node that corresponds to the entire feature space. The generic decision tree induction algorithm starts with the complete training dataset at the root node and partitions the data into lower level nodes based on a split criterion. Only nodes that contain a mix of different classes need to be split further. Eventually, the decision tree algorithm stops the tree from growing based on a stopping criterion. A generic example of a decision tree is presented in Figure 2.
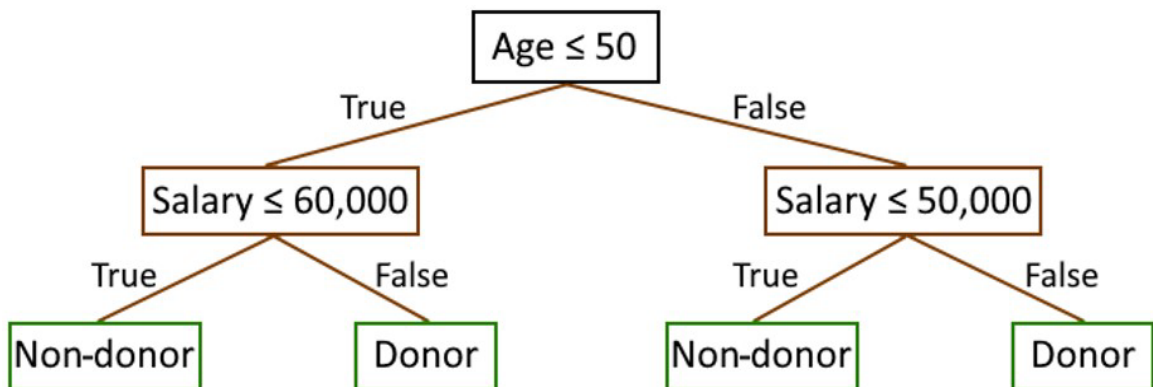


**Figure 2.** Generic example of a decision tree.

The simplest stopping criterion is one where all training examples in the leaf belong to the same class. One problem is that building the decision tree at this level may lead to overfitting, in which the model fits the random noise of the training data. In this case, this tree will have high variance and will not generalize well to unknown data. To try to reduce the loss of precision associated with overfitting, the classifier uses a pruning mechanism to remove nodes.

In general, simpler models (shallow decision trees) are preferable to more complex models (deep decision trees) if they produce the same error in the training data. Thus, a common stopping criterion is the use of a maximum number of levels (or maximum depth) that the model can reach.

Decision trees can be used for regression or classification and have found applications in different areas of structural engineering, as in [9], [11] and [12]. However, in recent studies, researchers tend to adopt enhanced versions of the classical decision tree algorithm, like random forests and boosting techniques.

## 2.3 Random Forest – RF

The random forest algorithm emerged as an evolution of decision trees. In general, the data split procedure in decision trees tends to lead to overfitting, when the model performs well with the training data but does not generalize as well to unknown data. The random forest tries to fix this problem by generating several decision trees (estimators), and was developed by Breiman [34].

Random forests are defined as a set of decision trees where randomness is explicitly inserted in the process of splitting the nodes of each tree. The idea is to use this randomness to generate less correlation between the components of the set, allowing each tree to specialize in a slightly different way from the others [28]. The result is the average of the individual results of each tree.

Bootstrapping is one of the sources of randomness in RF. According to Aggarwal [28], in the bootstrap method, the labeled data is sampled randomly and uniformly, with replacement, to create a bootstrapped training dataset that might possibly contain duplicates. The labeled data of size $n$ can be sampled $n$ times with replacement. This results in a training data with the same size as the original labeled data. However, the bootstrapped dataset typically contains duplicates and also misses some points in the original data. Therefore, each estimator in the random forest is trained using a slightly different dataset.

The results of the RF are usually more accurate than those of the simple decision tree and the model is resistant to noise and outliers, which made RF a popular technique nowadays. Recent structural engineering studies include [9]–[12] and [35].

## 2.4 Extreme Gradient Boosting – XGBoost

Tree boosting is the construction of decision tree models in sequence, iteratively, where a model is based on the results of the previous one. According to Aggarwal [28], the basic idea is to focus on the errors (residuals) and try to adjust the weights of each incorrectly classified instance to improve the next model. In gradient boosting, as the name suggests, the adjustment of the weights is performed through the gradient of the prediction error.

Extreme gradient boosting is a recent technique, developed in 2014 and published by Chen and Guestrin [36] as an evolution of traditional gradient boosting. It was developed to not only have high accuracy, but also low risk of overfitting. According to Chen and Guestrin [36], simple gradient boosting contains three main elements: a loss function to be optimized, a classification and regression tree (CART) for making predictions and a model for adding trees in sequence to minimize the loss function. As an improvement of this algorithm, XGBoost adds regularization to the objective function to avoid overfitting, along with many other enhancements. Russell and Norvig [37] also point out that XGBoost aims at being efficient, carefully organizing memory to avoid cache issues and allowing parallel computing across multiple machines, making it an easily scalable algorithm.

Chen and Guestrin [36] point that the tree ensemble model with regularization minimizes the objective function shown in Equation 1, where $i$ is the number of inputs, $N$ is the number of predictions and $K$ is the number of trees. The function $l$ is a differentiable convex loss function that measures the difference between the prediction $\hat{y}_i$ and the target $y_i$. The term $\Omega$ penalizes the complexity of the model, where $T$ is the number of leaves and $\gamma$ is the minimum loss reduction required to make a further partition on a leaf node of the tree. The additional L2 regularization term $\lambda$ helps to smooth the final learnt weights to avoid overfitting. When $\lambda$ is set to 0, the objective falls back to the traditional gradient tree boosting.

$$\mathcal{L}(\phi) = \sum_i^N l(\hat{y}_i, y_i) + \sum_k^K \Omega(f_k), \text{ where } \Omega(f) = \gamma T + \frac{1}{2}\lambda\|w\|^2 \tag{1}$$

Besides the regularized objective, two additional techniques are used to further prevent overfitting. The first technique is shrinkage, which scales newly added weights by a factor $\eta$ after each step of tree boosting. Similar to a learning rate in stochastic optimization, shrinkage reduces the influence of each individual tree and leaves space for future trees to improve the model. The second technique is feature subsampling, which is also used in RF in commercial software such as TreeNet, and helps to prevent overfitting even more [36].

According to Chen and Guestrin [36], the XGBoost uses a gain-based score to search for the best node splits when building a tree. Gain can be seen as the improvement in accuracy brought by a feature to the branches it is on. Equation 2

gives the gain at a leaf node during splitting. Nguyen et al. [10] explain that this formula is composed of four terms, which in turn represent the scores of the new left leaf ($g_L$), new right leaf ($g_R$), original left and right leaves ($h_L$, $h_R$), and the regularization of the additional leaf. The tree ceases growing when the gain becomes smaller than $\gamma$. In the ensemble model, the prediction scores of all trees are summed to obtain the final score.

$$Gain = \frac{1}{2}\left[\frac{g_L^2}{h_L+\lambda} + \frac{g_R^2}{h_R+\lambda} - \frac{(g_L+h_R)^2}{h_L+h_R+\lambda}\right] - \gamma \tag{2}$$

As it is a recent technique, there are still few civil engineering studies applying XGBoost, such as [10], [11] and [38]–[42].

## 3 PUNCHING SHEAR IN FLAT SLABS AND DESIGN CODE MODELS

The flat slab system of reinforced concrete has been used more frequently because it has some advantages when compared to conventional structural systems. Among these advantages, one can mention greater architectural freedom in defining internal environments or future layout changes; simplification of reinforcement and consequent reduction of labor and material costs; ease in the arrangement of installations and simplification of forms and framing. The system also has disadvantages compared to conventional ones, such as higher levels of vertical displacement of the structure, reduction of the global stability and the possibility of failure by punching shear [43].

Punching shear is a type of shear failure that can occur in plate elements subjected to a concentrated load or reaction applied transversally and is characterized by occurring abruptly, which can lead the structure to ruin through progressive collapse. The shear strength of the slab-column connection is one of the most important parameters in the design of flat slabs [44].

Wight and MacGregor [45] mention that the two-way shear involves a truncated cone or pyramid-shaped surface around the column. According to Muttoni [2], most design codes for punching shear base their verifications on a critical section, with the punching shear strength of slabs without shear reinforcement defined as a function of the concrete compressive strength and often of the reinforcement ratio. Some codes also account for size effect, membrane effect, or the ratio of column size to the depth of the slab. This critical section or control perimeter is defined as shown in Figure 3.
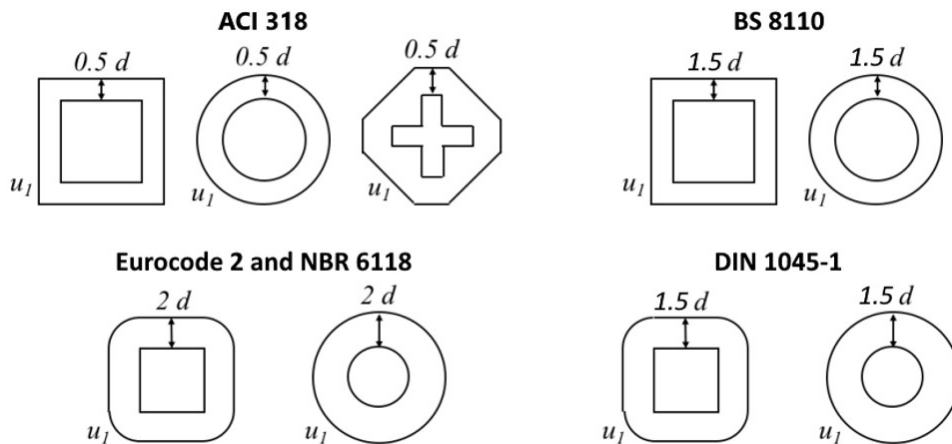


**Figure 3.** Control perimeters.

The design equations for calculating the punching shear resistance of flat RC slabs without shear reinforcement investigated herein are presented as follows. Note that, to ensure comparison with real failure data, no safety coefficients were introduced in the presented equations. Units are in SI.

### 3.1 Eurocode 2 (2004)

Eurocode 2 [23] uses Equation 3 for punching shear design, where $\rho_l$ is the longitudinal (flexural) reinforcement ratio, $f_c$ is the compressive strength of the concrete, $u_l$ is the control perimeter, $d$ is the effective depth of the slab and $\xi$ is the size effect factor, calculated by Equation 4.

$$V_{EC2,p} = 0.18\xi(100\rho_l f_c)^{1/3}u_1 d, \rho_l \leq 2\% \tag{3}$$

$$\xi = 1 + \sqrt{\frac{200}{d}} \leq 2 \tag{4}$$

## 3.2 ABNT NBR 6118 (2014)

NBR 6118 [21] uses Equations 5 and 6 for design, using the same procedure as Eurocode 2 [23], but without limitations on the reinforcement ratio and size effect factor.

$$V_{NBR,p} = 0.18\xi(100\rho_l f_c)^{1/3}u_1 d \tag{5}$$

$$\xi = 1 + \sqrt{\frac{200}{d}} \tag{6}$$

## 3.3 ACI 318M (2019)

Equation 7 is used in the design of flat slabs by ACI 318 [22], where $\alpha_s$ is equal to 20 for corner columns, 30 for edge columns and 40 for interior columns, $\beta$ is the ratio between the largest and smallest sides of the column and $\lambda_s$ is the modification factor related to the size effect, given by Equation 8.

$$V_{ACI,p} = \lambda_s \sqrt{f_c} u_1 d \min \begin{cases} \frac{1}{3} \\ \frac{1}{6}\left(1 + \frac{2}{\beta}\right) \\ \frac{1}{12}\left(2 + \frac{\alpha_s d}{u_1}\right) \end{cases} \tag{7}$$

$$\lambda_s = \sqrt{\frac{2}{1+0.004d}} \leq 1 \tag{8}$$

## 3.4 BS 8110 (1987)

The British standard BS 8110 [24] uses Equation 9 for punching shear design. Reinforcement ratio is capped at 3%. For concretes with $f_c$ above 25 MPa, the calculated value must be multiplied according to Equation 10. Equation 11 calculates the size effect factor.

$$V_{BS,p} = 0.79\xi(100\rho_l)^{1/3}u_1 d, \rho_l \leq 3\% \tag{9}$$

$$V_{BS,p} = V_{BS,p}\left(\frac{f_c}{25}\right)^{1/3} \text{ for } f_c \geq 25 \text{ MPa} \tag{10}$$

$$\xi = \sqrt[4]{\frac{400}{d}} \geq 1 \tag{11}$$

## 3.5 DIN 1045-1 (2008)

Equation 12 is used to calculate the punching shear resistance by the German standard DIN 1045-1 [25]. Equation 4 gives the size effect factor, corresponding to the same formulation as in Eurocode 2 [23].

$$V_{DIN,p} = 0.21\xi(100\rho_l f_c)^{1/3}u_1 d, \rho_l \leq 2\% \tag{12}$$

Rev. IBRACON Estrut. Mater., vol. 16, no. 4, e16405, 2023

7/18

## 4 DATA ENGINEERING

The dataset applied in this study is the same used by [11]. This is a database with experimental results of 519 flat slabs tested by several authors since 1938. A preliminary treatment is carried out to reduce the dimensionality of the problem, considering only the most relevant variables that were used in other papers on the subject, such as [10]–[12]. The selected input variables are: average effective depth of the slab ($d_{avg}$) in X and Y directions, effective column width ($b^*$), concrete compressive strength ($f_c$), steel yield strength ($f_y$) and average flexural reinforcement ratio ($\rho_{avg}$) in X and Y directions.

In most cases, the average compressive strength at time of slab testing was informed and, thus, this variable could be used directly. However, in some of the experimental tests, only the compressive strength at 28 days was reported. In these cases, strength at the time of slab testing was estimated from the strength at 28 days based on the elapsed time. Specimen details are presented in the original dataset.

In few cases, the longitudinal reinforcement bars of the slabs were arranged with non-uniform spacing along the section, and the reinforcement ratios employed herein had to be adjusted from the reported ones. The reinforcement ratio considered corresponded only to the region that passes through the column.

For the cases of rectangular or circular columns, $b^*$ is the width of the equivalent square area section, given by Equations 13a and 13b [11], where $D$ is the diameter and $b_1$ and $b_2$ are the smaller and larger side of the column, respectively. Thus, the number of features is reduced to five and the output variable is the punching shear strength of the slab ($P_u$).

$$b^* = \frac{\pi D}{4} \text{ (circular section)} \tag{13a}$$

$$b^* = \frac{b_1 + b_2}{2} \text{ (rectangular section)} \tag{13b}$$

As the objective of this study is to predict the punching shear failure load, 84 slabs that did not fail exclusively by this mechanism are excluded. In addition, missing values are identified in $f_y$ for 18 of the samples. These samples are removed from the dataset. Finally, 44 slabs that did not have longitudinal reinforcement in the region of the column are excluded, leaving 373 experimental results. Table 1 shows the descriptive statistics of the dataset after this treatment.

**Table 1.** Descriptive statistics of the dataset.

|  | $d_{avg}$ (mm) | $\bar{\rho}_{avg}$ (‰) | $b^*$ (mm) | $f_c$ (MPa) | $f_y$ (MPa) | $P_u$ (kN) |
|---|---|---|---|---|---|---|
| Mean | 110.73 | 12.98 | 180.95 | 32.80 | 461.63 | 384.30 |
| Std. dev. | 66.50 | 6.50 | 97.25 | 18.62 | 118.23 | 458.86 |
| Min. | 29.97 | 3.25 | 39.90 | 8.66 | 250.00 | 24.00 |
| 25% | 76.20 | 8.44 | 109.96 | 22.13 | 359.00 | 165.00 |
| 50% | 107.00 | 11.75 | 159.59 | 28.05 | 462.00 | 265.00 |
| 75% | 121.56 | 15.19 | 225.00 | 35.34 | 530.00 | 405.00 |
| Max. | 668.50 | 50.10 | 707.64 | 118.70 | 749.00 | 4915.00 |

A common step in the data preprocessing for ML models is data scaling. In the input data, the parameters usually have very different magnitudes and units from each other, which can lead the model to incorrectly assign greater importance to variables with higher numerical values. To prevent this problem, data is scaled so that the features are of the same order of magnitude (with values close to zero, usually between 0 and 1 or between -1 and 1). In this study, three scaling methods from the Python scikit-learn (sklearn) library are applied: StandardScaler, Normalizer and MinMaxScaler. According to the documentation of the sklearn library [46], the StandardScaler transforms the data through the z-score technique, setting null mean and unit standard deviation; the Normalizer normalizes the data by rescaling them to unitary norm; and MinMaxScaler scales the data so that the values are always between 0 and 1. For each ML algorithm, the scaling method that obtained the best results is used. Figure 4 shows the pairplots of the scaled variables after applying the StandardScaler.

Rev. IBRACON Estrut. Mater., vol. 16, no. 4, e16405, 2023

8/18
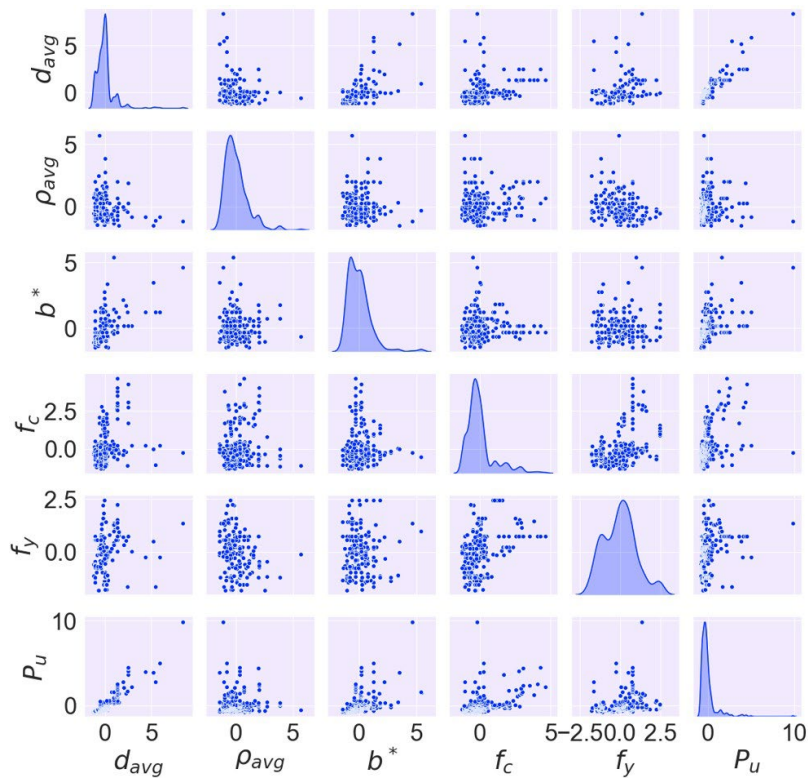
**Figure 4.** Pairplot.

A pairplot can be interpreted as a symmetric matrix of graphs, where kernel density estimation (KDE) graphs (equivalent to smoothed histograms) are plotted on the main diagonal and, in the other cells, the relationship between each variable and the others is observed through scatter plots. In this way, it is possible to analyze, in a preliminary way, if there is correlation between variables and what type of distribution they follow. Another way to get insights from data is by plotting a heatmap, which corresponds to a representation of data in the form of a diagram in which data values are represented with colors. Heatmap for the features in the dataset (with correlation values) is shown in Figure 5.
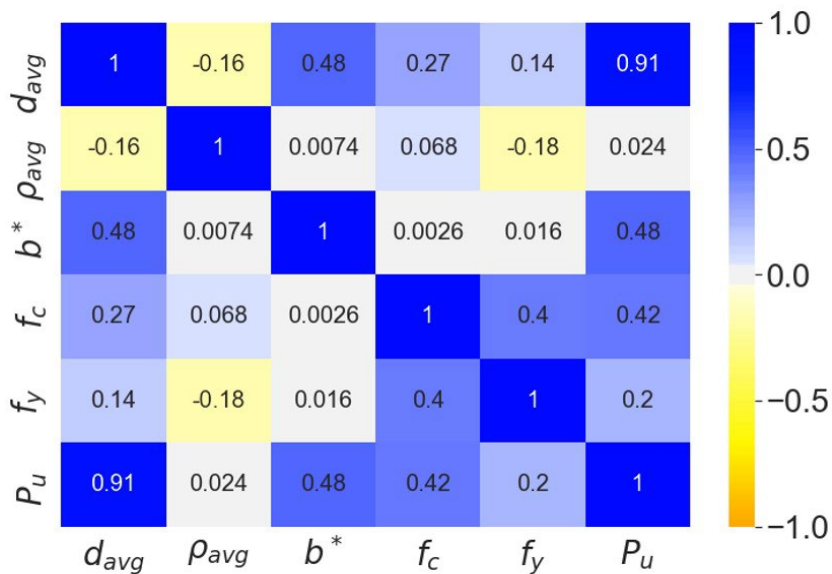


**Figure 5.** Heatmap.

Through Figures 4 and 5 it is observed that there is a strong correlation between the effective depth and the ultimate load. It is noticed that there is always some degree of positive correlation between individual parameters and the strength of the slabs: when increasing the width of the column, the strength of the concrete, the yield strength of the steel, the effective depth or the flexural reinforcement ratio, the punching shear strength also increases. It is also observed that, apparently, the geometric properties of the slabs ($d_{avg}$ and $b*$) show a proportional behavior, which can be explained by the fact that, in experimental tests, larger slabs (with higher widths) are usually supported on larger columns (larger $b*$).

Before running the ML algorithms, it is common to split the data into training and test sets. In this way, models are developed based on a portion of the dataset (training set) and tested with the remaining data (test set), to evaluate their accuracy with unknown data and avoid overfitting. For all models of this paper, the data are split in the proportion 70% training and 30% test, which is a common ratio used in the literature. Data scaling is performed only after this split to avoid issues like data leakage.

The repeated holdout technique is used for each algorithm. According to Aggarwal [28], the holdout consists of randomly dividing the data into two disjoint sets, corresponding to the training and test data. The repeated holdout, as the name suggests, repeatedly does this to find the best random state for the training/test split for a given problem. Random state is the seed (or starting point in random number generators), which is a value specified to control randomness and to generate reproducible results.

## 5 MODEL ENGINEERING

Python libraries sklearn for RF and DT, XGBoost for XGB and Tensorflow/Keras for ANN are used. Hyperparameters must be set to the ML algorithms. Hyperparameters are free parameters that are not determined by the learning algorithm, but rather specified as inputs to it [29]. Table 2 shows the settings used for each algorithm, with initial values based on [10] and [11] and subsequently adjusted via hyperparameter tuning with grid search. Grid search is the process of trying combinations of values in given intervals and seeing which performs best on the validation data [37]. Other hyperparameters take default values from their respective libraries.

**Table 2.** Hyperparameters used for each ML algorithm.

| Model | Parameters |
|---|---|
| ANN | Number of hidden layers = 2, number of neurons in each hidden layer = 94, activation function = ReLU, optimizer = Adam, learning rate = 0.3, loss function = RMSE, epochs = 50, random state = 0 |
| DT | Maximum depth = 10, random state = 0 |
| RF | Number of estimators = 69, random state = 0 |
| XGB | Number of estimators = 72, learning rate = 0.22, maximum depth = 5, random state = 0 |

The coefficient of determination ($R^2$) quantifies the fraction of variability in the series that is explained by the regression [28]. It is therefore desirable for this coefficient to be as close to 1 as possible. It provides an indication of goodness of fit and a measure of how well unseen samples are likely to be predicted by the model. Another metric is the RMSE, which measures the average error between predictions. It is desirable for this metric to be as close to zero as possible. Equations 14 and 15 give the $R^2$ and RMSE calculations, where $Y$ and $\hat{Y}$ are the actual and predicted values by the model, $N_t$ is the number of samples and $\bar{Y}$ is the mean.

$$R^2 = 1 - \frac{\sum_{i=1}^{N_t}(\hat{Y}_i - Y_i)^2}{\sum_{i=1}^{N_t}(\hat{Y}_i - \bar{Y}_i)^2} \tag{14}$$

$$RMSE = \sqrt{\frac{1}{n}\sum_{i=1}^{n}(\hat{Y}_i - Y_i)^2} \tag{15}$$

There are several rules in the literature for trying to choose the optimal number of hidden neurons in ANNs. However, most predicting research fields are heuristic in nature, and there is no generally accepted theory to determine how many hidden neurons are needed to approximate any given function [47]. Therefore, the use of systematic experimentation to discover what works best for a specific dataset may be the most general approach. In this paper, the number of hidden neurons is chosen so that $R^2$ is maximized and RMSE is minimized for test data. Figure 6 indicates that the optimal number of neurons to meet these conditions is 94 for the problem at hand.
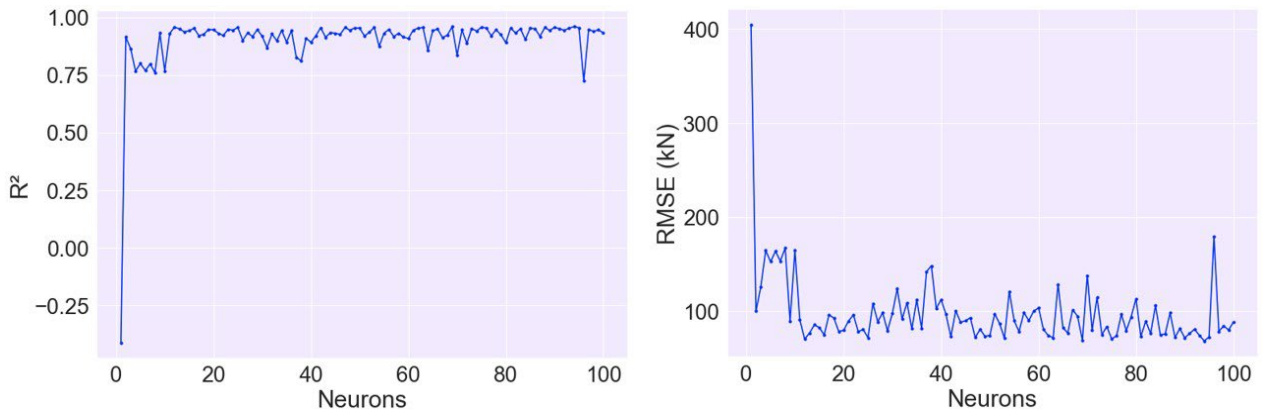
**Figure 6.** Experimentation of the number of neurons in the ANN.

A similar process is done to find the optimal maximum depth for the DT and number of estimators for the RF and XGB algorithms. Results are shown in Figures 7, 8 and 9, where optimal values are 10 levels for DT, 69 trees for RF and 72 trees for XGB. In Figures 7 and 8, it is observed that the prediction accuracy for test data starts to decrease after certain values of maximum tree depth (DT) and number of estimators (RF), which is a sign of overfitting. Figure 7 also indicates that the maximum possible depth for the DT is 18.
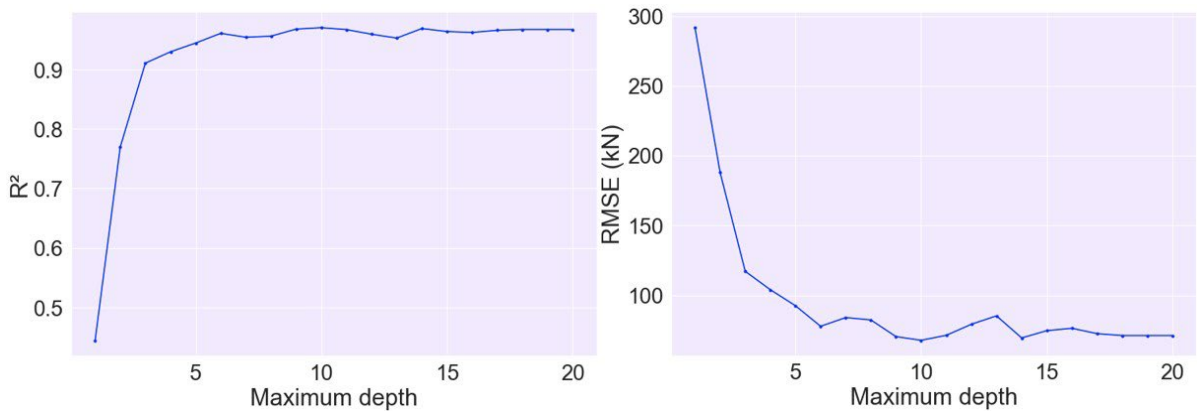


**Figure 7.** Experimentation of the maximum depth in the DT.
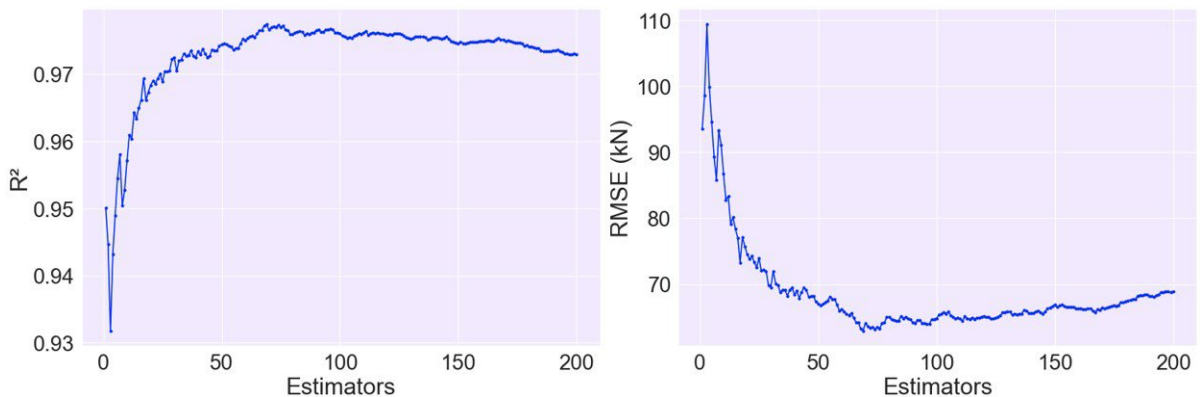


**Figure 8.** Experimentation of the number of estimators in the RF.
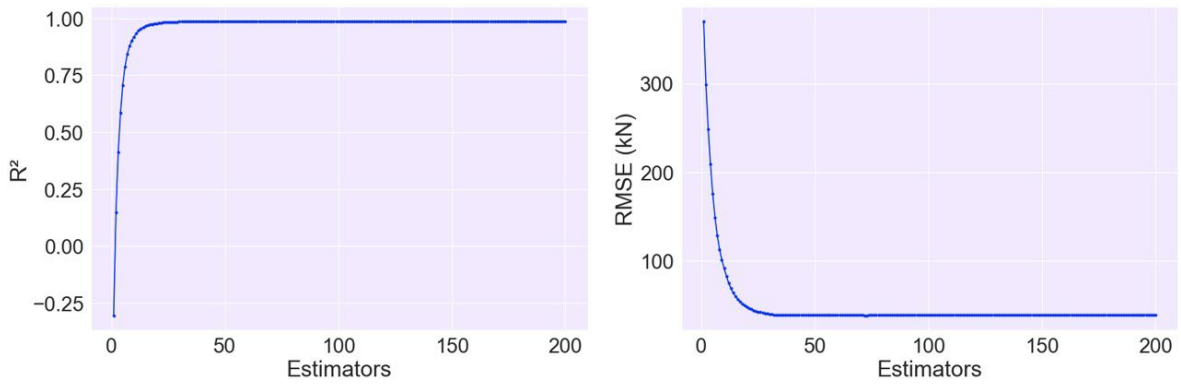
**Figure 9.** Experimentation of the number of estimators in the XGB.

# 6 RESULTS AND DISCUSSIONS

Figure 10 shows the results of the regression models (regplots) for training and test data and for the entire dataset. Results are presented from highest to lowest $R^2$ for test data.



**Figure 10.** Regplots.

Rev. IBRACON Estrut. Mater., vol. 16, no. 4, e16405, 2023

12/18
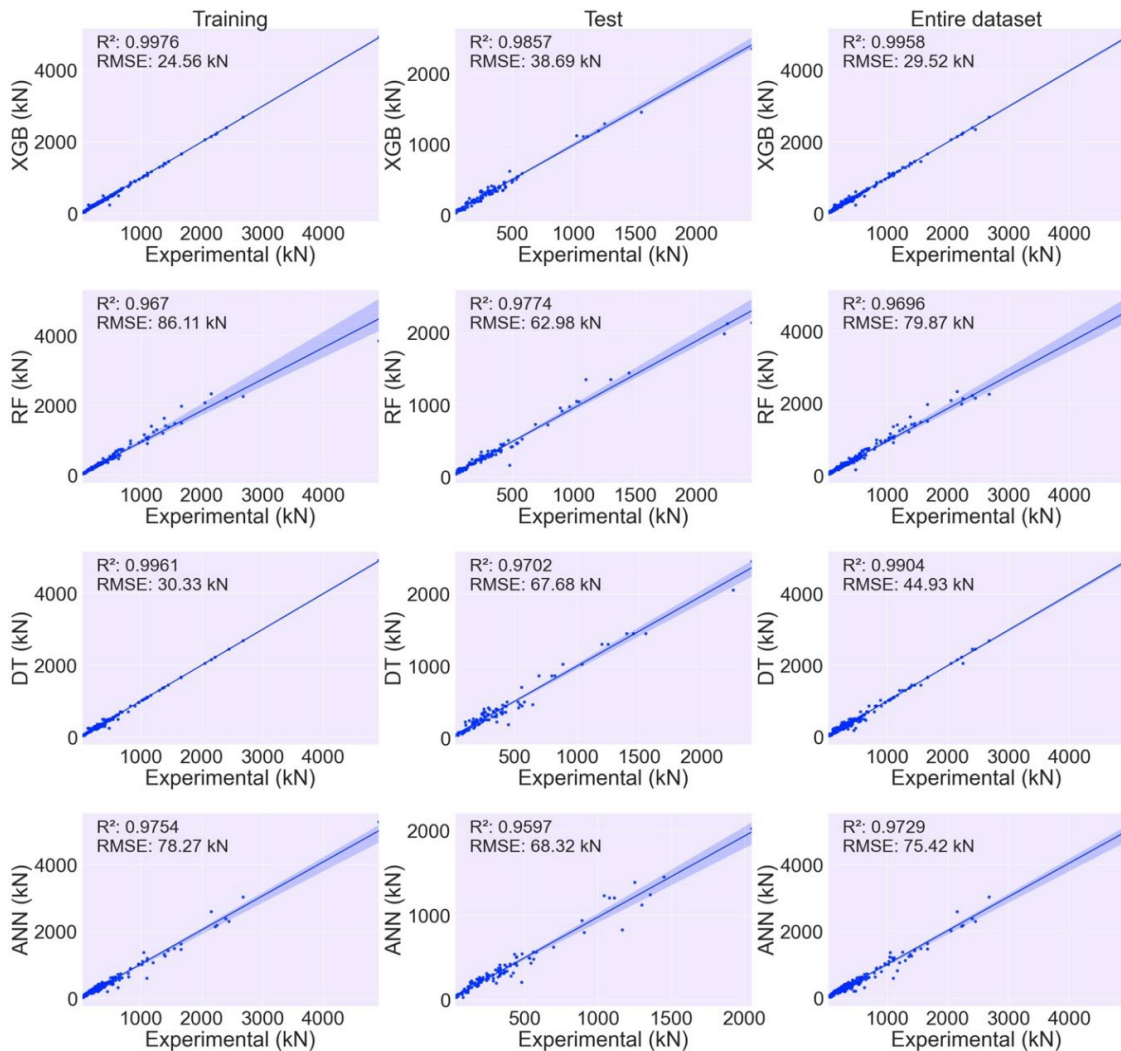
From Figure 10, XGB is the model with highest $R^2$ (0.9857) and lowest RMSE (38.69 kN) for test data. It is followed by RF and DT. The RF and DT models show similar performance; however, the RF has less variance (less overfitting or higher accuracy for test data). The DT and XGB models also present similar results, but the DT shows a significantly lower $R^2$ for the test data. The DT not performing as well to test data as it does to training data can be explained by the tendency to overfitting of the classical decision tree models. It is observed that ANN is the model that shows the lowest $R^2$ (0.9597) and highest RMSE (68.32 kN) for test data, but these results agree with what was found in the literature, as shown in section 1.

Figure 11 shows histograms of the $P_{u,pred}/P_{u,experimental}$ ratio (using the test sets of each model), with all models having values concentrated around 1. From a structural safety point of view, it is desirable that, if the model makes an incorrect prediction, its prediction must be in favor of safety (that is, that it underestimates the structural resistance). Therefore, ratios closer to 1 and lower standard deviations are desirable. The ANN outperforms the DT and RF models when analyzing this relationship, as opposed to what is observed in Figure 10. It is observed that the XGB (Figure 11d) shows the closest to 1 mean and the lowest standard deviation between the four models, and also the lowest maximum value.
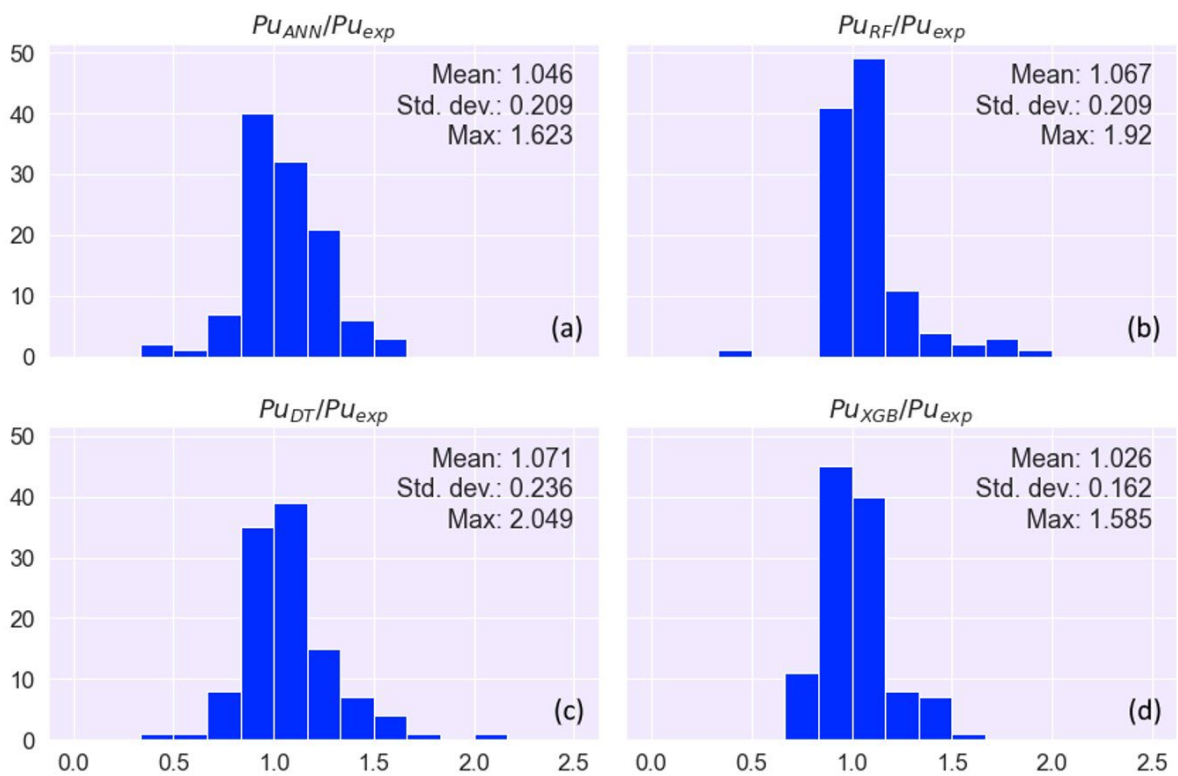


**Figure 11.** Histograms of the predicted/actual punching shear strength ratios.

In applications related to structural engineering, it is essential to understand whether the model usually leads to values in favor of safety, that is, conservative, or not. In this sense, the method proposed in [48] is employed herein to compare the different ML models. Table 3 presents the calculated conservatism indexes (C) and indicates that all models are considered slightly non-conservative according to the method, with negative values.

**Table 3.** Conservatism indexes.

| Model | C |
|---|---|
| XGB | -0.0262 |
| ANN | -0.0464 |
| RF | -0.0671 |
| DT | -0.0714 |

Therefore, considering the metrics in Figures 10 and 11 and Table 3, it is decided, from now on, to use only the XGB model for the purposes of comparison with design standard models in this study.

After selecting the best model, a feature importance analysis is performed to identify the impact of the input variables on the output. The bar graph in Figure 12 shows the feature importance through their gain. The feature importance based on this metric shows the average gain across all splits where a particular feature is used. Therefore, higher gain means higher importance. As presumed in the data engineering step, the effective depth is the most important variable, followed by the column dimension, reinforcement ratio and steel yield strength. The concrete strength is the variable that provides the smallest gain in this model. These results agree with what was observed by [10].
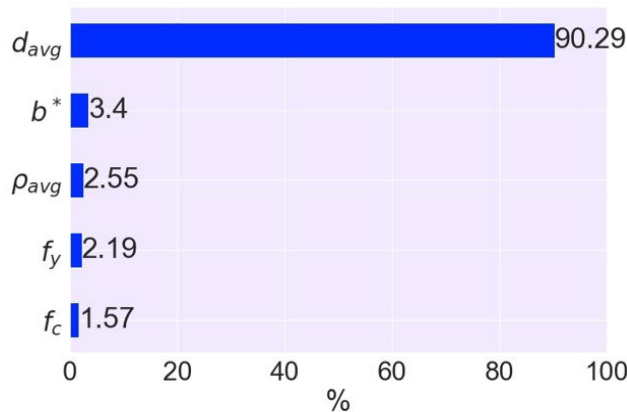


**Figure 12.** Relative feature importance in the XGB model.

## 7 COMPARATIVE STUDY OF MODELS

The equations for RC slab design according to the design standards [21]–[25] are presented in section 3. It is noted that none of these codes directly use the column width in their formulas. Instead, a critical perimeter around the column is considered, which depends on its dimensions and the effective depth of the slab. None of the standards uses the $f_y$ parameter in the design, while the American standard also ignores the longitudinal reinforcement ratio. Most standards differ in calculating the size effect factor.

In all evaluations performed with the standards, for a fair comparison with the XGB model, only the 112 slabs used in the XGB test dataset are considered. The regplots, $R^2$ and RMSE of the design code models and XGB are shown in Figure 13.
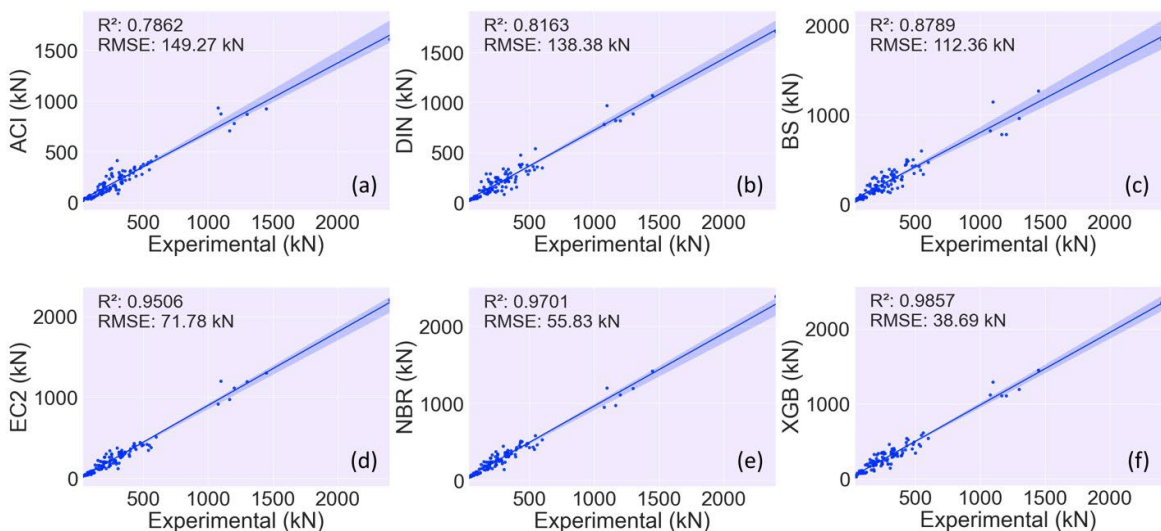


**Figure 13.** Regplots with design code results.

From Figure 13 it is observed that, although providing accurate results, all design models show inferior accuracy than the XGB. The ACI (Figure 13a) shows the least accurate results, followed by DIN (Figure 13b), BS (Figure 13c), EC2 (Figure 13d) and NBR (Figure 13e). The XGB (Figure 13f) is the model that shows the highest $R^2$ and the lowest RMSE.

The histograms of the $P_{u,pred}/P_{u,experimental}$ ratios are shown in Figure 14. Based on the results presented, there is a tendency for the ACI (Figure 14a) to underestimate the strength of the slabs, being a conservative model, due to the method used to calculate the control perimeter (only 0.5d away from the column face). The DIN (Figure 14b), BS (Figure 14c) and EC2 (Figure 14d) standards, in general, also show conservative results. These standards tend to underestimate the slabs resistances, as expected. The NBR (Figure 14e) shows better estimates than the other standards, as the NBR does not limit the size effect factor ($\xi$) and the reinforcement ratio in its formulas, obtaining results closer to reality than the other standards. Between the design models, the NBR shows the closest to 1 average error. Thus, the recommendation of NBR is the most indicated by the authors regarding the size effect.
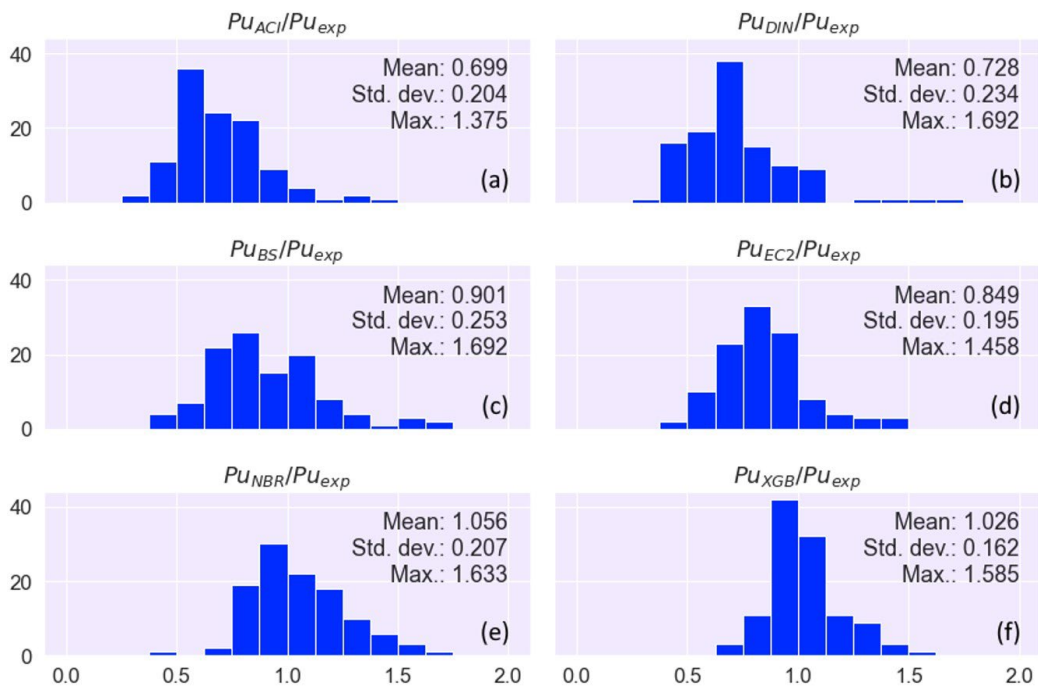


**Figure 14.** Histograms of the predicted/actual punching shear strength ratios with design code results.

From Figure 14, the ACI, DIN, BS, EC2 and NBR models estimate, on average, failure loads 30.1% lower, 27.2% lower, 9.9% lower, 15.1% lower and 5,6% higher than the real ones, respectively. On the other hand, the XGB estimates values, on average, 2.6% higher than the experimental ones.

Table 4 shows the descriptive statistics of the ultimate load for each model. The NBR and XGB showed similar statistics for the 112 slabs, with the NBR being closer to the actual mean and the XGB closer to the experimental standard deviation.

**Table 4.** Descriptive statistics of the results.

|  | Exp. (kN) | ACI (kN) | DIN (kN) | BS (kN) | EC2 (kN) | NBR (kN) | XGB (kN) |
|---|---|---|---|---|---|---|---|
| Mean | **320.02** | 225.95 | 233.85 | 275.50 | 278.07 | 322.18 | 323.87 |
| Std. dev. | **324.29** | 228.28 | 240.08 | 259.18 | 299.74 | 310.96 | 320.02 |
| Min. | **34.00** | 19.81 | 20.80 | 33.39 | 24.24 | 42.54 | 30.96 |
| 25% | **159.00** | 91.06 | 102.52 | 132.84 | 122.20 | 153.55 | 173.34 |
| 50% | **244.00** | 169.28 | 201.92 | 208.00 | 210.35 | 252.88 | 248.70 |
| 75% | **346.25** | 280.44 | 282.00 | 326.18 | 320.13 | 370.04 | 352.55 |
| Max. | **2400.00** | 1609.56 | 1710.26 | 1839.25 | 2201.13 | 2386.79 | 2348.72 |

Table 5 shows the results for conservatism indexes (C) calculated according to the method presented in [48], with results for the design code models. Despite presenting the lowest conservatism index and having predicted, on average, values greater than the real ones, it cannot be said that the NBR was against safety, as there may be other factors that influence resistance that were not addressed in this study. For example, according to Sousa and Debs [49], the aggregate interlock effect is not accounted in the ACI, EC2 and NBR standards, which is known to be an important factor in the shear resistance of concrete structures.

**Table 5.** Conservatism indexes with design code results.

| Model | C |
|---|---|
| ACI | 0.3011 |
| DIN | 0.2715 |
| EC2 | 0.1510 |
| BS | 0.0989 |
| NBR | -0.0557 |
| XGB | -0.0262 |

## 8 CONCLUSIONS

In this paper, four ML models were developed to predict the punching shear strength of RC flat slabs based on 373 experimental results. After a comparative analysis between them, the model based on extreme gradient boosting (XGB) was considered the best one, with higher $R^2$, lower RMSE and lower error ratio.

The XGB model was compared with models of five design standards: ABNT NBR 6118 [21], ACI 318 [22], Eurocode 2 [23], BS 8110 [24] and DIN 1145-1 [25]. It was observed that the standard models, although showing satisfactory results in general, presented lower accuracy not only in comparison with the XGB, but also with the other developed ML models. The design code models were compared to the experimental data, where the one that came closest to the real results was the NBR, while the ACI was the most distant from the actual resistances. It was found that the ACI, EC2, BS and DIN tend to underestimate the strength of the slabs, providing values on average lower than the real ones, being conservative.

As a result, the following conclusions are drawn:

1. The XGB model had the best performance between the developed ML models and it was closer to the real results than the studied design code models, showing good ability to predict the punching shear strength of flat RC slabs, with $R^2$ equal to 0.9857 and RMSE of 38.69 kN for the test data;
2. Between the five input variables of the XGB model, it was found that the effective depth of the slab is the most important, and the properties of concrete and steel are the least relevant;
3. Between the studied models from design codes, there were large discrepancies in the results and the NBR 6118 [21] model showed the best overall performance in predicting the failure load of the slabs, as well as the lowest conservatism, followed by Eurocode 2 [23], BS 8110 [24], DIN 1145-1 [25] and ACI 318 [22].

## ACKNOWLEDGEMENTS

## REFERENCES

[1] D. S. Lourenço, E. A. P. Liberati, M. G. Marques, L. C. Almeida, and L. M. Trautwein, "Reinforced concrete flat slabs with openings at different distances from the column," *Rev. IBRACON Estrut. Mater.*, vol. 14, no. 1, e14111, 2021, http://dx.doi.org/10.1590/s1983-41952021000100011.

[2] A. Muttoni, "Punching shear strength of reinforced concrete slabs without transverse reinforcement," *ACI Struct. J.*, vol. 105, no. 4, pp. 440–450, 2008. Accessed: May 20, 2022. [Online]. Available:
https://www.researchgate.net/publication/37455726_Punching_Shear_Strength_of_Reinforced_Concrete_Slabs_without_Transverse_Reinforcement

[3] R. A. Sanabria, L. M. Trautwein, and L. C. Almeida, "Análise numérica da resistência à punção em lajes de concreto armado sem armadura de cisalhamento," in *An. 59º CBC*, Bento Gonçalves, Nov., 2017, pp. 1–19.

[4] H. Avagyan, "Punching shear resistance of slab with shear reinforcement according to Armenian and foreign building standards," *Teh. Vjesn.*, vol. 26, no. 1, pp. 279–282, 2019, http://dx.doi.org/10.17559/TV-20170705153240.

[5] R. J. C. Silva, D. R. C. Oliveira, N. G. B. Albuquerque, F. E. S. Silva Júnior, and P. V. Sacramento, "Computational modeling of flat slabs: Influence of ribs and flexural reinforcement on shear strength," *Lat. Am. J. Solids Struct.*, vol. 17, no. 6, pp. 1–16, 2020, http://dx.doi.org/10.1590/1679-78256128.

[6] M. S. Issa and E. Ismail, "Punching strength of conventional reinforced concrete flat slabs," *HBRC J.*, vol. 17, no. 1, pp. 77–91, 2021, http://dx.doi.org/10.1080/16874048.2021.1901401.

[7] Z. Xu and J. H. Saleh, "Machine learning for reliability engineering and safety applications: Review of current status and future opportunities," *Reliab. Eng. Syst. Saf.*, vol. 211, pp. 1–50, 2021, http://dx.doi.org/10.1016/j.ress.2021.107530.

[8] M. Su, Q. Zhong, H. Peng, and S. Li, "Selected machine learning approaches for predicting the interfacial bond strength between FRPs and concrete," *Constr. Build. Mater.*, vol. 270, pp. 1–16, 2021, http://dx.doi.org/10.1016/j.conbuildmat.2020.121456.

[9] D. Feng, Z. Liu, X. Wang, Z. Jiang, and S. Liang, "Failure mode classification and bearing capacity prediction for reinforced concrete columns based on ensemble machine learning algorithm," *Adv. Eng. Inform.*, vol. 45, pp. 101–126, 2020, http://dx.doi.org/10.1016/j.aei.2020.101126.

[10] H. D. Nguyen, G. T. Truong, and M. Shin, "Development of extreme gradient boosting model for prediction of punching shear resistance of r/c interior slabs," *Eng. Struct.*, vol. 235, pp. 1–14, 2021, http://dx.doi.org/10.1016/j.engstruct.2021.112067.

[11] S. Mangalathu, H. Shin, E. Choi, and J. Jeon, "Explainable machine learning models for punching shear strength estimation of flat slabs without transverse reinforcement," *J. Build. Eng.*, vol. 39, pp. 1–10, 2021, http://dx.doi.org/10.1016/j.jobe.2021.102300.

[12] S. Lu, M. Koopialipoor, P. G. Asteris, M. Bahri, and D. J. Armaghani, "A novel feature selection approach based on tree models for evaluating the punching shear capacity of steel fiber-reinforced concrete flat slabs," *Materials*, vol. 13, no. 17, pp. 1–20, 2020, http://dx.doi.org/10.3390/ma13173902.

[13] H. Ly, T. Le, H. T. Vu, V. Q. Tran, L. M. Le, and B. T. Pham, "Computational hybrid machine learning based prediction of shear capacity for steel fiber reinforced concrete beams," *Sustainability*, vol. 12, no. 7, pp. 1–34, 2020, http://dx.doi.org/10.3390/su12072709.

[14] W. J. S. Gomes, "Shallow and deep artificial neural networks for structural reliability analysis," *J. Risk Uncertain Eng. Syst. Part B Mech. Eng.*, vol. 6, no. 4, pp. 1–8, 2020, http://dx.doi.org/10.1115/1.4047636.

[15] M. Bilgehan and P. Turgut, "The use of neural networks in concrete compressive strength estimation," *Comput. Concr.*, vol. 7, no. 3, pp. 271–283, 2010, http://dx.doi.org/10.12989/cac.2010.7.3.271.

[16] K. Yan and C. Shi, "Prediction of elastic modulus of normal and high strength concrete by support vector machine," *Constr. Build. Mater.*, vol. 24, no. 8, pp. 1479–1485, 2010, http://dx.doi.org/10.1016/j.conbuildmat.2010.01.006.

[17] J. Chou, C. Chiu, M. Farfoura, and I. Al-Taharwa, "Optimizing the prediction accuracy of concrete compressive strength based on a comparison of data-mining techniques," *J. Comput. Civ. Eng.*, vol. 25, no. 3, pp. 242–253, 2011, http://dx.doi.org/10.1061/(ASCE)CP.1943-5487.0000088.

[18] J. Chou, C. Tsai, A. Pham, and Y. Lu, "Machine learning in concrete strength simulations: Multi-nation data analytics," *Constr. Build. Mater.*, vol. 73, pp. 771–780, 2014, http://dx.doi.org/10.1016/j.conbuildmat.2014.09.054.

[19] P. Prasanna et al., "Automated Crack Detection on Concrete Bridges," *IEEE Trans. Autom. Sci. Eng.*, vol. 13, no. 2, pp. 591–599, 2014, http://dx.doi.org/10.1109/TASE.2014.2354314.

[20] K. THIYAGARAJAN, S. KODAGODA, N. ULAPANE, "Data-driven machine learning approach for predicting volumetric moisture content of concrete using resistance sensor measurements," in *Proc. 11th ICIEA*, Hefei, June, 2016, pp. 1288-1293, http://dx.doi.org/10.1109/ICIEA.2016.7603783.

[21] Associação Brasileira de Normas Técnicas, *Projeto de Estruturas de Concreto – Procedimento*, ABNT NBR 6118, 2014.

[22] American Concrete Institute, *Building Code Requirements for Structural Concrete and Commentary*, ACI 318M, 2019.

[23] European Committee For Standardization, *Design of Concrete Structures – Part 1-1: General Rules and Rules for Buildings*, Eurocode 2, 2004.

[24] British Standards Institution, *Structural Use of Concrete - Part 1: Code of Practice for Design and Construction*, BSI BS 8110, 1997.

[25] German Institute for Standardization, *Plain, Reinforced and Prestressed Concrete Structures-Part 1: Design and Construction*, DIN 1045-1, 2008.

[26] M. E. Fenner, *Machine Learning with Python for Everyone*, 1st ed. London: Pearson Educ., 2020.

[27] C. Albon, *Python Machine Learning Cookbook*, 1st ed. Sebastopol, CA, USA: O'Reilly Media, 2018.

[28] C. C. Aggarwal, *Data Mining: The Textbook*, 1st ed. New York, NY, USA: Springer, 2015, http://dx.doi.org/10.1007/978-3-319-14142-8.

[29] M. Mohri, A. Rostamizadeh, and A. Talwalkar, *Foundations of Machine Learning*, 2nd ed. London: MIT Press, 2018.

[30] J. D. Kelleher, B. M. Namee, and A. D'Arcy, *Fundamentals of Machine Learning for Predictive Data Analytics. Algorithms, Worked Examples, and Case Studies*, 2nd ed. London: MIT Press, 2020.

[31] W. J. S. Gomes, "Shallow and deep artificial neural networks for structural reliability analysis," *J. Risk Uncertain Eng. Syst. Part B Mech. Eng.*, vol. 5, no. 4, pp. 1–8, 2019, http://dx.doi.org/10.1115/1.4044040.

[32] M. Z. Naser, "Machine learning assessment of fiber-reinforced polymer-strengthened and reinforced concrete members," *ACI Struct. J.*, vol. 117, no. 6, pp. 237–251, 2020, http://dx.doi.org/10.14359/51728073.

[33] E. Darvishan, "The punching shear capacity estimation of FRP strengthened RC slabs using artificial neural network and group method of data handling," *J. Rehabil. Civ. Eng.*, vol. 9, no. 1, pp. 102–113, 2021, http://dx.doi.org/10.22075/jrce.2020.20335.1407.

[34] L. Breiman, "Random Forests," *Mach. Learn.*, vol. 45, no. 1, pp. 5–32, 2001, http://dx.doi.org/10.1023/A:1010933404324.

[35] O. B. Olalusi and P. O. Awoyera, "Shear capacity prediction of slender reinforced concrete structures with steel fibers using machine learning," *Eng. Struct.*, vol. 227, pp. 1–13, 2021, http://dx.doi.org/10.1016/j.engstruct.2020.111470.

[36] T. Chen and C. Guestrin, "XGBoost: a scalable tree boosting system," in *Proc. 22nd ACM SIGKDD Int. Conf. Knowl. Discovery Data Min.*, San Francisco (CA), Aug., 2016, pp. 785-794, http://dx.doi.org/10.1145/2939672.2939785.

[37] S. Russel and P. Norvig, *Artificial Intelligence – A Modern Approach*, 4th ed. Hoboken, NJ, USA: Pearson Education, 2021.

[38] J. Duan, P. G. Asteris, H. Nguyen, X.-N. Bui, and H. Moayedi, "A novel artificial intelligence technique to predict compressive strength of recycled aggregate concrete using ICA-XGBoost model," *Eng. Comput.*, vol. 37, no. 4, pp. 3329–3346, 2020, http://dx.doi.org/10.1007/s00366-020-01003-0.

[39] D. Sathyan, D. Govind, C. B. Rajesh, K. Gopikrishnan, G. Aswath Kannan, and J. Mahadevan, "Modelling the shear flow behaviour of cement paste using machine learning – XGBoost," *J. Phys. Conf. Ser.*, vol. 1451, no. 1, pp. 1–8, 2020, http://dx.doi.org/10.1088/1742-6596/1451/1/012026.

[40] M. Wang, D. Huang, G. Wang, and D. Li, "SS-XGBoost: a machine learning framework for predicting newmark sliding displacements of slopes," *J. Geotech. Geoenviron. Eng.*, vol. 146, no. 9, pp. 1–17, 2020, http://dx.doi.org/10.1061/(ASCE)GT.1943-5606.0002297.

[41] N. M. Shahani, X. Zheng, C. Liu, F. U. Hassan, and P. Li, "Developing an XGBoost regression model for predicting young's modulus of intact sedimentary rocks for the stability of surface and subsurface structures," *Front. Earth Sci.*, vol. 9, pp. 1–13, 2021, http://dx.doi.org/10.3389/feart.2021.761990.

[42] A. Kaveh, S. M. Javadi, and R. M. Moghanni, "Shear strength prediction of FRP-reinforced concrete beams using an extreme gradient boosting framework," *Period. Polytech. Civ. Eng.*, vol. 66, no. 1, pp. 18–29, 2022, http://dx.doi.org/10.3311/PPci.18901.

[43] G. S. Santos, W. G. Nicácio, A. W. Lima, and G. S. S. A. Melo, "Punching strengthening in flat plates of reinforced concrete with carbon fiber reinforced polymer (CFRP)," *IBRACON Struct. Mater. J.*, vol. 7, no. 4, pp. 592–625, 2014.

[44] M. H. Oliveira, M. J. M. Pereira Filho, D. R. C. Oliveira, M. P. Ferreira, and G. S. S. A. Melo, "Punching resistance of internal slab-column connections with double-headed shear studs," *Rev. IBRACON Estrut. Mater.*, vol. 6, no. 5, pp. 681–714, 2013., http://dx.doi.org/10.1590/S1983-41952013000500002.

[45] J. K. Wight and J. G. MacGregor, *Reinforced Concrete Mechanics and Design*, 6th ed. Upper Saddle River, NJ, USA: Pearson Educ., 2012.

[46] F. Pedregosa et al., "Scikit-learn: machine learning in Python," *J. Mach. Learn. Res.*, vol. 12, no. 85, pp. 2825–2830, 2011. Accessed: May 20, 2022. [Online]. Available: http://jmlr.csail.mit.edu/papers/v12/pedregosa11a.html

[47] K. G. Sheela and S. N. Deepa, "Review on methods to fix number of hidden neurons in neural networks," *Math. Probl. Eng.*, vol. 2013, pp. 1–11, 2013, http://dx.doi.org/10.1155/2013/425740.

[48] W. J. S. Gomes and A. T. Beck, "A conservatism index based on structural reliability and model errors," *Reliab. Eng. Syst. Saf.*, vol. 209, pp. 1–15, 2021, http://dx.doi.org/10.1016/j.ress.2021.107456.

[49] A. M. D. Sousa and M. K. El Debs, "Shear strength analysis of slabs without transverse reinforcement under concentrated loads according to ABNT NBR 6118:2014," *Rev. IBRACON Estrut. Mater.*, vol. 12, no. 3, pp. 658–693, 2019, http://dx.doi.org/10.1590/s1983-41952019000300012.

**Editors:** Leandro Mouta Trautwein, Guilherme Aris Parsekian.

Rev. IBRACON Estrut. Mater., vol. 16, no. 4, e16405, 2023

18/18

# IBRACON Structures and Materials Journal
## Revista IBRACON de Estruturas e Materiais

ORIGINAL ARTICLE

# Influential parameters in the shear strength of RC beams without stirrups

*Parâmetros que influenciam na resistência ao cisalhamento de vigas de concreto armado sem estribos*

Guilherme Frank Leme[a] (iD)
Elyson Andrew Pozo Liberati[b] (iD)
Marília Gonçalves Marques[c] (iD)
Leandro Mouta Trautwein[a] (iD)
Luiz Carlos de Almeida[a] (iD)

[a]Universidade Estadual de Campinas – UNICAMP, Faculdade de Engenharia Civil, Arquitetura e Urbanismo, Campinas, SP, Brasil.
[b]Universidade Estadual de Maringá – UEM, Departamento de Engenharia Civil, Maringá, PR, Brasil.
[c]Universidade Federal de Viçosa – UFV, Rio Paranaiba, MG, Brasil.

**Abstract:** Experimental investigations have been commonly used to improve the existing knowledge about structural design, presenting accurate conclusions regarding structure behavior. However, considering the limitations of experimental studies, such as restricted amount of strain gauges, unexpected pathologies, difficulties to foresee the correct position of cracks, or simply saving in costs, the use of numerical analysis can present some innovative approaches to understand the process of failure in concrete elements, presenting easier results where experimental programs can hardly report. This study presents the numerical analysis of eight beams experimented by Sherwood [26], with two different sizes and variable aggregate sizes, seeking to understand the influence of coarse aggregate size in shear strength of beams without stirrups. The numerical approach was used to derive the influence of each internal shear mechanism and to identify the specific amount of dowel force, shear transfer by uncracked compression zone and aggregate interlock portion. The results showed that fair results can be obtained by 2D smeared crack approaches, enabling the identification of major aggregate interlock portion in beams with bigger coarse aggregate sizes. Comparing the size effect in beams allowed us to conclude that a higher contribution of aggregate interlock contribution can be obtained in large beams, with almost 64% of the total contribution, whereas smaller beams had only 43%. To evaluate the accuracy of the studied mechanisms, the results of Sherwood [26] were compared with the standards Model Code [23], CSA-A.23.3 [24], NBR 6118 [38], and ACI 318 [39]. Regarding the prediction of element rupture by concrete internal mechanisms, the normative instructions Model Code [23] and CSA A.23.3 [24] were the closest to the experimental results.

**Keywords:** reinforced concrete, shear, numerical analysis, beams.

**Resumo:** Investigações experimentais têm sido comumente usadas para melhorar o conhecimento existente sobre o projeto estrutural, apresentando conclusões precisas sobre o comportamento da estrutura. No entanto, considerando as limitações dos estudos experimentais, como quantidade restrita de extensômetros, patologias inesperadas, dificuldades de previsão do correto posicionamento das fissuras ou simples economia de custos, o uso da análise numérica pode apresentar algumas abordagens inovadoras para a compreensão do processo de falha em elementos de concreto, apresentando resultados mais fáceis onde programas experimentais dificilmente podem relatar. Este estudo apresenta a análise numérica de oito vigas experimentadas por Sherwood [26], com dois tamanhos diferentes e agregados de tamanhos variados, buscando-se entender a influência do tamanho do agregado na resistência ao cisalhamento de vigas sem estribos. A abordagem numérica foi usada para avaliar a influência de cada mecanismo de cisalhamento interno e para identificar a quantidade específica de força de pino, transferência de cisalhamento na zona de compressão não fissurada e a parcela de intertravamento de agregados. Os resultados mostraram que resultados razoáveis podem ser obtidos por abordagens de fissuras distribuídas 2D, permitindo a identificação da maior porção de intertravamento do agregado em vigas com maiores tamanhos de agregado graúdo. A comparação do efeito de escala em vigas permitiu

concluir que uma maior contribuição do intertravamento de agregados pode ser obtida em vigas grandes, com quase 64% da contribuição total, enquanto as vigas menores tiveram apenas 43%. Os resultados de Sherwood [26] foram comparados com as normas Model Code [23], CSA-A.23.3 [24], NBR 6118 [38] e ACI 318 [39] para avaliar a precisão das normas estudadas. Com relação à previsão da ruptura dos elementos por meio dos mecanismos internos do concreto, as instruções normativas Model Code [23] e CSA A.23.3 [24] resultaram valores mais precisos.

**Palavras-chave:** concreto armado, cisalhamento, análise numérica, vigas.

# 1 INTRODUCTION

Several studies have attempted to understand the shear behavior of reinforced concrete (RC) beams, and various approaches to predict its strength have been proposed. Some important studies, primarily proposed by Ritter and Die Bauweise [1] and Mörsch [2], present the strength of concrete beams with stirrups as an analogy for a trussed system, wherein the steel and concrete stresses must be maintained under a factored capacity limit. This limit is considered as a function of the concrete and steel limits, assuming that only the stirrups resist the formation of cracks.

Without shear reinforcement, the strength mechanism of concrete typically relies solely on the nonlinear behavior of the concrete used, considering that the cracks can transmit normal and parallel forces to their formation site. These results in mechanical responses help avoid the failure of the structural element to a certain extent. Figure 1 shows the shear capacity mechanisms of reinforced concrete beams, where $V_{cz}$ is the shear strength of the un-cracked concrete in the compression zone [3]; $V_{agg}$ is the aggregate interlock interface shear transfer, also referred to as crack friction [4]–[10]; and $V_{dowel}$ is the dowel action due to the longitudinal reinforcement bars [3], [11]–[16].
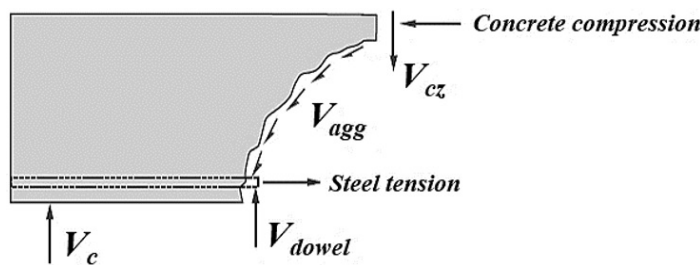


**Figure 1.** Shear transfer mechanism in RC beams.

Considering that the design codes are based on empirical equations, employing simple models - as the strut and tie models - on the structural members without transverse reinforcement results in an unsafe design. Bazant and Kazemi [17], Kani [18], and Taylor [19] tested beams based on empirical equations that are not applicable for practical situations.

Many studies have been conducted in the last 40 years on the internal capacity of concrete to resist shear strength, promotion owed to the continuing need to understand the real effect of these parameters on structural elements. To this end, several theoretical approaches have been proposed such as the modified compression filed theory (MCFT) by Vecchio and Collins [20], and Bentz et al. [21], and the critical shear crack theory (CSCT), developed by Muttoni and Fernández Ruiz [22]. MCFT and CSCT consider the influence of aggregate size, size effect, and strain on RC shear capacity. These methodologies compose the basis of recent design codes, such as Model Code [23] and CSA-A23.3 [24].

In the 1970s, Walraven [25] presented an experimental method to understand the influence of aggregate interlock mechanism on shear strength and found that raising coarse aggregate size resulted in increased major shear strength. Paulay et al. [14] compared longitudinal bars of different diameters, crossing a discontinuous surface on an experimental block, allowing for an investigation on the influence of the dowel force on shear strength. The study related higher shear strengths to larger bar diameters acting like dowels.

Despite the importance of these studies, no clear conclusions can be drawn regarding the influence of each mechanism on the total shear strength of RC beams. Other experimental studies such as those conducted by Sherwood [26], Daluga et al. [27], and Yang and Ashour [28] found that the influence of the coarse aggregate size could result in an increased shear capacity. However, to obtain a clearer understanding of stress and strain distribution inside RC beams, numerical modeling tools are still necessary.

Belbachir et al. [29] conducted an experimental study on three sizes of geometrically similar concrete beams without transverse reinforcements. The shear span-to-depth ratio ($a/d$) was set to 2.5. For the beams tested with this ratio, the aggregate interlock mechanism was not completely activated at the failure load, especially for smaller beams. This shear transfer mechanism exhibits size dependence, which is primarily related to the crack shape.

To contribute to the understanding of the shear strength mechanism in beams without stirrups, this study presents a numerical non-linear modeling for eight beams experimentally tested by Sherwood [26].

This study is motivated by the need to develop numerical approaches to analyze structural elements using computational tools and understand the role of each internal shear capacity mechanism on the strength of RC beams without stirrups. Performing numerical simulation of the experimental cases typically involves two main phases: calibrating the model; and analyzing internal cracks, strains, and stress (typically limited to obtaining measurements from sensors or strain gauges).

This study aims to deepen the studies on the phenomena of shear strength of reinforced concrete beams without stirrups, regarding the internal mechanisms of the concrete to resist the shear force of beams, usually called $V_c$ in technical standards.

In these design standards, $V_c$ is usually used as a shear strength contribution portion and is considered in the determination of shear reinforcement. The greater the portion of shear strength force by internal mechanisms, the smaller the portion of shear force that an engineer, instructed by technical standards will calculate and apply as a form of transverse reinforcement ratio.

## 2 EXPERIMENTAL PROGRAM

To investigate the influence of each internal strength mechanism on the total shear strength, the first step was to find an experimental program capable of standardizing many parameters and allowing for comparisons between the several shear-influencing factors. Based on these requirements, Sherwood [26] reported different campaigns of RC beams without stirrups, using different sizes of coarse aggregate and other similar attributes as premises. These methods, paired with an effective registration of the principal parameters experimentally obtained, make the study a useful reference for numerical analysis.

Table 1 shows the main characteristics of the specimens used as reference for the numerical analysis, where $b_w$ is the cross-section width, $d$ the effective depth, $L$ the effective beam length, $d_{ag}$ the aggregate diameter, $f_c$ the concrete compressive strength, and $A_{s+}$ is the cross-section of longitudinal tensile reinforcement. The aggregate diameter was used as an input parameter as recommended by the Model Code [23], such as: tensile strength, elasticity modulus, and Poisson coefficient. Sherwood [26] considered two categories of beam sizes and types in the experiment: eight beams of size $122 \times 363 \times 1,800$ mm, called the *Small* (*S*) *Series* and, eight beams of size $295 \times 1,510 \times 9,000$ mm, called the *Large* (*L*) *Series*. Figure 2 shows the characteristics of the beams analyzed in this study. The samples possess different concrete strengths. Four different sizes of coarse aggregate are used, with the major aggregate size varying from 9.5 mm to 51 mm. The specimens were not reinforced with stirrups and all experiments were loaded until shear failure.

Reinforcement yield stresses were experimentally evaluated and recorded. Table 2 shows the yield values and nominal areas.

**Table 1.** Experimental Series.

| Series | $b_w$ [mm] | $d$ [mm] | $L$ [mm] | $d_{ag}$ [mm] | $f_c$ [MPa] | $A_{s+}$ [mm²] |
|---|---|---|---|---|---|---|
| *S-Series* | | | | | | |
| S-10N1 | 122 | 280 | 1,620 | 9.5 | 41.9 | 285.2 |
| S-10N2 | 122 | 280 | 1,620 | 9.5 | 41.9 | 285.2 |
| S-20N1 | 122 | 280 | 1,620 | 19 | 39.2 | 285.2 |
| S-20N2 | 122 | 280 | 1,620 | 19 | 38.1 | 285.2 |
| S-40N1 | 122 | 280 | 1,620 | 38 | 29.1 | 285.2 |
| S-40N2 | 122 | 280 | 1,620 | 38 | 29.1 | 285.2 |
| S-50N1 | 122 | 280 | 1,620 | 51 | 43.5 | 285.2 |
| S-50N2 | 122 | 280 | 1,620 | 51 | 43.5 | 285.2 |
| *L-Series* | | | | | | |
| L-10N1 | 300 | 1,400 | 8,100 | 9.5 | 38.4 | 3,500.0 |
| L-10N2 | 300 | 1,400 | 8,100 | 9.5 | 40.4 | 3,500.0 |
| L-20N1 | 300 | 1,400 | 8,100 | 19 | 31.4 | 3,500.0 |
| L-20N2 | 300 | 1,400 | 8,100 | 19 | 33.2 | 3,500.0 |
| L-40N1 | 300 | 1,400 | 8,100 | 38 | 28.1 | 3,500.0 |
| L-40N2 | 300 | 1,400 | 8,100 | 38 | 28.5 | 3,500.0 |
| L-50N1 | 300 | 1,400 | 8,100 | 51 | 41.0 | 3,500.0 |
| L-50N2 | 300 | 1,400 | 8,100 | 51 | 40.1 | 3,500.0 |

S, and L – Smaller or larger specimen; 10, 20, 40, and 50 – Nominal aggregate sizes used in the test; N – Normal concrete compressive strength; 1, and 2 – Specimen 1 or 2 of the duplicated series.

**Table 2.** Experimental data on the steel bars used in the tests by Sherwood [26]. Where, $f_y$ is the yield strength of reinforcement.

| Bar type | Diameter [mm] | Area [mm²] | $f_y$ [MPa] |
|---|---|---|---|
| #3 | 10 | 71.3 | 494 |
| 20M | 20 | 300 | 484 |
| 30M | 30 | 700 | 452 |
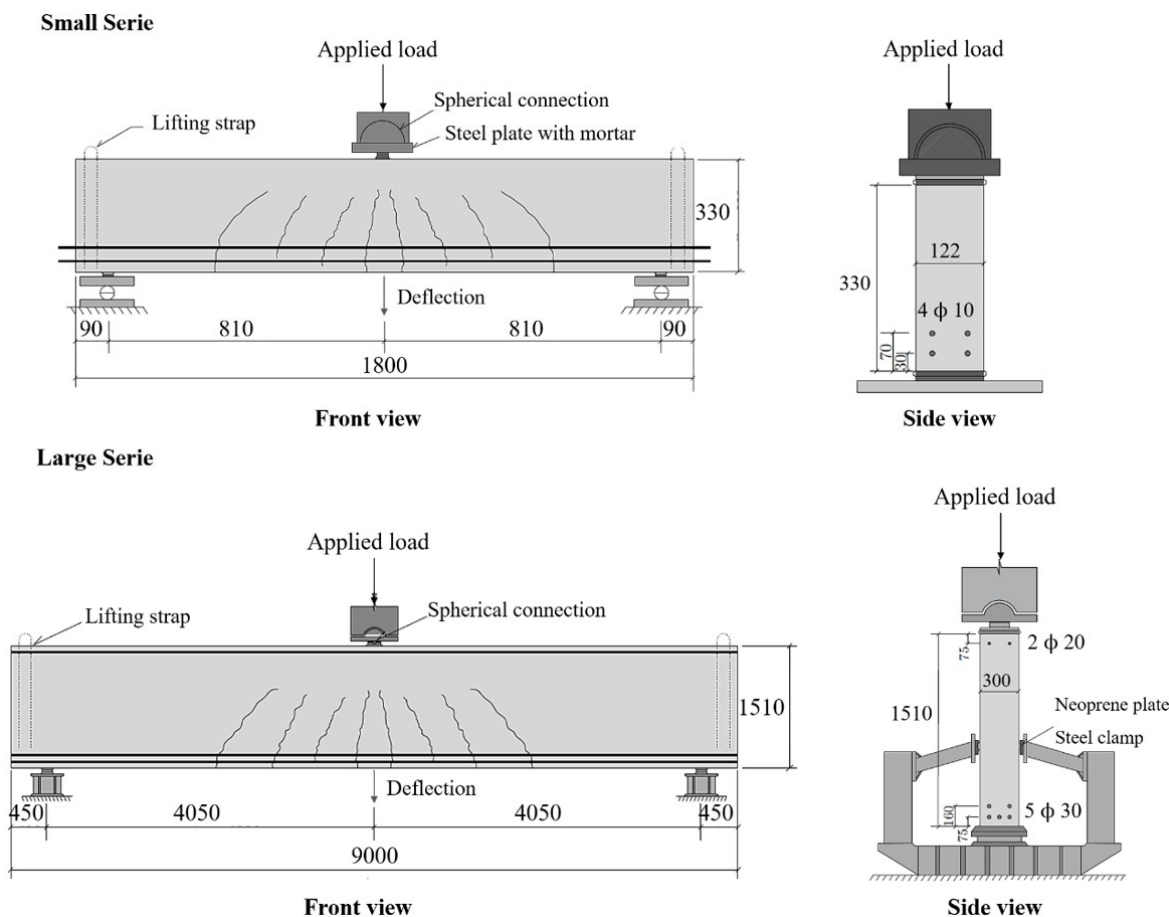


**Figure 2.** Beams of S-Series and L-Series of the experimental program (units in mm). Adapted by Sherwood [26].

# 3 NUMERICAL MODELS

A numerical model was developed to accurately simulate the experimental program. The problem was split into several partial problems and determined the internal relationship based their contour connectivity and characteristics. This is called the finite-element method (FEM). The FEM model must consider many effects to model the RC beams correctly and derive the basic conditions for the interaction between steel and concrete and the gradual formation of cracks.

The models tested in the laboratory were reproduced using DIANA 10.1. The discretization of the mesh in the S- Series used quadratic finite elements of approximately 26 × 26 mm, which is approximately 1/12 of the total beam height (330 mm), which has been by Feenstra et al. [30], Vecchio and Shim [31], and Pimentel et al. [32]. In the L- Series, the mesh proportion contained quadratic finite elements of approximately 75 × 75 mm, on the order of 1/20 of the total beam height (1,510 mm). Figure 3 shows the boundary conditions, load application points, and mesh sizes used in the FEM simulations.
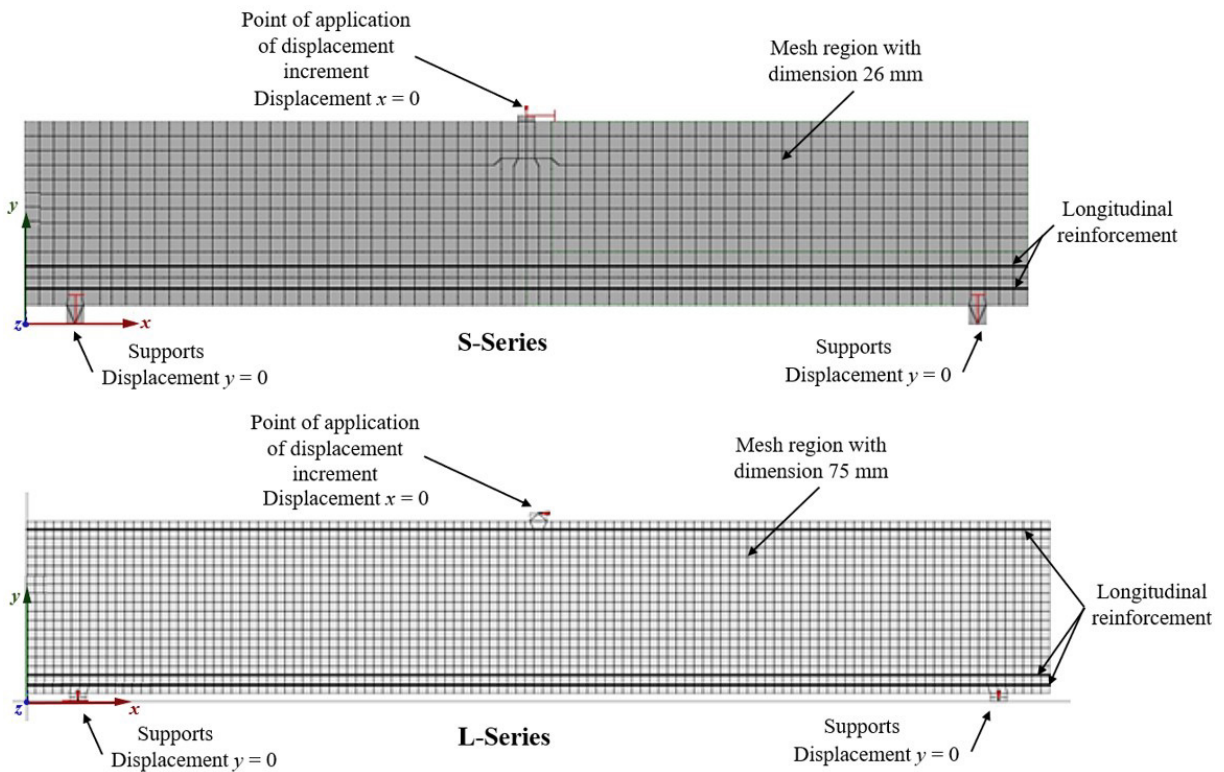
**Figure 3.** S and L series beams numerical model.

The models were constructed with 2D plane stress elements using square and triangular formats to represent the exact position of loads, restrictions, and longitudinal reinforcements. The longitudinal bars employ stiff beam elements for longitudinal and transverse displacements, particularly to act as dowels when the crack occur near the reinforcement.

The beams were configured to present two vertical restrictions at the supports, in addition to the horizontal restriction at the load point. The load was applied with a continuous displacement of 0.05 mm during each load step. The modified Newton-Raphson method was used to reach the convergence, with an internal energy-based criterion and a tolerance of 0.001. To accelerate the convergence, the line search and arc-length method were included in the model, according to the recommendations described in DIANA [33].

Table 3 shows the main parameters used to simulate the concrete and steel materials used in this study. These parameters were obtained with numerous analyses, aiming to ensure consistency between numerical models and the experimental program. The data obtained by Sheerwood [26] were used as values for $f_c$, the other properties were obtained based on the Model Code [23] recommendations, such as tensile strength of concrete, $(f_{ct})$, elasticity modulus of concrete $(E_c)$, and concrete Poisson coefficient $(\nu)$. Based on these values, calibrations were performed for each parameter and the ideal calibrated model was chosen.

The evaluation included 4 to 5 energy ranges from fracture to traction. The initial value was adopted as recommended by the CEB/FIP Model Code [34] with a maximum reduction of 40% for L-Series beams and up to 30% for S-Series beams.

Based on the parametric analysis performed, for the models studied, the increase in fracture energy proportionally reduced the load capacity of the analyzed beams, presenting reductions of 30-40% of the fracture energy in traction to better approach the experimental result. According to the CEB/FIP Model Code [34], the fracture energy can be estimated from Equation 1, which depends on the fracture energy base value, as shown in Table 4.

$$G_f = G_{F0} \left(\frac{f_c}{10}\right)^{0.7} \tag{1}$$

**Table 3.** Parametrization of concrete and steel at beams type S- and L-Series. Where: Exp.[1] refers to Exponential Tensile Softening.

| Specimen | S-10 | S-20 | S-40 | S-50 | L-10 | L-20 | L-40 | L-50 |
|---|---|---|---|---|---|---|---|---|
| $d_{ag}$ [mm] | 9.5 | 19 | 38 | 51 | 9.5 | 19 | 38 | 51 |
| $f_c$ [N/mm$^2$] | 41.9 | 38.1 | 29.1 | 43.5 | 38.4 | 31.4 | 28.1 | 40.1 |
| $f_{ct}$ [N/mm$^2$] | 2.5 | 2.4 | 2.1 | 2.3 | 2.35 | 1.96 | 1.94 | 2.20 |
| $E_c$ [N/mm$^2$] | 27,215 | 25,450 | 25,717 | 27,482 | 25,000 | 23,000 | 23,674 | 25,000 |
| í Poisson | 0.15 | 0.20 | 0.15 | 0.20 | 0.15 | 0.15 | 0.20 | 0.15 |
| $G_f$ [N mm/mm$^2$] | 0.049 | 0.065 | 0.090 | 0.078 | 0.040 | 0.045 | 0.069 | 0.072 |
| $G_c$ [N mm/mm$^2$] | 3.0 | 3.0 | 8.0 | 10.0 | 6.0 | 1.8 | 2.0 | 5.0 |
| Smeared Crack Model | Fixed | | | | Fixed | | | |
| Tensile Softening | Exp.[1] | Hordijk | Exp.[1] | Exp.[1] | Hordijk | | | |
| Compression Diagram | Parabolic | | | | Parabolic | | | |
| Shear Retention Mode | Constant | | | | Constant | | | |
| â Shear Retention | 0.01 | 0.03 | 0.008 | 0.013 | 0.033 | 0.033 | 0.043 | 0.033 |

**Table 4.** Reference value of fracture energy as a function of aggregate size by CEB/FIP Model Code [34].

| $d_{max}$ [mm] | $G_{F0}$ [N/mm] |
|---|---|
| 8 | 0.025 |
| 16 | 0.030 |
| 32 | 0.058 |

The results were compared not only based on the load-displacement behavior but also regarding cracking and longitudinal reinforcement strain. These results confirm the reliability of the proposed numerical models and enable indirect observation of the shear behavior.

# 4 RESULTS AND DISCUSSION

## 4.1. Load and displacement

Figure 4 shows the variation of load with displacement for the S-Series numerical models for concrete with aggregates size ranging from 9.5 mm to 51 mm, comparing them with the reference models used by Sherwood [26].

The 9.5 mm and 19 mm models showed greater rigidity behavior at the beginning of the curve, especially in the initial linear behavior of the parameterized concrete. When the specimens began to crack, they lost their rigidity and developed a similar behavior as that of three experimental reference models, obtaining an ultimate load close to the experimental value.

This rigid behavior is even more apparent in the numerical models for specimens with 38 mm and 51 mm aggregates. However, a trend like the experimental curve was observed throughout the development of the analysis.
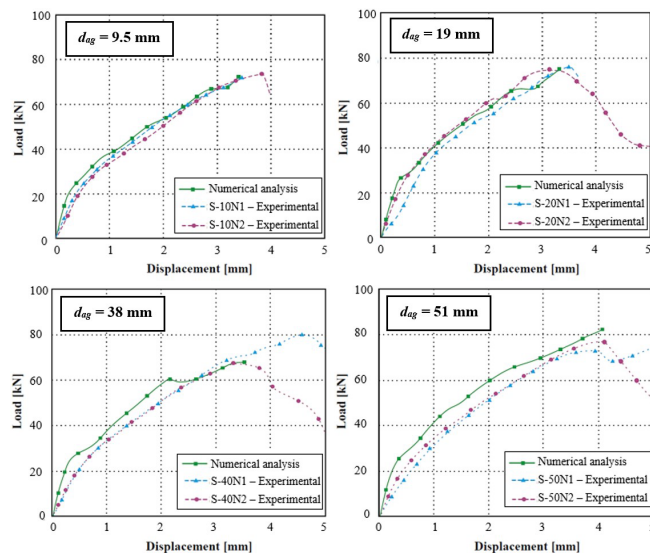


**Figure 4.** Load versus displacement curves for S-Series beams.

A varying load level, with a sequential increase in displacement, may lead to shear failure and the samples may become brittle like the experimental behaviors reported by Sherwood [26].

For the four numerical analyses conducted in the L-Series, the equivalence conditions between the numerical and experimental models showed similar characteristics, as shown in Figure 5. The choice of elasticity module at the beginning of loading did not show discrepancies.
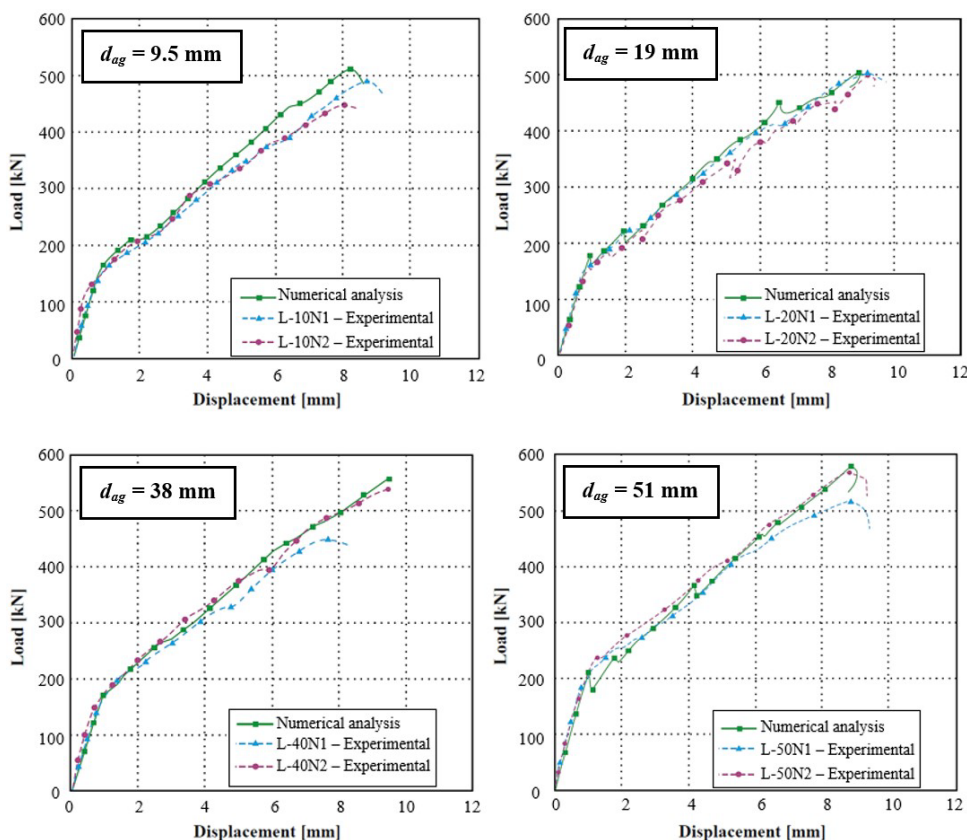


**Figure 5.** Load versus displacement curves for L-Series beams.

The variation between the behaviors of beams with different aggregate diameters can be understood by using the results for beams with 9.5 mm and 51 mm aggregates, which represent the two extreme aggregate sizes used in the analysis. Their concrete strengths show a difference of less than 2.0 MPa for experimental strength of concrete.

In the S-Series models, the ultimate load, ultimate displacement level, and ductility remained almost constant. The strength gain was more apparent for the L-Series, in the ultimate loads of both S and L-Series, with a difference of approximately 100 kN between the average values. The L-Series models exhibited similar stiffness and showed no major variations at the rupture.

## 4.2. Strains at the flexural reinforcement

The behavior of the longitudinal reinforcement of the model, referring to the axial deformations observed under the equilibrium torque of beams subjected to bending moment, can be observed for the analyzed beams, as shown in Figures 6 and 7. The values were compared with those obtained by strain gauges fixed to the reinforcements in the center of the span of the evaluated beams.

Rev. IBRACON Estrut. Mater., vol. 16, no. 4, e16406, 2023

7/17
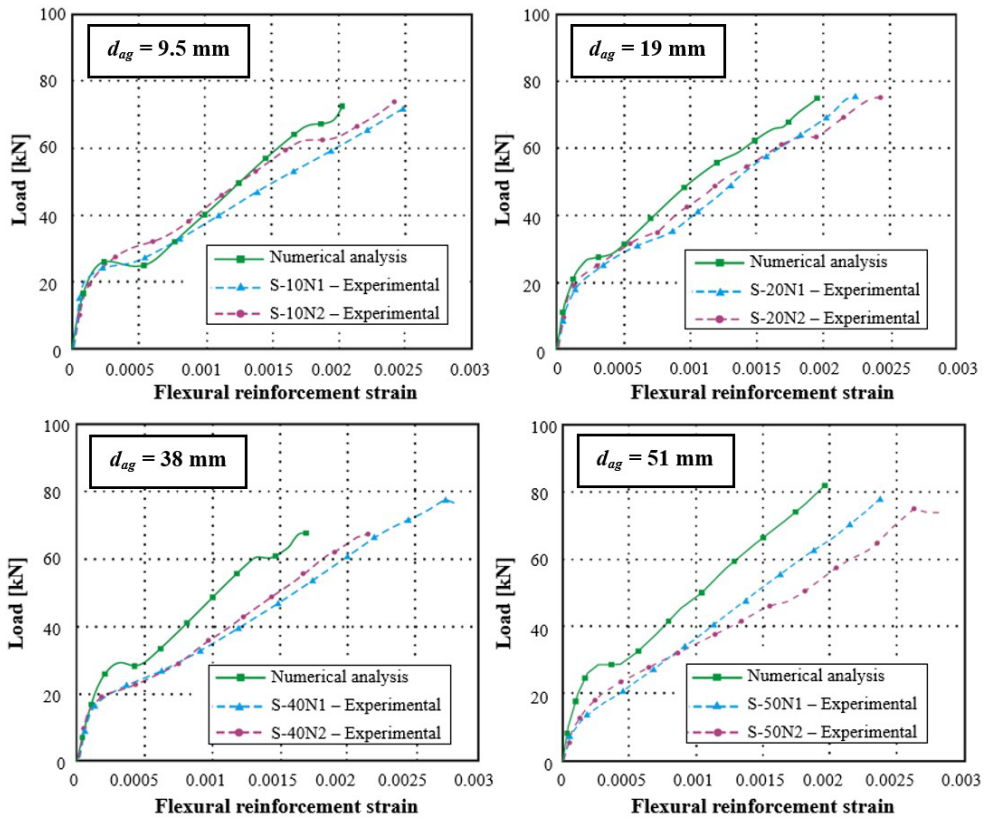
**Figure 6.** Load versus flexural reinforcement strain curves for S-Series beams.
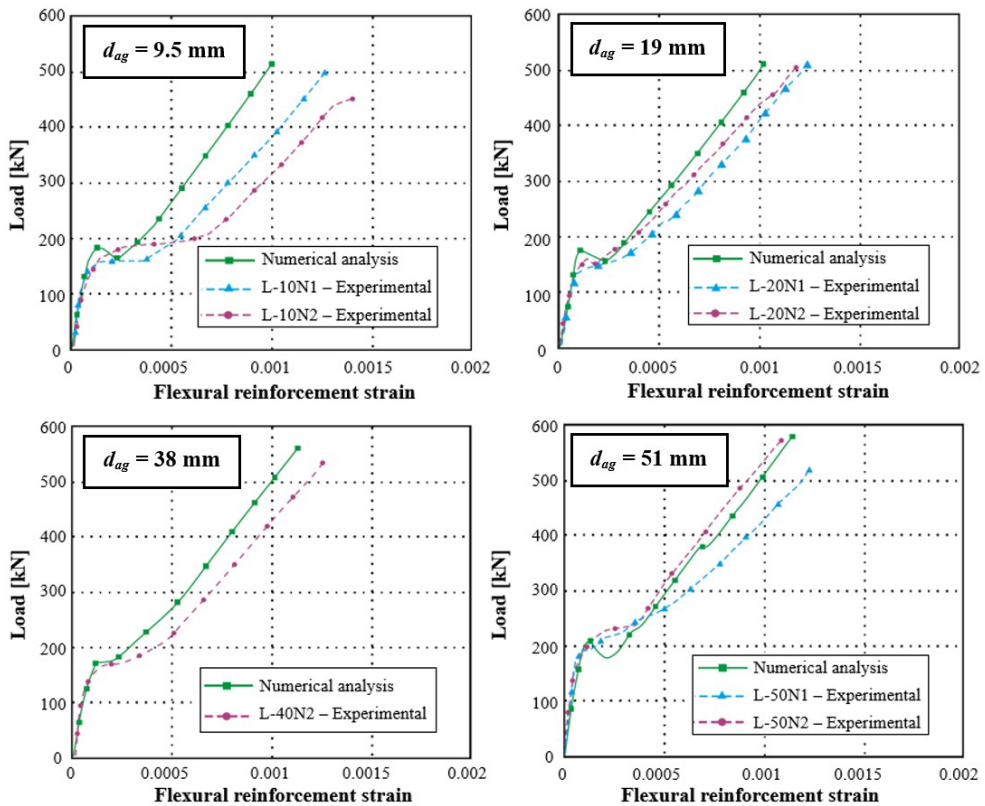


**Figure 7.** Load versus flexural reinforcement strain curves for L-Series beams.

Rev. IBRACON Estrut. Mater., vol. 16, no. 4, e16406, 2023

8/17

The numerical and experimental comparison of the reinforcements sought to understand the deformations verified by the structural response of the model, while ensuring that no equivalence between the curves (Figures 6 and 7) by any resistant phenomena, such as bending failures, and that the ultimate shear load that occurred in the experimental tests was preserved. Based on the results, it can be noted that despite the numerical models tending to behave more rigidly than the respective experimental values, good approximations were numerically registered, indicating an effective modeling of the deformation and rupture conditions of the experimental reference model.

## 4.3. Cracking patterns

Figures 8 and 9 show cracking occurring in the S and L-Series beams, respectively, with their critical crack loads marked. Based on the figures below, the influence of the diameter of the aggregate can be understood by comparing the samples sized from 9.5 mm to 51 mm. The inclination of the slope gradually reduced as the nominal size of the aggregate increased for the S-Series, representing only minor changes in the L-Series cracks.
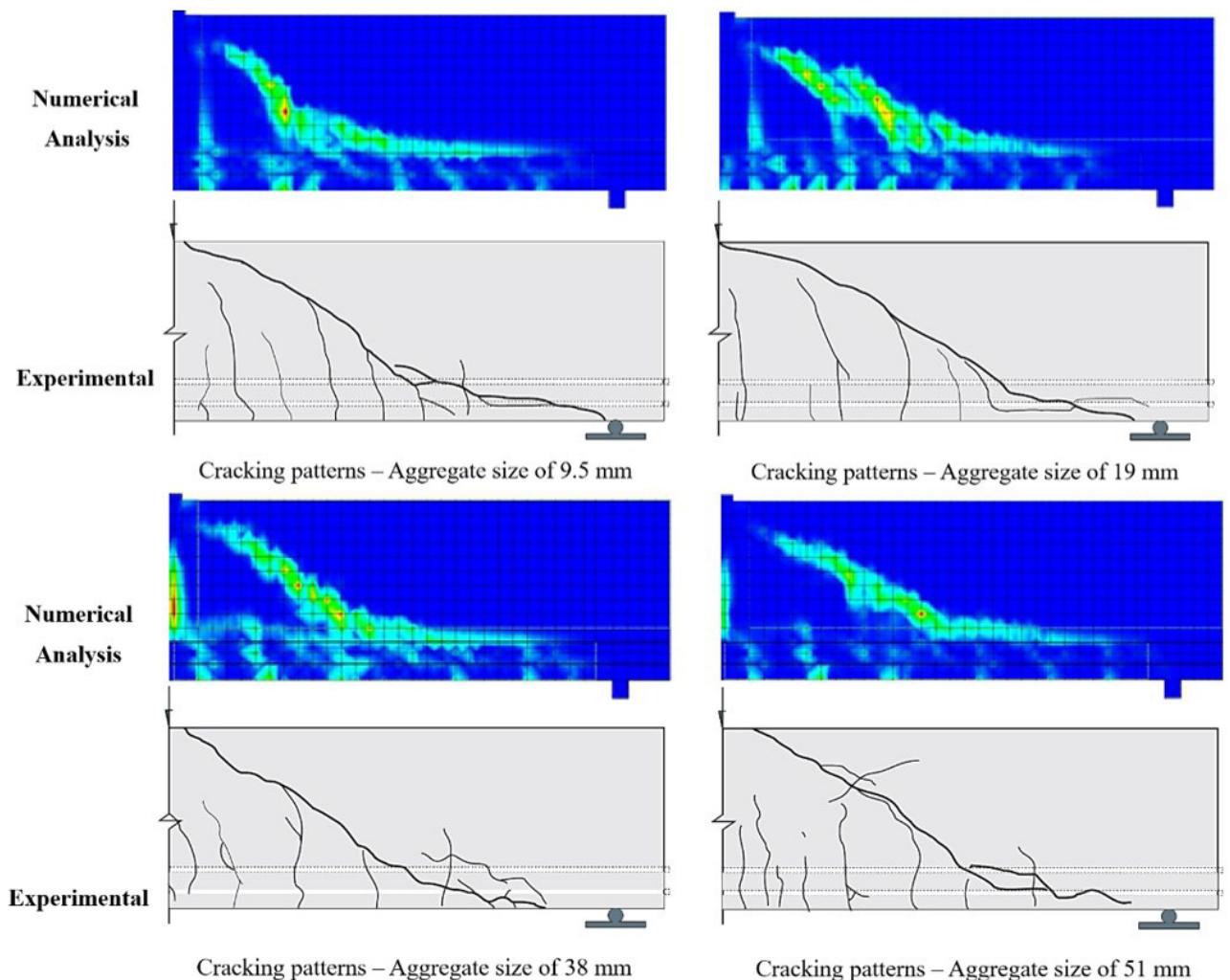


**Figure 8.** Numerical and experimental comparison for S-Series beams.

Rev. IBRACON Estrut. Mater., vol. 16, no. 4, e16406, 2023

9/17
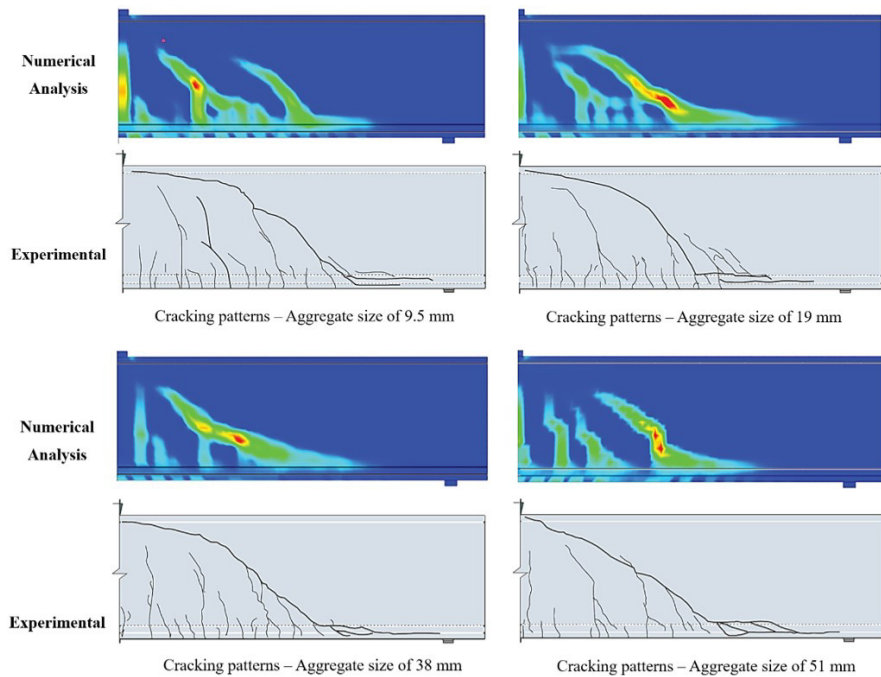
**Figure 9.** Numerical and experimental comparison for L-Series beams.

## 4.4. Internal shear strength mechanisms of RC beams without stirrups

The behaviors and derivations of the shear strength plots based on the internal concrete mechanisms in the immediate moments preceding the rupture were obtained from two distinct surveys. The first survey involved identifying a compressed strip of concrete just above the critical crack, and the second involved obtaining the shear force acting on the longitudinal reinforcement, identified as the dowel force. Figure 10 shows the horizontal compression stresses occurring in the beam with 9.5 mm aggregates for the S and L-Series beams, alongside the shear profile distributed in the area above the crack in two reference sections, A and B.
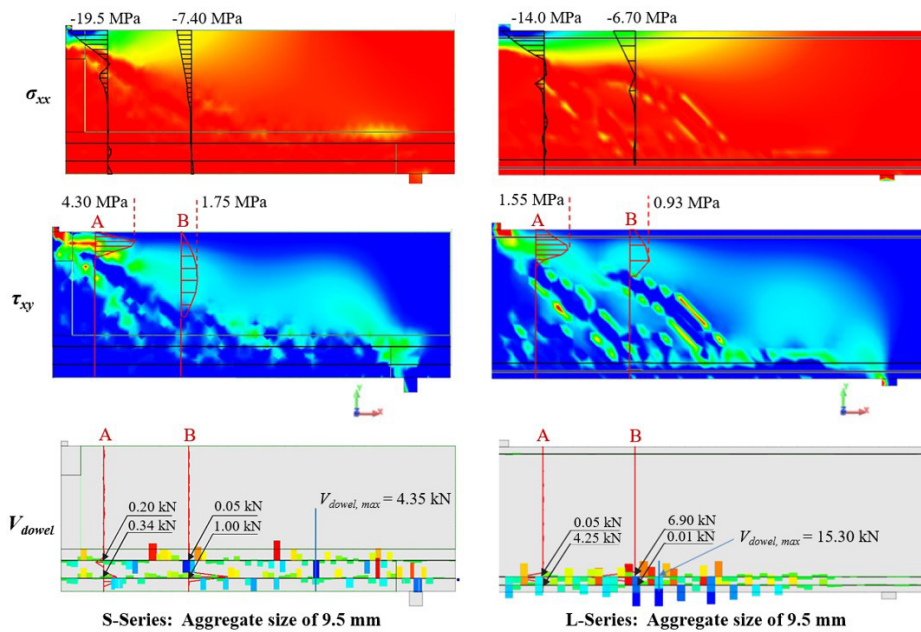


**Figure 10.** Compression and shear stresses and dowel effect for beams with 9.5 mm size aggregates.

Rev. IBRACON Estrut. Mater., vol. 16, no. 4, e16406, 2023

10/17

Section A is in the vicinity of the load, close to the top of the critical shear crack, and section B is at a distance $d$ from the center of the span of the beam, adopted as the authors' choice. In these studies, the chosen reference lines become relevant due to easily discriminating the influence of each of the plots at different distances from the supports, avoiding inconsistent readings on the real influence of each mechanism on the total shear force.

In the numerical analysis procedure, the steps for obtaining the shear plots were performed using the following criteria. Firstly, the intact and non-cracked regions of the compression zone above the critical crack are identified with a compression stress diagram in the horizontal direction of the stress map $\sigma_{xx}$. The end of the compressed zone is delimited using the correct coordinates of the point where the compressive stresses begin to be replaced by the tensile stresses. This premise is important since active shear stresses where the crack has occurred can also be observed from the shear distributions transferred by the beam body in the distributed crack mode. Thus, when the compression zone is properly delimited, the numerical procedure guarantees better precision and efficiency in the derivation of the shear strength plots.

Based on the distribution of shear stresses $\tau_{xy}$ obtained in sections A and B of the S and L-Series, one can conclude that the closer to the peak of the critical crack the stress is measured, the smaller is the compression zone, adding to the intensity of the shear stresses transmitted above the crack. Unlike the S-series, the larger scale beams of the L-series showed a lower shear stress intensity transferred through the compression zone, even with external loading intensities considerably higher than that of the S-Series. At points near the center of the span, the crushing stresses are also more concentrated, reaching almost 50% of the maximum concrete compressive strength ($f_c$). For section B, the maximum stresses are less intense, which is distributed over a larger compressed area above the crack.

Based on the analysis of Table 5, the shear force transferred by each of the complementary concrete mechanisms was quantified for the reference sections of the S- and L-series beams. In this study, the procedure consists of identifying the shear portion transferred by the compression zone $V_{cz}$ and the dowel action $V_{dowel}$ of the analyzed beams, and then subtracting the terms following the relation $\overline{V_{agg}} = V_{exp} - \overline{V_{cz}} - V_{dowel}$, where $V_{exp}$ is the experimental shear force, calculating the mean contribution to the total shear force by aggregate interlock mechanism in the reference sections A and B.

Comparing the values obtained for each strength phenomenon, $V_{agg}$ increased gradually as the maximum diameter of the aggregate in the mixture increased, as shown in the last column of Table 5, starting with $\%V_{agg}$. This behavior was also discussed by Queiroz [35] and MacGregor and Wight [36], in which they concluded that the shear force by aggregate interlock increases as the coarse aggregate increases its diameter, consequently, the rugosity of the crack surfaces also increases. In this way, a greater shear stress is transferred across the cracks.

**Table 5.** Plots of shear force obtained by numerical analysis of each of the internal mechanisms of resistant concrete.

| Specimen | $V_{exp}$ [kN] | Section | $V_{cz}$ [kN] | $\%V_{cz}$ [%] | $\overline{V_{cz}}$ [kN] | $V_{dowel}$ [kN] | $V_{agg}$ [kN] | $\%V_{agg}$ [%] | $\%\overline{V_{agg}}$ [%] |
|---|---|---|---|---|---|---|---|---|---|
| S-10 | 36.1 | A | 17.6 | 48.7 | 63.8 | 0.55 | 17.95 | 49.7 | 33.8 |
| | | B | 28.5 | 78.9 | | 1.05 | 6.55 | 18.0 | |
| S-20 | 37.4 | A | 16.7 | 44.6 | 50.3 | 1.15 | 19.55 | 52.0 | 41.3 |
| | | B | 21.0 | 56.1 | | 4.85 | 11.50 | 30.7 | |
| S-40 | 34.0 | A | 16.1 | 47.3 | 59.1 | 1.25 | 16.65 | 49.0 | 38.3 |
| | | B | 24.1 | 70.9 | | 0.50 | 9.40 | 27.6 | |
| S-50 | 41.2 | A | 13.4 | 32.5 | 52.3 | 1.05 | 26.75 | 65.0 | 45.5 |
| | | B | 29.7 | 72.1 | | 0.75 | 10.75 | 26.1 | |
| L-10 | 259.6 | A | 102.0 | 39.3 | 37.5 | 4.30 | 153.30 | 59.0 | 60.5 |
| | | B | 92.7 | 35.7 | | 6.90 | 160.00 | 62.0 | |
| L-20 | 254.4 | A | 106.9 | 42.2 | 44.1 | 2.00 | 145.50 | 57.0 | 54.4 |
| | | B | 117.5 | 46.2 | | 5.42 | 131.50 | 52.0 | |
| L-40 | 280.4 | A | 94.3 | 33.6 | 45.1 | 4.30 | 181.80 | 65.0 | 53.6 |
| | | B | 159.0 | 56.7 | | 2.75 | 118.60 | 42.3 | |
| L-50 | 288.6 | A | 81.9 | 28.4 | 24.1 | 8.11 | 198.60 | 68.8 | 73.1 |
| | | B | 57.1 | 19.8 | | 7.90 | 223.60 | 77.5 | |

The results of the S-series indicated that the aggregate interlock mechanism contributed to 34-46% of the shear force capacity. The predominant mechanism of shear capacity for this series was $V_{cz}$. The effect of the aggregate interlock mechanism is inversely proportional to the portion of the compression zone, which gradually decreases with

Rev. IBRACON Estrut. Mater., vol. 16, no. 4, e16406, 2023

11/17

an increase in the aggregate size. For the L-series, this mechanism is dominated by more than half of the total shear strength force (54-73%).

Observing the stress map $\sigma_{xx}$ of the compression zone, the rupture was unrelated to the crushing of the compression zone in all the models presented since stress levels were below the strength limit of concrete in each d sample.

These results confirm the conclusions proposed by Walraven and Reinhardt [37], who found that, in addition to concrete strength, the interlocking of aggregates plays an important role in the shear strength of beams. Comparing the 9.5 mm and 38 mm aggregate models, when using concrete with a lower strength, the use of aggregates with larger diameters could guarantee similar breaking loads.

During the experiments for understanding the influence of dowel action, difficulties were found in predicting the influence of the position of the bars on shear force. In distributed crack models, the deformation caused by dowel action is distributed over the width of the finite elements, not defining a perfect cut line on the bar. Therefore, shear force peaks of different intensities occur in numerous positions along the longitudinal beam. Table 6 shows the maximum shear force obtained in other sections of the analyzed beams.

**Table 6.** Maximum shear forces obtained by the dowel action on the results of numerical analysis.

| Specimen | $V_{exp}$ [kN] | $V_{dowel,max}$ [kN] | %$V_{dowel,max}$ [%] |
|---|---|---|---|
| S-10 | 36.1 | 4.35 | 12.0 |
| S-20 | 37.4 | 5.50 | 14.7 |
| S-40 | 34.0 | 4.70 | 13.8 |
| S-50 | 41.2 | 7.45 | 21.9 |
| L-10 | 259.6 | 15.30 | 5.9 |
| L-20 | 254.4 | 12.20 | 4.8 |
| L-40 | 280.4 | 11.70 | 4.2 |
| L-50 | 288.6 | 12.90 | 4.5 |

According to the results presented, the largest numerically evaluated beams, such as those represented by the L-series, did not benefit greatly from the strength mechanism of the dowel action, whose maximum contribution to the total shear strength was only 5%.

## 5 COMPARISON BETWEEN EXPERIMENTAL AND PREDICTED SHEAR STRENGTH FORCE

Understanding the methodologies used in the technical standards for predicting the shear strength mechanisms of concrete is a crucial part of studying shear in reinforced concrete beams. According to the Model Code [23], CSA-A.23.3 [24], NBR 6118 [38], and ACI 318 [39], the transverse reinforcements are usually dimensioned to resist all excess shear that the internal strength mechanisms of the concrete are unable to supply, as expressed in Equation 2.

$$V_s = V_u - V_c \qquad (2)$$

where $V_u$ = total strength shear force ($V_u = V_{exp}$); $V_s$ = shear strength force by transverse reinforcement; $V_c$ = shear strength force through internal concrete mechanisms.

If $V_c$ is overestimated, that is, $V_c$ values obtained by numerical analysis is higher than the actual values in their respective experimental models, beams may lack relevant transversal reinforcements, passing excessive responsibility to concrete to resist shear.

To guarantee an analysis that fits the beam condition, the formulations contained in the design codes that estimate the shear strength of beams (as detailed in Appendix A) can be applied and verified. The numerical tests and analyses performed in reference by design standards used an $L/h$ (beam length/height) ratio of 4.9 for the S-Series and of 5.3 for the L-Series.

The methods and limits applied in design standards are given below.

- CSA-A.23.3 [24]: calculation for beam elements with $L/h \geq 2.0$.
- NBR 6118 [38]: calculation for isostatic beam elements with $L/h \geq 2.0$ and for continuous elements with $L/h \geq 3.0$.
- ACI 318 [39]: calculation for beam elements with $L/h \geq 4.0$.

Rev. IBRACON Estrut. Mater., vol. 16, no. 4, e16406, 2023

12/17

Table 7 shows the shear strength predictions for the eight beam models tested by Sherwood [26] using the complementary concrete mechanisms recommended by the studied standards. The safety coefficients specified in each standard were not considered in the analysis.

Based on the results presented in Table 7, it can be observed that all design standards presented favorable safety estimates for the S-series beams, except the Brazilian standard, which presented unfavorable results for the design. During the verification of the L-Series beams, the standards failed to predict the rupture load. The ACI 318 [39] standard presented more conservative results.

**Table 7.** Comparison of analytical shear strength force with experimental results.

| Specimen | $V_{exp}$ [kN] | $V_{NBR}$ [kN] | $V_{MC}$ [kN] | $V_{CSA}$ [kN] | $V_{ACI}$ [kN] | $V_{exp}/V_{NBR}$ | $V_{exp}/V_{MC}$ | $V_{exp}/V_{CSA}$ | $V_{exp}/V_{ACI}$ |
|---|---|---|---|---|---|---|---|---|---|
| S-10N1 | 36.6 | 51.9 | 29.5 | 26.0 | 28.8 | 0.70 | 1.24 | 1.41 | 1.27 |
| S-10N2 | 38.3 | 51.9 | 28.7 | 25.3 | 28.8 | 0.74 | 1.34 | 1.52 | 1.33 |
| S-20N1 | 39.1 | 49.7 | 29.3 | 26.0 | 27.8 | 0.79 | 1.33 | 1.50 | 1.41 |
| S-20N2 | 38.2 | 48.7 | 29.4 | 26.1 | 27.4 | 0.78 | 1.30 | 1.47 | 1.39 |
| S-40N1 | 41.8 | 40.7 | 24.9 | 22.2 | 24.0 | 1.03 | 1.68 | 1.88 | 1.74 |
| S-40N2 | 34.9 | 40.7 | 28.1 | 25.1 | 24.0 | 0.86 | 1.24 | 1.39 | 1.46 |
| S-50N1 | 38.5 | 53.2 | 32.2 | 28.7 | 29.3 | 0.72 | 1.19 | 1.34 | 1.31 |
| S-50N2 | 40.6 | 53.2 | 31.1 | 27.7 | 29.3 | 0.76 | 1.30 | 1.46 | 1.39 |
| L-10N1 | 265.0 | 602.3 | 243.6 | 208.3 | 191.7 | 0.44 | 1.09 | 1.27 | 1.38 |
| L-10N2 | 242.0 | 623.1 | 262.0 | 224.1 | 196.6 | 0.39 | 0.92 | 1.08 | 1.23 |
| L-20N1 | 265.0 | 526.7 | 265.2 | 229.6 | 173.4 | 0.50 | 1.00 | 1.15 | 1.53 |
| L-20N2 | 266.0 | 546.7 | 272.3 | 235.8 | 178.3 | 0.49 | 0.98 | 1.13 | 1.49 |
| L-40N1 | 242.0 | 489.1 | 288.8 | 252.8 | 164.0 | 0.49 | 0.84 | 0.96 | 1.48 |
| L-40N2 | 288.0 | 493.8 | 264.6 | 231.6 | 165.2 | 0.58 | 1.09 | 1.24 | 1.74 |
| L-50N1 | 272.0 | 629.2 | 327.9 | 287.0 | 198.1 | 0.43 | 0.83 | 0.95 | 1.37 |
| L-50N2 | 298.0 | 620.0 | 307.8 | 269.4 | 195.9 | 0.48 | 0.97 | 1.11 | 1.52 |
| *Average* | | | | | | **0.64** | **1.15** | **1.30** | **1.44** |
| *CV (%)* | | | | | | **29.0** | **19.6** | **18.6** | **10.1** |

Assessing the accuracy of the studied standards in predicting the experimental shear force $V_{exp}$, Model Code [23] and CSA A.23.3 [24] proved the most capable in predicting rupture by the internal mechanisms of concrete. Model Code [23] presented the smallest variations, with a mean safety factor of 1.15 and a 19.6% variation coefficient.

For Model Code [23] and CSA A.23.3 [24], the importance of the influence of the aggregate diameter for the prediction of rupture by shear force can be inferred since they are based on MCFT.

Although NBR 6118 [38] showed fewer conservative results in the prediction of rupture for L-series beams, effective safety estimates were obtained for the S-series beams – those with a size range commonly used in most buildings – provided that all the recommended procedures and safety coefficients are applied.

## 6 CONCLUSIONS

Eight experimental RC beams without stirrups, separated into two series of different sizes, aggregate diameters, and compressive strength of the concrete, were studied by nonlinear numerical analysis using the DIANA software to understand the influences and contributions of the internal mechanisms of concrete on shear strength. The experimental results were compared with the estimates predicted by standards such as the Model Code [23], CSA-A.23.3 [24], NBR 6118 [38], and ACI 318 [39], to understand the ability of these codes in predicting the shear strength of beams by internal concrete mechanisms.

The nonlinear calculation method chosen in this study provided a satisfactory representation of the shearing behavior of the experimental models, showing good numerical-experimental approximations between the cracks pattern, ultimate load, strain in the longitudinal reinforcement, and the development of the deflection observed on the beam. It was concluded that the aggregate interlock phenomenon could be seen as the main form of failure for all the evaluated beams. This is due to the range of longitudinal stresses measured in the compression zone being unable to recognize the phenomenon of concrete crushing at the failure. Moreover, studying the rupture via the dowel effect of the reinforcement, which presented shear forces lower than a possible rupture, was impossible.

The outcomes suggest that, for a good approximation between the models studied, the $G_f$ values, initially adopted according to CEB/FIP Model Code [34], must range from 100% to 70% of the total value for the S-Series beams and from 100% to 60% of the total value for L-Series. Thus, the S10 model was 70%, the S20 model 85%, and the S40 model 73%.

For both S and L-Series, the percentages of influence of the aggregate interlock mechanism gradually increased as the diameter of the coarse aggregate of the mixture increased. Comparing the 9.5 mm and 51 mm extremes with the same characteristic strengths, an increase in the capacity of the model is evidenced. The strength force increased approximately by 10 kN in the S-Series samples and by 100 kN in the L-Series samples.

Based on the normative estimates, it is concluded that in the methodologies that incorporate the influence of the aggregate diameter on the shear strength in their design equations produced better predictions on the behavior of concrete without shear reinforcement, with less than 20% of variation from the comparative numerical-experimental model.

The results of the numerical tests, as well as in the experimental test carried out by Sheerwood [26], aimed to obtain a type of brittle failure in the beams that occurs by the formation of a typical critical crack. In the numerical model, some characteristics were verified to define this type of failure, such as: longitudinal reinforcement did not present high stress or close to the yield stress (eliminating the hypothesis of failure by bending); the compressed zone presented stresses, in any direction, always at levels significantly lower than the concrete strength; and the pattern of crack formation showed a typical typology of critical shear cracking.

Note that, the rupture moment was also assumed in the experimental tests by Sherwood [26] and showed correspondence with the numerical models, resulting in even more certainty about the model's rupture moment.

# 7 REFERENCES

[1]  W. Ritter and H. Die Bauweise, "Construction techniques of hennebique," *Schweiz. Bauzeitung Zurich*, vol. 33, no. 7, pp. 59–61, 1899.

[2]  E. Mörsch, *Der Eisenbetonbau, seine Theorie und Anwendung*, 1st ed. Stuttgart: Konrad Wittwer, 1908.

[3]  ASCE-ACI Committee 445, "Recent approaches to shear design of structural concrete," *J. Struct. Eng.*, vol. 124, no. 5, pp. 1375–1417, 1998.

[4]  S. Campana, M. Fernández Ruiz, A. Anastasi, and A. Muttoni, "Analysis of shear transfer actions on one-way RC members based on measured cracking pattern and failure kinematics," *Mag. Concr. Res.*, vol. 35, no. 6, pp. 386–404, 2013, http://dx.doi.org/10.1680/macr.12.00142.

[5]  S. D. Poli, P. G. Gambarova, and C. Karakoç, "Aggregate interlock role in R.C. Thin-webbed beams in shear," *J. Struct. Eng.*, vol. 113, no. 1, pp. 1–19, 1987.

[6]  M. Fernández Ruiz, A. Muttoni, and J. Segaseta, "Shear strength of concrete members without transverse reinforcement: a mechanical approach to consistently account for size and strain effects," *Eng. Struct.*, vol. 99, pp. 360–372, 2015.

[7]  T. Paulay and P. J. Loaber, *Shear Transfer by Aggregate Interlock* (Special Publication SP-42: Shear in Reinforced Concrete 1). Detroit: Am. Concr. Inst., pp. 1–16, 1990.

[8]  H. J. P. Taylor, *Investigation of the Forces Carried Across Cracks in Reinforced Concrete Beams in Shear by Interlock of Aggregate* (Technical Reports). London: Cement and Concrete Association, 1970, pp. 42–77.

[9]  J. C. Walraven, "Fundamental analysis of aggregate interlock," *J. Struct. Div.*, vol. 107, no. 11, pp. 2245–2270, 1981.

[10] P. D. Zararis, "Aggregate interlock and steel shear forces in the analysis of RC membrane elements," *ACI Struct. J.*, vol. 94, no. 2, pp. 159–170, 1997.

[11] P. S. Chana, "Investigation of the mechanism of shear failure of reinforced concrete beams," *Mag. Concr. Res.*, vol. 39, no. 141, pp. 196–204, Dec 1987.

[12] I. Jelic, M. N. Pavlovic, and M. D. Kostovos, "A study of dowel action in reinforced concrete beams," *Mag. Concr. Res.*, vol. 39, no. 141, pp. 196–204, 1999, http://dx.doi.org/10.1680/macr.1987.39.141.196.

[13] E. O. L. Lantsoght, C. van der Veen, J. C. Walraven, and A. De Boer, "Case study on aggregate interlock capacity for the shear assessment of cracked reinforced-concrete bridge cross sections," *J. Bridge Eng.*, vol. 21, no. 5, pp. 2016, 2016.

[14] T. Paulay, R. Park, and M. H. Philips, *Horizontal Construction Joints in Cast-in-Place Reinforced Concrete* (Special Publication SP-42: Shear in Reinforced Concrete 2). Detroit: Am. Concr. Inst., pp. 599–616, 1974.

[15] H. J. P. Taylor, *Investigation of the Dowel Shear Forces Carried by the Tensile Steel in RC Beams* (Technical Report TRA). London: Cement and Concrete Association, 1969.

[16] A. K. Tureyen and R. J. Frosch, "Concrete shear strength: another perspective," *ACI Struct. J.*, vol. 100, no. 5, pp. 609–615, 2003.

[17] Z. P. Bazant and T. Kazemi, "Size effect on diagonal shear failure of beams without stirrups," *J. Am. Concr. Inst.*, vol. 89, no. 3, pp. 268–276, 1991.

[18] G. N. J. Kani, "Basic facts concerning shear failure," *J. Am. Concr. Inst.*, vol. 63, no. 6, pp. 128–147, 1966.

[19] H. P. J. Taylor, *The Fundamental Behavior of Reinforced Concrete Beams in Bending And Shear* (Special Publication 42). Detroit: Am. Concr. Inst., pp. 43–77, 1974.

[20] F. J. Vecchio and M. P. Collins, "The modified compression-field theory for reinforced concrete elements subjected to shear," *ACI Struct. J.*, vol. 83, no. 2, pp. 219–231, 1986.

[21] E. C. Bentz, F. J. Vecchio, and M. P. Collins, "Simplified modified compression field theory for calculating shear strength of reinforced concrete elements," *ACI Struct. J.*, vol. 103, no. 4, pp. 614–624, 2006.

[22] A. Muttoni and M. Fernández Ruiz, "Shear capacity of members without transverse reinforcement as function of critical shear crack width," *ACI Struct. J.*, vol. 105, no. 2, pp. 163–172, 2008.

[23] Comité Euro-International du Béton, *Fib Model Code Design Code 2010: Final Draft* (Bulletin d'Information). Lousanne: CEB, 2010.

[24] Canadian Standard Association, *Design of Concrete Structures for Buildings*, CSA-A23.3-14, 2014.

[25] J. C. Walraven, *Aggregate Interlock: A Theoretical and Experimental Analysis*. Delft: Delft Univ. Press, 1980.

[26] E. G. Sherwood, "One-way shear behaviour of large, lightly-reinforced concrete beams and slabs," Ph.D. dissertation, Univ. Toronto, Toronto, 2008.

[27] D. Daluga, K. McCain, M. Murray, and S. Pujol, "Effect of geometric scaling on shear strength of reinforced concrete beams without stirrups," *ACI Struct. J.*, vol. 115, pp. 5–14, 2018.

[28] K. H. Yang and A. F. Ashour, "Aggregate interlock in lightweight concrete continuous deep beams," *Eng Struct. J.*, vol. 33, no. 1, pp. 136–145, 2011.

[29] A. Belbachir, S.-Y. Alam, M. Matallah, and A. Loukili, "Size effect on the contribution of the aggregate interlock mechanism in reinforced concrete beams without shear reinforcement," *Eur. J. Environ. Civ. Eng.*, vol. 24, no. 9, pp. 1363–1380, 2020.

[30] P. H. Feenstra, R. Borst, and J. G. Rots, "Numerical study on crack dilatancy I: models and stability analysis," *J. Eng. Mech.*, vol. 117, no. 4, pp. 733–753, 1991.

[31] F. J. Vecchio and W. Shim, "Experimental and analytical reexamination of classic concrete beam tests," *J. Struct. Eng.*, vol. 130, no. 3, pp. 460–469, 2004.

[32] M. Pimentel, P. Cachim, and J. Figueiras, "Deep-beams with indirect supports: numerical modelling and experimental assessment," *Comput. Concr.*, vol. 5, no. 2, pp. 117–134, 2008.

[33] DIANA TNO, *DIANA Finite Element Analysis User's Manual Release 10.1.* Delft, The Netherlands, 2017.

[34] CEB-FIP, *Bullettin d'Information 213/214 CEB-FIP Model Code 1990*. London: Thomas Telford, 1993.

[35] F. O. Queiroz Jr., "Análise de resistência ao cisalhamento em peças de seções circulares vazadas utilizando a teoria do campo de compressão modificada," M.S. thesis, Fed. Univ. Pernambuco, Recife, 2014. [Online]. Available: https://repositorio.ufpe.br/bitstream/123456789/10797/1/DISSERTA%C3%87%C3%83O%20Francinaldo%20Junior.pdf

[36] J. G. MacGregor and J. K. Wight, *Reinforced Concrete: Mechanics and Design*, 6th ed. New Jersey: Pearson Educ. Inc., 2012, 1157 p.

[37] J. C. Walraven and H. W. Reinhardt, "Theory and experiments on the mechanical behaviour of cracks in plain and reinforced concrete subjected to shear loading," *Heron*, vol. 26, no. 1A, pp. 1–68, 1981.

[38] Associação Brasileira de Normas Técnicas, *Design of Concrete Structures – Procedures*, NBR 6118, 2014.

[39] American Concrete Institute, *Building Code Requirements for Structural Concrete and Commentary*, ACI 318R-19, 2019.

**APPENDIX A. Design Codes.**

The design shear capacity attributed to the concrete can be taken by Mode Code [23] as

$$V_{MC} = V_{Rd,c} = k_v \frac{\sqrt{f_c}}{\gamma_c} z b_w \tag{A.1}$$

where $\gamma_c$ is the concrete's safety coefficient, adopted as a unit value in this study, and $z = 0.9d$.

The $k_v$ coefficient refers to the contribution of concrete to shear strength and, for Level 3 of approximation, it can be obtained by Equation A.2.

$$k_v = \begin{cases} \frac{0.4}{(1+1500\varepsilon_x)} \cdot \frac{1300}{(1000+0.7k_{dg} z)} \leq 0.15 \rightarrow \text{If } \rho_w = 0) \\ \\ \frac{0.4}{(1+1500\varepsilon_x)} \rightarrow \text{If } \rho_w \geq \frac{0.08 \sqrt{f_c}}{f_{yk}} \end{cases} \tag{A.2}$$

where,

$$k_{dg} = \frac{48}{16+d_g} \geq 1.15 \tag{A.3}$$

where $d_g$ is the aggregate diameter.

The parameter $\varepsilon_x$ represents the longitudinal strain at the mid-depth of the member and shall be taken as

$$\varepsilon_x = \frac{\frac{M_u}{z} + V_u}{2(E_s A_s)} \tag{A.4}$$

where $z$ is the distance between the compressed and the stretched chord of the truss model ($0.9d$); $\rho$w is the transverse reinforcement ratio; $M_u$ is the ultimate bending moment ($M_u = V_u l/4$); $V_u$ is the ultimate shear force; $E_s$ is the Young's modulus of the flexural reinforcement and; $A_s$ is the longitudinal reinforcement area.

The standard CSA-A.23.3 [24] presents the verification of the shear safety condition through the product between the shear retention factor $\beta$ and the root of the concrete's compressive strength ($\sqrt{f_c}$).

The capacity shear force can then be obtained by multiplying $\beta\sqrt{f_c}$ and the properties of the cross section such as width $b_w$ and effective height to shear $d_v$, lessened by parameters referring to concrete mixing conditions $\lambda$, and a strength reduction factor $\phi_c$.

$$V_{CSA} = V_c \phi_c \lambda \beta \sqrt{f_c} b_w d_v \tag{A.5}$$

where the effective shear height ($d_v$) can be taken as the highest value between $0.9d$ and $0.72h$.

The parameter $s_{ze}$ for beams without transverse reinforcement is given by Equation A.6.

$$s_{ze} = \frac{35s_z}{15+a_g} \geq 0.85s_z \tag{A.6}$$

where $a_g$ is aggregate diameter, and $s_z$ refers to the distance between the vertical stirrups of the structural element.

The strain effect factor ($\beta$) is given by Equation A.7.

$$\beta = \frac{0.4}{1+1500\varepsilon_x} \cdot \frac{1300}{1000+s_{ze}} \tag{A.7}$$

Rev. IBRACON Estrut. Mater., vol. 16, no. 4, e16406, 2023

16/17

where,

$$\varepsilon_x = \frac{\frac{M_u}{d_v} + V_u}{2\,(E_s\,A_s)} \qquad\qquad\qquad\qquad\qquad\qquad\qquad\qquad\text{(A.8)}$$

According to the standard NBR 6118 [38], the values of the shear-resistant portion by internal concrete mechanisms will vary based on the load condition to which the beams will be subjected.

Thus, considering the calculation model I of the Brazilian standard, in which the strut has an inclination of $\theta = 45°$ and adopting the beam subjected to simple bending,

$$V_{NBR} = V_c = 0.6\,f_{ctd}\,b_w d \qquad\qquad\qquad\qquad\qquad\qquad\qquad\text{(A.9)}$$

$$f_{ctd} = \frac{0.21}{\gamma_c} f_c^{2/3} \qquad\qquad\qquad\qquad\qquad\qquad\qquad\qquad\text{(A.10)}$$

where, $f_c$ is the compressive concrete strength; $b_w$ is the width of the element; $d$ is the distance from extreme compression fiber to centroid of longitudinal tensile reinforcement and $\gamma_c$ is the concrete's safety coefficient, adopted as a unit value in this work.

According to ACI 318 [39], the shear strength of non-prestressed members is a function of concrete strength, axial load acting on section, size effect, section area, effective depth, member width, and longitudinal reinforcement ratio. For beams without shear reinforcement ($A_v$), the shear strength of the concrete ($V_{ACI}$) is given by Equation A.11.

$$V_{ACI} = V_c = \left( 0.66\lambda_s\,\lambda(\rho_w)^{1/3}\sqrt{f_c} + \frac{N_u}{6A_g} \right) b_w d \qquad\qquad\qquad\text{(A.11)}$$

where $N_u$ is the axial load; $A_g$ applies to the gross cross-sectional area; $\rho_w$ is the longitudinal reinforcement ratio of the tension reinforcement ($\rho_w = A_s/b_w d$); and $\lambda$ is the factor for standard or lightweight concrete. The $N_u/6A_g$ value shall not greater than $0.05f_c$.

The size effect modification factor shall be determined by Equation A.12.

$$\lambda_s = \sqrt{\frac{2}{1 + 0.004d}} \leq 1.0 \qquad\qquad\qquad\qquad\qquad\qquad\qquad\text{(A.12)}$$

Additionally, the shear strength $V_c$ is limited to the maximum *value* $V_{c,max}$ as

$$V_{c,max} = 0.42\lambda\sqrt{f_c}\,b_w d \qquad\qquad\qquad\qquad\qquad\qquad\qquad\text{(A.13)}$$

# IBRACON Structures and Materials Journal
## Revista IBRACON de Estruturas e Materiais

ORIGINAL ARTICLE

# Design of reinforced concrete structures from three-dimensional stress fields

## Dimensionamento de estruturas de concreto armado a partir de campos de tensão tridimensionais

Reinaldo Chen[a]
Túlio Nogueira Bittencourt[a]
João Carlos Della Bella[a]

[a]Universidade de São Paulo – USP, Escola Politécnica, Departamento de Engenharia de Estruturas e Geotécnica, São Paulo, SP, Brasil

**Abstract:** The design of reinforced concrete structures starting from a linear analysis is allowed by design codes and leads to safe solutions. The structural model built for the analysis may be composed not only of bar and shell elements, but also solid elements. In the present work, the formulation of the Reinforced Solid Method (RSM) was reviewed and applied to the Ultimate Limit State design of a reinforced concrete member, with the computation of the required reinforcement and concrete check of each individual solid element within the structural model. The results were visualized in a post-processor and validated by numerical simulations. The RSM effectively allows for the design of concrete structures with general geometry and loading conditions, whilst identifying local effects throughout the volume of the structure.

**Keywords:** solid elements, reinforced concrete, design, reinforced solid method, three-dimensional elasticity.

**Resumo:** O dimensionamento de estruturas de concreto armado a partir de esforços provenientes de análise linear é permitido pelas normas e conduz a estruturas seguras. O modelo estrutural elaborado para a análise pode ser composto não somente de elementos de barra e de casca, mas também de elementos sólidos. Neste trabalho, a formulação do Método dos Sólidos Armados (MSA) foi revista e a aplicada ao dimensionamento em ELU de uma peça de concreto, com cálculo da armadura e verificação do concreto em cada um dos elementos sólidos componentes do modelo estrutural. Os resultados foram visualizados em um pós-processador e validados por simulações numéricas. O MSA permite o dimensionamento de estruturas com geometria e carregamento genéricos, identificando, ao mesmo tempo, efeitos localizados no interior do volume da estrutura.

**Palavras-chave:** elementos sólidos, concreto armado, dimensionamento, método dos elementos armados, elasticidade tridimensional.

## 1 INTRODUCTION

A concrete structure may be idealized from the composition of linear (bars), shell (membranes, plates, and shells), and solid elements. The utilization of finite solid elements may be justified when designing structural members with complex geometry and loadings, for which the application of unidimensional or bidimensional elements turns out to be insufficient to capture the load paths within the structure, such as those comprising industrial or hydraulic facilities (Figure 1). A linear analysis may be performed to determine the internal stress distribution throughout the three-dimensional structure for the ultimate limit state design, according to design codes [3]–[5]. The stress fields obtained

from the analysis consists of six stress components at each integration point of the solid elements comprising the structural model. Limiting state conditions are not directly expressed in terms of sectional forces, and the problem of dimensioning the required reinforcement and checking concrete in the presence of the applied stresses is then posed.



(a)    (b)
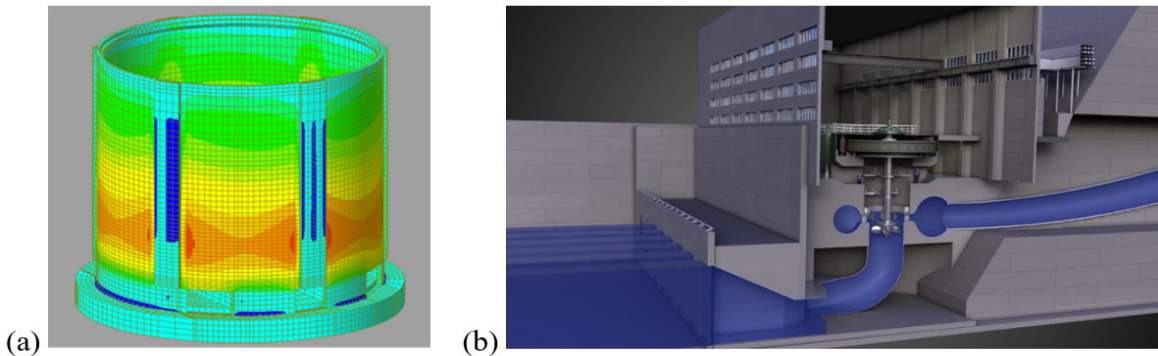
**Figure 1.** (a) Finite solid element model for a clinker storage silo of the Ramliya Cement Plant (Dianafea [1]); (b) concrete hydroelectric structure (Wikimedia Commons [2])

A solution for the design would be to provide reinforcement to resist the major principal stress in the principal directions. However, in design practice it is impossible to provide reinforcement following the randomly oriented principal tensile stresses within the structure, even more considering that a structural member is designed for multiple loading conditions. Alternatively, reinforcement could be arranged in three orthogonal directions to resist the major principal tensile stress in the three reinforcement directions. But this solution is also disregarded in design practice since uneconomical layouts would be attained, especially when crack directions draw close to any of the reinforcement directions. In another attempt, designers previously utilized the incomplete method of defining working sections and integrating the normal stress patterns over their surfaces and then calculating the reinforcement from the total sectional forces. For example, Boer [6] proposed the so-called "Theory on composing results to lower model type results" where one should proceed to the back-substitution of stresses from a solid model to reference elements: either by integration of stress components along the height of a structure to a bidimensional model at the level of a reference plane (Figure 2a), or by integration of stresses along both height and width of an elected cross-section to a unidimensional model at the level of a reference line (Figure 2b). Dolgikh and Podvysotskii [7] proposed, independently, the "Method of equivalent shells", which consisted basically in the same procedure as the one proposed by Boer, and applied it to the design of a concrete spillway (Figure 3). The method of composing results in reference elements, however, has restrict application to members with uniform geometry and loadings, so that a sectional design may effectively be performed. It cannot be applied in discontinuity regions such as joints of frames or zones of application of concentrated loads. As pointed out by Lisichkin [8], the results obtained by integration methods are "not rigorous since they did not incorporate either the tangential stresses or the effects of the resistance in the reinforcement to shearing in other directions."



(a)    (b)
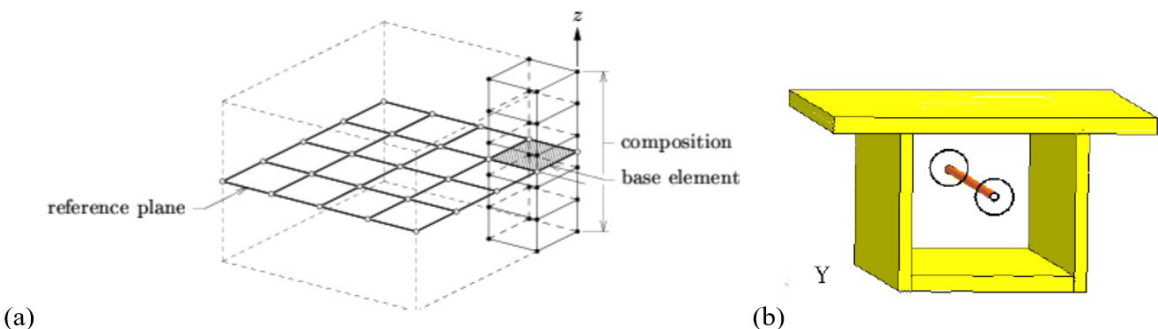
**Figure 2.** Composition of results from solid elements: (a) in a quadrangular reference plane or (b) in a reference line [6]
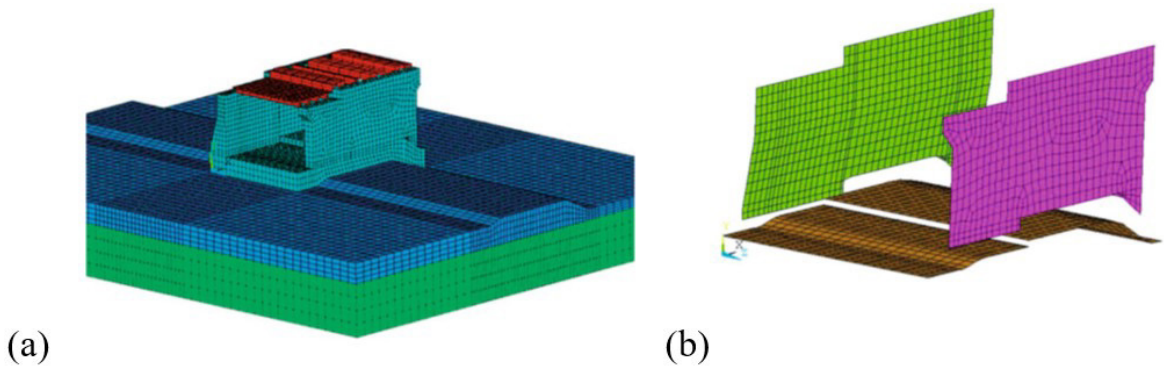
**Figure 3.** Finite element model for a concrete spillway: (a) with solid elements; (b) with equivalent shell elements (Dolgikh and Podvysotskii [7])

The solution for the Ultimate Limit State (ULS) then relied on the definition of a resistant mechanism equilibrating the applied stress tensors. Smirnov [9], addressed, for the first time, equations for the reinforcement design in concrete solid elements from three-dimensional stress tensors, focusing on the application in hydroelectric structures. Kamezawa et al. [10] proposed additional formulas for the computation of the required reinforcement, but these were still limited to stress combinations yielding reinforcement in three directions. Marti, Mojsilović and Foster published two thorough detailed works on the subject [11], [12], clearly identifying biaxial and uniaxial compression design cases, and representing graphically the solution with the aid of Mohr circles. Their formulation was later reproduced in the *fib* Bulletin [13], which was a practical guide to finite element modelling of reinforced concrete structures. In this publication, however, no new information about the subject were brought. Hoogenboom and Boer [14], [15] categorized the solution into three subgroups, namely "corner", "edge" and "interior solution", according to the requirement of reinforcement in one, two or three orthogonal directions, respectively. They also implemented this solution in a numerical algorithm searching for the solution that minimized the total required steel. Su et al. [16] presented a genetic algorithm to examine all possible solutions and to find, among then, the one that provided the optimal reinforcement. Zalesov et al. [17] and Lisichkin [8] treated the theme with a different approach, where reinforcement incorporated shearing resistance. Since the solution was not analytical, but rather based upon coefficients determined experimentally, the derived equations are not presented in this work. Finally, Nielsen and Hoang presented the complete formulation in the third edition of the book *Limit Analysis and Concrete Plasticity* [18]. Former editions, dated of 1984 and 1999, still did not address this theme. The authors brought out the physical interpretation of the applied shear stresses and elegantly deducted analytically the complete set of design formulas of the reinforced solid method (RSM).

## 2 THE REINFORCED SOLID METHOD

The reinforced solid method (RSM) for the design of reinforced concrete structures combines linear stress analysis with limit design. A plastic method is in fact applied, and the lower bound theorem is recalled twice: first in the selection of a linear elastic statically admissible stress field equilibrating the design load (at the level of the global structure), and then in the calculation of the equivalent stresses on reinforcement and concrete composing a system of resistance that is statically able to carry the applied stresses, where the yield stress is nowhere violated (at the level of each individual element comprising the structure). The design load will be a safe estimate of the ultimate load of the structural member.

### 2.1. Application of limit analysis to structural concrete

Limit analysis was formulated for rigid-plastic materials and deals with the collapse load or the load-carrying capacity of a body at the yield point. The lower-bound theorem of limit analysis states that:

*"Any load corresponding to a statically admissible state of stress (a state of stress that satisfies the equilibrium conditions and the statical boundary conditions for the actual load) everywhere at or below yield is not higher than the ultimate load."*

A state of stress obtained from a linear elastic analysis represents a statically admissible stress field since equilibrium and static boundary conditions are satisfied. Concepts of limit analysis and their application to reinforced concrete were carefully reviewed and organized by several researchers [18]–[21]. Muttoni et al. [19] detailed the lower bound theorem for the application in reinforced concrete enunciating:

*"In a plastic design a stress field is chosen such that the equilibrium conditions and the statical boundary conditions are fulfilled. The dimensions of cross-section and the reinforcement have to be proportioned such that the resistances are everywhere greater than or equal to the corresponding internal forces."*

Kaufmann and Mata-Falcón [22] refer to Nielsen, Thürlimann and his coworkers as the pioneers in applying the theory of plasticity to reinforced concrete back to the second half of the last century, stating that "they were of course fully aware of the limited ductility of concrete and even reinforcement. Therefore, they completely neglected the tensile strength of concrete and addressed further concerns regarding ductility by providing minimum reinforcement and using conservative limits of the so-called effective concrete compressive strength as well as upper limits for the reinforcement quantities and corresponding compression zone depths (to avoid brittle failures due to concrete crushing)." Since then, design methods for three-dimensional structures based on the limit analysis have been developed, including the strut-and-tie method (STM) and the stress field method (SFM), (extensively reviewed in a state-of-the-art report *fib* bulletin [23]), and the reinforced solid method (RSM) [14], [15], [9]–[12], [18].

## 2.2. Idealization of material response

Limit analysis assumes that materials behave in a rigid-plastic manner. Since the material response is not perfectly plastic, equivalent reduced plastic strengths need to be defined for the application of the RSM:

Yielding conditions for concrete. The compressive strength of concrete $f_c$ is considered with a reduced value to account for the material brittleness and effects of transversal strains. The tensile strength of concrete is neglected for equilibrium.

Yielding conditions for reinforcement. Reinforcing bars are assumed to be perfectly plastic, capable to resist only axial stresses. They are also assumed to be perfectly bonded to the concrete and distributed at such small intervals that the forces in them can be replaced by an equivalent stress distribution in the concrete. All these assumptions are allowed with basis on the lower bound theorem, once they will result in stresses in the reinforcement that are statically admissible. Kaufmann [20] contextualizes objectively the above-mentioned considerations: *Apart from the assumption of perfectly plastic reinforcement, these idealizations are quite crude. In a real structure, reinforcing bars are not infinitely thin, and considerable transverse shear may occur in reinforcement ("dowel action"). Bond stresses are limited by the bond strength, resulting in finite development lengths. The crack spacings are not infinitely small and tension stiffening effects occur. On the other hand, the analysis of a structure is simplified to a great extent by these assumptions, and their influence on the ultimate load is often negligible.*"

Yielding conditions for reinforced concrete. Until now, yielding conditions were set for each material individually and not for reinforced concrete, a heterogenous material. In the application of limit analysis methods to structural concrete, concrete and reinforcement are considered together as a continuum with resistance given by the linear combination of the resistances of the individual materials. Limit analysis may be applied to reinforced concrete if there is sufficient deformation capacity to develop the plastic stress redistribution required in the element.

## 2.3 RSM: the applied stresses

In the three-dimensional space, the stresses at a point referred to a rectangular coordinate system *x*, *y* and *z* are completely defined by the symmetrical stress tensor:

$$S = \begin{bmatrix} \sigma_x & \tau_{xy} & \tau_{xz} \\ \tau_{xy} & \sigma_y & \tau_{yz} \\ \tau_{xz} & \tau_{yz} & \sigma_z \end{bmatrix} \tag{1}$$

The positive sign convention for the six stress components is shown in Figure 4a: normal stresses $\sigma_x$, $\sigma_y$ and $\sigma_z$ are positive as tensile stresses; shear stresses $\tau_{xy}$ and $\tau_{xz}$ are positive in the coordinate directions in a section with the *x*-axis as an outwardly directed normal of the element face; shear stresses $\tau_{xy}$ and $\tau_{yz}$ are positive in the coordinate directions in a section with the *y*-axis as an outwardly directed normal of the element face; shear stresses $\tau_{xz}$ and $\tau_{yz}$ are positive in the coordinate directions in a section with the *z*-axis as an outwardly directed normal of the element face.
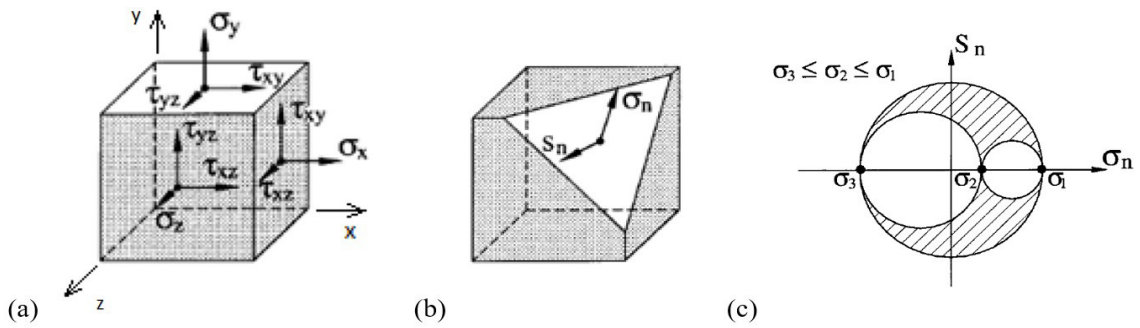
**Figure 4.** (a) Stress components in a solid element; (b) normal and shear stresses in an arbitrary plane; (c) Mohr circle for 3-D stresses in a point (adapted from Foster et al. [12])

For any oblique plane having a unit normal $\boldsymbol{n} = \{n_x, n_y, n_z\}$ passing through a point $P$, the stresses at point $P$ can resolved into a component normal to the plane ($\sigma_n$) and a shear component parallel to the plane ($S_n$), as shown in Figure 4b. For a stress to be principal, $S_n = 0$ which implies that:

$$\begin{cases} \sigma_x n_x + \tau_{xy} n_y + \tau_{xz} n_z = \sigma_n n_x \\ \tau_{xy} n_x + \sigma_y n_y + \tau_{yz} n_z = \sigma_n n_y \\ \tau_{xz} n_x + \tau_{yz} n_y + \sigma_z n_z = \sigma_n n_z \end{cases} \tag{2}$$

As all three components of $\boldsymbol{n}$ cannot be zero, the solution is nontrivial only if the determinant of the coefficients $\lvert \sigma \rvert = 0$, that is:

$$\begin{vmatrix} \sigma_x - \sigma_n & \tau_{xy} & \tau_{xz} \\ \tau_{xy} & \sigma_y - \sigma_n & \tau_{yz} \\ \tau_{xz} & \tau_{yz} & \sigma_z - \sigma_n \end{vmatrix} = 0 \tag{3}$$

Expansion of the equation above leads to the characteristic equation:

$$\sigma_n^3 - I_1 \sigma_n^2 + I_2 \sigma_n - I_3 = 0 \tag{4}$$

where $I_1$, $I_2$ and $I_3$ are the invariants of the stress tensor given by:

$$\begin{aligned} I_1 &= \sigma_x + \sigma_y + \sigma_z = \sigma_1 + \sigma_2 + \sigma_3 \\ I_2 &= \sigma_x \sigma_y + \sigma_y \sigma_z + \sigma_x \sigma_z - \tau_{xy}^2 - \tau_{yz}^2 - \tau_{xz}^2 = \sigma_1 \sigma_2 + \sigma_2 \sigma_3 + \sigma_1 \sigma_3 \\ I_3 &= \sigma_x \sigma_y \sigma_z + 2 \tau_{xy} \tau_{xz} \tau_{yz} - \sigma_x \tau_{yz}^2 - \sigma_y \tau_{xz}^2 - \sigma_z \tau_{xy}^2 = \sigma_1 \sigma_2 \sigma_3 \end{aligned} \tag{5}$$

where $\sigma_1$, $\sigma_2$ e $\sigma_3$ are the principal stresses, ordered such that $\sigma_3 \le \sigma_2 \le \sigma_1$. The principal stress directions $\boldsymbol{n}_i = \{n_{ix}, n_{iy}, n_{iz}\}$ ($i = 1, 2, 3$) are obtained from:

Rev. IBRACON Estrut. Mater., vol. 16, no. 4, e16407, 2023

5/20

$$n_{ix} = -\frac{c_{iy}c_{iz}}{C_i}; \quad n_{iy} = -\frac{c_{ix}c_{iz}}{C_i}; \quad n_{ix} = -\frac{c_{ix}c_{iy}}{C_i} \tag{6}$$

where $C_i = \sqrt{c_{ix}^2 \, c_{iy}^2 + c_{ix}^2 \, c_{iz}^2 + c_{iy}^2 \, c_{iz}^2}$ and

$$c_{ix} = (\sigma_x - \sigma_i)\,\tau_{yz} - \tau_{xy}\tau_{xz}; \quad c_{iy} = (\sigma_y - \sigma_i)\,\tau_{xz} - \tau_{xy}\tau_{yz}; \quad c_{iz} = (\sigma_z - \sigma_i)\,\tau_{xy} - \tau_{xz}\tau_{yz} \tag{7}$$

Once that the principal stresses have been found in magnitude and direction, the stresses on any oblique plane can be determined from:

$$\sigma_n = \sigma_1 n_1^2 + \sigma_2 n_2^2 + \sigma_3 n_3^2; \quad S_n^2 = \sigma_1^2 n_1^2 + \sigma_2^2 n_2^2 + \sigma_3^2 n_3^2 - \sigma_n^2 \tag{8}$$

where $n_1$, $n_2$, $n_3$ are the direction cosines relative to the principal axes of a vector normal to the plane. The point $(\sigma_n, S_n)$ lies within the hatched region in Figure 4c. For the planes $yz$, $xz$ and $xy$, the shear stresses are calculated, respectively, by:

$$S_x = \sqrt{\tau_{xy}^2 + \tau_{xz}^2}; \quad S_y = \sqrt{\tau_{xy}^2 + \tau_{yz}^2}; \quad S_z = \sqrt{\tau_{xz}^2 + \tau_{yz}^2} \tag{9}$$

**Notes on shear stresses.** There are eight combinations of signs for given absolute values of the shear stresses $\tau_{xy}$, $\tau_{xz}$ and $\tau_{yz}$, as shown in Table 1, that can be grouped into two subgroups. Let us consider a stress state with three positive shear stresses (sign combination #1). If the coordinate system is rotated $180^0$ about the $x$-axis, the same shear stresses referred to the new coordinate system should be written with the sign combination #2; if the original coordinate system is rotated $180^0$ about the $y$-axis, the shear stresses should be written with the sign combination #3; if, however, the original coordinate system is rotated $180^0$ about the $z$-axis, shear stresses should be written with the sign combination #4. These transformations are represented in Figure 5, showing the physical equivalence between the so-called *positive shear stress Case 1*. Let us now consider a stress state with all three shear stresses being negative. Similarly, sign combinations #6 to #8 are physically equivalent to sign combination #5, and they all can be grouped into the so-called *negative shear stress Case 2*, as shown by the transformations in Figure 6.

**Table 1.** Shear stress sign combinations

| Case 1 | Sign combination | | | Case 2 | Sign combination | | |
|---|---|---|---|---|---|---|---|
| | $\tau_{xy}$ | $\tau_{xz}$ | $\tau_{yz}$ | | $\tau_{xy}$ | $\tau_{xz}$ | $\tau_{yz}$ |
| # 1 | + | + | + | # 5 | - | - | - |
| # 2 | - | - | + | # 6 | + | + | - |
| # 3 | - | + | - | # 7 | + | - | + |
| # 4 | + | - | + | # 8 | - | + | + |

Rev. IBRACON Estrut. Mater., vol. 16, no. 4, e16407, 2023

6/20

(a): (+,+,+)    (b): (-,-,+)    (c): (-,+,-)    (d): (+,-,-)

**Figure 5.** Positive shear stresses in Case 1



(a): (-,-,-)    (b): (+,+,-)    (c): (+,-,+)    (d): (-,+,+)
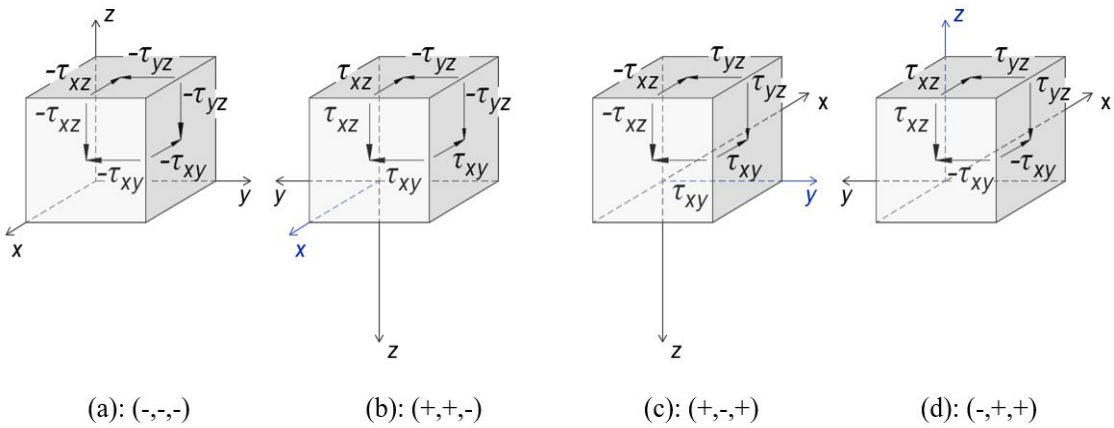
**Figure 6.** Negative shear stresses in case 2. Legend: (±, ±, ±) = (signal of $\tau_{xy}$, signal of $\tau_{xz}$, signal of $\tau_{yz}$)

## 2.4 RSM: the system of resistance

Let us consider a concrete cube with smeared reinforcement in the $x$-, $y$- and $z$-directions, delimited by an inclined plane corresponding to a crack, this plane being orthogonal to the larger principal stress (Figure 7). It is assumed that the crack face is crossed by the reinforcement in three directions but is free from any normal or shear stresses. The applied stresses ($S$) are resisted by equivalent stresses on concrete ($S_c$) and equivalent reinforcement stresses ($S_s$), as shown in Figure 8a:

$$S = S_c + S_s$$

$$\begin{bmatrix} \sigma_x & \tau_{xy} & \tau_{xz} \\ \tau_{yx} & \sigma_y & \tau_{yz} \\ \tau_{zx} & \tau_{zy} & \sigma_z \end{bmatrix} = \begin{bmatrix} \sigma_x - f_{tx} & \tau_{xy} & \tau_{xz} \\ \tau_{yx} & \sigma_y - f_{ty} & \tau_{yz} \\ \tau_{zx} & \tau_{zy} & \sigma_z - f_{tz} \end{bmatrix} + \begin{bmatrix} f_{tx} & 0 & 0 \\ 0 & f_{ty} & 0 \\ 0 & 0 & f_{tz} \end{bmatrix} \tag{10}$$

Concrete must resist both the difference between the normal applied stresses and the normal stresses carried by the reinforcement ($\sigma_{ci} = \sigma_i - f_{ti}$), and the three shear stress components ($\tau_{xy}$, $\tau_{xz}$, $\tau_{yz}$); reinforcement, on the other hand, must resist the equivalent reinforcement stresses $f_{tx}$, $f_{ty}$, $f_{tz}$ (reinforcement bar stresses distributed over the concrete area). It is assumed that reinforcing steel cannot carry shear stress.
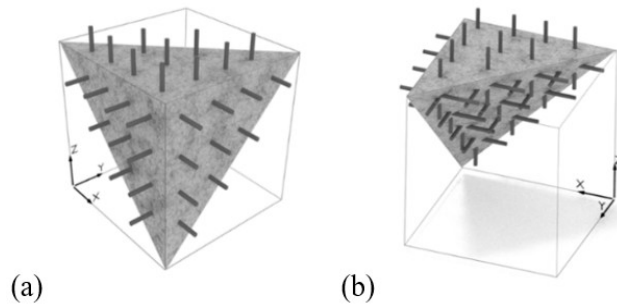
**Figure 7.** Cracked solid element with reinforcement in three orthogonal directions: (a) side view; (b) view of the inclined crack plane crossed by the reinforcement

The principal concrete stresses are derived from the concrete characteristic equation:

$$\sigma_n^3 - I_{c1}\sigma_n^2 + I_{c2}\sigma_n - I_{c3} = 0 \tag{11}$$

where the $I_{c1}$, $I_{c2}$, $I_{c3}$ are the invariants of the concrete stress tensor:

$$I_{c1} = \sigma_{cx} + \sigma_{cy} + \sigma_{cz} = \left(\sigma_x + \sigma_y + \sigma_z\right) - \left(f_{tx} + f_{ty} + f_{tz}\right)$$

$$I_{c2} = \sigma_{cx}\sigma_{cy} + \sigma_{cy}\sigma_{cz} + \sigma_{cx}\sigma_{cz} - \tau_{xy}^2 - \tau_{yz}^2 - \tau_{xz}^2 \tag{12}$$

$$I_{c3} = \sigma_{cx}\sigma_{cy}\sigma_{cz} + 2\tau_{xy}\tau_{xz}\tau_{yz} - \sigma_x\tau_{yz}^2 - \sigma_y\tau_{xz}^2 - \sigma_z\tau_{xy}^2$$

When one principal concrete stress is zero ($\sigma_{c1}=0$), the third invariant of the concrete stresses $I_{c3} = 0$, and the latter the characteristic equation reduces to:

$$\sigma^2 - I_{c1}\sigma + I_{c2} = 0 \tag{13}$$

which has the roots:

$$\left.\begin{array}{l}\sigma_{c2} = \sigma_{II}\\ \sigma_{c3} = \sigma_{III}\end{array}\right\} = \frac{1}{2}\left(I_{c1} \pm \sqrt{I_{c1}^2 - 4I_{c2}}\right) \tag{14}$$

The first term in Equation 14 defines the center of the 2 to 3 principal concrete stress circle and the second term, the radius. Figure 8b plots the Mohr's circle for the applied stresses and, within the circles, the stress ($\sigma_i$, $S_i$), with $i = x$, $y$, $z$. They are resisted by equivalent concrete stresses ($\sigma_{ci}$, $S_{ci}$) and by equivalent steel stresses $f_{ti} = (\rho_{si} \times \sigma_{si})$, where $\rho_{si}$ are the reinforcement ratios in the $i$-th directions, and $\sigma_{si}$ are the equivalent steel stresses in the $i$-th directions.
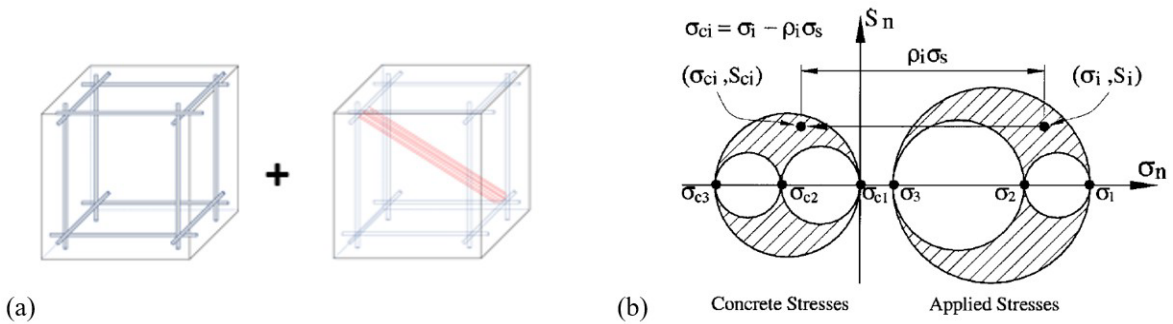
**Figure 8.** (a) System of resistance for a reinforced solid; (b) Mohr´s circle for the applied stresses and equivalent stresses on concrete and reinforcement [11]

## 2.5 RSM: equivalent stresses computation

From the eight combinations of signs of the three shear stresses, it is only necessary to consider two cases: all shear stresses positive or all shear stresses negative (or equivalently two shear stresses positive and one negative). This separation leads the ensuing formulation. For the complete deduction, please refer to Nielsen and Hoang [18].

### 2.5.1 Case 1a: positive shear stresses, reinforcement in three directions

Initially, the concrete normal stresses $\sigma_{cx}$, $\sigma_{cy}$, $\sigma_{cz}$ are expressed as a function of the given shear stresses $\tau_{xy}$, $\tau_{xz}$, $\tau_{yz}$ and the Euler angles $\Psi$, $\theta$, $\phi$ (angles used to describe the rotation for going from a rectangular coordinate $x$, $y$, $z$-system to the $\xi$, $\eta$, $\zeta$-system when describing a stress state, as shown in Figure 9).

$$\sigma_{cx} = -\frac{\tau_{xy}\sin\psi\cos\theta + \tau_{xz}\sin\theta}{\cos\psi\cos\theta} \;;\; \sigma_{cy} = -\frac{\tau_{xy}\cos\psi\cos\theta + \tau_{yz}\sin\theta}{\sin\psi\cos\theta} \;;\; \sigma_{cz} = -\frac{\tau_{xz}\cos\psi\cos\theta + \tau_{yz}\sin\psi\cos\theta}{\sin\theta} \tag{15}$$

These formulas make possible to express the equivalent reinforcement stresses $f_{tx}, f_{ty}, f_{tz}$ as:

$$f_{tx} = \sigma_x + \tau_{xy}\tan\psi + \tau_{xz}\frac{\tan\theta}{\cos\psi} \;;\; f_{ty} = \sigma_y + \tau_{xy}\frac{1}{\tan\psi} + \tau_{yz}\frac{\tan\theta}{\sin\psi} \;;\; f_{tz} = \sigma_z + \tau_{xz}\frac{\cos\psi}{\tan\theta} + \tau_{yz}\frac{\sin\psi}{\tan\theta} \tag{16}$$
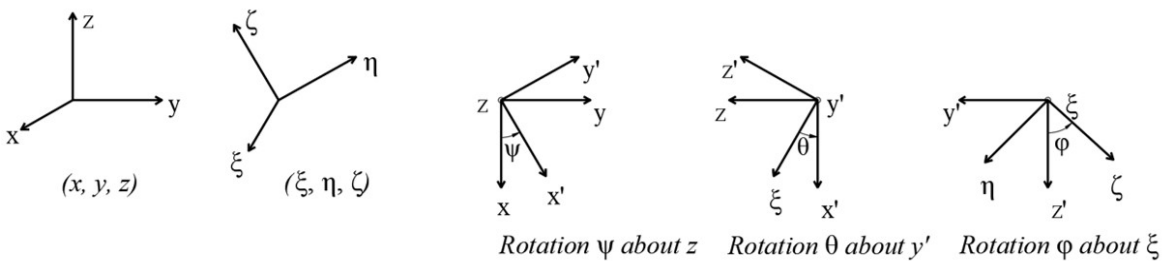


**Figure 9.** Euler angles

The total reinforcement consumption $R = f_{tx} + f_{ty} + f_{tz}$ is calculated by:

$$R = f_{tx} + f_{ty} + f_{tz} = \sigma_x + \sigma_y + \sigma_z + \tau_{xy}\left(\tan\psi + \frac{1}{\tan\psi}\right) + \tau_{xz}\left(\frac{\tan\theta}{\cos\psi} + \frac{\cos\psi}{\tan\theta}\right) + \tau_{yz}\left(\frac{\tan\theta}{\sin\psi} + \frac{\sin\psi}{\tan\theta}\right) \tag{17}$$

whose minimum is found for $\tan \psi = 1$ and $\tan \theta = \sqrt{2}/2$. Inserting these values into Equation 16, we find:

$$f_{tx} = \sigma_x + \left( \tau_{xy} + \tau_{xz} \right); \; f_{ty} = \sigma_y + \left( \tau_{xy} + \tau_{yz} \right); \; f_{tz} = \sigma_z + \left( \tau_{xz} + \tau_{yz} \right) \tag{18}$$

Concrete stresses are only dependent on the shear stresses:

$$\sigma_{cx} = \sigma_x - f_{tx} = -\left( \tau_{xy} + \tau_{xz} \right); \; \sigma_{cy} = \sigma_y - f_{ty} = -\left( \tau_{xy} + \tau_{yz} \right); \; \sigma_{cz} = \sigma_z - f_{tz} = -\left( \tau_{xz} + \tau_{yz} \right) \tag{19}$$

and the corresponding principal stresses are:

$$\left. \begin{array}{l} \sigma_{II} = \sigma_{c2} \\ \sigma_{III} = \sigma_{c3} \end{array} \right\} = -\left( \tau_{xy} + \tau_{xz} + \tau_{yz} \right) \mp \sqrt{\left( \tau_{xy} + \tau_{xz} + \tau_{yz} \right)^2 - 3\left( \tau_{xy}\tau_{xz} + \tau_{xz}\tau_{yz} + \tau_{yz}\tau_{xy} \right)} \tag{20}$$

### 2.5.2 Case 1b: positive shear stresses, reinforcement in two directions

   i.   If $f_{tx}$ comes out negative in Equation 18, then:

$$f_{tx} = 0; \qquad f_{ty} = \sigma_y + \tau_{yz} + \tau_{xy} \overbrace{\frac{\tau_{xy} + \tau_{xz}}{|\sigma_x|}}^{>0}; \qquad f_{tz} = \sigma_z + \tau_{yz} + \tau_{xz} \overbrace{\frac{\tau_{xy} + \tau_{xz}}{|\sigma_x|}}^{>0} \tag{21}$$

   ii.   If $f_{ty}$ comes out negative in Equation 18, then:

$$f_{tx} = \sigma_x + \tau_{xz} + \tau_{xy} \overbrace{\frac{\tau_{xy} + \tau_{yz}}{|\sigma_y|}}^{>0}; \qquad f_{ty} = 0; \qquad f_{tz} = \sigma_z + \tau_{xz} + \tau_{yz} \overbrace{\frac{\tau_{xy} + \tau_{yz}}{|\sigma_y|}}^{>0} \tag{22}$$

   iii.   If $f_{tz}$ comes out negative in Equation 18, then:

$$f_{tx} = \sigma_x + \tau_{xy} + \tau_{xz} \overbrace{\frac{\tau_{xz} + \tau_{yz}}{|\sigma_z|}}^{>0}; \qquad f_{ty} = \sigma_y + \tau_{xy} + \tau_{yz} \overbrace{\frac{\tau_{xz} + \tau_{yz}}{|\sigma_z|}}^{>0}; \qquad f_{tz} = 0 \tag{23}$$

Concrete stresses are no longer only dependent on the shear stresses:

$$\sigma_{cx} = \sigma_x - f_{tx}; \quad \sigma_{cy} = \sigma_y - f_{ty}; \quad \sigma_{cz} = \sigma_z - f_{tz} \tag{24}$$

### 2.5.3 Case 1c: positive shear stresses, reinforcement in one direction

   i.   If $f_{ty}$ comes out negative in Equation 21 or $f_{tx}$ comes out negative in Equation 22:

$$f_{tx} = 0; \quad f_{ty} = 0; \quad f_{tz} = \sigma_z + \frac{2\tau_{xy}\tau_{xz}\tau_{yz} - \sigma_x\tau_{yz}^2 - \sigma_y\tau_{xz}^2}{\sigma_x\sigma_y - \tau_{xy}^2} \tag{25}$$

ii.    If $f_{tz}$ comes out negative in Equation 21 or $f_{tx}$ comes out negative in Equation 23:

$$f_{tx} = 0; \quad f_{ty} = \sigma_y + \frac{2\tau_{xy}\tau_{xz}\tau_{yz} - \sigma_x\tau_{yz}^2 - \sigma_z\tau_{xy}^2}{\sigma_x\sigma_z - \tau_{xz}^2}; \quad f_{tz} = 0 \tag{26}$$

iii.    If $f_{tz}$ comes out negative in Equation 22 or $f_{ty}$ comes out negative in Equation 23:

$$f_{tx} = \sigma_x + \frac{2\tau_{xy}\tau_{xz}\tau_{yz} - \sigma_y\tau_{xz}^2 - \sigma_z\tau_{xy}^2}{\sigma_y\sigma_z - \tau_{yz}^2}; \quad f_{ty} = 0; \quad f_{tz} = 0 \tag{27}$$

Concrete stresses, once again, do not depend only on the shear stresses:

$$\sigma_{cx} = \sigma_x - f_{tx}; \ \sigma_{cy} = \sigma_y - f_{ty}; \ \sigma_{cz} = \sigma_z - f_{tz} \tag{28}$$

**2.5.4 Case 1d: positive shear stresses, no reinforcement required**

When $f_{tx}$, $f_{ty}$ and $f_{tz}$ all become negative in Equations 26 through 28, no reinforcement is required. This condition occurs when:

$$\sigma_x\sigma_y\sigma_z + 2\tau_{xy}\tau_{xz}\tau_{yz} - \sigma_x\tau_{yz}^2 - \sigma_y\tau_{xz}^2 - \sigma_z\tau_{xy}^2 < 0 \tag{29}$$

In this case, all principal stresses are negative (compressive).

**2.3.5 Case 2a: negative shear stresses, biaxial concrete compression**

The shear stresses with the larger absolute values are considered positive and the shear stress with the smaller absolute value is considered negative. Analyzing Equation 20 for the concrete principal stresses, biaxial compression ($\sigma_{II}$ e $\sigma_{III} < 0$) occurs if:

$$\tau_{xy}\tau_{xz} + \tau_{xz}\tau_{yz} + \tau_{xy}\tau_{yz} > 0 \tag{30}$$

In this case, the formulas for Case 1 may be used when $|\tau_{yz}|$ is the smaller absolute shear stress. Otherwise, the designer should rename axes according to the following scheme:

If $|\tau_{xy}|$ is the smaller one: $x \rightarrow y \quad y \rightarrow z \quad z \rightarrow x$ \hfill (31)

If $|\tau_{xz}|$ is the smaller one: $x \rightarrow z \quad y \rightarrow x \quad z \rightarrow y$ \hfill (32)

## 2.5.6 Case 2b: negative shear stresses, uniaxial concrete compression

Once again, the shear stresses with the larger absolute values are considered positive and the shear stress with the smaller absolute value is considered negative. Analyzing Equation 20 for the concrete principal stresses, uniaxial compression (only $\sigma_{III} < 0$) occurs when

$$\tau_{xy}\tau_{xz} + \tau_{xz}\tau_{yz} + \tau_{xy}\tau_{yz} < 0 \tag{33}$$

Considering that $|\tau_{yz}|$ is the smaller absolute shear stress, the equivalent reinforcement stresses are:

$$f_{tx} = \sigma_x - \frac{\tau_{xy}\tau_{xz}}{\tau_{yz}}; \; f_{ty} = \sigma_y - \frac{\tau_{xy}\tau_{yz}}{\tau_{xz}}; \; f_{tz} = \sigma_z - \frac{\tau_{xz}\tau_{yz}}{\tau_{xy}} \tag{34}$$

If $f_{tx}$ turns out negative in Equation 34, Formula 21 from Case 1 is valid; if $f_{ty}$ comes out negative in Equation 34, Formula 22 is valid; if, finally, $f_{tz}$ comes out negative in Equation 34, Formula 23 is valid. One may continue using the formulas from Case 1, Equations 25 to 27 and 30, when further negative values appear. Concrete stresses are calculated by

$$\sigma_{cx} = \sigma_x - f_{tx} = \frac{\tau_{xy}\tau_{xz}}{\tau_{yz}}; \quad \sigma_{cy} = \sigma_y - f_{ty} = \frac{\tau_{xy}\tau_{yz}}{\tau_{xz}}; \quad \sigma_{cz} = \sigma_z - f_{tz} = \frac{\tau_{xz}\tau_{yz}}{\tau_{xy}} \tag{35}$$

Concrete principal stresses are

$$\sigma_{II} = 0; \quad \sigma_{III} = \sigma_{cx} + \sigma_{cy} + \sigma_{cz} = \underbrace{\frac{\tau_{xy}\tau_{xz}}{\tau_{yz}} + \frac{\tau_{xy}\tau_{yz}}{\tau_{xz}} + \frac{\tau_{xz}\tau_{yz}}{\tau_{xy}}}_{<0} \tag{36}$$

When $|\tau_{xy}|$ is the smaller shear stress, Formulas 34 to 36 for Case 2b may be applied when transformations in Equation 31 are applied. When $|\tau_{xz}|$ is the smaller one, the transformations (32) apply.

The design equations for cases 1a, 1b, 1c, 1d, 2a, and 2b are summarized in Table 2.

## 2.6 RSM: reinforcement design and concrete verification

Reinforcement is designed on the assumption of utilization of the bars up to the design value, and stresses must be limited to:

$$f_{tx} \le \rho_{sx}f_{yd}; \quad f_{ty} \le \rho_{sy}f_{yd}; \quad f_{tz} \le \rho_{sz}f_{yd} \tag{37}$$

where $\rho_{sx}$, $\rho_{sy}$, $\rho_{sz}$ are the reinforcement ratio in the x-, y- and z-directions, respectively, and $f_{yd}$ is the design value of the reinforcement steel yield stress.

Concrete stresses are required to satisfy:

$$-\sigma_{III} \le \nu f_{cd} \tag{38}$$

where $f_{cd}$ is the design compression strength of concrete, and $v$ is the efficiency factor introduced to account for both confinement effects, as in the case of concrete in biaxial or triaxial compression, disturbance effects such as caused by transmission of tension fields through compression fields, and micro-cracking in the concrete paste due to shrinkage. Then, $v$ accounts for the imperfect assumption that concrete behaves as a rigid-plastic material and ensures that ductility demands are met. The following values of $v$ are indicated by the *fib* Model Code [4]:

i. If no reinforcement has yielded and at least one principal stress is in tension, then:

$$v = \frac{1,18}{1,14 + 0,00166\sigma_{si}} \leq 1 \tag{39}$$

where $\sigma_{si}$ is the maximum tensile stress (in MPa) in any layer of the reinforcing steel

ii. If one or more layers of reinforcement yield:

$$v = \left(1 - 0,032|\delta_i|\right)\frac{1,18}{1,14 + 0,00166 f_{yd}} \tag{40}$$

where $\delta_i$ is given by Equation 42 ($i = x, y, z$).

iii. If all principal stresses are compressive, $v$ may be taken as 1,0 or determined in accordance with more elaborate expressions for the strength under multiaxial states of stress, such as the one given by Ottosen [4], [24]:

$$\alpha\frac{J_2}{f_{cm}^2} + \lambda\frac{\sqrt{J_2}}{f_{cm}} + \beta'\frac{I_1}{f_{cm}} - 1 = 0 \tag{41}$$

where $I_1$ and $J_2$ characterize the state of stress considered, and $f_{cm}$ is the concrete uniaxial compressive strength.

In a solid subject to increasing loads, the stress field is continuously redistributed, starting from an initial approximately elastic state, followed by cracking of concrete, and yielding of steel. Through this process, elements shall be capable of allowing for sufficient plastic strains to prevent local rupture before the calculated stress distribution has been attained. Foster et al. [12] alert that "*designers must critically examine the load path being assumed to satisfy themselves that a sufficient level of ductility is available to meet the demands of the imposed tractions.*" For this purpose, they presented an expression for the enclosed angle between the principal direction of the applied stresses and those of the concrete stresses:

$$\delta_i \leq \cos^{-1}\left|n_{ix}n_{cix} + n_{iy}c_{ciy} + n_{iz}n_{ciz}\right| \tag{42}$$

where $n_{ci}$ ($i = 1, 2, 3$) are the direction cosines of the concrete stress tensor, as shown in Figure 10. They suggested a limit of 25 degrees to $\delta_i$, value that was later revised by the Model Code [4] to 15 degrees.
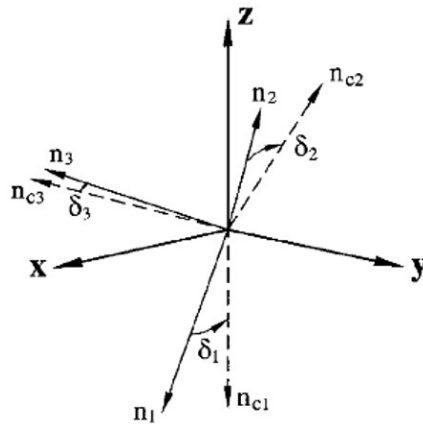
**Figure 10.** Comparison of concrete principal stress directions and the principal stress directions for the case of optimum reinforcement [12]

**Table 2.** Summary of design equations for individual elements

| Reinf | Cases | $f_{tx}$ | $f_{ty}$ | $f_{tz}$ | Condition |
|---|---|---|---|---|---|
| ⊥ | 1a +++ | $\sigma_x + \left(\tau_{xy} + \tau_{xz}\right)$ | $\sigma_y + \left(\tau_{xy} + \tau_{yz}\right)$ | $\sigma_z + \left(\tau_{xz} + \tau_{yz}\right)$ | $f_{tx}, f_{ty}, f_{tz} > 0$ |
| ʼʼ | 2a ++- | $\sigma_x + \left(\tau_{xy} + \tau_{xz}\right)$ | $\sigma_y + \left(\tau_{xy} + \tau_{yz}\right)$ | $\sigma_z + \left(\tau_{xz} + \tau_{yz}\right)$ | $f_{tx}, f_{ty}, f_{tz} > 0$<br>$\tau_{xy}\tau_{xz} + \tau_{xz}\tau_{yz}$<br>$+ \tau_{xy}\tau_{yz} > 0$ |
| ʼʼ | 2b ++- | $\sigma_x - \dfrac{\tau_{xy}\tau_{xz}}{\tau_{yz}}$ | $\sigma_y - \dfrac{\tau_{xy}\tau_{yz}}{\tau_{xz}}$ | $\sigma_z - \dfrac{\tau_{xz}\tau_{yz}}{\tau_{xy}}$ | $f_{tx}, f_{ty}, f_{tz} > 0$<br>$\tau_{xy}\tau_{xz} + \tau_{xz}\tau_{yz}$<br>$+ \tau_{xy}\tau_{yz} < 0$ |
| ⊥ | 1b/ 2 | $\sigma_x + \tau_{xy} - \tau_{xz}\dfrac{\tau_{xz} + \tau_{yz}}{\sigma_z}$ | $\sigma_y + \tau_{xy} - \tau_{yz}\dfrac{\tau_{xz} + \tau_{yz}}{\sigma_z}$ | $0$ | $f_{tz} < 0$<br>$f_{tx}, f_{ty} > 0$ |
| ⊥ | 1b/ 2 | $\sigma_x + \tau_{xz} - \tau_{xy}\dfrac{\tau_{xy} + \tau_{yz}}{\sigma_y}$ | $0$ | $\sigma_z + \tau_{xz} - \tau_{yz}\dfrac{\left(\tau_{xy} + \tau_{yz}\right)}{\sigma_y}$ | $f_{ty} < 0$<br>$f_{tx}, f_{tz} > 0$ |
| ⊥ | 1b/ 2 | $0$ | $\sigma_y + \tau_{yz} - \tau_{xy}\dfrac{\tau_{xy} + \tau_{xz}}{\sigma_x}$ | $\sigma_z + \tau_{yz} - \tau_{xz}\dfrac{\tau_{xy} + \tau_{xz}}{\sigma_x}$ | $f_{tx} < 0$<br>$f_{ty}, f_{tz} > 0$ |
| ⊥ | 1c/ 2 | $\sigma_x + \dfrac{2\tau_{xy}\tau_{xz}\tau_{yz} - \sigma_y\tau_{xz}^2 - \sigma_z\tau_{xy}^2}{\sigma_y\sigma_z - \tau_{yz}^2}$ | $0$ | $0$ | $f_{ty}, f_{tz} < 0$<br>$f_{tx} > 0$ |
| ⊥ | 1c/ 2 | $0$ | $\sigma_y + \dfrac{2\tau_{xy}\tau_{xz}\tau_{yz} - \sigma_x\tau_{yz}^2 - \sigma_z\tau_{xy}^2}{\sigma_x\sigma_z - \tau_{xz}^2}$ | $0$ | $f_{tx}, f_{tz} < 0$<br>$f_{ty} > 0$ |
| ⊥ | 1c/ 2 | $0$ | $0$ | $\sigma_z + \dfrac{2\tau_{xy}\tau_{xz}\tau_{yz} - \sigma_x\tau_{yz}^2 - \sigma_y\tau_{xz}^2}{\sigma_x\sigma_y - \tau_{xy}^2}$ | $f_{tx}, f_{ty} < 0$<br>$f_{tz} > 0$ |
| ⊥ | 1d/ 2 | $0$ | $0$ | $0$ | $\sigma_x\sigma_y\sigma_z + 2\tau_{xy}\tau_{xz}\tau_{yz}$<br>$-\sigma_x\tau_{yz}^2 - \sigma_y\tau_{xz}^2$<br>$-\sigma_z\tau_{xy}^2 < 0$ |

Notes:
(1) Sign convention: positive normal stress for tension.
(2) Case 1: (sign of $\tau_{xy}$, sign of $\tau_{xz}$, sign of $\tau_{yz}$) = (+, +, +), (+, -, -), (-, +, -), (-, -, +) → consider $+|\tau_{xy}|$, $+|\tau_{xz}|$ and $+|\tau_{yz}|$
(3) Case 2: (sign of $\tau_{xy}$, sign of $\tau_{xz}$, sign of $\tau_{yz}$) = (+, +, -), (+, -, +), (-, +, +), (-, -, -)
    → If $|\tau_{yz}|$ is the smallest absolute shear stress: consider $+|\tau_{xy}|$, $+|\tau_{xz}|$ and $-|\tau_{yz}|$.
    → If $|\tau_{xy}|$ is the smallest absolute shear stress: x→y, y→z, z→x . Consider: $+|\tau_{xy}|$, $+|\tau_{xz}|$ and $-|\tau_{yz}|$. Calculate reinf. and retrieve original axes.
    → If $|\tau_{xz}|$ is the smallest absolute shear stress: x→z, y→x, z→y . Consider $+|\tau_{xy}|$, $+|\tau_{xz}|$ and $-|\tau_{yz}|$. Calculate reinf. and retrieve original axes.
(4) Concrete stresses (all cases): $\sigma_{cx} = \sigma_x - f_{tx}$; $\sigma_{cy} = \sigma_y - f_{ty}$; $\sigma_{cz} = \sigma_z - f_{tz}$. Concrete verification as described in section 2.5.
(5) Reinforcement: $\rho_{sx} = f_{tx}/f_y$; $\rho_{sy} = f_{ty}/f_y$; $\rho_{sz} = f_{tz}/f_y$; and $a_s = \rho_s \cdot A_c$

# 3 METHODOLOGY FOR THE DESIGN OF A STRUCTURAL MEMBER

As an example of the herein proposed methodology, the design of a reinforced concrete member by the RSM was performed according to the steps 1 to 3 described below:

**Step 1: Linear analysis.** An initial linear analysis was performed with the software *STRAP* version 12.5 from *Atir Engineering Software Development Ltd.* [25]. The structure was modeled with finite solid elements assuming uncracked material, linear stress-strain relationships, and the mean value of the concrete modulus of elasticity. From this initial model two output *.lst* files were obtained: one containing the geometry definition (nodal coordinates and element nodal incidence), and the other containing the complete stress field deriving from the analysis (nodal stresses).

**Step 2: Data processing – individual element RSM design.** An application was developed with Java programming language for data treatment using *Java Development Kit JDK 17*. This application was built to: (i) read the data from the *.lst* files created in step 1; (ii) treat the data, computing stress invariants, principal stresses and directions, and equivalent resisting stresses in each model node (both reinforcement stresses $f_{tx}, f_{ty}, f_{tz}$ and concrete stresses); (iii) automatically assemble the calculated quantities into a *.vtk* file to be later accessed by a post processor. The flowchart of the application structure is presented in Figure 11.

**Step3: Data analysis and structural member RSM design.** The *.vtk* file was loaded into the software *Paraview* version 5.9.1 from *Kitware Inc.* This software, described by Ahrens et al. [26], is an open-source software system for 3D computer graphics, modeling, volume rendering and information visualization by operations such as clipping, slicing, filtering, or generating contours from the loaded data. At this point, a thorough analysis of the reinforcement requirements and concrete stresses sufficed for the global structural design and subsequent detailing by delimitation of zones with constant reinforcement ratio.

The methodology was applied to the RSM design of a structural component: a pile cap with dimension 1,90 m x 1,90 m, 0,80 m depth, concrete C30, supported by four rectangular 0,30 m x 0,30 m piles, subjected to a design load of $P_d = 1\ 380$ kN acting on the top of a 0,30 m x 0,80 m rectangular column. Though less usual in design practice, rectangular piles were chosen to facilitate modelling and visualization. For step 1, the definition of a 0,10 m mesh size led to a structural model with 3 400 cubic solid elements, as shown in Figure 12.
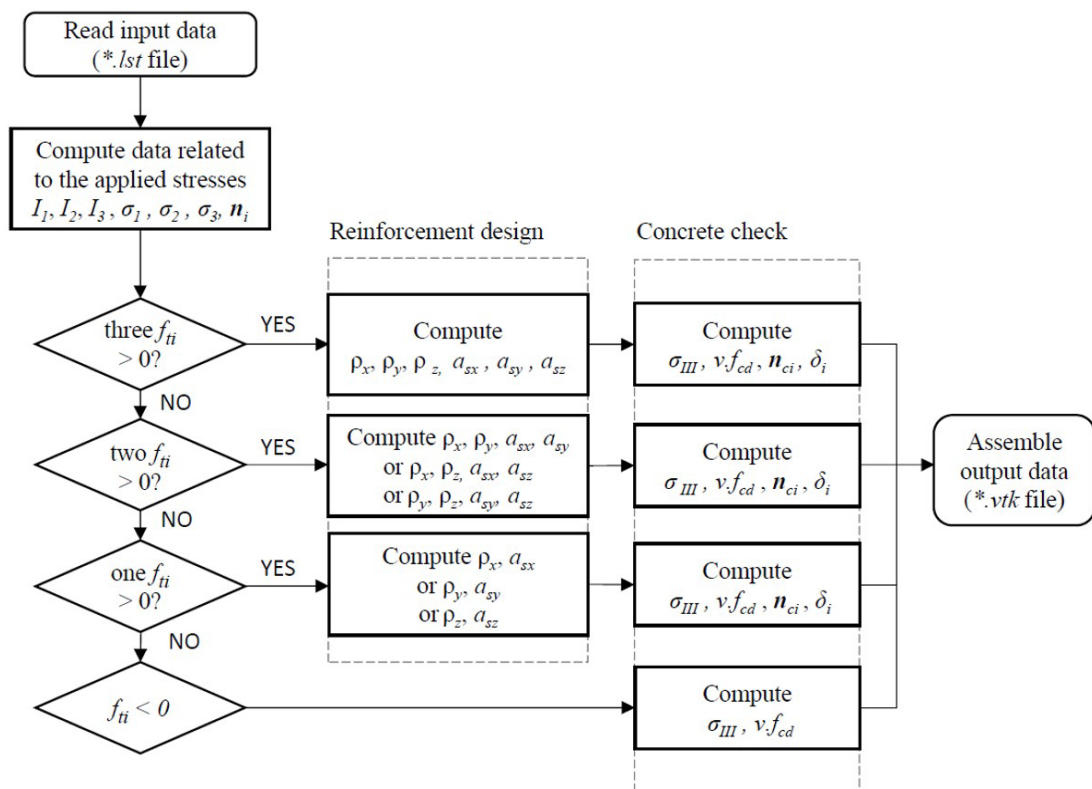


**Figure 11.** Flowchart of the developed application
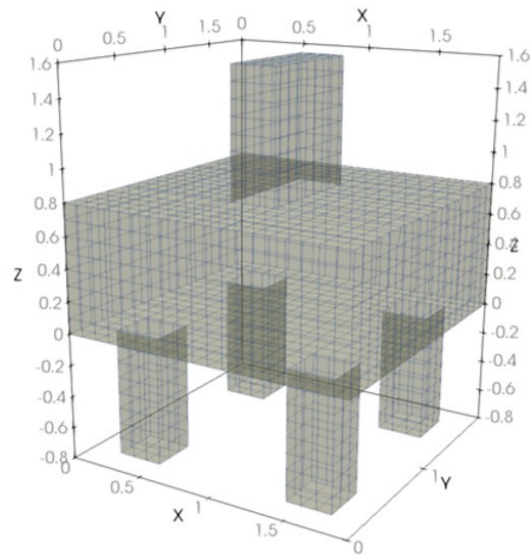
**Figure 12.** Structural solid model of a four-pile cap for the step 1 of the methodology

# 4 RESULTS AND DISCUSSIONS

## 4.1 Results for the four-pile cap designed by the RSM

The distribution of equivalent reinforcement stresses in the $x$- and $y$-directions, in cross sections passing through the center of gravity of the cap, are illustrated in Figure 13a and b, respectively. It should be noted that, according to the design, it was necessary to distribute reinforcement in the two lower thirds of the cap depth. It was proposed to reinforce the lower 0,25 m of the cap depth with reinforcement ratio $\rho_x = \rho_y = 0,5 \cdot (1,8+0,9)/435 = 0,31\%$, and the intermediate 0,25 m of the cap depth with $\rho_x = \rho_y = 0,5 \cdot (0,9+0)/435 = 0,10\%$. Doing so, the smeared total horizontal reinforcement amounted to $A_{sx} = A_{sy} = 19,5$ cm². Equivalent reinforcement stresses were also detected in the $z$-direction, as shown in Figure 14a, mainly at the regions highlighted by the red color, which corresponded to the intersection between the mid-depth plane and the compression struts. The maximum $f_{tz}$ value was equal to 0,79 MPa and indicated the necessity of $z$-reinforcement at a ratio of $\rho_z = 0,79/435 = 0,18\%$. The largest equivalent concrete principal stresses were clearly distributed following the direction of the compressive struts, as shown in Figure 14b, where the solid elements with $\sigma_{c3} = \sigma_{III} < -1,0$ MPa were filtered.



(a)                            (b)
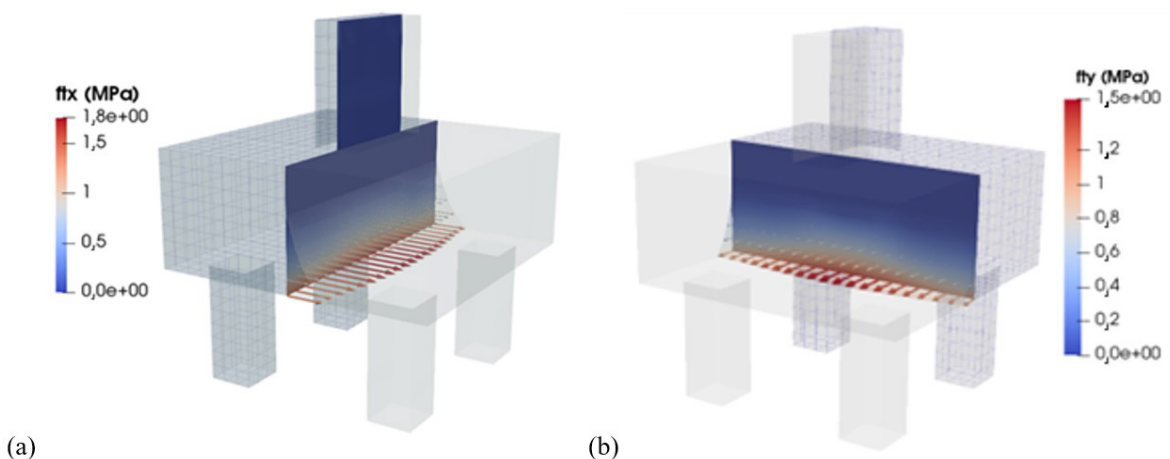
**Figure 13.** Four-pile cap analysis: reinforcement equivalent stresses (a) $f_{tx}$ and (b) $f_{ty}$
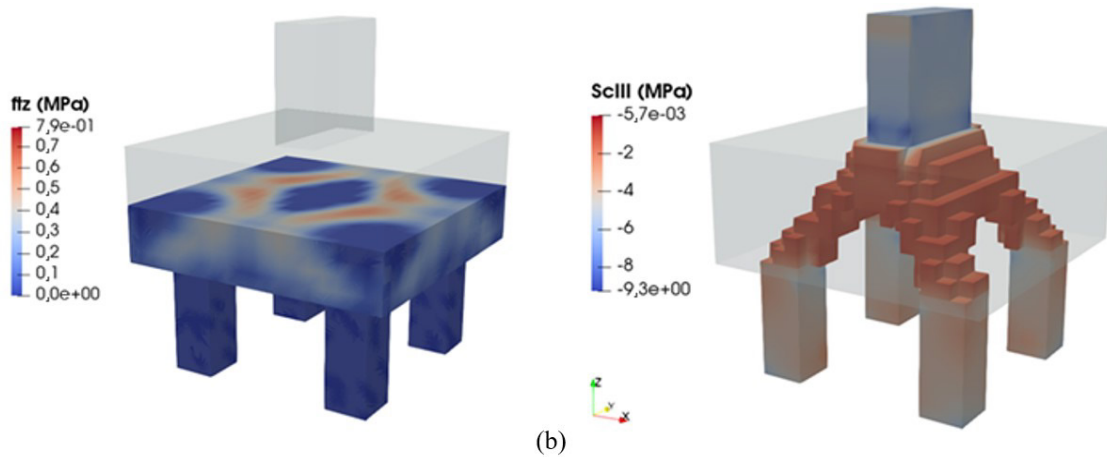
**Figure 14.** Four-pile cap: (a) reinforcement equivalent stress $f_{tz}$; (b) elements with concrete principal stress $\sigma_{III}$ lower than -1,0 MPa

## 4.2 Validation of the RSM

Numerical simulations of the four-pile cap were performed using the software *ATENA 3D* version 5.9.0 from Červenka Consulting [27] to validate the design achieved for the four-pile cap. A fracture-plastic material model based on the classical orthotropic smeared crack formulation (CC3NonLinCementitious2) was assigned to the concrete elements; reinforcement was modeled either by discrete or smeared bars, considering bilinear stress-strain law for steel, with maximum strain limited to 10‰. The partial factor method (as prescribed in the *fib* Model Code [4] and in *Guidelines for Nonlinear Finite Element Analysis of Concrete Structures* [28]) was selected as the safety format for the non-linear analyses, meaning that design values were assigned to the basis variables. The arc-length solution method was selected as the solution scheme.

Five models were tested up to failure, two of which designed by the Strut and Tie Method (STM), and the other three designed by the Reinforced Solid Model (RSM). Model ⑤ was elaborated considering the discrete reinforcement designed by the STM; initially, we considered neglecting the concrete tensile strength just as it is done in the STM. However, for convergence purposes, a reduced $f_{ctd}$ was set for concrete: $f_{ctd, reduced} = 0,10$ MPa $\approx 0,07\ f_{ctd}$. The ultimate load for this model, just 2% higher the design load ($P_d = 1\ 412$ kN), indicates the proper calibration of both material models and solution method chosen for the simulations. Model ③ was built with smeared reinforcement in three directions designed by the RSM, while in model ④ reinforcement in the z-direction was suppressed. Both models considered the reduced tensile strength so that a direct comparison could be established between the RSM and the STM results. The ultimate loads obtained by the simulations were, respectively, 1,54 x $P_d$ and 1,46 x $P_d$. Model ① was built with smeared reinforcement designed by the RSM (see Figure 15a), and model ② with discrete reinforcement designed by the STM. Both considered $f_{ctd} = 1,46$ MPa as input value. The ultimate loads obtained by the simulations were, respectively, 1,78 $P_d$ and 1,52 $P_d$. Figure 15b and Figure 16 plot the reinforcement stresses for the last step of the nonlinear analyses, where the x-reinforcement yielded with 10‰ strain. The load displacement curves for all performed numerical simulations are presented in Figure 17.
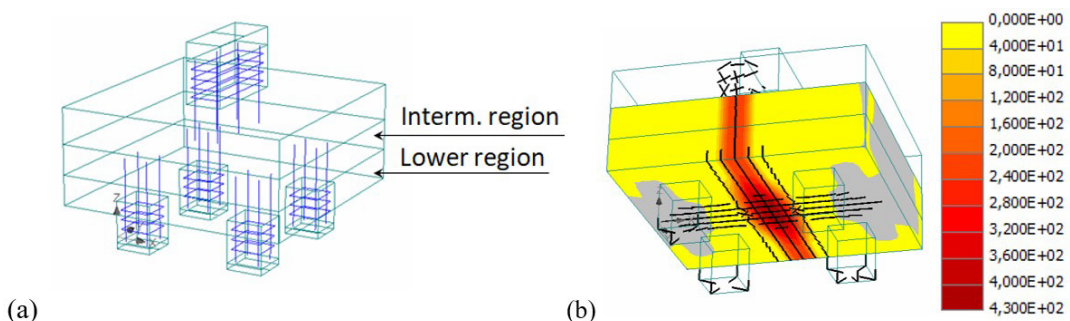


**Figure 15.** Numerical model ①: (a) reinforcement zones; (b) x-reinf. stresses (MPa) with crack pattern (crack widths > 0,1 mm only)
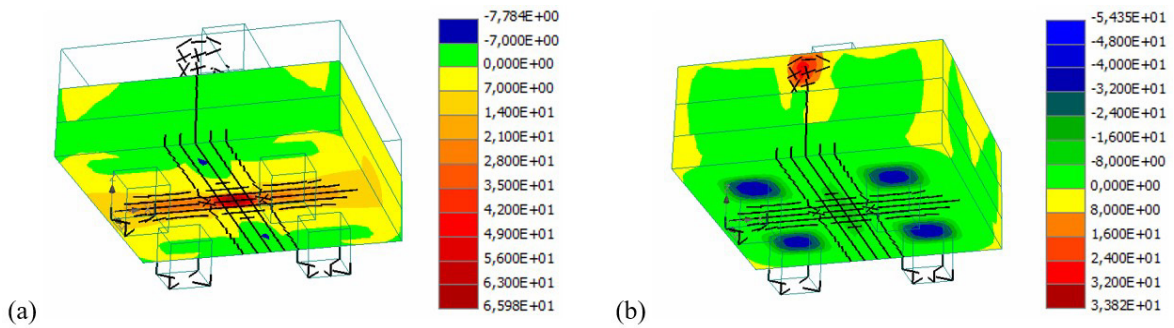
**Figure 16.** Numerical model ①: (a) *y*-reinf. stresses (MPa); (b) *z*-reinf. stresses (MPa)
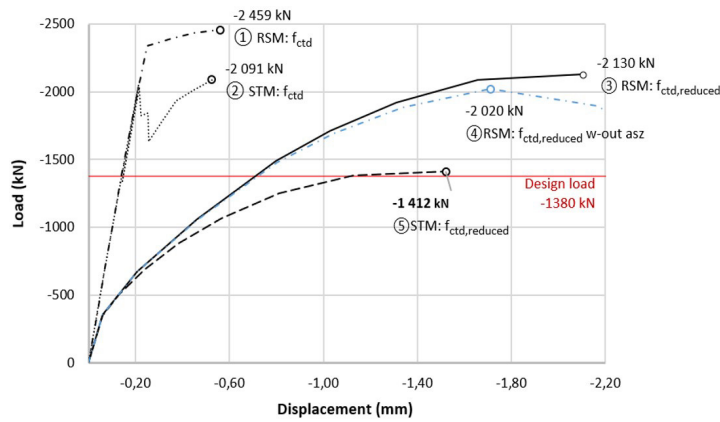


**Figure 17.** Load displacement curves for the performed numerical simulations

## 4.3 Discussion

The methodology presented for the RSM was applied to the design of a simple structural component to confirm the applicability of the proposed design method and to facilitate the discussion on the design variables.

**Four-pile cap.** The total required horizontal reinforcement for the RSM design was $A_{sx} = A_{sy} = 19,5$ cm$^2$, higher than the required reinforcement for a STM design ($A_{sx} = A_{sy} = 12,0$ cm$^2$) in which reinforcement in the *x*- and *y*-directions were all arranged at the bottom of the cap, maximizing the internal lever arm between tie and compression zone. The numerical simulations of models ③ and ④ indicated that reinforcement in the *z*-direction had little influence on the pile-cap collapse load, and this could be accounted on plastic redistribution of the equivalent reinforcement stresses in the *z*-direction. The pile cap could certainly be designed according to other well-established solutions. Brazilian design code [3] even explicitly recommends that the reinforcement be concentrated over the top of the piles when designing pile caps. However, the proposed application of methodology not only presents an alternative safe solution, but, more importantly, illustrates a procedure whose application may be efficiently extended to very complex structures.

**Benefits of the method.** Four main aspects are herein highlighted on behalf of the RSM for the design of structures with solid elements. First, the method predicates that all the structure volume participates in the resisting scheme, differently from the STM or the SFM, where stress fields are developed quantitatively in a few elements, and stress-free zones are disregarded outside the strut/tie zones. Second, the method relies neither on the development of a strut-and-tie scheme (or combined strut-and-tie schemes), nor on the definition of nodal geometries, nor on the application of an iterative procedure for the adjustment of the truss internal arms. Third, the method is applicable to the design or assessment of structural elements with general geometry, from the simplest to the most complex, subjected to any loading condition, even in discontinuity regions. Last, the RSM does not require running nonlinear analyses as in the application of strength reduction numerical methods. Examples of these methods are those presented by Mergny et al. [29], Abra and Ftima [30], and Yun et al. [31], which allow for the degradation of concrete by gradually reducing its tensile strength during the analysis in an iterative finite element analysis framework. The RSM is yet believed to be an efficient alternative in engineering practice due to its non-iterative application.

**Reinforcement layout**. The application of the RSM provides the designer a field of required reinforcement throughout the structural volume, expressed in terms of a reinforcement ratio distribution. In this way, opposed to STM, where the reinforcement layout is often concentrated, the RSM leads to a distributed reinforcement layout.

**Plasticity.** In the RSM design, since the final resisting model follows the elastic solution element by element, and reinforcement is provided throughout the structure volume, less stress redistribution and less plastic deformation are expected than in the STM design. Consequently, a more distributed crack pattern and smaller crack widths are also expected, improving the structural performance in both Ultimate and Serviceability Limit States.

**Design practice.** Structural models in current design practice are predominantly composed of bar and shell elements, while the use of solid elements is still largely ignored. This condition may be ascribed to two main reasons: difficulties arisen in treating the large amount of data resulting from the finite element linear analysis and, probably, the lack of knowledge of the rules for proportioning the required reinforcement. This paper disclosures the established design rules and presents an example of an effective design tool for the application of the RSM. Finally, it is worth noting that a paragraph of the Model Code [5] entitled "3D Solids" is dedicated to this design method. Further studies of this subject, including those accounting on serviceability states and detailing aspects, though still missing in recent references, shall enhance its application.

## 5 CONCLUSIONS

The following conclusions have been derived from this research:

- The RSM for the ULS design of structures is justified by the static method, based on the lower bound theorem of the Limit Analysis of the Theory of Plasticity, and yields safe solutions. It can be applied to any kind of structure, from the simplest to those with complex geometry and loading conditions, including discontinuity regions.
- There is a full set of equations for the *reinforcement design* and *concrete verification* of individual solid elements from three-dimensional stress fields obtained from linear analyses. Any applied stress state can be resisted by equivalent stresses in the concrete and in the reinforcement distributed in up to three orthogonal directions.
- A computational routine was developed for the automatic design of all set of individual elements within a structural model.
- The utilization of a post processor for the visualization of the resistance system (i.e., concrete and reinforcement equivalent stresses) provided a clear understanding of both overall structural behavior and local effects.
- Verifications assisted by numerical simulations confirmed the safety of the Reinforced Solid Method, as expected. In the case of the analyzed four-pile cap, the design resistance resulted approximately 50% higher than the design load.

## ACKNOWLEDGEMENTS

## REFERENCES

[1]  DIANAFEA. "Clinker silo." https://dianafea.com/project-clinkersilo (accessed May 1, 2022).

[2]  W. Commons. "Hydroelectric dam animation." https://commons.wikimedia.org/wiki/File:Hydroelectric_dam_animation_esp.ogv (accessed May 1, 2022).

[3]  Associação Brasileira de Normas Técnicas, *Projeto de Estruturas de Concreto: Procedimento*, NBR-6118, 2014.

[4]  International Federations for Structural Concrete, *fib Model Code for Concrete Structures 2010.* Berlin: Ernst & Sohn, 2013.

[5]  ACI Committee 318, *Building Code Requirements for Structural Concrete.* Detroit: Am. Concr. Inst., 2019.

[6]  A. Boer, "Design strategy structural concrete in 3D: focusing on uniform forces results and sequential analysis," Ph.D. dissertation," Tech. Univ. Delft, Delft, 2010.

[7]  A. P. Dolgikh and A. Podvysotskii, "A. Strength analysis of massive reinforced concrete structures using the method of equivalent shells," *Power Technol. Eng.*, vol. 44, no. 5, pp. 1, 2011.

[8]  S. Lisichkin, "Safety enhancement in large hydraulic structures from new spatial reinforcement methods," *Hydrotechnical Constr.*, vol. 35, no. 3, pp. 116–123, 2001.

[9]  S. B. Smirnov, "Problems of calculating the strength of massive concrete and reinforced concrete elements of complex hydraulic structures," *Power Technol. Eng.*, vol. 17, no. 9, pp. 471–476, 1983.

[10]  Y. Kamezawa, N. Hayashi, I. Iwasaki, and M. Tada, "A study on design methods of RC structures based on FEM analysis," *Proc. Jpn. Soc. Civ. Eng.*, vol. 25, no. 502, pp. 103–122, Nov 1994. [in Japanese].

[11] P. Marti, N. Mojsilović, and S. J. Foster, "Dimensioning of orthogonally reinforced concrete solids," in *Struct. Concr. Switzerland, fib-CH, fib-Congr.*, Osaka, Japan, 2002, pp. 18–23.

[12] S. J. Foster, P. Marti, and N. Mojsilović, "Design of reinforcement concrete solids using stress analysis," *ACI Struct. J.*, vol. 100, pp. 758–764, 2003.

[13] International Federations for Structural Concrete, *Practioners's Guide to Finite Element Modelling of Reinforced Concrete Structures, State-of-Art Report* (*fib* Bulletin 45). Lausanne: *fib*, 2008.

[14] P. C. J. Hoogenboom and A. Boer, "Computation of reinforcement for solid concrete," *Heron*, vol. 53, no. 4, pp. 247–271, 2008.

[15] P. C. J. Hoogenboom and A. Boer, "Computation of optimal concrete reinforcement in three dimensions," in *Computational Modelling of Concrete Structures*, N. Bicanic, R. De Borst, H. Mang and G. Meschke, Eds., London: Taylor & Francis, 2010, pp. 639–646.

[16] R. K. L. Su, L. W. Yan, C. W. Law, J. L. Huang, and Y. M. Cheng, "The provision of reinforcement in concrete solids using the generalized genetic algorithm," *J. Comput. Civ. Eng.*, vol. 25, no. 3, pp. 211–217, Jan 2010.

[17] A. S. Zalesov, O. D. Rubin, and S. E. Lisichkin, "Higher safety of massive hydraulic structures based on improved design norms," *Hydrotechnical Constr.*, vol. 28, no. 9, pp. 554–558, 1994.

[18] M. P. Nielsen and L. C. Hoang, *Limit Analysis and Concrete Plasticity*, 3rd ed. Boca Raton: CRC Press, 2011.

[19] A. Muttoni, J. Schwartz, and B. Thürlimann, *Design of Concrete Structures with Stress Fields.* Basel: Birkhäuser, 1996.

[20] W. Kaufmann, "Strength and deformations of structural concrete subjected to in-plane shear and normal forces," Ph.D. dissertation," Inst. Struct. Eng., Swiss Fed. Inst. Technol., Zurich, 1998.

[21] K. P. Larsen, "Numerical limit analysis of reinforced concrete structures: computational modeling with finite elements for lower bound limit analysis of reinforced concrete structures," Ph.D. dissertation," Tech. Univ. Denmark, Denmark, 2010.

[22] W. Kaufmann and J. Mata-Falcón, "Structural concrete design in the 21st century: are limit analysis methods obsolete?," in *24th Czech Concr. Days*, Litomyšl, 2017.

[23] International Federations for Structural Concrete, *fib Bulletin 100, Design and Assessment with Strut-and-Tie Models and Stress Fields: from Simple Calculations to Detailed Numerical Analysis – State-of-the-Art Report*. Lausanne: *fib*, Sep. 2021.

[24] N. S. Ottosen, "A failure criterion for concrete," *J. Eng. Mech. Div.*, vol. 103, pp. 527–534, 1977.

[25] ATIR, *STRAP Structural Analysis Programs – User´s Manual.* Israel: ATIR Eng. Software Dev., Dec. 2005.

[26] J. Ahrens, B. Geveci, and C. Law, "ParaView: an end-user tool for large data visualization" in *Visualization Handbook*, C. D. Hansen and C. R. Johnson, Eds., Paises Bajos: Elsevier, 2005.

[27] V. Cervenka, L. Jendele, and J. Cervenka, *ATENA Program Documentation – Part 1: Theoryi.* Prague: Červenka Consulting Ltd., 2005.

[28] M. Hendriks, A. Boer, and B. Belletti, *Guidelines for Nonlinear Finite Element Analysis of Concrete Structures*. Netherlands: Rijkswaterstaat Centre Infrastruct., 2016.

[29] E. Mergny, M. Ansriou, A. Lespagnard, A. Ouaar, and P. Latteur, "Stress analysis for the reinforcement of concrete massive structures, compatible with building methods," in *Proc. Int. Assoc. Shell Spatial Struct (IASS) Symp 2015*, Amsterdam, 2015.

[30] O. Abra and M. Ben Ftima, "Strength reduction design method for reinforced concrete structures: generalization," *Eng. Struct.*, vol. 258, pp. 114134, Mar 2022.

[31] Y. M. Yun, H. Chae, and J. A. Ramirez, "A three-dimensional strut-and-tie model for a four-pile reinforced concrete cap," *J. Adv. Concr. Technol.*, vol. 17, no. 7, pp. 365–380, Jul 2019.

Rev. IBRACON Estrut. Mater., vol. 16, no. 4, e16407, 2023

20/20

# IBRACON Structures and Materials Journal
## Revista IBRACON de Estruturas e Materiais

ORIGINAL ARTICLE

# Numerical analysis of the explosion of gas tanks using computational fluid dynamics

## Análise numérica da explosão de tanques de gás com o uso da fluidodinâmica computacional

Tiago Rodrigues Coelho de Moura[a] (iD)
Murilo Limeira da Costa Neto[b] (iD)
Graciela Nora Doz[a] (iD)

[a]Universidade de Brasília – UnB, Departamento de Engenharia Civil e Ambiental, Brasília, DF, Brasil
[b]Instituto de Educação Superior de Brasília – IESB, Departamento de Engenharia Civil, Brasília, DF, Brasil

**Abstract:** Buildings are composed of several systems, each with specific designs and regulations to ensure that constructions are safe and viable. Many residential, commercial, and industrial buildings have systems with gas central storage, which must be subjected to strict safety criteria to avoid accidents. In addition to the safety mechanisms provided by manufacturers, designers of these gas central storage must consider other devices to reduce explosion risk and mitigate the damaging blast effects. Explosions are physical-chemical phenomena that are characterized by the sudden expansion of a material and, consequently, energy release. When an accidental explosion occurs, much damage is caused by the shock wave and fragments. In the case of pressure vessels, a mechanical explosion can occur. Studying this explosion is essential to developing a more reliable, safe design for surrounding buildings and its users. This work aims to study the effects of gas tank explosions. In this study, the Autodyn computational tool based on fluid dynamics (CFD) is used. This software allows the modeling of complex explosion scenarios and the evaluation of blast wave parameters. For each numerical model, the overpressure levels outdoors and indoors are evaluated. The results indicated how the wave overpressures are distributed in different scenarios, and from them, it was possible to analyze the damaging levels.

**Keywords:** explosion, LPG tank, shock wave, overpressure, damage.

**Resumo:** As edificações são compostas por vários sistemas, cada um com projetos e normas específicas para garantir que as construções sejam seguras e viáveis. Muitos edifícios residenciais, comerciais e industriais possuem sistemas com centrais de gás, as quais devem ser submetidas à rigorosos critérios de segurança para evitar acidentes. Além dos mecanismos de segurança fornecidos pelos fabricantes, os projetistas dessas centrais de gás devem considerar outros dispositivos para reduzir o risco de explosão e mitigar os efeitos danosos da explosão. As explosões são fenômenos físico-químicos que se caracterizam pela expansão súbita de um material e, consequentemente, liberação de energia. Quando ocorre uma explosão acidental, muitos danos são causados pela onda de choque e fragmentos. No caso de vasos sob pressão, pode ocorrer a explosão mecânica e a compreensão dos efeitos desse evento é essencial para o desenvolvimento de projetos mais confiáveis e seguro para as edificações e seus usuários. Este trabalho tem como objetivo o estudo dos efeitos da explosão de tanques de gás. Neste estudo, é utilizada uma ferramenta computacional baseada em fluidodinâmica computacional (CFD); o Autodyn. Esse software permite a modelagem de cenários complexos de explosão e a avaliação de parâmetros de ondas de choque. Para cada modelo numérico, são avaliados os níveis de sobrepressão no exterior e no interior. Os resultados indicaram como se deu a distribuição das sobrepressões da onda em diversos cenários e partir deles foi possível traçar estimativas de dano.

**Palavras-chave:** explosão, tanque de GLP, onda de choque, sobrepressão, danos.

**Corresponding author:** Tiago Rodrigues Coelho de Moura. E-mail: tiago.trcm@email.com

# 1 INTRODUCTION

Residential and commercial buildings are composed of several systems, for example, structural, hydraulic, electrical, gas and others. In many constructions, there are gas supply systems, and, in some cases, this gas is stored in stationary tanks placed outside the building. These kinds of tanks are designed for high-pressure gas storage, the most common being LPG. There is an inherent risk of explosion when a gas tank is being used, and this risk can be related to manufacturing failures, careless maintenance, fire, incidents, and even criminal acts.

An explosion is a complex and non-linear phenomenon that results from a sudden energy release, and its magnitude is related to the amount of energy released [1]. The explosions can be originated from solid materials (plastic explosives, for example), liquids, or gas clouds, and they can be classified according to their nature as mechanical, chemical, or nuclear. Furthermore, there are also electrical explosions resulting from high-intensity electrical discharges. Chemical explosions occur through detonation (supersonic combustion process) or deflagration (subsonic combustion process).

The shock wave physics and its equations were studied by Zel'dovich and Raizer [2], who also explained the Lagrangian and Eulerian approaches applied to numerical analysis. An elementary and detailed explosion description and its effects can be found in the works of Kinney and Graham [1] and Needham [3].

This study focuses on mechanical explosion, which can be observed during the failure of a pressurized vessel. About this kind of explosion, Salzano et al. [4], Schleyer [5], and Ferradás et al. [6] presented a mathematical model to evaluate LPG tanks in a fire environment coupled with a risk analysis, an analysis of loading on structures and analysis the blast effects on buildings, respectively. The safety distance from a vapor cloud rapid deflagration was investigated by Li and Hao [7] using a numerical tool. In the context of a gas cloud, numerical simulations in environments with complex geometry were performed by Vianna and Cant [8], Ferreira and Vianna [9], [10], and Quaresma et al. [11]. These researchers used a computational tool with meshes based on Porosity Distributed Resistance (PDR). In the PDR approach, objects smaller than the computational grid occupy only part of each computational cell; thus, only part of the cell volume is available for flow [12]. According to Cain [13], the blast wave emanating from the bursting pressure vessel is somewhat similar to that caused by a high explosive detonation; however, the blast wave overpressure values may diverge at short standoff distances. Therefore, a suitable prediction of energy loss by dissipation process is needed in order to achieve accurate results when simulating stored energy using high explosives. Molkov and Kashkarov [14] compiled some methods in their research to predict mechanical energy stored in gas-pressurized tanks.

Gas explosion overpressures in confined spaces were numerically simulated by Wang et al. [15] and Li et al. [16]. In addition to these studies, using computational fluid dynamics, Cen et al. [17] and Pang et al. [18] performed gas tank explosion simulations in an apartment and in a kitchen, respectively. Numerical research about explosion overpressures in urban and residential environments and the use of obstacles to mitigate shock wave effects was carried out by Costa and Doz [19] and Vyazmina et al. [20].

Most recorded explosions involving gas tanks occur accidentally. Therefore, there is little data about overpressures and shock wave propagation from these explosions. Most information about these events is related to residual damage of damaged buildings. Despite this scenario, Stawczyk [21] and Tschirschwitz et al. [22] carried out experiments with exploding gas tanks, and a study about high-speed fragments from pressure vessel explosions was presented by Vaidogas [23].

Semi-empirical models are a reliable approach to studying explosion phenomena, and they can be used as an alternative to real-scale experiments that are expensive and dangerous to carry out. However, these models are unable to represent complex events such as shock wave reflections and channeling. Numerical methods are essential tools to overcome these limitations.

Currently, there are some numerical tools for explosion simulation, for example, Autodyn, FLACS, and STOKES (Shock Towards Kinetic Explosion Simulator). According to Quaresma et al. [11], the STOKES is a PDR-based code that can be used to modeling gas explosions in complex environments, the porous mesh generated by STOKES can evaluate the effects of small scale obstacles without the need of considerable mesh refinement. Autodyn is a tool that can simulate detonations, impacts and other severe loading problems, where the results can be remapped to other analysis systems within the Ansys® Workbench for further analysis. According to Tham [24], one unique feature of Autodyn is it allows different parts of a single problem to be modeled with their appropriate numerical formulation, allowing a user to couple different numerical solution techniques in a single problem.

This work aims the analysis of a gas tank blast effects in terms of overpressure data on close buildings. A correlation between the overpressure levels and the threshold parameters for buildings and its users is performed. The computational fluid dynamics (CFD) tool Autodyn from the Ansys® package is used for this research.

# 2 EXPLOSION PARAMETERS

Several parameters can influence gas tank explosion analysis, such as the amount of stored energy, explosion standoff distance, tank geometry and overpressures distribution. In order to achieve reliable results these parameters must be correctly addressed by the predictive methods and numerical approach.

## 2.1 Method of predicting mechanical energy in pressure vessels

A reliable prediction of the stored energy in pressure vessels is an essential part of explosion analysis. Molkov and Kashkarov [14] presented a compilation of several methods to calculate the energy of a physical explosion, such the Brode's equation, the isentropic expansion, the isothermal expansion and thermodynamic availability that are related with ideal gas model. The isothermal and thermodynamic availability models are restricted to cases where the temperature at the beginning and end of the process is the same. The energies obtained by the Brode models and isentropic expansion are similar and smaller than that obtained by previous two models, where, in this case, the Brode model is more realistic with less restricting assumptions. Molkov and Kashkarov [14] suggested also the Abel-Noble equation of state to non-ideal gas analysis, which improves the predictive capacity of energy stored in gas tanks, as it represents a more realistic situation of the problem. In a hermetically sealed vessel filled with pressurized gas, the mechanical energy can be calculated as the product of the mass of the gas, specific heat at constant volume, and temperature [14].

Introducing the Abel-Noble equation for energy calculation, we have Equation 1. Equation 2 is the gas co-volume expression [25], a parameter that represents the volume occupied by gas molecules per unit mass.

$$E = \left( \frac{P_g - P_0}{(R_u / M)T + b(P_g - P_0)} \right) V_g \left( \frac{C_v}{M} \right) T \tag{1}$$

$$b = \frac{RT_c}{8P_c} \tag{2}$$

Where $E$ = stored mechanical energy (J); $P_g$ = stored gas pressure (Pa); $P_0$ = ambient pressure (approximately equal to 101325,0 Pa at sea level); $V_g$ = stored gas volume (m³); $C_v$ is the specific heat at constant volume (J/mol·K); $T$ = gas temperature (K); $R_u$ = universal gas constant (equal to 8,314462618 J/mol·K); $M$ = molar mass of gas (kg/mol); $b$ = co-volume of gas (m³/kg); $R$ = gas constant (J/kg·K), $T_c$ = critical point temperature (K); and $P_c$ = pressure of the critical point of the gas (Pa).

## 2.2 TNT-equivalent mass

Gas tank explosions can be analyzed using methodologies classified into three categories according to their nature: the TNT (trinitrotoluene) equivalence method, blast curve methods and numerical simulations [26]. Sochet [27] presents an overview of analytical models for explosion analysis and highlights their limitations.

TNT-equivalent method is an analytical model that uses the scaled distance and semi-empirical equations (detailed in the following item) to evaluate the overpressure peaks. Crowl and Louvar [28] mentioned that the main advantage of this method is the simple to use, this advantage was observed by Lopes and Melo [29] in the study on the explosion of hydrogen cylinders in nuclear power plants. As noted by Cain [13], the TNT-equivalent method can be used to estimate the gas tank explosion overpressure in the far field. In the nearby field, López et al. [30] observed that it is possible to use this method when the explosion yield is correctly adjusted to the model in order not to overestimate the overpressures.

The methodology adopted in this paper is a mixed process that involves analytical and numerical methods. The use of analytical models is related to predicting the mechanical energy stored in the tank, the TNT-equivalent mass, and the blast wave overpressure at validation points. TNT detonation and shock wave propagation analysis in complex scenarios are performed using numerical models.

In this study, only the mechanical energy of the explosion was considered since the contribution of the chemical portion only occurs if the gas mixture is ignited. Thus, the TNT-equivalent mass was obtained by the direct correlation between the mechanical energy stored in the gas tank and the specific energy released in a TNT explosion. This specific energy is approximately equal to 4.184 MJ/kg, Bolonkin [31]. The explosion yield in terms of the generated shock wave was estimated in an energy loss analysis detailed below in item 3.4.

## 2.3 Analytical equations for predicting explosion overpressures

Shock waves are disturbances that propagates through the air carrying a large amount of kinetic energy, the typical overpressures distribution of a shock wave is shown in Figure 1. Overpressure is an important parameter in a prior damage assessment, it is defined as the difference between the shock wave pressure and the ambient pressure.

Figure 1 also illustrates the shock wave phases. The positive phase of the shock wave shows a higher overpressure magnitude but a short duration when compared to the negative phase.
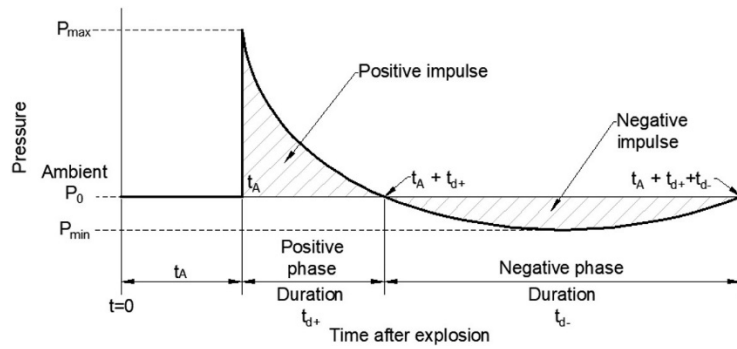
**Figure 1.** Typical scheme of a shock wave from an ideal explosion from a spherical source in an open environment [32] - adapted.

Semi-empirical methods can be used for a preliminary overpressure analysis, those methods are related with scaled distance (Equation 3) that measures the effects of the explosion in terms of energy dispersion by relating the standoff distance with explosive mass.

$$Z = \frac{R}{\sqrt[3]{W}}$$
(3)

Were $Z$ = scaled distance (m/kg$^{1/3}$); $R$ = distance from explosion center to analysis point (m); and $W$ = TNT mass (kg).

The overpressures can be predicted with the semi-empirical models shown in Table 1, that are valid for open-air explosions from spherical explosive charges.

**Table 1.** Semi-empirical overpressure ($\Delta P$) prediction equations [33].

| Author | Prediction formulas | | Requirement | Unit |
|---|---|---|---|---|
| Brode | $\Delta P = \dfrac{6,7}{Z^3} + 1$ | (4) | $\Delta P > 10$ | Bar |
| | $\Delta P = \dfrac{0,975}{Z} + \dfrac{1,455}{Z^2} + \dfrac{5,85}{Z^3} - 0,019$ | (5) | $0,1 < \Delta P < 10$ | Bar |
| Henrych | $\Delta P = \dfrac{14,072}{Z} + \dfrac{5,540}{Z^2} - \dfrac{0,357}{Z^3} + \dfrac{0,00625}{Z^4}$ | (6) | $0,05 \leq Z \leq 0,3$ | Bar |
| | $\Delta P = \dfrac{6,194}{Z} - \dfrac{0,326}{Z^2} + \dfrac{2,132}{Z^3}$ | (7) | $0,3 \leq Z \leq 1$ | Bar |
| | $\Delta P = \dfrac{0,662}{Z} + \dfrac{4,05}{Z^2} + \dfrac{3,288}{Z^3}$ | (8) | $1 \leq Z \leq 10$ | Bar |
| Mill | $\Delta P = \dfrac{1772}{Z^3} - \dfrac{114}{Z^2} + \dfrac{108}{Z}$ | (9) | - | kPa |
| Kinney | $\dfrac{\Delta P}{P_0} = \dfrac{808\left[1 + \left(\dfrac{Z}{4,5}\right)^2\right]}{\sqrt{1 + \left(\dfrac{Z}{0,048}\right)^2}\sqrt{1 + \left(\dfrac{Z}{0,32}\right)^2}\sqrt{1 + \left(\dfrac{Z}{1,35}\right)^2}}$ | (10) | - | - |
| Newmark | $\Delta P = 6784\dfrac{W}{R^3} + 93\left(\dfrac{W}{R^3}\right)^{1/2}$ | (11) | - | Bar |

Rev. IBRACON Estrut. Mater., vol. 16, no. 4, e16408, 2023

4/15

## 2.4 Overpressure limits for damage to humans and structures

Overpressure levels can be directly related with building damage assessment, as shown in Table 2. According to Baker et al. [35] the damaging effects of explosions on building users can be direct and indirect. The direct effects are related to the shock wave overpressures (Table 3) and the indirect effects are related with debris at high speed from damaged materials.

When a shock wave collides with a living being, part of its energy is reflected, and another fraction is absorbed and transmitted to body tissues. As a result, the absorbed kinetic energy causes stress waves, leading to rapid physical deformation that can result in a tissue rupture [32].

**Table 2.** Shock wave effects on structures [34].

| Damage | Overpressure (ΔP) | |
|---|---|---|
| | **Bar** | **psi** |
| Glass breakage | 0,01 – 0,015 | 0,15 – 0,22 |
| Minimal damage to buildings | 0,035 – 0,075 | 0,52 – 1,12 |
| Damage to metal panels | 0,075 – 0,125 | 1,12 – 1,87 |
| Failure of wooden panels (buildings) | 0,075 – 0,15 | 1,12 – 2,25 |
| Failure in brick walls | 0,125 – 0,2 | 1,87 – 3 |
| Rupture of refinery tanks | 0,2 – 0,3 | 3 – 4,5 |
| Damage to buildings (metallic structures) | 0,3 – 0,5 | 4,5 – 7,5 |
| Damage to concrete structures | 0,4 – 0,6 | 6,0 – 9,0 |
| Probable total destruction of most buildings | 0,7 – 0,8 | 10,5 - 12 |

**Table 3.** List of some damages caused to humans [34].

| Damage | Overpressure (ΔP) | |
|---|---|---|
| | **Bar** | **psi** |
| Tolerable (does not cause damage) | up to 0,0001 | up to 0,0015 |
| Fall | 0,07 – 0,1 | 1,05 – 1,5 |
| Eardrum rupture | 0,35 – 1,0 | 5,25 – 15 |
| Lung injuries | 2,0 – 5,0 | 30 – 75 |
| Lethality | 7,0 – 15,0 | 105 – 225 |

## 3 PRELIMINARY ANALYSISL

### 3.1 Gas tanks normative parameters

In this study, LPG tanks are considered static, that is, placed in fixed locations on the ground surface or underground. The design parameters established by ABNT [32] were considered in all modeled gas tanks, as summarized in Table 4.

**Table 4.** Types and characteristics of tanks according to ABNT [36].

| Tank type | | Tank volume | Distance from the tank to the building and openings | Model identification |
|---|---|---|---|---|
| Aboveground | A | up to 0,5 m³ | next to the building and 3 m from the opening | model 1 |
| | B | from 0,5 to 2,0 m³ | 1,5 m from the building and 3 m from the opening | model 2 |
| | C | from 2,0 to 5,5 m³ | 3 m from the building | model 3 |
| | D | from 5,5 to 8,0 m³ | 7,5 m from the building | model 4 |
| | E | from 8,0 to 120,0 m³ | 15 m from the building | model 5 |
| Underground | A | up to 8,0 m³ | 3 m from the building | model 6 |
| | B | from 8,0 to 120,0 m³ | 15 m from the building | model 7 |

### 3.2 Tank manufacturing parameters

LPG tanks are hermetically sealed vessels resistant enough to withstand high internal pressures. Generally, these tanks have a rounded geometry to minimize the risk of rupture due to stress concentration.

In this work, the most common high-pressure design (2.0 MPa) was considered for all LPG tanks. These high pressures that keep the gas in a liquid state and vary as a function of the temperature and proportion of the hydrocarbon mixture.

### 3.3 Gas properties

Propane gas requires more pressure to liquefy than other hydrocarbons that compose LPG. Therefore, it represents a riskier situation when compared to other hydrocarbons. Table 5 presents the propane properties adopted in the energy prediction of all the tanks studied in this work.

**Table 5.** Physical and chemical propane gas properties adopted [25] – adapted.

| Reference temperature (T) | 15° C (288,2 K) |
|---|---|
| Specific mass in liquid state ($\rho$) | 581 kg/m³ |
| Specific heat at constant pressure ($C_p$) | 74,057 J/mol·K |
| Specific heat at constant volume ($C_v$) | 65,744 J/mol·K |
| Specific heat ratio ($\gamma$) | 1,126 |
| Molar mass (M) | 0,044097 kg/mol |
| Molar constant (R) | 188,5 J/kg·K |
| Critical point temperature ($T_c$) | 370 K |
| Critical point pressure ($P_c$) | 4,26 MPa |
| Co-volume (b) – obtained by Equation 2 | 0,00205 m³/kg |

### 3.4 Energy loss analysis

It should be pointed out that energy from an explosion is dissipated in several ways, such as shock waves, heat, sound, movement of fragments, and others. Therefore, not all the energy released in the explosion is carried by the shock wave, some part of this energy is lost. In a pressure vessel explosion, this energy loss is related with tank deformation and rupture process.

According to Lees [37], about 40% to 80% of the energy of the explosion is carried by the shock wave, it is possible to infer that the energy loss is a calibration factor. In order to calibrate the energy loss to the simulated models, a preliminary simulation based on the experiments of Tschirschwitz et al. [22] was made. The tank properties and the measured overpressures at gauges positions are shown in Table 6.

**Table 6.** Experimental data from Tschirschwitz et al. [22].

| Tank | | Moment of rupture | | Overpressures ($\Delta P$) | | |
|---|---|---|---|---|---|---|
| Identification | Volume | Pressure in the tank | Gas temperature | (L = 5 m) | (L = 7 m) | (L = 9 m) |
| PC07 (experiment 1) | 0,0272 m³ | 82,1 bar | 111,4 °C | 0,15 bar | 0,11 bar | 0,09 bar |
| PC09 (experiment 2) | 0,0272 m³ | 86,9 bar | 97,0 °C | 0,15 bar | 0,11 bar | 0,10 bar |

Note: L is the distance from the overpressure sensor to the center of the explosion.

The simulation results were compared with experimental and semi-empirical models, as shown in Figure 2. In this case, it is possible to see that the semi-empirical methods are not accurate enough for close range explosions because they do not account the shock wave reflection phenomena on the ground.

The estimated energy loss was initially recalculated through a model update process based on the experimental results. It was possible to define the value of energy loss at approximately 25%, which is within the values range exposed by Lees [37]. In this sense, the explosion yield concerning the portion of energy involved in the shock wave formation is 75%. This value was considered in subsequent simulations that share similar modeling.
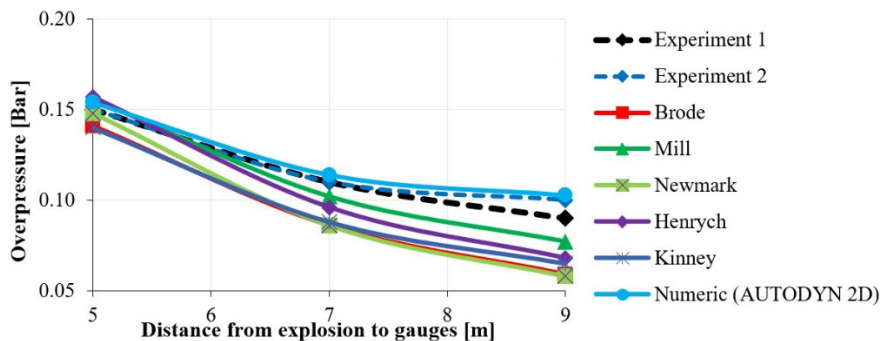


**Figure 2.** Overpressures as a function of the explosion distance of a propane gas tank with a volume of 27.2 liters.

Rev. IBRACON Estrut. Mater., vol. 16, no. 4, e16408, 2023

6/15

## 3.5 TNT equivalent mass for each type of tank

The TNT equivalent mass was obtained considering the energy loss and the mechanical energy formulation from Equation 1, as shown in Table 7.

**Table 7.** Stored energy and TNT equivalent mass in each tank type.

| Tank type | | Mechanical energy stored in the tank [J] | Energy loss rate | Specific energy of the TNT explosion [J/g] | TNT equivalent mass [kg] |
|---|---|---|---|---|---|
| Aboveground | A | 7.005.291,9 | 25,0% | 4184,0 | 1,256 |
| | B | 28.021.167,7 | 25,0% | 4184,0 | 5,023 |
| | C | 77.058.211,2 | 25,0% | 4184,0 | 13,813 |
| | D | 112.084.670,8 | 25,0% | 4184,0 | 20,092 |
| | E | 1.681.270.061,9 | 25,0% | 4184,0 | 301,375 |
| Underground | A | 112.084.670,8 | 25,0% | 4184,0 | 20,092 |
| | B | 1.681.270.061,9 | 25,0% | 4184,0 | 301,375 |

## 4 NUMERIC SIMULATIONS

The simulations were performed using Autodyn from Ansys® Workbench, this software uses explicit time integration to solve the fundamental equations of fluid dynamics: the equation of continuity, momentum, and energy. Several materials and problems can be modelled in Autodyn, where the mathematical relationships between internal energy, density, pressure, stresses, and strains are summarized in an Equation of State (EOS), strength constitutive model and failure criteria, also cell erosion conditions can be enabled.

Autodyn is suited to modelling severe and fast loading problems such that involving impacts, explosions, and fragmentation.

Previous numerical simulations showed that mesh size influences the numerical accuracy and the computation time consumption as well. The influence of mesh size for all simulated models results was investigated.

## 4.1 Problems modelling

Two environments that represents common situations in typical urban buildings were simulated (Figures 3 and 4). These models were built to meet the standoff specifications described by the ABNT [36], as presented in Table 4.

The walls and slabs' thickness are 100 mm in all models, and the height between the floor and slab is 2900 mm. Walls and slabs are made of 35 MPa concrete, and the ground is composed of sand. All materials used are present in the Autodyn library.
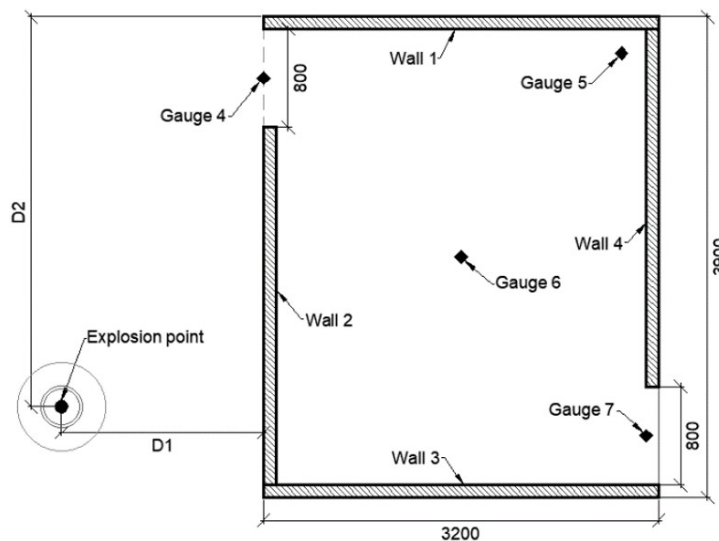


**Figure 3.** Floor plan for models 1 and 2 (All dimensions are in millimeters)

Rev. IBRACON Estrut. Mater., vol. 16, no. 4, e16408, 2023

7/15
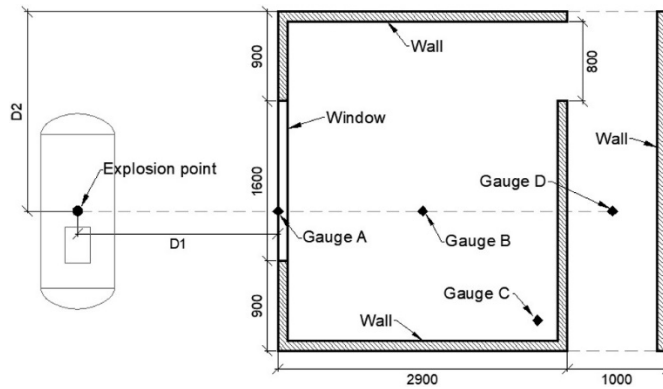
**Figure 4.** Floor plan for models 3 to 7 (All dimensions are in millimeters)

The main objective of the simulations was to measure the overpressure peaks around and inside the building in the first few milliseconds after detonation (between 20 ms and 40 ms). The simulation of large deformations, strain, and fragmentation may lead to an increased simulation time. To avoid this nuisance, rigid solid elements were used as boundary conditions, this consideration had a minor impact on overpressure final peak results. This consideration was also adopted in the simulations carried out by Luccioni, Ambrosini, and Danesi [38]. The solid elements were discretized with a Lagrangian mesh and the air with a Eulerian mesh. The boundary condition imposed on the faces of the air domain was "flow out" to not reflect the shock wave.

Table 8 shows the tank details for each model, where distance D1 is equal to half of the tank diameter added to the minimum distance provided in Table 4.

**Table 8.** Detailing of the tanks in each model.

| Model | Tank situation | Tank diameter [mm] | Distances of the explosion in relation to the building | | Explosion point height from ground level [mm] |
|---|---|---|---|---|---|
| | | | D1 [mm] | D2 [mm] | |
| 1 | aboveground | 1000 | 500 | 3900 | + 1200 |
| 2 | aboveground | 1200 | 2100 | 3050 | + 1200 |
| 3 | aboveground | 2000 | 4000 | 2000 | + 1200 |
| 4 | aboveground | 2200 | 8600 | 2000 | + 1200 |
| 5 | aboveground | 2400 | 16200 | 2000 | + 1300 |
| 6 | underground | 2000 | 4000 | 2000 | - 1500 |
| 7 | underground | 2400 | 16200 | 2000 | - 1700 |

Note: the plus sign (+) indicates the explosion point is above ground level and the minus sign (-) indicates the point is below ground level.

Before discretizing the entire models in the Autodyn 3D environment, the TNT explosives were simulated as wedge elements. The wedge element is one-dimensional, so the processing time is faster. Figure 5 presents the wedge concept of spherical geometry and the discretization in Autodyn. After this first approach for detonation, the explosion data was remapped to the three-dimensional models.
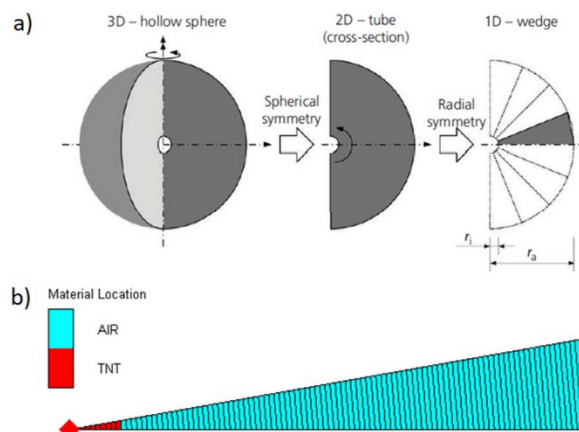


**Figure 5.** a) Wedge model for spherically symmetric problems [39]; b) Discretized wedge with air and TNT on Autodyn.

## 4.2 Aboveground stationary tank simulations

Aboveground stationary tanks are placed outside the building. The overpressure gauges were placed at the corners (200 mm from building wall surface), the middle of the door, room center, and windows.

In larger models, some gauges were placed in the external space next to the explosion. Gauges 1, 2, and 3 are placed in positions where there was no effect of shock wave reflection influence on initial results. The data obtained from these three overpressure gauges were compared with the results of the semi-empirical methods.

**Table 9.** Discretization data for models 1 and 2 with 25 mm mesh.

| Part | Origin point coordinates | | | Dimensions in each direction [mm] | | | Number of mesh elements in each direction | | |
|---|---|---|---|---|---|---|---|---|---|
| | x | y | z | Dx | Dy | Dz | Nx | Ny | Nz |
| Air | 0 | 0 | 0 | 5800 | 3100 | 3900 | 232 | 124 | 156 |
| Ground | 0 | 0 | 0 | 5800 | 100 | 3900 | 232 | 4 | 156 |
| Wall 1 | 2600 | 100 | 0 | 3200 | 2900 | 100 | 128 | 116 | 4 |
| Wall 2 | 2600 | 100 | 900 | 100 | 2900 | 2900 | 4 | 116 | 116 |
| Wall 3 | 2600 | 100 | 3800 | 3200 | 2900 | 100 | 128 | 116 | 4 |
| Wall 4 | 5700 | 100 | 100 | 100 | 2900 | 2900 | 4 | 116 | 116 |
| Slab | 2600 | 3000 | 0 | 3200 | 100 | 3900 | 128 | 4 | 156 |

Models 1, 2, 3, and 4 were discretized with 100, 50, and 25 mm meshes. The model 5 was discretized with 100 and 50 mm meshes only, due its large geometric dimensions. Table 9 presents the discretization data of models 1 and 2, and Figure 6 shows them already discretized in Autodyn. All other models followed the same discretization procedure.
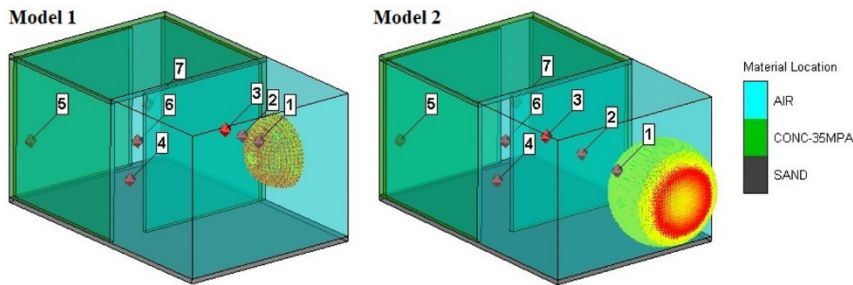


**Figure 6.** Models 1 and 2 discretized in Autodyn.

The modelled space of models 3 to 7 were wider because the tanks are bigger in size, as presented in Figure 4.

Figure 7 presents the models 3, 4 and 5 in Autodyn interface. The external gauges are identified with numbers and the internal ones with letters. The internal gauges are arranged in the same positions for all models.
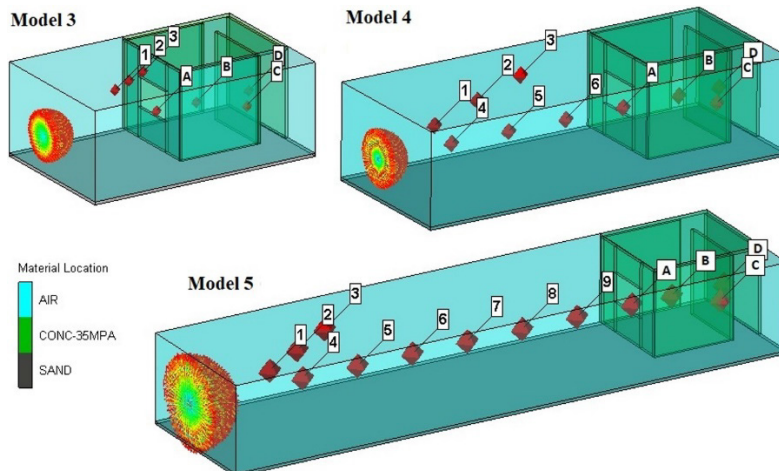


**Figure 7.** Models 3, 4 and 5 discretized on Autodyn.

Rev. IBRACON Estrut. Mater., vol. 16, no. 4, e16408, 2023

9/15

The distances of the external gauges to the explosion center are detailed in Table 10.

**Table 10.** Distance in meters from the external gauges to the explosion center.

| Gauge | 1 | 2 | 3 | 4 | 5 | 6 | 7 | 8 | 9 |
|---|---|---|---|---|---|---|---|---|---|
| Model 1 | 1,594 | 2,790 | 3,986 | - | - | - | - | - | - |
| Model 2 | 1,368 | 2,438 | 3,509 | - | - | - | - | - | - |
| Model 3 | 2,689 | 3,087 | 3,735 | - | - | - | - | - | - |
| Model 4 | 2,112 | 3,697 | 5,281 | 2,600 | 4,600 | 6,600 | - | - | - |
| Model 5 | 3,040 | 4,050 | 5,070 | 4,200 | 6,200 | 8,200 | 10,200 | 12,200 | 14,200 |

## 4.3 Underground stationary tank simulations

The tank's arrangement is underground because they are inserted in reinforced concrete shelters below ground level as shown in Figure 8. The simulated models 6 and 7 share the same building design as presented in Figure 4 as well the minimum safety distances according to ABNT [36] recommendations summarized in Table 4. Figure 9 presents models 6 and 7 discretized in Autodyn.
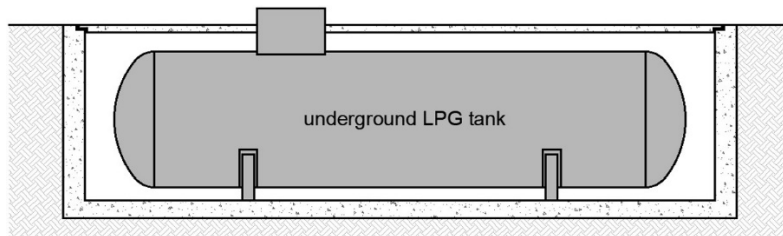


**Figure 8.** Sectional diagram of the concrete shelter for the underground tanks.
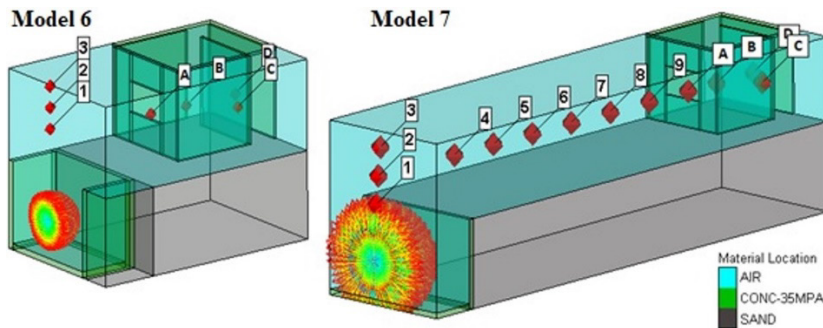


**Figure 9.** Models 6 and 7 discretized in Autodyn.

The sealing of the upper part of the shelter (the cover) was disregarded to analyze a critical situation for all models. Table 11 presents the distances of the external gauges to the explosion center.

The models 6 was discretized with 100, 50, and 25 mm meshes and the model 7 was discretized with 100 and 50 mm meshes only.

**Table 11.** Distance in meters from the external gauges to the explosion center.

| Gauge | 1 | 2 | 3 | 4 | 5 | 6 | 7 | 8 | 9 |
|---|---|---|---|---|---|---|---|---|---|
| Model 6 | 3,000 | 3,700 | 4,400 | - | - | - | - | - | - |
| Model 7 | 2,009 | 3,015 | 4,020 | 4,200 | 6,200 | 8,200 | 10,200 | 12,200 | 14,200 |

Note: the distances from gauges 4 to 9 refer to the horizontal components for model 7. The explosion point is below ground level.

Rev. IBRACON Estrut. Mater., vol. 16, no. 4, e16408, 2023

10/15

## 4.4 Numerical models validation

Figures 10, 11, and 12 present the overpressure results for gauges 1, 2, and 3 of all models. It is possible to observe a good convergence between the numerical and semi-empirical results.
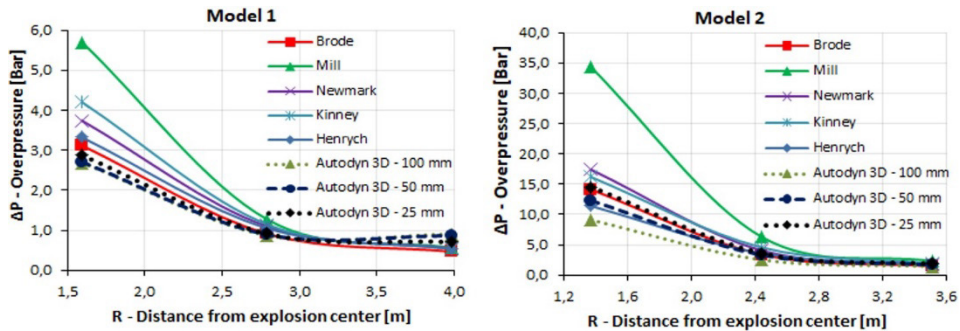


**Figure 10.** Overpressure peaks on gauges 1, 2, and 3 for models 1 and 2.
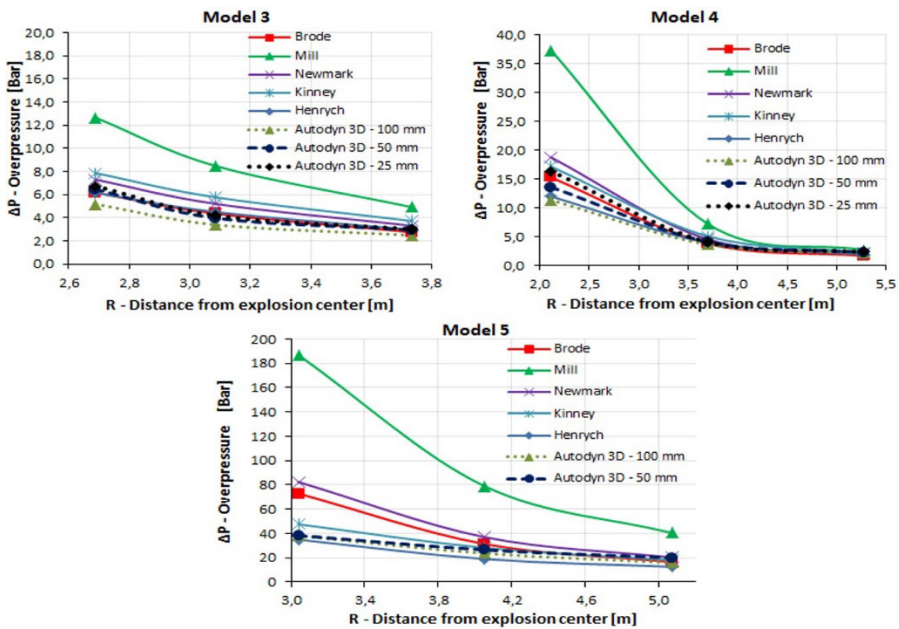


**Figure 11.** Overpressure peaks in gauges 1, 2, and 3 for models 3 to 5.
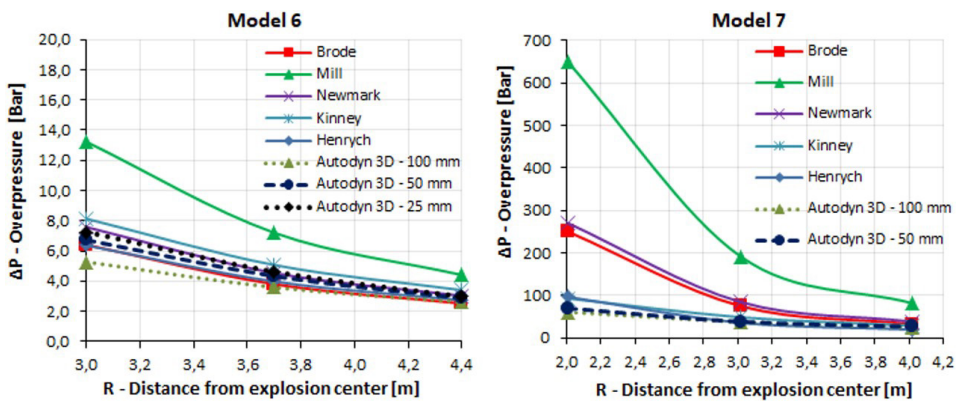


**Figure 12.** Overpressure peaks in gauges 1, 2, and 3 for models 6 and 7.

Rev. IBRACON Estrut. Mater., vol. 16, no. 4, e16408, 2023

11/15

## 5 RESULTS AND DISCUSSIONS

Figures 13, 14, and 15 presents the overpressure results of all models. It is possible to see that more refined mesh tends to show higher overpressure values, this can be related with the more accurate interaction of the shock wave reflections.

The aboveground tank explosion simulation results showed that peak overpressure decreases as the explosion distance increases.

It is possible to notice the effect of the shock wave reflection in gauge 5 when comparing models 1 and 2. In quantitative terms, considering the models 1 and 2 of 25 mm mesh size, the overpressure increased 87,6% at gauge 5.

The channeling effect caused by shock wave confinement was noticed in models 3, 4, and 5, which can be identified by the overpressure levels in gauge D.

Considering the underground tank explosion, the results showed a substantial reduction in overpressure levels when compared to aboveground tanks. In model 6, for example, which is based on an underground tank, the overpressure peaks of most gauges are lower than the measured values of the model 3 aboveground tank, which has a smaller volume.

When comparing models 5 and 7, it is clear that the underground tank model showed many advantages in terms of safety over the stationary open-air models.

Considering the damage assessment, it is clear that all accidental explosions simulated in this paper may represent some risk level for both the building and its users. These risks can be identified by correlating the simulation results with the parameters of Tables 2 and 3. It was noted that there is no risk of death in the indoor environments of all analyzed models; however, several injuries can occur, such as eardrum rupture and lung damage.

The observed overpressure levels can result in glass breakage, brick wall failure, and even possible minor damage to structural components.
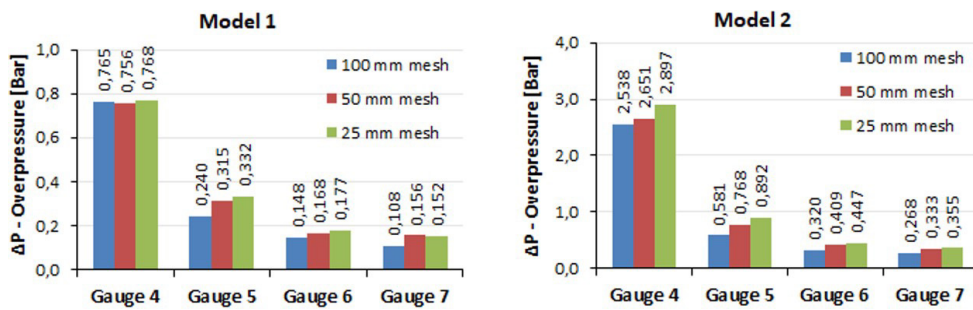


**Figure 13.** Overpressure peaks in gauges 4 to 7 of models 1 and 2 (explosions of aboveground tanks with volumes of 0,5 m³ and 2,0 m³).
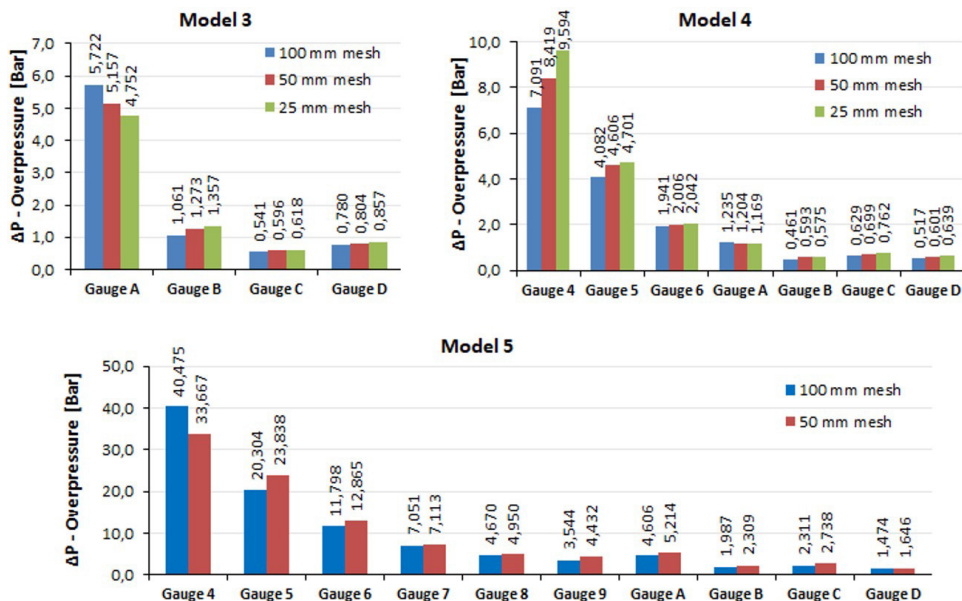


**Figure 14.** Overpressure peaks in gauges of models 3, 4, and 5 (explosions of aboveground tanks with volumes of 5,5 m³, 8,0 m³, and 120 m³).

Rev. IBRACON Estrut. Mater., vol. 16, no. 4, e16408, 2023

12/15
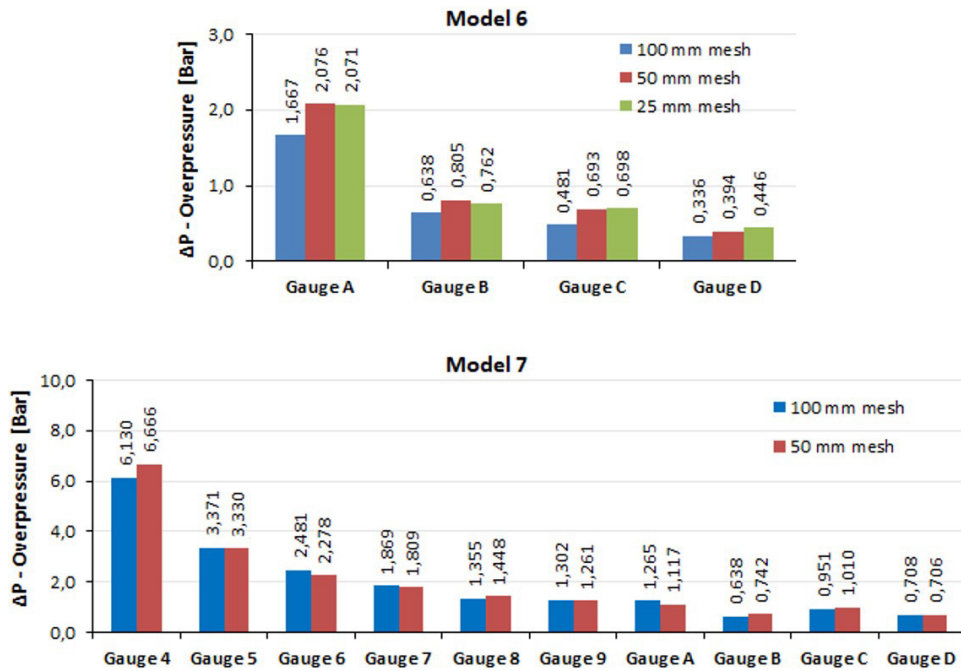
**Figure 15.** Overpressure peaks in the indicated gauges of models 6 and 7 (explosions from underground tanks with volumes of 8,0 m$^3$ and 120 m$^3$).

## 6 CONCLUSION

In this work, numerical simulations were performed with TNT-equivalent mass to represent the propane tanks explosion.

It was observed in the numerical simulations that there is an overpressure increase in models with refined meshes, this can be related with the more precise interaction of the shock wave with solid surfaces that leads to a more accurate shock wave reflection modeling.

The results also showed that the shock wave reflection and channeling phenomena directly influenced the overpressure results. Reflection phenomenon occurred mainly in the building internal environments and its effects were more evident in the corners. Shock wave channeling occurred in the models with narrow corridors.

The underground tanks simulations results showed a different shock wave behavior around the explosion. In this case, there is predominantly a redistribution of the blast energy through the medium since the dispersions by the tank sides tend to be contained by the ditch and redirected upwards. Therefore, the energy that reaches the building represents a small portion of what was released by the explosion. It is possible to conclude that underground tanks represent a very efficient technique to mitigate the accidental explosion effects, which justifies its use in urban environments.

Numerical simulations validated by experimental data can be a useful tool to provide a reliable data about the overpressure distributions in close range standoffs that can aid building designers to a safer placement of gas tanks considering distances from buildings and pedestrian walkways.

## REFERENCES

[1] G. F. Kinney and K. J. Graham, *Explosive Shocks in Air*, 2nd ed. New York: Springer Science+Business Media, 1985.

[2] Y. B. Zel'dovich and Y. P. Raizer, *Physics of Shock Waves and High-Temperature Hydrodynamic Phenomena.* New York: Academic Press, 1966.

[3] C. E. Needham, *Blast Waves*, 2nd ed. Berlin: Springer, 2010.

[4] E. Salzano, B. Picozzi, S. Vaccaro, and P. Ciambelli, "Hazard of pressurized tanks involved in fires," *Ind. Eng. Chem. Res.*, vol. 42, no. 8, pp. 1804–1812, 2003, http://dx.doi.org/10.1021/ie020606r.

[5] G. K. Schleyer, "Predicting the effects of blast loading arising from a pressure vessel failure: a review," *Proc. Inst. Mech. Eng., E J. Process Mech. Eng.*, vol. 218, no. 4, pp. 181–190, 2004, http://dx.doi.org/10.1243/0954408042466936.

[6] E. G. Ferradás, F. D. Alonso, J. F. S. Pérez, M. D. Miñarro, A. M. Aznar, and J. R. Gimeno, "Consequence analysis to buildings from bursting cylindrical vessels," *Process Saf. Prog.*, vol. 28, no. 2, pp. 179–189, Jun 2009, http://dx.doi.org/10.1002/prs.10311.

[7] J. D. Li and H. Hao, "Investigation of safety distance effect on gas storage tanks subjected to vapor cloud fast deflagration by using flacs," in *EASEC16* (Lecture Notes in Civil Engineering 101), C. M. Wang, V. Dao and S. Kitipornchai, Eds., Singapore: Springer Nature Singapore Pte Ltd., 2021, pp. 667–676.

[8] S. S. V. Vianna and R. S. Cant, "Modified porosity approach and laminar flamelet modelling for advanced simulation of accidental explosions," *J. Loss Prev. Process Ind.*, vol. 23, no. 1, pp. 3–14, Jan 2010, http://dx.doi.org/10.1016/j.jlp.2009.08.002.

[9] T. D. Ferreira and S. S. V. Vianna, "The Gilbert Johnson Keerthi distance algorithm coupled with computational fluid dynamics applied to gas explosion simulation," *Process Saf. Environ. Prot.*, vol. 130, pp. 209–220, Oct 2019, http://dx.doi.org/10.1016/j.psep.2019.08.010.

[10] T. D. Ferreira and S. S. V. Vianna, "Collision of convex objects for calculation of porous mesh in gas explosion simulation," *J. Loss Prev. Process Ind.*, vol. 69, pp. 104347, Mar 2021, http://dx.doi.org/10.1016/j.jlp.2020.104347.

[11] T. L. S. Quaresma, T. D. Ferreira, and S. S. V. Vianna, "A hybrid BML-fractal approach for the mean reaction rate modelling of accidental gas explosions in partially confined obstructed geometries," *Process Saf. Environ. Prot.*, vol. 152, pp. 414–426, Aug 2021, http://dx.doi.org/10.1016/j.psep.2021.06.008.

[12] T. D. Ferreira, S. S. V. Vianna, and R. G. Santos, "PFS - Porosity Flow Solver: an alternative computational tool for complex flow modelling," in *An. Cong. Bras. Eng. Quím.*, Fortaleza, 2016.

[13] M. R. Cain, *Pressure Vessel Burst Test Study*. Titusville, 1996. [Online]. Available: https://apps.dtic.mil/sti/pdfs/ADA322032.pdf

[14] V. Molkov and S. Kashkarov, "Blast wave from a high-pressure gas tank rupture in a fire: Stand-alone and under-vehicle hydrogen tanks," *Int. J. Hydrogen Energy*, vol. 40, no. 36, pp. 12581–12603, 2015, http://dx.doi.org/10.1016/j.ijhydene.2015.07.001.

[15] D. Wang, X. Qian, M. Yuan, T. Ji, W. Xu, and S. Liu, "Numerical simulation analysis of explosion process and destructive effect by gas explosion accident in buildings," *J. Loss Prev. Process Ind.*, vol. 49, pp. 215–227, 2017, http://dx.doi.org/10.1016/j.jlp.2017.07.002.

[16] Z. Li, J. Wu, M. Liu, Y. Li, and Q. Ma, "Numerical analysis of the characteristics of gas explosion process in natural gas compartment of utility tunnel using FLACS," *Sustainability*, vol. 12, no. 1, pp. 153, 2019, http://dx.doi.org/10.3390/su12010153.

[17] K. Cen, B. Song, R. Shen, Y. Zhang, W. Yu, and Q. Wang, "Dynamic characteristics of gas explosion and its mitigation measures inside residential buildings," *Math. Probl. Eng.*, vol. 2019, pp. 1–15, 2019, http://dx.doi.org/10.1155/2019/2068958.

[18] L. Pang, Q. Hu, M. Jin, and K. Yang, "Effect of congestion on flow field of vented natural gas explosion in a kitchen," *Adv. Civ. Eng.*, vol. 2021, pp. 1–22, 2021, http://dx.doi.org/10.1155/2021/6671875.

[19] M. L. Costa No. and G. N. Doz, "Study of blast wave overpressures using the computational fluid dynamics," *Rev. IBRACON Estrut. Mater.*, vol. 10, no. 3, pp. 669–686, Jun. 2017, http://dx.doi.org/10.1590/s1983-41952017000300007.

[20] E. Vyazmina, S. Jallais, A. Beccantini, and S. Trélat, "Protective walls against effects of vapor cloud fast deflagration: CFD recommendations for design," *Process Saf. Prog.*, vol. 37, no. 1, pp. 56–66, 2018, http://dx.doi.org/10.1002/prs.11930.

[21] J. Stawczyk, "Experimental evaluation of LPG tank explosion hazards," *J. Hazard. Mater.*, vol. 96, no. 2–3, pp. 189–200, 2003, http://dx.doi.org/10.1016/S0304-3894(02)00198-X.

[22] R. Tschirschwitz et al., "Mobile gas cylinders in fire: consequences in case of failure," *Fire Saf. J.*, vol. 91, pp. 989–996, 2017, http://dx.doi.org/10.1016/j.firesaf.2017.05.006.

[23] E. R. Vaidogas, "Predicting the ejection velocities of fragments from explosions cylindrical pressure vessels: uncertainty and sensitivity analysis," *J. Loss Prev. Process Ind.*, vol. 71, pp. 104450, 2021, http://dx.doi.org/10.1016/j.jlp.2021.104450.

[24] C. Y. Tham, "Numerical simulation on the interaction of blast waves with a series of aluminum cylinders at near-field," *Int. J. Impact Eng.*, vol. 36, no. 1, pp. 122–131, Jan 2009, http://dx.doi.org/10.1016/j.ijimpeng.2007.12.011.

[25] Y. A. Çengel and M. A. Boles, *Thermodynamics: An Engineering Approach*, 8th ed. New York: McGraw-Hill, 2014.

[26] Center for Chemical Process Safety, *Guidelines for Vapor Cloud, Explosion, Pressure Vessel Burst, BLEVE and Flash Fire Hazards*, 2nd ed. New York: Wiley, 2010.

[27] I. Sochet, "Blast effects of external explosions," in *Proc. Eighth Int. Symp. Hazards, Prev. Mitig. Ind. Explos.*, Yokohama, Japan, 2010.

[28] D. A. Crowl and J. F. Louvar, *Chemical Process Safety: Fundamentals with Applications*, 4th ed. New Jersey: Pearson Prentice Hall, 2020.

[29] K. B. Lopes and P. F. F. Melo, "Analysis of the effects of explosion of a hydrogen cylinder on the transfer of radioactive liquid wastes at nuclear power stations," in *Proc. 2011 Int. Nucl. Atl. Conf. – INAC 2011*, 2011.

[30] E. López, R. Rengel, G. W. Mair, and F. Isorna, "Analysis of high-pressure hydrogen and natural gas cylinders explosions through TNT equivalent method," *V Iber. Symp. Hydrog. Fuel Cells Adv. Batter.*, 2015, http://dx.doi.org/10.13140/RG.2.1.2336.8401.

[31] A. Bolonkin, "Cumulative thermonuclear inertial reactor," *Energy Sustain. Soc.*, vol. 6, no. 1, pp. 8, 2016, http://dx.doi.org/10.1186/s13705-016-0074-z.

[32] I. Cernak, "Animal models for concussion: molecular and cognitive assessment - relevance to sport and military concussions," in *Brain Neurotrauma*, 1st ed., F. H. Kobeissy, Ed., Gainsville: CRC Press, 2015, pp. 674–687.

[33] M. L. Costa No. and G. N. Doz, "Estudo numérico das pressões de onda de choque em diferentes meios e sua transmissão," *Rev. Sul-americana Eng. Estrut.*, vol. 14, no. 2, pp. 55–76, 2017, http://dx.doi.org/10.5335/rsaee.v14i2.7219.

[34] W. C. L. Silva, "Blast – efeitos da onda de choque no ser humano e nas estruturas," M.S. thesis, Ins. Tecnol. Aeronaut., São José dos Campos, 2007.

[35] W. E. Baker, P. A. Cox, P. S. Westine, J. J. Kulesz, and R. A. Strehlow, *Explosion Hazards and Evaluation.* Amsterdam: Elsevier Science, 1983.

[36] Associação Brasileira de Normas Técnicas, *Liquefied Petroleum Gas Central Storage – LPG*, ABNT NBR 13523, 2019.

[37] F. P. Lees, *Loss Prevention in the Process Industries: Hazard Identification, Assessment and Control*, 2nd ed. Oxford: Butterworth-Heinemann, 1996.

[38] B. Luccioni, D. Ambrosini, and R. Danesi, "Blast load assessment using hydrocodes," *Eng. Struct.*, vol. 28, no. 12, pp. 1736–1744, Oct 2006, http://dx.doi.org/10.1016/j.engstruct.2006.02.016.

[39] J. Zimbelmann and C. Boley, "Underground explosions: Estimating the safe distance," *Geotech. Res.*, vol. 3, no. 3, pp. 67–89, 2016, http://dx.doi.org/10.1680/jgere.16.00005.

**Editors:** Osvaldo Manzoli, Guilherme Aris Parsekian.

# IBRACON Structures and Materials Journal
## Revista IBRACON de Estruturas e Materiais

ORIGINAL ARTICLE

# Structural analysis of RC infilled frames with participating masonry: a proposal procedure for multi-strut models

*Análise estrutural de pórticos de concreto armado preenchidos com alvenarias participantes: proposta de procedimento para o uso de modelos de múltiplas diagonais*

Lucas Ferreira Galvão[a] (iD)
Gerson Moacyr Sisniegas Alva[a] (iD)

[a]Universidade Federal de Uberlândia – UFU, Faculdade de Engenharia Civil, Uberlândia, MG, Brasil

**Abstract:** In this paper, a procedure is proposed for the use of multi-strut models for the structural analysis of RC frames infilled with participating masonry subjected to lateral loads. It is therefore proposed that the eccentricities of the equivalent struts be obtained from the equivalent strut width of the classic single-strut model, whose value can be estimated from analytical expressions in the literature. The proposed models are validated by Finite Element Method (FEM) modeling, which simulates the contact between the infill masonry and the frame. It could be concluded that the proposed modeling provided better results than the classic single-strut model in obtaining the maximum shear force acting in the columns. It was also noted that the differences of the equivalent strut models in relation to the FEM results were higher with the increase of the participating masonry stiffness.

**Keywords:** infilled frames, participating masonry, equivalent strut models, RC structures, structural analysis.

**Resumo:** Neste trabalho é proposto um procedimento para o uso de modelos de diagonais equivalentes múltiplas na análise estrutural de pórticos de concreto armado preenchidos com alvenarias participantes submetidos a carregamentos horizontais. Propõe-se que as excentricidades das diagonais equivalentes sejam obtidas a partir da largura da diagonal equivalente do modelo clássico de diagonal única, cujo valor pode ser obtido a partir de expressões analíticas da literatura. Os modelos propostos são validados por meio de modelagem via Método dos Elementos Finitos (MEF) que simula o contato alvenaria-pórtico. Concluiu-se que a modelagem proposta forneceu resultados melhores que o modelo clássico de diagonal única na obtenção da máxima força cortante atuante nos pilares. Notou-se também que as diferenças dos modelos de diagonais equivalentes em relação aos resultados MEF foram maiores com o aumento da rigidez da alvenaria participante.

**Palavras-chave:** pórticos preenchidos, alvenarias participantes, modelos de diagonal equivalente, estruturas de concreto armado, análise estrutural.

# 1 INTRODUCTION

The recognized influence of masonry infill walls on the static and dynamic behavior of framed structural systems, subjected to lateral loads, is documented in international research, and has been investigated in Brazil in the last two decades (studies are cited in section 2 of this paper). However, the masonry infill walls with a structural role on the framed building structures has still not been consolidated into Brazilian structural design offices.

The masonry infill walls with a structural role are denominated as *participating masonry.* According to the definition of the recently updated Standard Brazilian code of structural masonry – ABNT NBR 16868-1 [1] – the participating masonry is the structural masonry built within a frame, which is intentionally designed and built as part of the bracing system.

In annex D of ABNT NBR 16868-1 [1], the equivalent strut model is recommended for simulating the contribution of participating masonry on frame stiffness, observing that the elements of the frame should be designed for the additional shear forces introduced by diagonal strut action, due to the contact of the wall with the beams and the columns. However, the code does not present an equivalent strut model that is specific to such a consideration. Since the classic single-strut models are not capable of capturing additional shear forces produced on the contact between masonry wall and frame, the use of two-strut and three-strut models becomes more appropriate for this purpose.

The main objective of this paper is to present a proposal for the definition of the eccentricities of diagonal struts in multiple equivalent strut models (specifically two-struts and three-struts models). It is proposed that these eccentricities be calculated as a function of the equivalent strut width, which can be obtained from the expressions available in specialized literature. Numerical simulations of RC frames infilled with participating masonry were conducted to evaluate the maximum shear force acting on the column, using Finite Element Method (reference model, which simulates the infill wall-frame contact problem) and using the proposed procedure for multi-strut models. Additionally, an analysis is made concerning the influence of the equivalent strut width expression used in the simulations and the influence of the stiffness of the masonry in the quality of the results provided by the proposed procedure. It is also noteworthy that the masonry was considered as a material with orthotropic behavior in the analyzes conducted.

## 2 PREVIOUS RESEARCH

In international specialized literature, several experimental and numerical studies on the behavior of masonry infilled frames subjected to lateral loads are found, where most of such studies are dedicated to seismic loads. In Brazil, even with the number of studies being small regarding international research, the theme has more recently gained prominence, especially over the last two decades. From these national studies, the following can be cited: Alvarenga [2], Santos [3], Silva [4], Sousa [5], Alva et al. [6], Pitanga [7], Montandon [8], Grandi [9], Medeiros [10], Santos [11], Queiroz [12], Rigão [13] and Galvão [14].

Following the growing development of the theme in Brazil, it can be quoted the addition of an informative annex (annex D) in the recent update to the Brazilian code of structural masonry – ABNT NBR 16868-1 [1] –, which addresses the consideration of participating masonry.

Among the pioneering authors in the study of infilled frames, Polyakov [15] should be mentioned, who after conducting a series of experiments and describing the behavior of the infill-frame ensemble, when submitted to lateral loads, proposes an analytical technique in which the masonry infilled frame system is equivalent to a frame where the masonry is substituted by an equivalent diagonal strut. This structural model is denominated as the Equivalent Strut Model (ESM).

The originally proposed ESM consists in simulating the masonry wall by a pin-jointed diagonal strut, defined on the beam-column connection points of the frame. In this way, this model can be denominated as classic ESM. Based on the classic ESM, other analytical models have been proposed in the literature, including those with multiple struts simulating the behavior of masonry.

To apply the classic ESM, it is necessary to define the mechanical and geometric properties of the equivalent strut. Models proposed by Polyakov [15], Holmes [16], Stafford-Smith [17]–[20], Stafford-Smith and Carter [21] and Hendry [22] use different parameters for the equivalent strut, but all of them are dependent on the dimensions and mechanical properties of the infill masonry and the frame members.

One of the key parameters on the classic ESM is the width of the equivalent strut, which can be calculated by analytical expressions proposed by different authors, as: Mainstone [23], Liauw and Kwan [24], Decanini and Fantin [25], Paulay and Priestley [26], Durrani and Luo [27], Chrysostomou and Asteris [28] and Montandon [8].

Despite the existence of various expressions for calculating the width of the equivalent strut, their results tend to differ one from the other. Thus, the choice of the most adequate expression for the equivalent strut width is a difficult task. In their respective studies, Montandon [8] and Queiroz [12] confirm these differences, with variations of up to 212% in the values obtained for the width of the equivalent strut.

Still regarding the classic ESM, it is noteworthy that due to its ease application, such model has become the most studied and widespread in technical community. This model is also recommended by different codes, including American codes FEMA 306 [29] and TMS 402/602 [30], Canadian code CSA S304 [31], New Zealand code NZS 4230 [32], and the Brazilian code ABNT NBR 16868-1 [1].

However, although it is the best known and most used for considering the contribution of masonry walls in infilled frames, the classic ESM does not provide satisfactory results concerning the local effects on the frame members, mainly when it comes to internal shear forces and the bending moment acting on columns and beams. Statements confirming

the can be found in studies by El-Dakhakhni et al. [33], Crisafulli and Carr [34], Yekrangnia and Mohammadi [35], Rigão [13] and Galvão [14]. From such assumption, these authors proposed analytical models with modifications regarding the classic ESM, on which the masonry wall is simulated by equivalent multiple struts.

To illustrate that the classic single-strut ESM is inadequate for capturing the maximum shear force in the column (that occurs in the contact region with the infill masonry), some results obtained by Galvão [14] are represented in Figure 1. The author analyzed RC frames, infilled with participating masonry, subjected to a monotonic lateral load. Masonries with different modulus of elasticity were analyzed, and in Figure 1 are shown the results for three cases, containing the shear force diagram for the column of the frame, which are obtained by classic single-strut models and by a Finite Element Method (FEM) model, used as a reference. It should be noted that were used the expressions from Mainstone [23], Durrani and Luo [27] and ABNT NBR 16868-1 [1] for the calculation of the equivalent strut width, which are represented, respectively, as MA, DL and NBR in Figure 1.
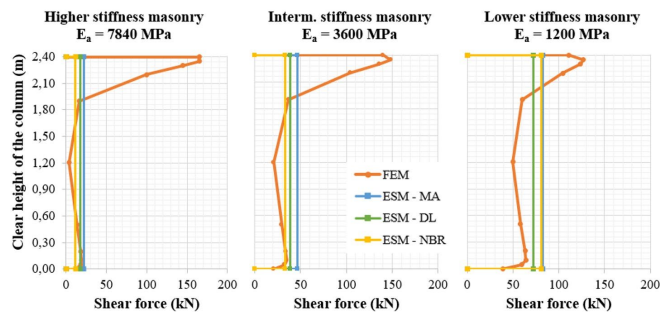


**Figure 1.** Shear force diagram along the clear height of the column (FEM x Classic single-strut ESM) – Galvão [14].

From Figure 1, it can be noticed that the classic model does not provide satisfactory results for the maximum shear force acting in the column, which occurs at the contact region with the infill wall. The stiffer the infill masonry, the more inaccurate are the results provided by the classic model.

## 3 PROPOSED PROCEDURE FOR MULTIPLE STRUT MODEL

With the aim of obtaining analytical models that predict in an efficient and precise manner the behavior of infilled frames with participating masonry subjected to lateral loads, and which have a simple and practical application, a procedure for the elaboration of ESM models with two and three struts was proposed for considering the contribution of the participating masonry.

Different to the classic ESM, in which the single diagonal strut is defined on the intersection between the beam and column nodes, the models with multiple struts present eccentric struts, which are defined through a given eccentricity from the beam-column joint. Crisafulli and Carr [34] emphasize that these eccentricities affect the lateral stiffness of the structure and are important parameters to be obtained.

The procedure proposed in this study was elaborated based on ESM preliminary models analyzed by Crisafulli and Carr [34], represented in Figure 2. In these models, the sum of the areas of the cross sections of the equivalent struts was considered as equal for all situations, adopting, in this sense, the following considerations: on two-strut ESM, both have the same area of cross section, equivalent to half of the area of the strut on the classic ESM; on the three-strut ESM, the area of the cross section of the central strut was adopted as being twice that of the eccentric struts, as illustrated in Figure 2c. In regard to the position of the eccentric struts, the authors consider the values of the eccentricities as equal to fractions of the contact length ($\alpha_H$) estimated by the expressions of Stafford-Smith and Carter [21] and Hendry [22].
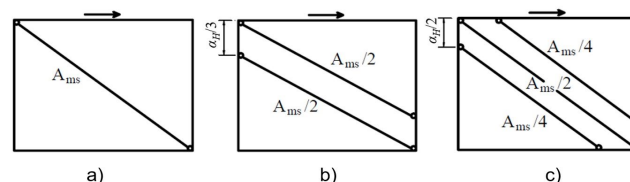


**Figure 2.** a) Classic ESM (single strut). b) Two-strut ESM. c) Three-strut ESM – Crisafulli and Carr [34].

For the model proposed in the present study, the distribution of struts and the consideration of their cross-sectional areas were adopted as being equal to those indicated in the preliminary models of Crisafulli and Carr [34]. However, the eccentricities were obtained by a different procedure, which was based on conclusions obtained by Montandon [8] and Di Nino [36]. These authors pointed out that the contact lengths given by the expressions of Stafford-Smith and Carter [21] and Hendry [22] were significantly higher than those observed in their reference models simulated via FEM.

Thus, aiming to achieve appropriate eccentricities for the equivalents struts, the procedure proposed in this paper is that the eccentricities of the diagonal struts be calculated as a function of the width of the equivalent strut ($w$), which in turn can be calculated by different expressions and procedures available in the literature and in normative codes.

In Figure 3 is shown a general infilled framed and its equivalent strut, where $w$ is the equivalent strut width and $\theta$ is the angle between the equivalent strut and the horizontal axis. From these two parameters, the proposal procedure consists in obtaining the effective contact lengths between column and infill wall ($\alpha_{ef,H}$) and between beam and infill wall ($\alpha_{ef,L}$) through geometric calculations. Once these geometries are defined, the eccentricities $e_H$ and $e_L$ are obtained through geometry, being also dependent on the dimensions of the cross sections of the column ($h_p$) and of the beam ($h_v$) on the plane of the infilled frame.
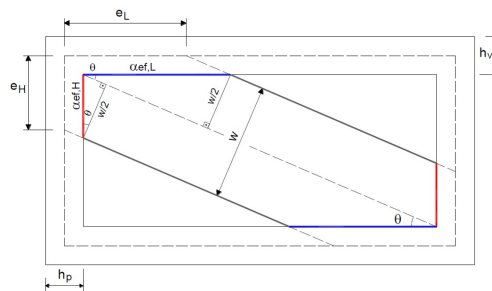


**Figure 3.** Parameters for the application of the proposed models

Thus, the expressions for the calculations of the parameters $\alpha_{ef,H}$, $\alpha_{ef,L}$, $e_H$ and $e_L$ are presented in Equations 1 to 4.

$$\alpha_{ef,H} = \frac{w}{2 \cdot \cos \theta} \tag{1}$$

$$\alpha_{ef,L} = \frac{w}{2 \cdot \text{sen}\,\theta} \; or \; \frac{\alpha_{ef,H}}{\tan \theta} \tag{2}$$

$$e_H = \frac{h_v}{2} + \alpha_{ef,H} - \frac{h_p}{2} \cdot \tan \theta \tag{3}$$

$$e_L = \frac{h_p}{2} + \alpha_{ef,L} - \frac{h_v}{2 \cdot \tan \theta} \tag{4}$$

With the definition of the eccentricities, the positioning of the equivalent struts on the models of two and three struts are represented in Figures 4a and 4b, respectively.
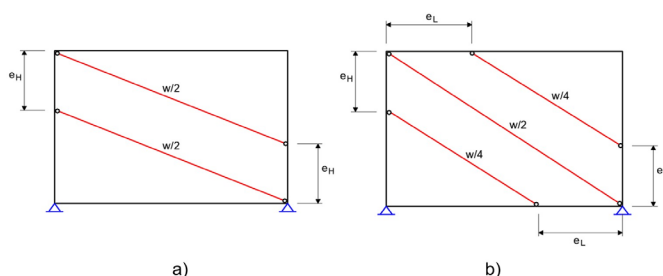


**Figure 4.** a) Model with two equivalent struts. b) Model with three equivalent struts.

## 4 NUMERICAL SIMULATIONS

To evaluate the behavior of the proposed procedure for ESM models with two or three struts, numerical simulations were performed on frames infilled with participating masonry, for different geometric and mechanical properties. The results obtained from these simulations were compared to the results obtained through the employment of the Finite Elements Methods (FEM) and with the classic ESM. As the FEM has a more refined analysis (higher hierarchy), the results obtained from such models were considered as a reference for the analyses.

The FEM models were developed on the computer program ANSYS, Mechanical platform APDL version 2021 R1. For the ESM models, the plane frame structural analysis program FTOOL was employed.

### 4.1 General parameters

Numerical models were developed for single-story, single-bay participating masonry RC infilled frame without openings. The models were subjected only to a monotonic lateral load. The static scheme is illustrated in Figure 5. Highlighted here is that linear elastic analyses were performed for all models.
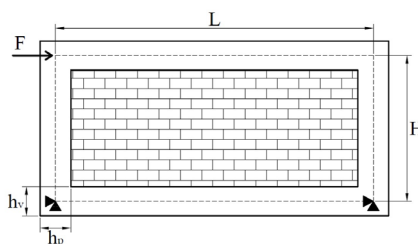


**Figure 5.** Static scheme of the infilled frame models

The members of the frame are composed of reinforced concrete, which was assumed linear-elastic isotropic material as a simplification. For the participating masonry, it was assumed ungrouted hollow concrete/clay structural blocks, with different values for the characteristic axial compressive strength ($f_{bk}$). The mechanical properties of the masonry, values of compressive strength of the mortar ($f_a$) and the prism ($f_{pk}$), as well as the minimum face shell thickness of the block, were all estimated by means of specifications suggested by ABNT NBR 16868-1 [1], which is a function of the material and strength of the block adopted for each model. On the other hand, the infill masonry was assumed as linear elastic orthotropic material.

### 4.2 FEM modeling

In accordance with the classification proposed by Lourenço [37], a macro-modeling was used for the numerical simulation of the behavior of the participating masonry, i.e., without distinction between blocks and mortar, treating the masonry as a continuous and homogenous element. This a more practical approach, due to the reduction in time and of computational requirements for processing the models.

The finite element PLANE182 was chosen for the modeling of the concrete frame and the infill wall. This finite element is applicable to the plane stress state and is defined by four nodes, with two degrees of freedom at each node, which are the translations in the $x$ and $y$ directions. These directions define the $xy$ plane, where is located the infilled frame. Based on a mesh refinement study, finite elements of 5 cm x 5 cm were employed for the frame, as well as for the masonry. The convergence study included the analysis of stabilization of penetrations and contact pressures among the frame-masonry surfaces. Figure 6 represents one of the infilled frame models simulated on FEM.
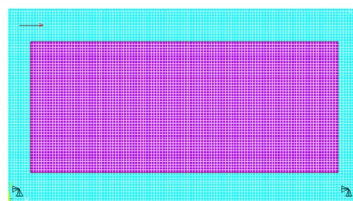


**Figure 6.** Infilled frame model simulated using FEM (ANSYS).

For the analysis of infilled frames using FEM, contact modeling between the elements of the frame and the masonry is necessary, to allow for sliding and separation between contact surfaces. This modeling is described in section 4.2.1.

## 4.2.1 Contact modeling at frame-infill wall interface

The consideration of the contact between the infill wall and the frame is of extreme importance in the modeling of infilled frames, since when subjected to lateral loads, there is a stress concentration on the compression corners of the infill wall and separation of the elements in the opposite corners. This behavior is represented in Figure 7a, obtained from the simulation of one of the models analyzed in this study. In Figure 7b are the principal compressive stresses acting in the masonry wall for the same model are illustrated, where it can be noticed the expected formation of diagonal compression in the masonry.



a)                                                      b)
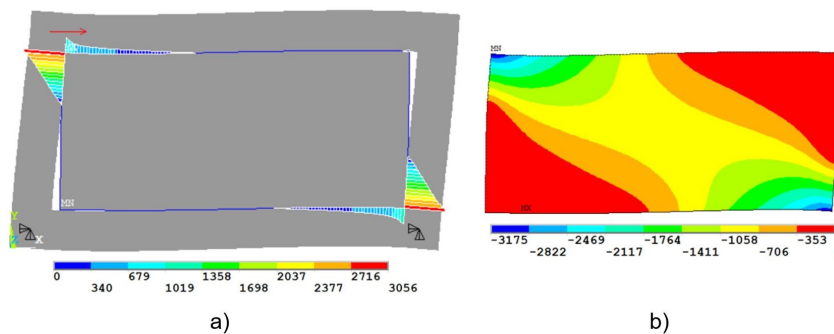
**Figure 7.** a) Deformed shape of the infilled frame and contact pressure between frame and wall (kPa). b) Principal compressive stresses in the masonry (kPa).

Figure 7a shows the contact pressure that acts on the frame members. This contact pressure causes an addition of shear forces on the columns and beams of the frame. This behavior is one of the focuses of this study for using of multiple strut models.

To simulate slippage and the separation between surfaces (contact problem), elements CONTA172/TARGE169 were employed.

Ideally, there should be no penetration between the surfaces of the RC frame and the infill masonry wall. However, the numerical techniques usually applied in the solution of the contact problem may imply the existence of a small penetration. On the ANSYS computer program, two coefficients were used for controlling penetration: FKN (normal stiffness factor) and FTOLN (penetration tolerance factor). The methodology employed for choosing from these coefficients were the same as those used by Montandon [8] and Queiroz [12], which were substantiated in the study by Silva [38]. The FKN factor was calibrated for each model in order that the lowest penetration possible be obtained between the surfaces, without causing numerical inconsistencies (convergence problems); the FTOLN factor was maintained using the value standardized by ANSYS, equal to 0.1.

Other parameters to be defined in the contact problem are the friction coefficient between the frame-masonry surfaces ($\mu$), the maximum shear strength (stress) between the surfaces ($f_{v,max}$) and cohesion ($\tau_0$). The friction coefficient ($\mu$) and cohesion ($\tau_0$) were obtained from ABNT NBR 16868-1 [1] recommendations, which are a function of the average compressive strength of the mortar ($f_a$), that can be defined as a function compressive strength of the unit ($f_{bk}$).

However, the maximum shear strength (stress) ($f_{v,max}$) was determined by Equation 5 (where $\theta$ is the inclination angle of the strut with respect to the horizontal), obtained by assuming that $f_{v,max}$ cannot be higher than the shear strength of the masonry wall. Highlighted here is that, in the deduction of Equation 5, the vertical component of the compression strut force was considered, while the vertical compression stress due to masonry self-weight was disregarded.

$$f_{v,max} = \frac{\tau_0}{1 - \mu \cdot tan\theta} \tag{5}$$

## 4.2.2 Obtaining shear force in the columns

The shear forces acting on the columns were obtained by numerical integration of the shear stresses along the cross section of these members, which were provided by program ANSYS. This process is presented in more details by Galvão [14].

## 4.3 FEM model validation

The accuracy of the FEM modeling procedure was made with experimental results available in the literature. Van and Lau [39] conducted an experimental study on half-scale, single-story, single-bay RC frames with unreinforced masonry infills under monotonic and cyclic loadings. As only monotonic loads were applied in the present paper, only the experimental specimens with this characteristic were analyzed for the validation of the FEM model (specimens BF1, IF1 and IF3 of Van and Lau's [39] study).

In Figure 8a is illustrated the geometry and reinforcing details of RC frames of the specimens, while in Figure 8b the lateral load-drift ratio responses of test specimens subjected to lateral monotonic loading is represented.



**Figure 8.** a) Geometry and reinforcing details of RC frames (dimensions in mm). b) Lateral load-drift ratio responses of test specimens subjected to lateral monotonic loading – Van and Lau [39].

As only linear elastic analyzes were performed in the present paper, the initial stiffness of the experimental specimens (determined from the load and the displacement at starting of crack) were compared with the FEM models outcome. The results are disposed in the Table 1 and illustrated in Figure 8b (the dashed lines represent the initial stiffness obtained in FEM models).

**Table 1.** Load of first crack, displacement and initial stiffness of experimental specimens and FEM models.

| Specimen | Load at starting of crack (kN) | Van and Lau [39] | | FEM models | |
|---|---|---|---|---|---|
| | | Displacement (mm) | Init. stiffness (kN/mm) | Displacement (mm) | Init. stiffness (kN/mm) |
| BF1 | 11.38 | 3.74 | 3.04 | 3.64 | 3.12 (+ 3%) |
| IF1 | 9.42 | 0.55 | 17.13 | 0.51 | 18.56 (+ 8%) |
| IF3 | 11.38 | 0.48 | 23.71 | 0.50 | 22.77 (- 4%) |

Analyzing the results, low differences were observed between the initial stiffness obtained experimentally and numerically (FEM), indicating that the modeling used in this paper provides satisfactory results for linear elastic analyzes of RC frames infilled with masonry.

## 4.4 ESM modeling

Classic ESM models (single equivalent strut defined on the beam-column joint) and ESM models with two or three equivalent struts were simulated, in accordance with the procedures proposed in section 3.

Based on studies by Montandon [8] and Queiroz [12], the choice was made for using the expressions from Mainstone [23] and Durrani and Luo [27] for the equivalent strut width, since those ones present better results when compared to results via FEM modeling. The expressions used for calculating the equivalent strut width (*w*) are shown on Table 2 (including ABNT NBR 16868-1 [1]). The parameters used by the expressions are illustrated in Figure 9.

Highlighted here is that for the recommended expression by ABNT NBR 16868-1 [1], the equivalent strut width is the effective width ($w_{eff}$) and the masonry thickness is $t_{ap}$ (described below).

**Table 2.** Analytical equations for calculation of the equivalent strut width.

| Authors | Expression |
|---|---|
| Mainstone [23] | $$w = 0.175 \cdot (\lambda_H)^{-0.4} \cdot D$$ $$\lambda_H = H \cdot \sqrt[4]{\frac{E_a \cdot t \cdot sen(2\theta)}{4 \cdot E_p \cdot I_p \cdot h}}$$ |
| Durrani and Luo [27] | $$w = \gamma \cdot sen(2\theta) \cdot D$$ $$\gamma = 0.32 \cdot \sqrt{sen(2\theta)} \left( \frac{H^4 \cdot E_a \cdot t}{m \cdot E_p \cdot I_p \cdot h} \right)^{-0.1}$$ $$m = 6 \cdot \left( \frac{1 + 6 \cdot E_v \cdot I_v \cdot H}{\pi \cdot E_p \cdot I_p \cdot L} \right)$$ |
| ABNT NBR 16868-1 [1] | $$w_{eff} = \frac{\sqrt{\alpha_H^2 + \alpha_L^2}}{2} \leq \frac{D}{4}$$ $$\alpha_H = \frac{\pi}{2} \cdot \sqrt[4]{\frac{4 \cdot E_p \cdot I_p \cdot h}{E_a \cdot t_{ap} \cdot sen(2\theta)}}$$ $$\alpha_L = \pi \cdot \sqrt[4]{\frac{4 \cdot E_v \cdot I_v \cdot l}{E_a \cdot t_{ap} \cdot sen(2\theta)}}$$ |
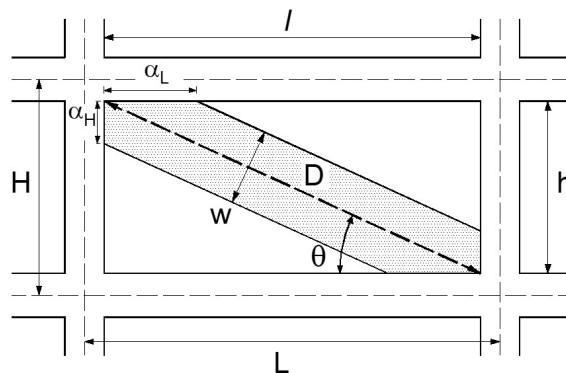


**Figure 9.** Parameters for the calculation of the equivalent strut width – Silva [4].

where:
$D$ – diagonal length of the masonry infill wall;
$E_a$ – modulus of elasticity of the masonry infill wall;
$E_p$ – modulus of elasticity of the column;
$E_v$ – modulus of elasticity of the beam;
$H$ – height between beam axes (floor-to-floor distance)
$h$ – height of masonry infill wall;
$I_p$ – second moment of area of the column;
$I_v$ – second moment of area of the beam;
$L$ – distance between column axes;
$l$ – length of the masonry infill wall;
$t$ – wall thickness;
$t_{ap}$ – equals two times the sum of the face shells thickness for hollow block units or the thickness of the wall for solid or fully grouted hollow block units;
$w$ – equivalent strut width;

Rev. IBRACON Estrut. Mater., vol. 16, no. 4, e16409, 2023

8/18

$w_{eff}$ – effective equivalent strut width;

$\alpha_H$ – column-infill wall contact length;

$\alpha_L$ – beam-infill wall contact length;

$\theta$ – angle of diagonal strut measured from the horizontal;

$\lambda_H$ – dimensionless relative stiffness parameter.

The static scheme adopted for the classic ESM model is represented in Figure 10. For those models with two or three struts, the scheme is analogous.
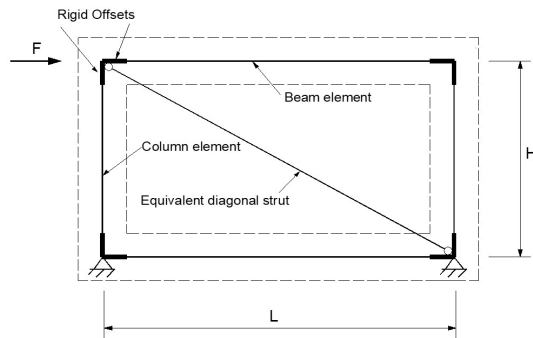


**Figure 10.** Infilled frame static scheme simulated by classic ESM – Alva et al. [6].

### 4.4.1 Analysis of the effective stiffness of the equivalent strut

For the ESM models, where the recommendations of ABNT NBR 16868-1 [1] are adopted, it was necessary to perform an additional procedure for the analysis of the effective stiffness of the equivalent strut. The Brazilian code indicates that the effective stiffness of the equivalent strut ($K_{eff}$) used in the calculations of the internal forces and displacements is defined according to Equation 6.

$$K_{eff} = \frac{\varphi_{st} \cdot w_{eff} \cdot t_{ap} \cdot E_a}{l_s} \tag{6}$$

where $\varphi_{st}$ is the factor to account stiffness reduction in the equivalent strut (equal to 0.5) for the analysis of wall cracking (not applied in this study, since only linear elastic analyses were performed) and $l_s$ is the design length of the equivalent strut, obtained through the subtraction of the diagonal length ($D$) by its effective width ($w_{eff}$).

Based on mechanical problems of frames members, the axial stiffness of a member is represented by *EA/L*, where *A* is the area of the cross section, *E* is the modulus of elasticity and *L* is the theoretical length of this element (calculated from the coordinates of the start node and end node of the element). In the case of the equivalent strut, the theoretical length considered by the program is obtained from the origin of the axes of the frame elements. However, the length $l_s$ is lower than the theoretical length of the equivalent strut. As such, it is necessary to adjust the axial stiffness of this strut in programs for plane frames analysis. The proposal is made in this study that this adjustment be performed by means of the inclusion of a coefficient $\beta$ according to Equation 7:

$$\beta = \frac{\sqrt{H^2 + L^2}}{\sqrt{h^2 + l^2} - w_{eff}} \tag{7}$$

Highlighted here is that Equation 7 was applied only to the classic ESM models (with a single strut), calculated using the recommendations from ABNT NBR 16868-1 [1]. For models with two and three equivalent struts, the expression undergoes some changes, being obtained in an analogous manner to that presented above.

Rev. IBRACON Estrut. Mater., vol. 16, no. 4, e16409, 2023

9/18

## 4.5 Analysis of orthotropic masonry

Masonry is a material that presents a complex behavior, due to its anisotropic and heterogeneous properties, which difficult the definition of the parameters that should be adopted in the numerical models. It is for this reason that on many occasions it becomes convenient to use masonry as a material with an isotropic behavior in numerical simulations, with the aim of simplifying the model, since it reduces the number of material parameters. Such simplifications were employed by Montandon [8] and Queiroz [12], based on the conclusions by Doudoumis [40].

However, studies such as those from El-Dakhakhni et al. [33] and Cavaleri et al. [41] investigated masonry as an orthotropic material, in a way to approximate the anisotropic behavior in numerical simulations. El-Dakhakhni et al. [33] suggested adopting the modulus of elasticity parallel to bed joints ($E_x$) at a value of 70% the modulus of elasticity parallel to the head joints ($E_y$), which in turn is equivalent to the elasticity modulus normally employed in analyses that consider masonry as an isotopic material ($E_a$).

Cavaleri et al. [41] proposed an expression for calculating the modulus of elasticity of the infill masonry along the diagonal direction ($E_d$), which was obtained by means of experiments performed with distinct types of masonry. In addition, to obtain the expression, the authors consider masonry as an orthotropic material. As such, the modulus of elasticity $E_d$ is obtained by means of Equation 8, where it is dependent on the modulus $E_x$ and $E_y$, on the inclination angle of the diagonal ($\theta$), as well as on the shear modulus of elasticity ($G$) and Poisson's coefficient ($v$), both related to the $xy$ plane.

$$\frac{1}{E_d} = \frac{1}{E_x} \cdot (\cos\theta)^4 + \left[\frac{1}{G} - \frac{2v}{E_x}\right] \cdot (sen\,\theta \cdot \cos\theta) + \frac{1}{E_y} \cdot (sen\,\theta)^4 \tag{8}$$

In Figure 11, the scheme that considers the modulus of elasticity of the masonry in the diagonal direction is represented.
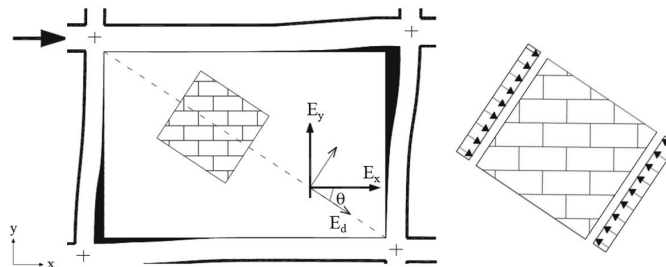


**Figure 11.** Scheme for considering the modulus $E_d$ – Cavaleri et al. [41].

The simulation of the FEM models in this study took into consideration the recommendation of El-Dakhakhni et al. [33], when considering masonry as orthotropic material ($E_x = 0,7 \cdot E_y$). However, for the ESM models, the $E_d$ modulus was employed, which was calculated by Equation 8, as proposed in Cavaleri et al. [41], with the recommendation of El-Dakhakhni et al. [33] for the obtainment of the modulus $E_x$ and $E_y$.

## 4.6 The analyzed models

Twenty-four different models of RC frames infilled with participating masonry subjected to monotonic lateral loads were simulated, following the static scheme already illustrated in Figure 6. The properties of the infilled frames to be analyzed were chosen to simulate the structural condition of a frame belonging to a tall building subjected to lateral wind loads. The masonry was considered as material with orthotropic behavior for all the models and the analyses were linear elastic. For all the models, the following properties were considered:

- Span of the beam (distance between column axes) ($L$) = 6.0 m;
- Floor-to-floor distance ($H$) = 3.0 m;
- Wall thickness ($t$) = 19 cm;
- Modulus of elasticity of reinforced concrete ($E_c$) = 35 GPa;
- Cross section of beams ($b_v$ x $h_v$) = 19 cm x 60 cm.

The parameters varied between the models were: the dimensions of the cross sections of the RC columns, the structural block of the participating masonry and the lateral load applied ($F$). The cross-section heights analyzed for the column ($h_p$) were 60, 80, 100 and 120 cm, while its width ($b_p$) was considered the same in all models, equals to 19 cm.

Regarding the masonry, six distinct types of structural blocks were considered, arranged in Table 3, where the prefix were used to name the numerical models.

**Table 3.** Structural blocks analysed.

| Prefix | Structural Block Type | $f_{bk}$ (MPa) | $E_a$ (MPa) |
|--------|----------------------|---------------|-------------|
| BVC04 | Hollow concrete block | 4.0 | 2560 |
| BVC14 | Hollow concrete block | 14.0 | 7840 |
| BVC24 | Hollow concrete block | 24.0 | 10800 |
| BCPV04 | Clay block with hollow walls | 4.0 | 1200 |
| BCPM10 | Clay block with solid walls | 10.0 | 3600 |
| BCPM18 | Clay block with solid walls | 18.0 | 6480 |

### 4.6.1 Determination of the lateral load applied in each model

To determine the value of the lateral load ($F$) applied on each model, it was considered the model proposed by Liberatore and Decanini [42] to estimate the maximum strength of the infill masonry. This model was studied by Noh et al. [43].

Firstly, for each model analyzed in this paper, were calculated the corresponding failure stresses for four masonry failure modes: (a) diagonal tension; (b) sliding shear; (c) corner crushing; and (d) diagonal compression. Then, if the infill strength corresponds to the minimum value among the four-failure modes, the strength of the equivalent strut was obtained. The lateral load to be applied to the infilled frame that causes in the equivalent strut (whose properties were estimated by the procedure proposed by Liberatore and Decanini [42]) a diagonal force with the same magnitude as the infill strength previously obtained. This lateral load ($F$) was calculated and applied in each one of the numeric models of this paper, which values are shown in Table 4.

It is important to highlight that the analyzes performed were linear elastic. In a real design application, it is necessary to consider the non-linear effects, even in a simplified way (e.g., linear analysis with global stiffness reductions applied in the structural elements, which is recommended by several structural design codes).

**Table 4.** Lateral load ($F$) applied in each numeric model.

| Model | F (kN) | Model | F (kN) |
|-------|--------|-------|--------|
| BVC04P60 | 166 | BVC04P100 | 154 |
| BVC14P60 | 345 | BVC14P100 | 319 |
| BVC24P60 | 337 | BVC24P100 | 312 |
| BCPV04P60 | 191 | BCPV04P100 | 177 |
| BCPM10P60 | 372 | BCPM10P100 | 344 |
| BCPM18P60 | 350 | BCPM18P100 | 324 |
| BVC04P80 | 160 | BVC04P120 | 149 |
| BVC14P80 | 331 | BVC14P120 | 308 |
| BVC24P80 | 324 | BVC24P120 | 301 |
| BCPV04P80 | 184 | BCPV04P120 | 171 |
| BCPM10P80 | 357 | BCPM10P120 | 332 |
| BCPM18P80 | 336 | BCPM18P120 | 312 |

### 4.6.2 Remaining parameters

The remaining parameters of the numerical models were obtained according to the procedures commented in the previous sections of this paper. As an example, the parameters used for the BVC24P60 model are shown in Tables 5, 6 and 7.

Rev. IBRACON Estrut. Mater., vol. 16, no. 4, e16409, 2023

11/18

**Table 5.** Parameters for the model BVC24P60 – FEM.

| Reinforced Concrete | | | Participating Masonry | | | | | |
|---|---|---|---|---|---|---|---|---|
| $E_c$ (GPa) | $\acute{\imath}$ | $E_x$ (MPa) | $E_y$ (MPa) | $\acute{\imath}$ | $\grave{\imath}$ | $\^{o}_0$ (MPa) | $f_{v,max}$ (MPa) | |
| 35 | 0.2 | 7560 | 10800 | 0.2 | 0.5 | 0.35 | 0.450 | |

**Table 6.** Parameters for the model BVC24P60 – ESM.

| Calculation method | $E_d$ (MPa) | Strut width | | Strut thickness | | Eccentricities | |
|---|---|---|---|---|---|---|---|
| | | $w$ (cm) | $w_{eff}$ (cm) | $t$ (cm) | $t_{ap}$ (cm) | $e_H$ (cm) | $e_L$ (cm) |
| Mainstone [23] | 8469 | 67.82 | - | 19 | - | 54 | 46 |
| Durrani and Luo [27] | 8469 | 84.21 | - | 19 | - | 63 | 66 |
| ABNT NBR 16868-1 [1] | 8469 | - | 147.73 | - | 10 | 98 | 144 |

**Table 7.** Coefficient $\beta$ for the model BVC24P60.

| Calculation method | Number of struts | Position of strut | $\^{a}$ |
|---|---|---|---|
| ABNT NBR 16868-1 [1] | 1 | Central | 1.764 |
| | 2 | Ends | 1.487 |
| | 3 | Central | 1.477 |
| | 3 | Ends | 1.707 |

It is noteworthy that, for each of the twenty-four models, were simulated infilled frames applying the FEM (reference models), the classic ESM (single-strut), and also the two-strut and three-strut ESM (procedure proposed in section 3).

## 5 ANALYSES OF RESULTS

The lateral displacements of the infilled frame and the maximum shear force ($V$) in the column were analyzed. The lateral displacements were measured on the same point of the applied force $F$, while the maximum shear force was obtained in the contact region between the column and the infill masonry.

For the exhibiting of the results for each model, the following nomenclature was adopted:

- Expression from Maintone [23] – MA;
- Expression from Durrani and Luo [27] – DL;
- Expression from ABNT NBR 16868-1 [1] – NBR;
- Classic ESM (single-strut) – 1S;
- Two-strut ESM – 2S;
- Three-strut ESM – 3S.

Tables 8 and 9 show the results obtained. It was chosen the models with $h_p$ equals to 60 cm (P60) to illustrate the order of magnitude of the values. It is noteworthy that, for the other models, the order of magnitude of the results were similar.

**Table 8.** Maximum shear force in the column (kN) for models P60.

| Model | FEM | MA-1S | DL-1S | NBR-1S | MA-2S | DL-2S | NBR-2S | MA-3S | DL-3S | NBR-3S |
|---|---|---|---|---|---|---|---|---|---|---|
| BVC04P60 | 90.57 | 47.46 | 42.98 | 39.01 | 83.20 | 83.15 | 83.24 | 64.98 | 62.57 | 62.07 |
| BVC14P60 | 196.95 | 56.48 | 48.60 | 38.82 | 172.59 | 172.53 | 172.99 | 112.69 | 108.26 | 103.94 |
| BVC24P60 | 203.75 | 45.08 | 38.34 | 29.41 | 168.54 | 168.51 | 169.14 | 104.50 | 100.56 | 95.56 |
| BCPV04P60 | 92.92 | 69.49 | 65.13 | 71.64 | 95.86 | 95.81 | 95.94 | 82.52 | 80.22 | 85.01 |
| BCPM10P60 | 185.28 | 92.32 | 82.28 | 77.85 | 186.33 | 186.19 | 186.49 | 138.29 | 132.80 | 133.83 |
| BCPM18P60 | 193.44 | 64.26 | 55.75 | 39.77 | 175.14 | 175.05 | 175.49 | 118.02 | 113.32 | 105.70 |

Rev. IBRACON Estrut. Mater., vol. 16, no. 4, e16409, 2023

12/18

**Table 9.** Lateral displacements (mm) for models P60.

| Model | FEM | MA-1S | DL-1S | NBR-1S | MA-2S | DL-2S | NBR-2S | MA-3S | DL-3S | NBR-3S |
|---|---|---|---|---|---|---|---|---|---|---|
| BVC04P60 | 1.83 | 2.03 | 1.84 | 1.67 | 2.26 | 2.15 | 2.31 | 2.06 | 1.88 | 1.86 |
| BVC14P60 | 2.15 | 2.42 | 2.09 | 1.67 | 2.88 | 2.65 | 2.96 | 2.49 | 2.16 | 1.99 |
| BVC24P60 | 1.82 | 1.93 | 1.65 | 1.27 | 2.36 | 2.16 | 2.44 | 2.00 | 1.72 | 1.54 |
| BCPV04P60 | 2.67 | 2.96 | 2.78 | 3.05 | 3.19 | 3.08 | 3.51 | 3.00 | 2.82 | 3.21 |
| BCPM10P60 | 3.29 | 3.94 | 3.52 | 3.33 | 4.49 | 4.09 | 4.81 | 4.03 | 3.61 | 3.76 |
| BCPM18P60 | 2.40 | 2.75 | 2.39 | 1.71 | 3.24 | 2.99 | 3.02 | 2.83 | 2.47 | 2.04 |

To analyze the results, it was decided to normalize both the maximum shear force in the column and the lateral displacements. The normalization was performed through the ratio between the results obtained in the ESM models and the results obtained in reference models (FEM). The normalized results are displayed in sections 5.1 and 5.2 of this paper.

## 5.1 Maximum shear force in the column

The normalized maximum shear force in the column for each model are displayed in Figures 12 to 15, while the summary of the values grouped by ESM model are shown in Table 10.
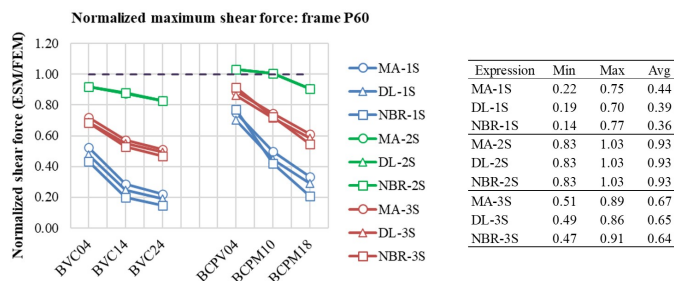


**Figure 12.** Normalized maximum shear force, frame P60.
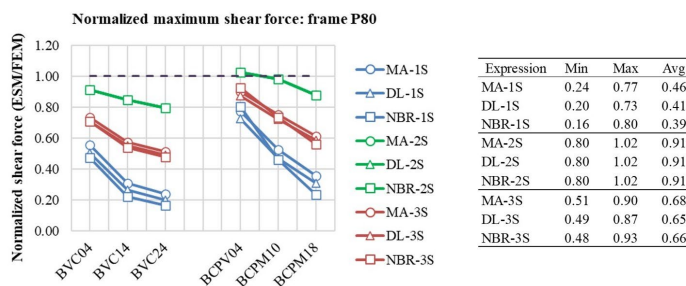


**Figure 13.** Normalized maximum shear force, frame P80.
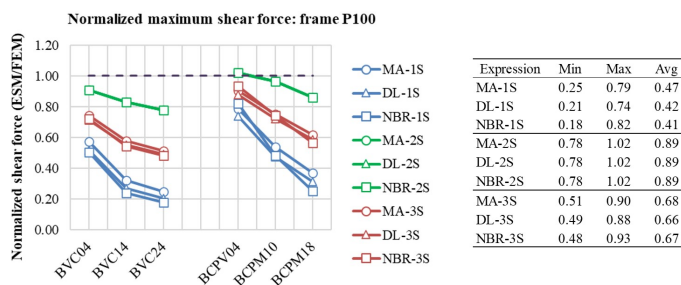


**Figure 14.** Normalized maximum shear force, frame P100.

**Normalized maximum shear force: frame P120**



| Expression | Min | Max | Avg |
|---|---|---|---|
| MA-1S | 0.26 | 0.80 | 0.49 |
| DL-1S | 0.21 | 0.74 | 0.43 |
| NBR-1S | 0.19 | 0.83 | 0.43 |
| MA-2S | 0.76 | 1.01 | 0.88 |
| DL-2S | 0.76 | 1.01 | 0.88 |
| NBR-2S | 0.76 | 1.01 | 0.88 |
| MA-3S | 0.52 | 0.90 | 0.69 |
| DL-3S | 0.49 | 0.88 | 0.66 |
| NBR-3S | 0.49 | 0.93 | 0.67 |
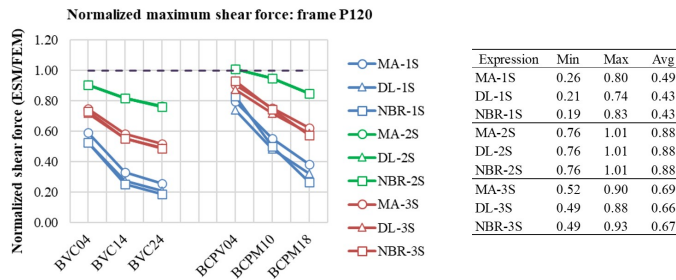
**Figure 15.** Normalized maximum shear force, frame P120.

**Table 10.** Summary (grouped by ESM model) – normalized maximum shear force.

| Model | Min | Max | Avg |
|---|---|---|---|
| 1S | 0.14 | 0.83 | 0.42 |
| 2S | 0.76 | 1.03 | 0.90 |
| 3S | 0.47 | 0.93 | 0.67 |

Based on the results obtained, it can be noted that the classic ESM (single-strut model) is inadequate to predict the maximum shear force in the column (in the region of contact with the infill masonry). On average, the shear force provided through the single-strut model represented only around 42% of the maximum shear force provided by the FEM results (Table 10). For masonry of higher stiffness, this discrepancy is even greater, with the single-strut model providing a maximum shear force that represents only 14% of the value provided by FEM, in the most against safety situation (BVC24P60V60, with the expression NBR-1S).

The two-strut model was the one that predicted, in a more satisfactory way, the maximum shear force in the column, providing, on average, values 10% lower than the maximum shear force from FEM models (Table 10). For frames infilled with masonry of higher modulus of elasticity, the two-strut model provided lower results relative to FEM, with a difference of up to 24% (BVC24P120V60); for frames infilled with masonry of lower modulus of elasticity, the results were closer to the reference, with two-strut models providing results up to 3% higher in relation to FEM (BCPV04P60V60). It should be noted that the expression used to calculate the properties of the equivalent strut practically does not change the value of the maximum shear force in the two-strut models, which is why in Figures 12 to 15 it is not possible to observe the results of the MA-2S and DL-2S, which are covered by the NBR-2S results.

The three-strut model provided better results than those of the classic single-strut model; however, it did not provide satisfactory results when compared to the two-strut model. The maximum shear force provided by the three-strut model were lower in relation to FEM in all cases analyzed (as well as the single-strut model) with differences around 33%, on average (Table 10). For frames infilled with masonry of higher modulus of elasticity, the difference was up to 53% (BVC24P60V60, with the expression NBR-3S), while for frames infilled with masonry of lower modulus of elasticity, it was up to 7% (BCPV04P60V60, with the NBR-3S expression). The two-strut and three-strut models (modeled according to the procedure proposed in this paper) provided less satisfactory results for masonry of high stiffness.

For the three-strut model, the expression from Mainstone [23] was the one that provided the most satisfactory results (taking as criterion an analysis in favor of safety and closest as possible to the FEM results), with values on average 32% lower than the maximum shear force provided by the reference models (Figures 12 to 15).

Thus, it was confirmed that the classic single-strut model underestimates the maximum shear force in the column (this model cannot describe properly the local effects resulting from the interaction between the infill wall and surrounding frame, as mentioned in section 2). On the other hand, the two-strut and three-strut models can predict additional shear forces in the column caused by the contact pressure between frame and wall, since these models possess struts that is not connected to the beam-column joints (eccentric struts).

Analyzing the results shown in Figures 12 to 15, it is clearly seen that, for both type of structural blocks (concrete and clay), the stiffer the masonry, more the results of the ESM models were against safety, i.e., lower than reference results (FEM models). Regarding the variation of the cross section of the columns, no significant differences were noted on the results.

Rev. IBRACON Estrut. Mater., vol. 16, no. 4, e16409, 2023

14/18

## 5.2 Lateral displacement

The normalized lateral displacement for each model is displayed in Figures 16 to 19, while the summary of the values grouped by ESM model are shown in Table 11.
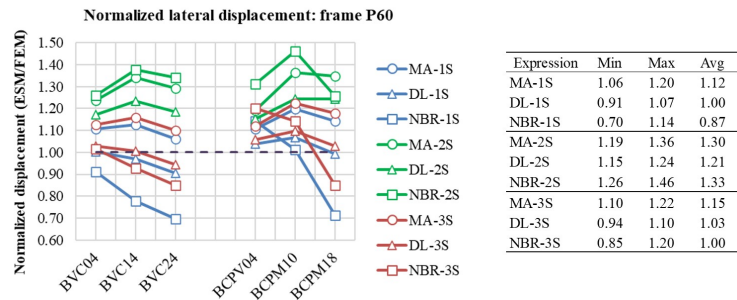


**Figure 16.** Normalized lateral displacement, frame P60.

| Expression | Min | Max | Avg |
|---|---|---|---|
| MA-1S | 1.06 | 1.20 | 1.12 |
| DL-1S | 0.91 | 1.07 | 1.00 |
| NBR-1S | 0.70 | 1.14 | 0.87 |
| MA-2S | 1.19 | 1.36 | 1.30 |
| DL-2S | 1.15 | 1.24 | 1.21 |
| NBR-2S | 1.26 | 1.46 | 1.33 |
| MA-3S | 1.10 | 1.22 | 1.15 |
| DL-3S | 0.94 | 1.10 | 1.03 |
| NBR-3S | 0.85 | 1.20 | 1.00 |
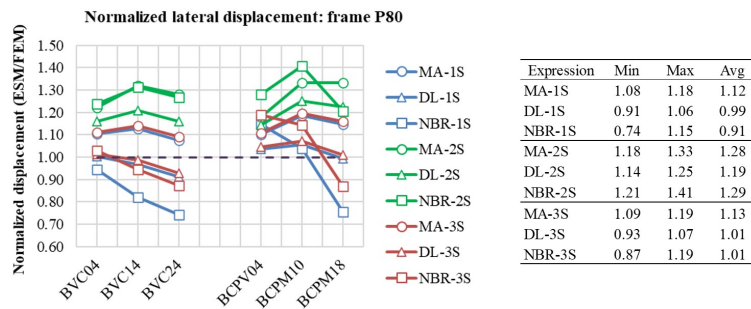


**Figure 17.** Normalized lateral displacement, frame P80.

| Expression | Min | Max | Avg |
|---|---|---|---|
| MA-1S | 1.08 | 1.18 | 1.12 |
| DL-1S | 0.91 | 1.06 | 0.99 |
| NBR-1S | 0.74 | 1.15 | 0.91 |
| MA-2S | 1.18 | 1.33 | 1.28 |
| DL-2S | 1.14 | 1.25 | 1.19 |
| NBR-2S | 1.21 | 1.41 | 1.29 |
| MA-3S | 1.09 | 1.19 | 1.13 |
| DL-3S | 0.93 | 1.07 | 1.01 |
| NBR-3S | 0.87 | 1.19 | 1.01 |
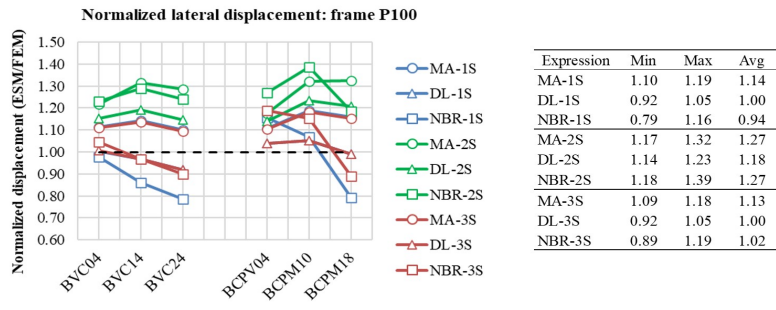


**Figure 18.** Normalized lateral displacement, frame P100.

| Expression | Min | Max | Avg |
|---|---|---|---|
| MA-1S | 1.10 | 1.19 | 1.14 |
| DL-1S | 0.92 | 1.05 | 1.00 |
| NBR-1S | 0.79 | 1.16 | 0.94 |
| MA-2S | 1.17 | 1.32 | 1.27 |
| DL-2S | 1.14 | 1.23 | 1.18 |
| NBR-2S | 1.18 | 1.39 | 1.27 |
| MA-3S | 1.09 | 1.18 | 1.13 |
| DL-3S | 0.92 | 1.05 | 1.00 |
| NBR-3S | 0.89 | 1.19 | 1.02 |
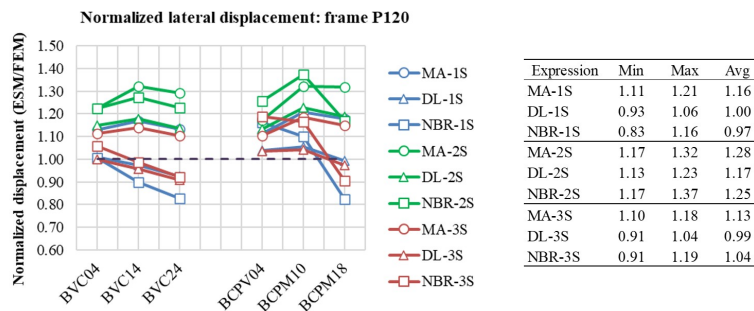


**Figure 19.** Normalized lateral displacement, frame P120.

| Expression | Min | Max | Avg |
|---|---|---|---|
| MA-1S | 1.11 | 1.21 | 1.16 |
| DL-1S | 0.93 | 1.06 | 1.00 |
| NBR-1S | 0.83 | 1.16 | 0.97 |
| MA-2S | 1.17 | 1.32 | 1.28 |
| DL-2S | 1.13 | 1.23 | 1.17 |
| NBR-2S | 1.17 | 1.37 | 1.25 |
| MA-3S | 1.10 | 1.18 | 1.13 |
| DL-3S | 0.91 | 1.04 | 0.99 |
| NBR-3S | 0.91 | 1.19 | 1.04 |

**Table 11.** Summary (grouped by ESM model) – normalized lateral displacement.

| Model | Min | Max | Avg |
|---|---|---|---|
| 1S | 0.70 | 1.21 | 1.02 |
| 2S | 1.13 | 1.46 | 1.25 |
| 3S | 0.85 | 1.22 | 1.05 |

By analyzing the results obtained, the differences between the ESM and FEM (reference) models, on average, were: 2% for the single-strut model; 25% for the two-strut model; 5% for the three-strut model (Table 11). Thus, the classic single-strut model was the one that provided the closest displacements compared to the FEM (on average). However, single-strut model showed results up to 30% lower than the reference (BVC24P60V60, with the expression NBR-1S), while in the three-strut model, the biggest difference against safety was 15% (BVC24P60V60, with the expression NBR-3S).

The two-strut model provided the largest displacements. Its results were higher than the reference ones in all analyzed cases, with values up to 46% higher than those provided by the FEM (BCPM10P60V60, with the NBR-3S expression). The single-strut and three-strut models provided higher and lower results than the FEM. For the single-strut model: the maximum differences (higher in relation to FEM) and minimum (lower in relation to FEM) were 21% and 30%, respectively. Similarly, for the three-strut model, such differences were 22% and 15% (Table 11).

The expression from Durrani and Luo [27] was the one that provided the closest displacements in relation to FEM. In the three-strut model, the maximum difference (in favor of safety) and minimum (against safety) in relation to the FEM models were 10% (Figure 16) and 9% (Figure 19), respectively. In analogous comparison, for the three-strut model, the expression from Mainstone [23] provided results higher than FEM in all cases, with displacements 14% higher, on average; as for the ABNT NBR 16868-1 [1] expression, the differences in relation to the MEF were 20% (maximum) and 15% (minimum), both displayed at Figure 16.

The displacements provided by three-strut models were slightly larger in relation to the classic single-strut model, with difference of 3%, on average (Table 11). It is worth noting that, in the single-strut and three-strut models, the procedure of ABNT NBR 16868-1 [1] was the one that provided more less satisfactory results (against to safety), when compared to the reference displacements.

It can be concluded that, differently from observed about the maximum shear force in the column (section 5.1), the classic single-strut model can provide an adequate estimation of the lateral displacement of the infilled frame (although against safety in some situations). It indicates that this model can still be an adequate tool when the analysis is focused on the global response of the structure.

For the multi-strut models, it is important to highlight that the values of the eccentricities significantly influence the stiffness of the infilled frame. The application of the proposed procedures showed that the two-strut models are more flexible than the reference model (FEM). The three-strut models provided more reasonable results (displacements) than the classic ESM, when compared to reference models. Even though, the three-strut models provided results against safety for the maximum shear force in columns.

Regarding the variation in the cross section of the columns, no significant differences were noted in the results. In relation to the stiffness of the infill masonry, it is not possible to clearly see its influence from the results shown in Figures 16 to 19. However, it can be noticed that the increase in masonry stiffness provided lower displacements as compared to FEM in the single-strut and three-strut models with the expressions from Durrani and Luo [23] and from ABNT NBR 16868-1 [1].

## 6 CONCLUSIONS

In this study a procedure for equivalent multi-strut models were proposed, where the eccentricity of the equivalent struts is calculated as a function of the equivalent strut width, which can be obtained from any expression found in literature. For this purpose, three expressions were investigated: Mainstone [23], Durrani and Luo [27] and the ABNT NBR 16868-1 [1]. It is noteworthy that linear elastic analyzes were conducted and that the orthotropy of the infill masonry was considered. Based on the numerical simulations performed in this study, the following are highlighted as the main conclusions:

- The classic single-strut model is not appropriate to predict the maximum shear forces in the column, that occurs in the region of contact with the infill masonry, providing significantly lower values than those obtained with the FEM models (58% lower, on average); it is noteworthy that the difference is even more expressive when analyzing the frames infilled with masonry of higher modulus of elasticity, reaching up to 86% of difference (against safety). The two-strut model was able to satisfactorily predict the maximum shear force on the column, regardless of the expression used to determine the properties of the equivalent struts, with results about 10% lower than the reference ones. Although the three-strut model provided less satisfactory results than the two-strut one (33% lower in relation to FEM), it was better than the classic single-strut model for obtaining the maximum shear force in the column.

- Regarding lateral displacements, the three-strut model provided satisfactory results (5% higher in relation to FEM), with displacements slightly higher than those obtained in single-strut model. It was noted that the expression from ABNT NBR 16868-1 [1] applied to the three-strut model brings better results than when applied to the classic single-strut one. On the other hand, the two-strut model significantly overestimated the lateral displacements; in this model, the expression from Durrani and Luo [27] was the one that led to closer results in relation to FEM (19% higher displacements, on average). It is noteworthy that the expression from Mainstone [23], applied to the three-strut model, provided results in favor of safety in all analyzed cases, with displacements about 14% higher than the reference ones.

- Masonry stiffness influenced the results of the ESM models. Especially about the maximum shear force in the column, it was noted that the ESM models provided less satisfactory results for masonry of high stiffness, when compared to the FEM models. The stiffness of the column did not significantly influence the models analyzed in this study.

- Taking as a criterion an analysis in favor of safety and closest as possible to the FEM results, the expression from Mainstone [23] applied to the three-strut model is recommended to obtain the lateral displacement of the infilled frame; to obtain the maximum shear force in the column, the two-strut model is recommended, regardless of the expression used to determine the properties of the equivalent diagonals.

## ACKNOWLEDGEMENTS

## REFERENCES

[1] Associação Brasileira de Normas Técnicas, *Alvenaria Estrutural – Parte 1: Projeto*, NBR 16868-1, 2020.

[2] R. Alvarenga, "Análise teórico-experimental de estruturas compostas de pórticos de aço preenchidos com alvenaria de concreto celular autoclavado," Ph.D. dissertation, Univ. São Paulo, São Carlos, 2002. [Online]. Available: https://www.teses.usp.br/teses/disponiveis/18/18134/tde-22032016-102411/pt-br.php

[3] E. Santos, "Influência da alvenaria no comportamento estrutural de edifícios altos de concreto armado," M.S. thesis, Univ. Catol. Pernambuco, Recife, 2007. [Online]. Available: https://bdtd.ibict.br/vufind/Record/UCAP_1a457f6ecad042d1ffe0c54d696767d6

[4] L. Silva, "Modelagem de pórticos de concreto armado preenchidos com a consideração de aberturas nos painéis de alvenaria," M.S. thesis, Univ. Fed. Santa Maria, Santa Maria, 2014. [Online]. Available: https://repositorio.ufsm.br/handle/1/7850

[5] P. Sousa, "Efeito dos painéis de vedação nas características dinâmicas de edificações de concreto armado," M.S. thesis, Univ. Fed. Rio de Janeiro, Rio de Janeiro, 2014. [Online]. Available: http://www.coc.ufrj.br/pt/dissertacoes-de-mestrado/380-msc-pt-2014/4439-paulo-victor-almeida-de-sousa

[6] G. Alva, J. Kaminski Jr., G. Mohamad, and L. Silva, "Serviceability limit state related to excessive lateral deformations to account for infill walls in the structural model," *Ibracon Struct. Mater. J.*, vol. 8, no. 3, pp. 390–426, 2015. https://doi.org/10.1590/S1983-41952015000300008.

[7] M. Pitanga, "Contribuição ao estudo de pórticos de concreto armado preenchidos com alvenaria de blocos cerâmicos," Ph.D. dissertation, Univ. Fed. Pernambuco, Recife, 2016. [Online]. Available: https://repositorio.ufpe.br/handle/123456789/25297

[8] G. Montandon, "Modelos estruturais para a análise de pórticos preenchidos com blocos cerâmicos em edifícios de concreto armado," M.S. thesis, Univ. Fed. Uberlândia, Uberlândia, 2018. [Online]. Available: https://repositorio.ufu.br/handle/123456789/22409

[9] A. Grandi, "Avaliação experimental por meio de ensaios cíclicos de pórtico de aço preenchido com alvenaria participante," M.S. thesis, Univ. Fed. Viçosa, Viçosa, 2018. [Online]. Available: https://www.locus.ufv.br/handle/123456789/20571

[10] W. Medeiros, "Pórticos em concreto pré-moldado preenchidos com alvenaria participante," M.S. thesis, Univ. Fed. São Carlos, São Carlos, 2018. [Online]. Available: https://repositorio.ufscar.br/handle/ufscar/10029?show=full

[11] R. Santos, "Avaliação numérica de pórticos de aço preenchidos com painéis de alvenaria estrutural de blocos de concreto submetidos à carregamentos cíclicos," M.S. thesis, Univ. Fed. Viçosa, Viçosa, 2019. [Online]. Available: https://www.locus.ufv.br/handle/123456789/26820

[12] L. Queiroz, "Alvenarias participantes: consideração e efeitos em edifícios de concreto sob ações horizontais," M.S. thesis, Univ. Fed. Uberlândia, Uberlândia, 2020, http://dx.doi.org/10.14393/ufu.di.2020.377.

[13] A. Rigão, "Modelagem de pórticos em concreto armado preenchidos com alvenaria participante," Ph.D. dissertation, Universidade Federal de Santa Maria, Santa Maria, 2022. [Online]. Available: https://repositorio.ufsm.br/handle/1/24212

[14] L. Galvão, "Contribuições à análise numérica de edifícios com alvenarias paricipantes," M.S. thesis, Universidade Federal de Uberlândia, Uberlândia, 2022. [Online]. Available: https://repositorio.ufu.br/handle/123456789/34463

[15] S. Polyakov, *On the Interaction Between Masonry Filler Walls and Enclosing Frame When Loaded in the Plane of the Wall*. São Francisco, CA: Earthquake Engineering Research Institute, 1960, pp. 36–42.

[16] M. Holmes, "Steel frames with brickwork and concrete infilling," *Proc.- Inst. Civ. Eng.*, vol. 19, no. 4, pp. 473–478, 1961, http://dx.doi.org/10.1680/iicep.1961.11305.

Rev. IBRACON Estrut. Mater., vol. 16, no. 4, e16409, 2023

17/18

[17] B. Stafford-Smith, "Lateral stiffness of infilled frames," *J. Struct. Div.*, vol. 88, no. 6, pp. 183–199, 1962., http://dx.doi.org/10.1061/JSDEAG.0000849.

[18] B. Stafford-Smith, "Behaviour of square infilled frames," *J. Struct. Div.*, vol. 92, no. 1, pp. 381–403, 1966., http://dx.doi.org/10.1061/JSDEAG.0001387.

[19] B. Stafford-Smith, "The composite behaviour of infilled frames," in *Tall Buildings*, A. Coull and B. Stafford-Smith, Ed., London: Pergamon Press, 1967, pp. 481–495.

[20] B. Stafford-Smith, "Methods of predicting the lateral stiffness and strenght of multi-storey infilled frames," *Build. Sci.*, vol. 2, no. 3, pp. 247–257, 1967., http://dx.doi.org/10.1016/0007-3628(67)90027-8.

[21] B. Stafford-Smith and C. Carter, "A method of analysis for infilled frames," *Proc.- Inst. Civ. Eng.*, vol. 44, no. 1, pp. 31–48, 1969., http://dx.doi.org/10.1680/iicep.1969.7290.

[22] A. Hendry, *Structural Brickwork.* London: MacMillan, 1981.

[23] R. Mainstone, *Supplementary Note on the Stiffness and Strengths of Infilled Frames*. Garston, UK: Building Research Station, 1974.

[24] T. Liauw and K. Kwan, "Nonlinear behavior of non-integral infilled frames," *Comput. Struc.*, vol. 18, no. 3, pp. 551–560, 1984., http://dx.doi.org/10.1016/0045-7949(84)90070-1.

[25] L. Decanini and G. Fantin, "Modelos simplificados de la mampostería incluida en porticos: caracteristicas de rigidez y resistencia lateral en estado limite," *J. Argentinas de Ing. Estruct.*, vol. 2, pp. 817–836, 1987.

[26] T. Paulay and M. Priestley, *Seismic Design of Reinforced Concrete and Masonry Buildings*. New York: Wiley, 1992, http://dx.doi.org/10.1002/9780470172841.

[27] A. Durrani and Y. Luo, "Seismic retrofit of flat-slab buildings with masonry infills," in *Proc. NCEER Workshop on Seismic Response of Masonry Infills*, Buffalo, NY, 1994, pp. 1–8.

[28] C. Chrysostomou and P. Asteris, "On the in-plane properties and capacities of infilled frames," *Eng. Struct.*, vol. 41, pp. 385–402, 2012., http://dx.doi.org/10.1016/j.engstruct.2012.03.057.

[29] Applied Technology Council, *Evaluation of Earthquake Damaged Concrete and Masonry Wall Buildings, FEMA 306*, 1998.

[30] Masonry Standards Joint Committee, *Building Code Requirements for Masonry Structures*, TMS 402-16, 2016.

[31] Canadian Standards Association, *Design of Masonry Structures*, S304-14, 2014.

[32] New Zealand Standard, *Design of Reinforced Concrete Masonry Structures*, NZS 4230, 2004.

[33] W. El-Dakhakhni, M. Elgaaly, and A. Hamid, "Three-strut model for concrete mansory-infilled steel frames," *J. Struct. Eng.*, vol. 129, no. 2, pp. 177–185, 2003., http://dx.doi.org/10.1061/(ASCE)0733-9445(2003)129:2(177).

[34] F. Crisafulli and A. Carr, "Proposed macro-model for the analysis of infilled frame structures," *Bull. N. Z. Soc. Earthq. Eng.*, vol. 40, no. 2, pp. 69–77, 2007., http://dx.doi.org/10.5459/bnzsee.40.2.69-77.

[35] M. Yekrangnia and M. Mohammadi, "A new strut model for solid masonry infills in steel frames," *Eng. Struct.*, vol. 135, pp. 222–235, 2017., http://dx.doi.org/10.1016/j.engstruct.2016.10.048.

[36] S. Di Nino, "Numerical investigations on infilled frames and predictive formulae in the elastic regime," *Eng. Struct.*, vol. 250, no. 113349, pp. 113349, 2022., http://dx.doi.org/10.1016/j.engstruct.2021.113349.

[37] P. Lourenço, "Computacional strategies for masonry structures," Ph.D. dissertation, Delft Univ. Technol., Delft, 1996. [Online]. Available: https://repository.tudelft.nl/islandora/object/uuid%3A4f5a2c6c-d5b7-4043-9d06-8c0b7b9f1f6f

[38] G. Silva, "Escolha de parâmetros para análise de contato entre corpos elásticos usando elementos finitos e redes neurais," M.S. thesis, Univ. Est. Campinas, Campinas, 2009. [Online]. Available: https://www.repositorio.unicamp.br/handle/REPOSIP/265005

[39] T. Van and T. Lau, "Experimental evaluation of reinforced concrete frames with unreinforced masonry infills under monotonic and cyclic loadings," *Int. J. Civ. Eng.*, vol. 19, no. 4, pp. 401–419, 2021., http://dx.doi.org/10.1007/s40999-020-00576-7.

[40] I. Doudoumis, "Finite element modelling and investigation of the behaviour of elastic infilled frame under monotonic loading," *Eng. Struct.*, vol. 29, no. 6, pp. 1004–1024, 2007., http://dx.doi.org/10.1016/j.engstruct.2006.07.011.

[41] L. Cavaleri, M. Papia, G. Macaluso, F. Di Trapani, and P. Colajanni, "Definition of diagonal Poisson's ratio and elastic modulus foi infill masonry walls," *Mater. Struct.*, vol. 47, no. 1-2, pp. 239–262, 2014., http://dx.doi.org/10.1617/s11527-013-0058-9.

[42] L. Liberatore and L. Decanini, "Effect of infills on the seismic response of high-rise RC buildings designed as bare according to Eurocode 8," *Ing. Sism.*, vol. 28, no. 3, pp. 7–23, 2011.

[43] N. Noh, L. Liberatore, F. Mollaioli, and S. Tesfamariam, "Modelling of masonry infilled RC frames subjected to cyclic loads: State of the art review and modelling with OpenSees," *Eng. Struct.*, vol. 150, pp. 599–621, 2017., http://dx.doi.org/10.1016/j.engstruct.2017.07.002.

---

# IBRACON Structures and Materials Journal
## Revista IBRACON de Estruturas e Materiais

ORIGINAL ARTICLE

# Computational modeling of structural masonry shear walls considering cracking effects at mortar joints

*Modelagem computacional de paredes de contraventamento de alvenaria estrutural considerando os efeitos de fissuração nas juntas de argamassa*

Nicole Nahara Souza de Oliveira[a]  ID
Joel Araújo do Nascimento Neto[a]  ID
Guilherme Aris Parsekian[b]  ID

[a]Universidade Federal do Rio Grande do Norte – UFRN, Programa de Pós-graduação em Engenharia Civil, Natal, RN, Brasil
[b]Universidade Federal de São Carlos – UFSCar, Programa de Pós-graduação em Engenharia Civil, São Carlos, SP, Brasil

**Abstract:** This study presents a computational model to analyze structural masonry shear walls behavior considering the effects of mortar joint cracking on loss of stiffness. The simplified equivalent frame model was used but including link elements between the frame node to simulate the effects of cracking. The analyses were conducted using the SAP2000 computer program and consisted of modeling four shear walls on a 1/3 scale which were experimentally assessed. The results indicated that the proposed computational modeling approach consistently reproduced the effects of cracking at mortar joints, accurately simulating the nonlinear behavior of masonry.

**Keywords:** structural masonry, shear wall, computational modeling, equivalent frame method (EqFM), nonlinear analysis, cracking effects.

**Resumo:** O presente trabalho consistiu na elaboração de um modelo computacional para avaliar o comportamento de paredes de contraventamento de alvenaria estrutural de blocos considerando-se os efeitos da fissuração das juntas de argamassa na perda de rigidez. Com esse intuito foi utilizado o modelo simplificado de barras equivalentes, incluindo-se elementos de ligação entre as barras para simular numericamente os efeitos da fissuração. As análises foram realizadas utilizando-se o programa computacional SAP2000 e consistiram na modelagem de quatro paredes de contraventamento na escala 1/3 que foram ensaiadas experimentalmente. Os resultados indicaram que a modelagem computacional idealizada reproduziu de forma consistente os efeitos da fissuração na junta de argamassa, simulando adequadamente o comportamento não linear da alvenaria.

**Palavras-chave:** alvenaria estrutural, paredes de contraventamento, modelagem computacional, modelo de barras equivalentes (MBEq), análise não-linear, efeitos de fissuração.

## 1. INTRODUCTION

The structural masonry construction system has been widely used throughout Brazil over the past few years, due to its proven benefits such as speed in construction, economy of materials and improvement of workmanship. Experimental, theoretical and/or numerical studies on structural masonry buildings have been developed concurrently with its increasing use, contributing to a better understanding of how these structures behave and thereby optimizing construction processes and design.

Computational modeling is a valuable tool, since it allows the evaluation of different wall configurations subjected to different support conditions, applied load and analysis criteria. Computational models are usually validated by experimental tests, which, in turn, represent the characteristics of the structure under study. The present study aimed to evaluate the accuracy of the equivalent frame method (EqFM) computational model, developed by Nascimento et al. [1], to simulate the cracking effects of structural masonry walls in the building bracing system. The classic frame model was modified to allow simulation of the cracking nonlinear effects. The results of experimental tests reported by Nascimento [2] were used to validate the model. This study is justified by the fact that the loss of stiffness associated with shear wall cracking is still not fully understood by the technical-scientific community, and to allow better structural design of masonry buildings.

## 2 THEORETICAL FRAMEWORK

### 2.1 Shear walls in structural masonry buildings

In structural masonry buildings, shear walls are responsible for the overall stability of the building, providing rigidity and resistance to horizontal and vertical forces.

Parsekian et al. [3] reported that shear walls with a predominant length in the two main directions are necessary to provide rigidity to the building. According to Paes [4], these walls can be classified into those that brace the structure and those that are braced by other structural members. Despite being part of the structure, the element that is braced plays a minimal role in resistance when subjected to horizontal forces. On the other hand, bracing walls provide stability to the structure and resist the internal forces arising from the action of horizontal forces.

According to Parsekian et al. [3] and Mata [5], the behavior of these walls depends on several factors, such as boundary conditions and type of connections, magnitude of applied loads, type of materials used, type of masonry (reinforced or unreinforced), wall dimension, and existence of openings (doors and/or windows), among others. Nascimento [6] remarks that the resistance of a bracing wall is dependent on the stiffness developed in its own plane, meaning that stiffness to displacements outside this plane are neglectable. This aspect is of considerable importance in the behavior of the bracing walls when incorporating transverse walls as flanges.

### 2.2 Nonlinearity in structural masonry

Gomes [7] reports that a satisfactory nonlinear analysis of masonry must include the nonlinear behavior of the material, such as cracking, softening and hardening behavior, multiaxial stress states, and the behavior of the contact interface between block and mortar, including cracking. For these reasons, non-linear analyses of structural masonry are essential to validate theoretical models, to a better understanding how the structure behaves and conduct novel studies in this area.

According to Peleteiro [8], the nonlinear behavior of masonry is caused primarily by two effects: progressive rupture and nonlinear characteristics of the constituent materials. For the material model to represent the behavior of the masonry, both effects must be included. According to Andreaus [9], the failure of masonry walls subjected to loads in their own plane may be attributed to three basic mechanisms: sliding of the horizontal mortar joints, cracking of the units/blocks and splitting of the vertical mortar joint.

Most nonlinear models use so-called micro-modeling, which is characterized by the separate discretization of the units/blocks and the mortar, and, in some cases, the interface between them. However, this type of modeling only applies to analysis of small elements to assess the localized behavior of the masonry, as in the study of prisms and small walls. When a larger region of the structure is modeled to assess the global behavior, the best option is to use macro-modeling, where the masonry is treated as homogenized material whose mechanical and elastic properties are equivalent to the average characteristics of a given non-homogeneous material.

Examples of this type of modeling can be found in the studies of van Zijl [10], Garbor et al. [11] and Zucchini and Lourenço [12]. These studies are based on numerical models with results compared to experimental models of masonry panels subjected to horizontal forces. In all the studies, the authors performed micro-modeling of the masonry, with separate discretization of the block and mortar elements, attributing to them the specific properties of each material to simulate the masonry nonlinear behavior of individual panels. In the case of several wall members, such as those in building analysis, the use of micro-modeling is not adequate due to the number of unknowns in the numerical solution. In this case, the use of macro-modeling is preferable, as can be seen in the studies of Medeiros [13] and Lopes [14], who conducted linear analysis.

The study of Belmouden and Lestuzzi [15] is another example of macro-modeling application. The authors presented an equivalent planar-frame model with openings validated by an experimental study. The model deals with seismic analysis using the Pushover method for masonry and reinforced concrete buildings. In the model, based on the finite element method, were inserted nonlinear flexural springs at the ends of the piers and spandrel elements. For the development of capacity curves, the obtained results from the proposed model showed good agreement with experimental results.

The study of Voon and Ingham [16] presents two types of strut-and-tie models to evaluate wall strength compared with experimental tests. The first type was a simplified strut-and-tie model, which assumed that all panels were pinned at the bond beam center and that lateral force was applied to the bracing panels at the center of the bond beam. A second set of strut-and-tie models considered the lateral force to be applied as a single point load at the center of the wall top. Strength prediction by the simplified strut-and-tie method was found to closely match the test results of masonry walls with a single opening, but significant underestimation of strength by this method was found for walls with two openings.

In a recent study, Pirsaheb et al. [17] developed a model established on truss elements which have been improved in a second study reported by Pirsaheb et al. [18]. In both the models, namely Multi-Pier-Macro (MPM), the masonry is simulated by an assemblage of pier (vertical trusses) and diagonal connecting elements (braces). A validation analysis to correctly reproduce masonry behavior under axial loads, combined shear and compression stresses and bending and shear actions were developed. In sequence, four masonry full scale shear walls with different length to width ratios and presence or absence of openings were analyzed in the non-linear static range. The results obtained showed good agreement to experimental tests simulating in each step of loading the spreading and position of tensile and shear cracks.

## 2.3 Equivalent frame method (EqFM)

An experimental study of shear walls requires a high-quality laboratory, which is why so much experimental research use small scale models, given their large actual dimensions and the need for robust equipment. After proper calibration, computational modeling may become an alternative to experimental studies since computational resources are essential to research development. Thus, the present study consisted of evaluating a computational model that simulated the lack of stiffness resulting from the cracking of walls subjected to horizontal forces.

The equivalent frame method (EqFM), developed by Nascimento et al. [1], uses beam elements to discretize the wall and simulate stiffness in its own plane, thereby distributing stresses and strains in the masonry. This model was initially calibrated by Medeiros [13], Lopes [14] and Barbosa [19], albeit conducting linear analyses.

According to Medeiros [13], the discretization adopted in the model consists of arranging vertical bars in the hollows of the blocks and horizontal bars at the level of each course, considering the gross or net area of the masonry for both bars. In sections that exhibit grouting, the corresponding effect of increasing stiffness may be considered when adopting the modulus of elasticity of grouted masonry, even if the reference area is the gross section. Figure 1 illustrates a masonry wall discretized using the equivalent frame method (EqFM), showing the distribution of the bars and their position coincident with the center of gravity of the hollow blocks. In this numerical model the bars are represented by classical beam elements with six degrees of freedom in the ends and linear approximation for the displacements function. The specific properties of each bar are presented in the following.
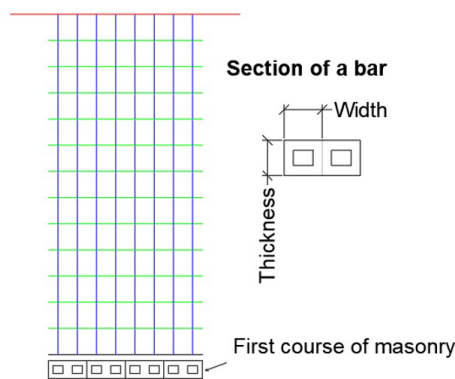


**Figure 1.** Discretization of a masonry wall using the equivalent frame method (EqFM).

## 2.4 Link elements in modeling

Link elements can be used in computational modeling to simulate the interaction at the interface between distinct parts of a structural member and may also be interpreted as contact nonlinearity. The link element used by Guerrante [20] to simulate cracking in reinforced concrete beams was the equivalent of six independent springs, one for each of the six degrees of freedom of deformation (one translation and one rotation along the normal axis of the contact plane, two translations and two rotations along the axes contained in the contact plane). The author studied the reinforcement of these beams using three-dimensional finite elements in the discretization, and GAP-type link elements, implemented in the SAP2000 software model library, which were arranged between the solid elements used in the beam simulation and the elements of reinforcement. The analysis consisted of comparing the numerical models developed by Guerrante [20] and the experimental results from Simões [21]. The results indicated that the modeling carried out by the author [20] was satisfactory, and all the elements used in the model adequately simulated the behavior observed in the experiment.

## 3 METHODOLOGY

The SAP2000 program was used to build the computational modeling of four walls selected from Nascimento [2]. The equivalent frame method (EqFM) was used, with the addition of link elements to simulate cracking in mortar joints.

## 3.1 Description of tests performed by Nascimento [2]

Nascimento [2] conducted tests with different configurations of 1:3 small scale walls. Of the walls evaluated, those denominated PISG1, PICG1, PPSG1 and PPCG1 were selected for computational modeling. Walls that did not display an opening were denominated individual walls, also used in the following analyses, whose dimensions in centimeters are shown in Figure 2. The PISG1 wall represents an unreinforced masonry wall, and PICG1 a reinforced masonry wall with grouting at the ends. Figure 2c illustrates part of the instrumentation used in the tests for measuring horizontal displacements. The horizontal displacements measured by transducers T1 and T2 were used for comparison purposes with computational models. In the walls, reinforced concrete elements (slab strips) were placed at the base and at the top to improve the distribution of vertical and horizontal forces.
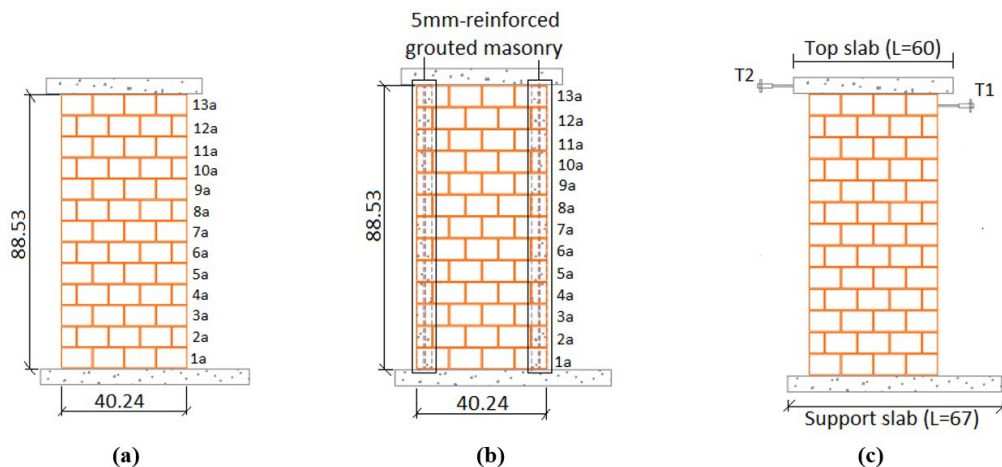


**Figure 2.** Individual shear wall (dimensions in centimeters). (a) PISG1 Wall; (b) PICG1 Wall; (c) Displacement measurement locations. (Source: adapted from Nascimento [2]).

Figure 3 illustrates the geometry, grouting locations, and part of the instrumentation used in the tests to measure the horizontal displacements of walls with typical door opening.
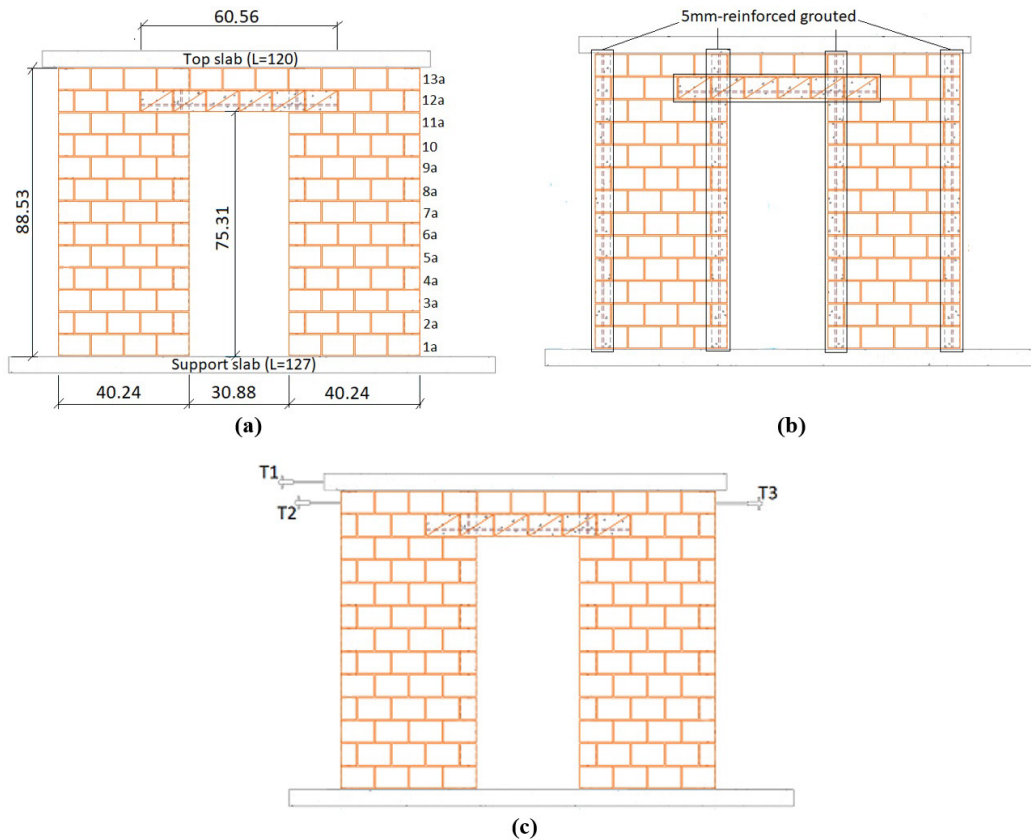
**Figure 3.** Walls with door opening. (a) PPSG1 Wall; (b) PPCG1 Wall; (c) Displacement measurement locations. Measurements in centimeters (Source: adapted from Nascimento [2]).

The experimental tests were performed using the apparatus illustrated in Figure 4 in accordance with the following procedure:

a) Previous vertical loading: three cycles of 8 kN each one was applied to the shear wall;

b) Vertical load referring to the pre-compression: vertical force equals to 30.5 kN were applied to obtain pre-compression equals to 1.64 MPa;

c) Monotonically horizontal force was applied to the shear wall reaches the total collapse.
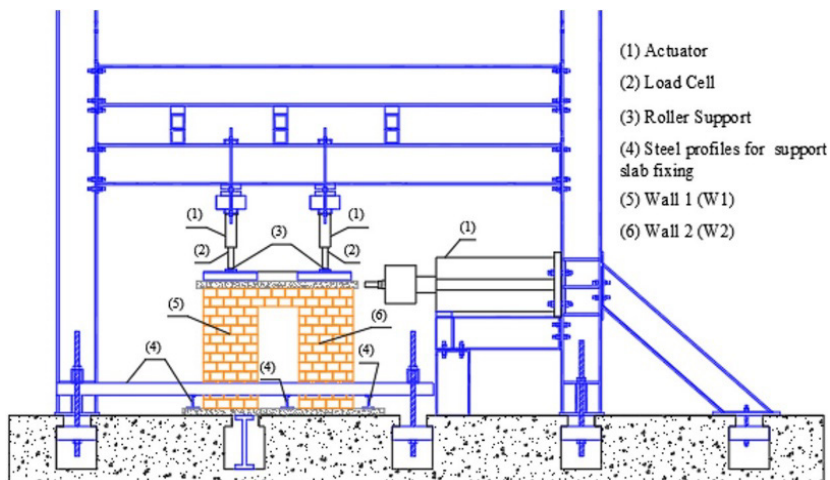


**Figure 4.** Test apparatus for shear walls.

## 3.2 Walls modeling

Computational modeling was performed by applying the equivalent frame method (EqFM), using SAP2000 software. Discretization consisted of arranging vertical bars at each block hole and horizontal bars in the mortar joints. The top slab was simulated using a horizontal bar with the properties of the reinforced concrete used in the test. The horizontal and vertical displacements were restrained at the base of the wall to simulate its support in the laboratory reaction slab. The spacing of the bars and the dimensions of the sections that each represents are shown in Figure 5. The bars in the numerical model are represented by the classical beam elements with six degrees of freedom in the ends and linear approximation for displacements function, as mentioned before. More details about the models can be found in Oliveira [22].

### 3.2.1 Model 1 and Model 2

In Model 1, which represents the PISG1 Wall, only vertical bars with non-grouted masonry properties were used (Figure 5a). In Model 2, which represents the PICG1 Wall, bars with grouted masonry properties were also inserted in the position of the end holes, in addition to bars with the elastic properties of steel arranged beside the grouted bars (Figure 5b). Model 2 also displays a variation, divided into Model 2a, which considers reinforcement on the tensioned and compressed sides, and Model 2b, which considers reinforcement only on the tensioned side (right side).
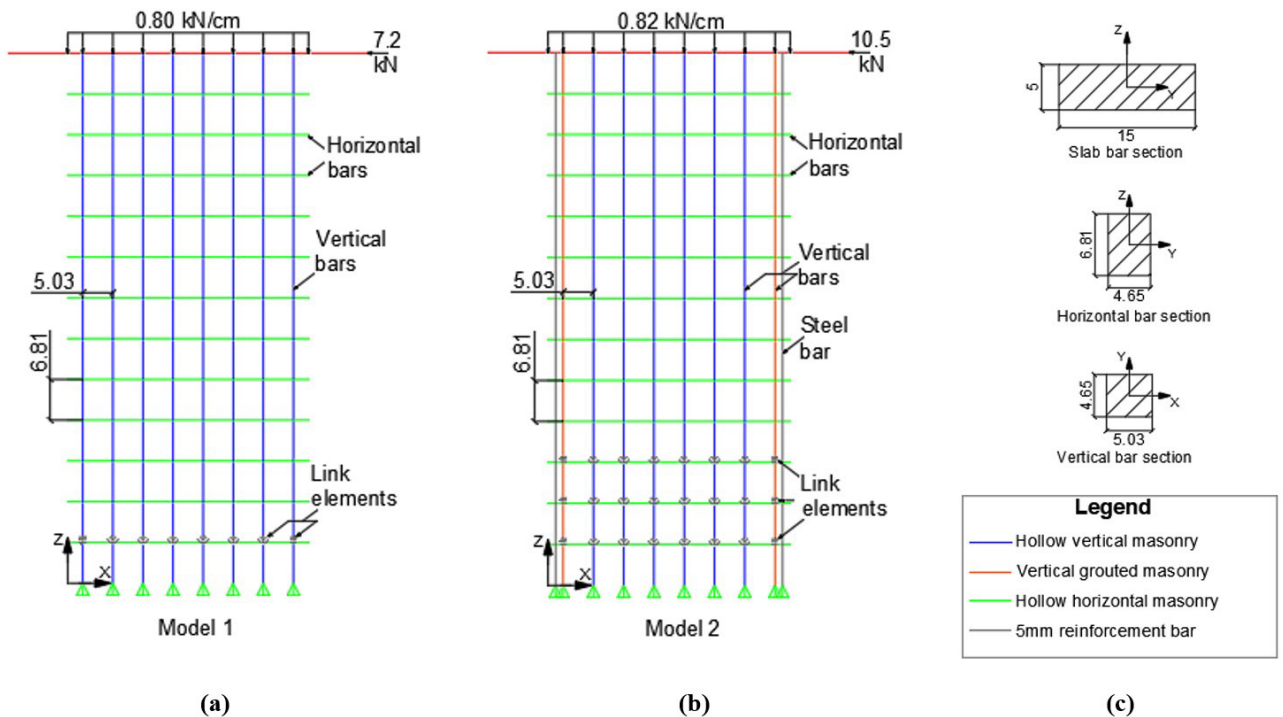


**Figure 5.** Representation of Models 1 and 2 with the cross sections and applied load. (Dimensions in centimeters).

In the SAP2000 software there are link elements available in its element library, which exhibit the length defined by the distance between the two nodes that will be connected by this element. Each type of link allows specific degrees of freedom to be associated with a linear or non-linear analysis, as well as the force-displacement law possible for each degree [16]. Thus, to simulate the effect of cracking on mortar joints, a combination of two links available in the software was selected: the GAP and the T/C Friction Isolator (T/C-FI).

The GAP element only allows compression stresses, leaving it completely free for separation between the nodes to occur in the normal direction along the contact line without mobilizing any type of bond and/or degree of freedom. The T/C Friction Isolator element allows the occurrence of both tensile and compression stresses in the normal direction along the contact line, in addition to the insertion of resistance parameters in the other two orthogonal directions, making it possible to consider the shear resistance. These two types of link elements were used in the simulations.

Rev. IBRACON Estrut. Mater., vol. 16, no. 4, e16410, 2023

6/15

The link elements were positioned based on the behavior observed in the tests. In the case of the PISG1 wall, cracking was restricted to the horizontal joint at the base. Thus, in the computational model that represents this wall (Model 1), the link elements were introduced just above the first course, as illustrated in Figure 5a. With respect to the elastic properties, since the PISG1 wall was not grouted, the modulus of elasticity of non-grouted masonry in the gross area of the section (6165 MPa), obtained experimentally by Nascimento [2] was used.

The authors comment that for walls quite different from the ones evaluated in this study, the links allocation can be defined from a previous numerical simulation, observing the occurrence of tensile stresses.

In relation to the PICG1 wall, several configurations for the link elements were evaluated before obtaining the one illustrated in Figure 5b. The presence of grouting and vertical reinforcement at the ends of the section resulted in excessive stiffness when adopting the same configuration as in Model 1, making some adjustments necessary. These modifications involved using link elements in the first three courses, consistent with the cracking observed in the test. Two vertical bars were used at the ends, one simulating grouted masonry with the presence of link elements to simulate the occurrence of separation/cracking between courses, and another simulating the reinforcement, in which no link elements were included, allowing the continuity of the reinforcement and the transfer of stresses through the crack (Figure 5b). Thus, in addition to reducing the stiffness of the computational model, the intention was to simulate the cracking that occurred in the first three courses during the PICG1 wall test.

A combination of two connecting elements was used because in tests performed using only the GAP in all the bars of a course, shear stress distribution in the model was incompatible with that obtained in the test, since the GAP only works under compression and the test also involved application of horizontal forces, thereby causing shear stress. The exclusive use of the T/C FI caused the more flexible Model 1 not to resist the addition of horizontal loading and showed inconsistent displacement before reaching the collapse load obtained in the test. Thus, the T/C FI element was used only in the internal vertical bars of the two models and the GAP in the external vertical bars (Figure 6). Regarding nodes where link elements were not used, the bars are completely connected.
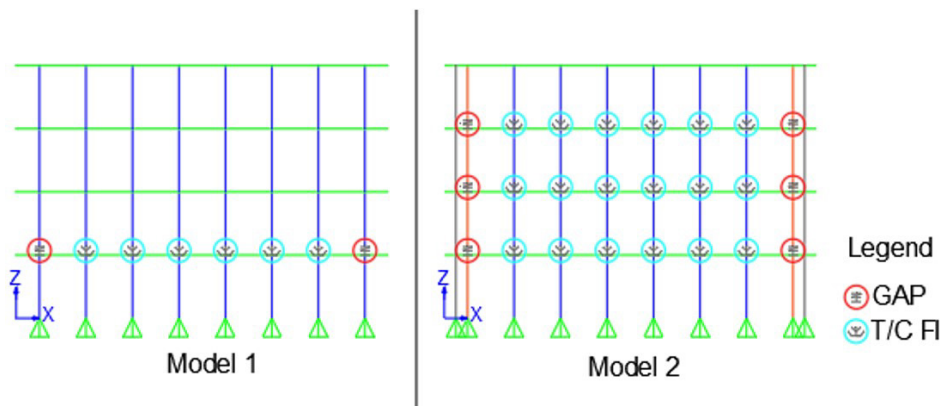


**Figure 6.** The first 4 courses of Models 1 and 2 with the position of GAP and T/C FI elements

### 3.2.2 Models 3 and 4

Models 3 and 4 refer to the modeling of walls PPSG1 and PPCG1, respectively, and were created by connecting the individual walls discretized by Models 1 or 2 using a lintel. With respect to Model 3, a combination of two Model 1 walls was used, denominated W1 and W2 for each of the wall regions (Figure 7a). According to Nascimento [2], different elastic moduli were established for the two regions from measurements taken on the wall during vertical loading, namely 8099 MPa and 4831 MPa for regions W1 and W2, respectively.

In Model 4, the combination consisted of two walls similar to Model 2, adopting the same name for the wall regions (Figure 7b). Based on the previous justification, W1 and W2 were assigned a modulus of elasticity equals to 8007 MPa and 9377 MPa, respectively, obtained from Nascimento [2]. The difference between these models and Models 1 and 2 is that only the T/C Friction Isolator link element was used, instead of combining it with the GAP element. In the tests performed, this configuration proved to be sufficient and satisfactory in tests with walls PPSG1 and PPCG1.

With respect to properties associated with GAPs and T/C FIs, as mentioned above, stiffness can be assigned at each degree of freedom direction. The nonlinear behavior and properties of the GAP were defined in relation to the vertical

direction of the wall (U1), axial to its cross section, since this is the direction of the cracks in the mortar joints. For T/C FI, in addition to the properties related to the axial direction, those pertaining to the transverse direction (U2) were also defined, in the same direction as the horizontal force applied. A summary of the properties is shown in Table 1.
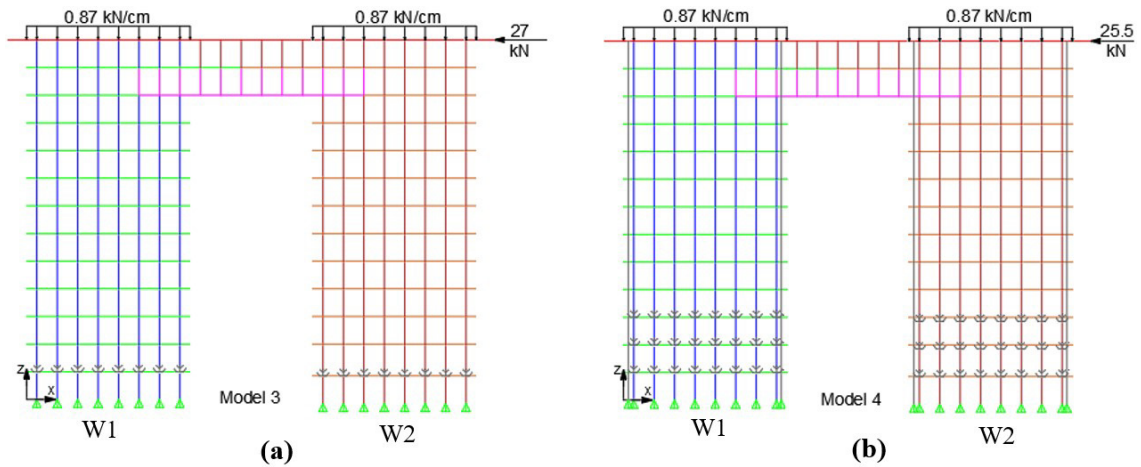


**Figure 7.** Loading illustration for Models 3 and 4

**Table 1.** GAP and T/C Friction Isolator property elements

| Property | GAP | T/C FI |
|---|---|---|
| Compressive stiffness ($k_{U1}$) (kN/cm) | 2117.42 | 2117.42 |
| Tensile stiffness ($k_{U1}$) (kN/cm) | - | 0 |
| Transverse stiffness ($k_{U2}$), when U1 refer to Tension or Compression (kN/cm) | - | 179.65 |
| Opening (cm) | 0 | 0 |
| Friction coefficient | - | 1 |

The compressive stiffness ($k_{U1}$) was determined from the classical strength of materials theory (Equation 1).

$$k_{U1} = \frac{EA}{L} \tag{1}$$

In which: $E$ is the longitudinal elasticity modulus of non-grouted masonry; $A$ represents the cross-sectional area of a masonry bar; $L$ is the length of a masonry bar.

The transversal stiffness value ($k_{U2}$) was calculated by Equation 2, which refers to the inverse of the displacement due to shear force, according to the classical concepts of structural theory.

$$k_{U2,U3} = \frac{G_a \times A}{c \times H} \tag{2}$$

In Equation 2, $G_a$ is the transversal elasticity modulus obtained from Equation 3:

$$G_a = \frac{E_a}{2 \times (1+v)} \tag{3}$$

In which: $E_a$ is the longitudinal elasticity modulus of non-grouted masonry; $v$ is the coefficient of poisson; $A$ represents the cross-sectional area of a masonry bar; $c$ is a corrective factor of the shear stress distribution (equals to 1.2 for rectangular sections); and $H$ is the height of the wall.

About the initial null opening value, tests that varied this parameter found no influence on the results obtained. This was expected, since this parameter is associated with the mobilization of degrees of freedom corresponding to compressive stresses, and the nonlinearity evaluated is related to the mobilization of tensile stresses. A length of 1.0 cm was adopted for the link elements because lower values resulted in numerical inconsistency. The friction coefficient was obtained from preliminary analyzes performed by the authors, varying this parameter between 0.5 and 1.0. The tests results showed that this coefficient did not have much influence. Therefore, based on recommendations from

Canadian Standards Association (S304-14) [23] and the studies of Parsekian et al. [3] and Pasquantonio et al. [24], the authors decided to adopt 1.0 as the value of the friction coefficient. In their work, Pasquantonio et al. [24] presents a table with five other references about the coefficient of friction at the interface between masonry and mortar. The average value of the coefficient of friction ($\mu$) founded by those researchers was equal to 1.07, while the value of 0.61 was obtained by Pasquantonio et al. [24] in the experiments carried out in their research.

### 3.3 Loading Cases

Given that the purpose of computational modeling was to evaluate the reduction of wall stiffness caused by cracking, loading was applied incrementally. Thus, a combination of geometric nonlinear loading was used, consisting of vertical loading and horizontal forces (Figure 5). All the models were submitted to pre-compression equals to 1.64 MPa corresponding to vertical load equals to 0.80 kN/cm and 0.82 kN/cm for Models 1 and 2, respectively. The horizontal forces were incrementally applied to the computational model up to collapse load achieved in the test, with intensities of 7.2 kN and 10.5 kN, corresponding to Models 1 and 2, respectively. Models 3 and 4 were submitted to a vertical load of 0.87 kN/cm on each of the regions. The maximum horizontal load applied in Models 3 and 4 was 27 kN and 25.5 kN, respectively (Figure 7). Thus, the following procedure was adopted for the loads considered in the computational models:
- Exclusive application of vertical loading to obtain the initial state of compressive stresses in the walls.
- Based on the initial stress state in the wall, horizontal force was introduced in 1.0 kN increments, up to the maximum value obtained in each of the tests. The aim was to induce the formation and propagation of cracking in the wall and incrementally assess the progressive lack of stiffness.

It is important to emphasize that no non-linear behavior was considered for the masonry materials; only the effects arising from cracking in the horizontal mortar joints were evaluated.

## 4 RESULTS AND DISCUSSIONS

### 4.1 Analysis of horizontal displacements

According to Nascimento's study [2], the horizontal displacements measured by transducers T1 and T2 were used for comparison purposes with the results of computational models, as illustrated in Figure 2c, associated with the top slab and the top masonry course, respectively. In the following graphs (Figure 8 and Figure 9), the solid lines represent the experimental results (Exp.), and the dashed lines the computational modeling results.

### 4.1.1 Results of unreinforced walls

Figure 8 illustrates the horizontal displacements associated with walls PISG1 and PPSG1. According to Nascimento [2], in the case of PISG1, linear behavior was characterized as the horizontal force ranged between 1 kN and 3.5 kN, after which nonlinear behavior was identified and intensified after the first visible crack at 5.7 kN. According to the author, total wall failure occurred with a horizontal force intensity of 6.7 kN. Nascimento [2] also reports that the horizontal section of the curve corresponds to a rigid body movement which, in turn, may be associated with hinge formation at the base of the wall, where residual resistance could be linked to the formation of a diagonal strut. Under these stress distribution conditions; the wall was already about to fail.

As can be seen in Figure 8a, the numerical model displayed a tendency to behave similarly to its experimental counterpart, despite being more flexible. A section with linear behavior is observed until the intensity of the horizontal force reaches 3.5 kN, with initial nonlinear behavior between 3.5 kN and 4.8 kN, whose effect intensified from 5.0 kN onwards, just before the experimental result. The maximum displacement achieved with the computational model was 8.84 mm, in transducer 1, 1.7 times higher than that recorded in the test, equals to 5.2 mm. This greater flexibility in the computational model can be attributed to its simpler simulation using discrete elements (bars), which therefore may not represent smooth crack propagation. Another factor that could have influenced stiffness in the computational model is the greater complexity of simulating a non-reinforced element, which can make it difficult to achieve equilibrium during nonlinear processing. The results obtained with the computational model corroborate Nascimento's description [2], in which he considered a main crack in the base as the most important part of nonlinear wall behavior.

One aspect that was not well represented in the computational result was the rigid body movement described by the author of the tests. This effect is difficult to simulate, especially when plasticity and/or rupture criteria are not used for masonry, leaving these aspects to be explored in future research. Nevertheless, the proposed model did yield the final objective, which was the simulation of stiffness degradation from the cracking process at the base of the wall.

Furthermore, for the purpose of evaluating stiffness lack in building walls, the model exhibits result that favor safety, since a greater lack is estimated than that obtained experimentally.

The results obtained for wall PPSG1 (Figure 8b) showed the same tendency as those of PISG1, where the computational model was more flexible than its experimental counterpart, whose collapse was occurred with a horizontal force of 24 kN. In contrast to what occurred with PISG1, the maximum displacements associated with the computational model were close to those obtained experimentally. This result may be attributed to less cracking in the wall region to the left of the opening, as described by Nascimento [2], thereby reducing the effects of wall stiffness lack and making the assembly less unstable and the computational simulation less complex. According to the author, linear behavior is acceptable up to a horizontal force of 15 kN, after which nonlinear behavior is observed, intensifying at 18 kN after the first visible crack. Model 3 shows linear behavior up to approximately 11 kN of horizontal force, where nonlinearity is characterized, intensifying from 15 kN onwards, results similar to those obtained experimentally. As previously mentioned, including plasticity and/or rupture criteria may further improve these results, which could be investigated in future research.

With respect to the models with no reinforcement or vertical grouting, it should be noted that building codes stipulate the use of reinforcement whenever tensile stresses occur in the structural walls. The results presented here do not apply to unreinforced shear wall situations with tension loads. The aim is to validate the computational modeling proposed based on the behavior of a difficult computational simulation due to the absence of vertical reinforcement.
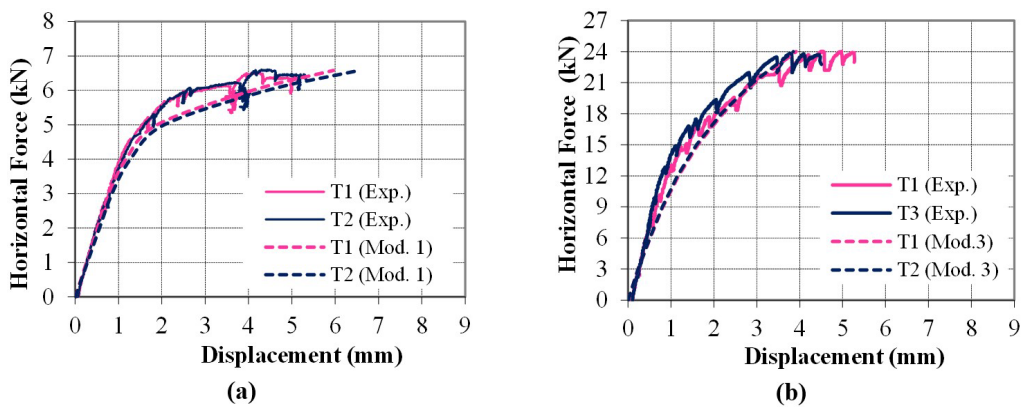


**Figure 8.** Horizontal force × horizontal displacement graph: (a) PISG1 Wall and Model 1; (b) PPSG1 Wall and Model 3.

### 4.1.2 Results of reinforced walls

Figure 9 illustrates the results of walls PICG1 and PPCG1. With respect to the experimental results for PICG1, Nascimento [2] found that the linear section was formed between horizontal forces of 1.0 kN and 4.5 kN, followed by the onset of nonlinear behavior, with the first visible crack observed at 7.0 kN. According to the author, the wall failed at a horizontal force intensity of 10.5 kN and, unlike PISG1, without the occurrence of rigid body movement and the appearance of a horizontal section in the curve. The absence of the horizontal section, lower stiffness lack, and greater horizontal failure load of PICG1 in relation to its PISG1 counterpart may be attributed to the effect of grouting and vertical reinforcement at the ends. In contrast to PISG1, cracking in PICG1 occurred in three courses at the base, underscoring the effect of vertical reinforcement on the transfer of tensile stresses through these cracks.

Two Model 2 configurations were assessed, considering or not reinforcement at the compressed end of the wall. This variation in the computational model was based on the study conducted by Camacho et al. [25], Oliveira [22], who found that different reinforcement ratios did not influence the compressive strength of concrete block prisms. The results obtained showed no significant differences, except for the section after a horizontal force of 9.0 kN was applied, where the model without compressed reinforcement showed more intense nonlinearity. Thus, only the results of the model with compression reinforcement were displayed.

Comparison of the results obtained for Model 2 and wall PICG1 demonstrated statistically similar absolute values. Assessment of the initial linear section of the computational model revealed that it was limited by the intensity of the horizontal force of approximately 4.0 kN, 11.31% below the experimental value. Intensified nonlinear behavior was identified starting at a force of 6.0 kN, a value 14.3% lower than that associated with the appearance of the first visible

crack during the test. PICG1 failed at a top displacement of 6.2 mm, while Model 2 resulted in a top displacement of 5.71 mm, corresponding to a difference of -7.9%.
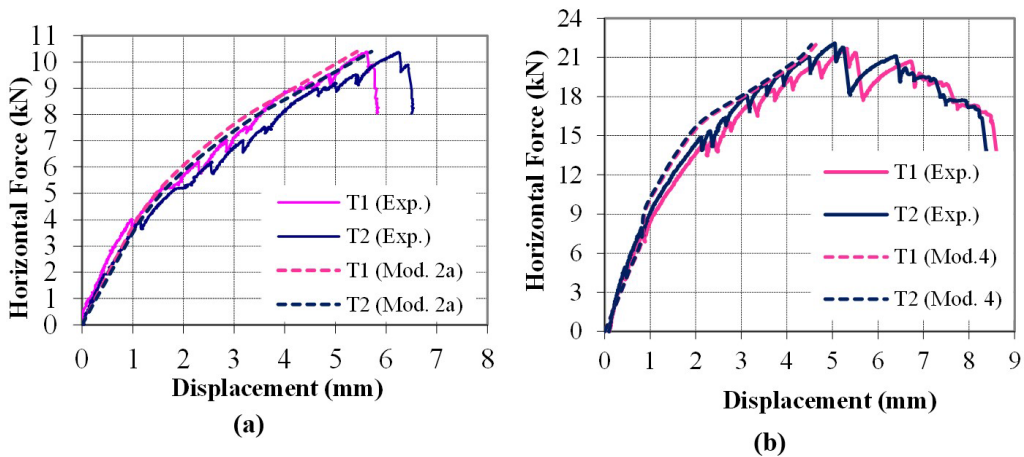


**Figure 9.** Horizontal force × horizontal displacement graph: (a) PICG1 Wall and Model 2; and (b) PPCG1 Wall and Model 4.

About the PPCG1 wall, the similarity between the results of the computational (Model 4) and experimental models is also significant. As reported by Nascimento [2], greater stiffness lack occurred starting at 18 kN and the test reached a maximum horizontal force intensity of 22 kN. Model 4 shows that intensification began at approximately 16 kN (11.1% lower). The post-peak sections observed in the experimental results could not be simulated in the computational model, and since the main objective was to evaluate the lack of stiffness from cracking, failure and plasticity criteria were not considered for masonry in this study.

## 4.2 Analysis of normal stress distribution in computational modeling

### 4.2.1 Models 1 and 3

Analysis of normal stress distribution is associated with the corresponding models submitted to the maximum intensity of the horizontal force measured in the tests, namely 7.2 kN in Model 1 and 27 kN in Model 3. Figure 10 illustrates the normal force distribution in Model 1, on computational modeling (Figure 10a) and experimental tests (Figure 10b). As expected, compressive forces were concentrated on the left edge of the wall, increasing from the top to the base, suggesting the formation of a diagonal strut. Figure 10c illustrates the stress distribution at the base of the wall, showing a section to the left with a region subjected to compressive stresses in the base course, with a maximum intensity of -1.33 kN/cm², a long central stress-free section, associated with the horizontal crack in the mortar joint, and, finally, very low tensile stresses at the other end of the wall. A horizontal cross section in the second course of the wall showed no tensile stresses, indicating adequate simulation of cracking in the horizontal joint.

In relation to Model 3, Figure 10a-10b demonstrate the normal stress distribution, with a formation of a possible diagonal strut in the region of the wall to the left of the opening, starting from the upper right corner at the connection point with the lintel, towards the lower left corner at the base of the wall. In the region on the right, there is a small concentration of compressive stresses in the lower left corner, and a section at the top of the wall with high intensities caused by horizontal forces. Stress distribution in horizontal cross sections at the base of this wall, as seen in Figure 11c, was consistent with the cracking observed during the test. No stress occurred over most of the cross section of the wall region to the right of the opening, which was subjected to compressive stress equivalent to the length of only one block. In the wall region to the left of the opening, the stress-free region was limited to nearly half the width of the region, where the region submitted to compressive stresses exhibited maximum intensities 2.50 times greater than those of the other wall region.

**(a)**

**(b)**



**(c)**
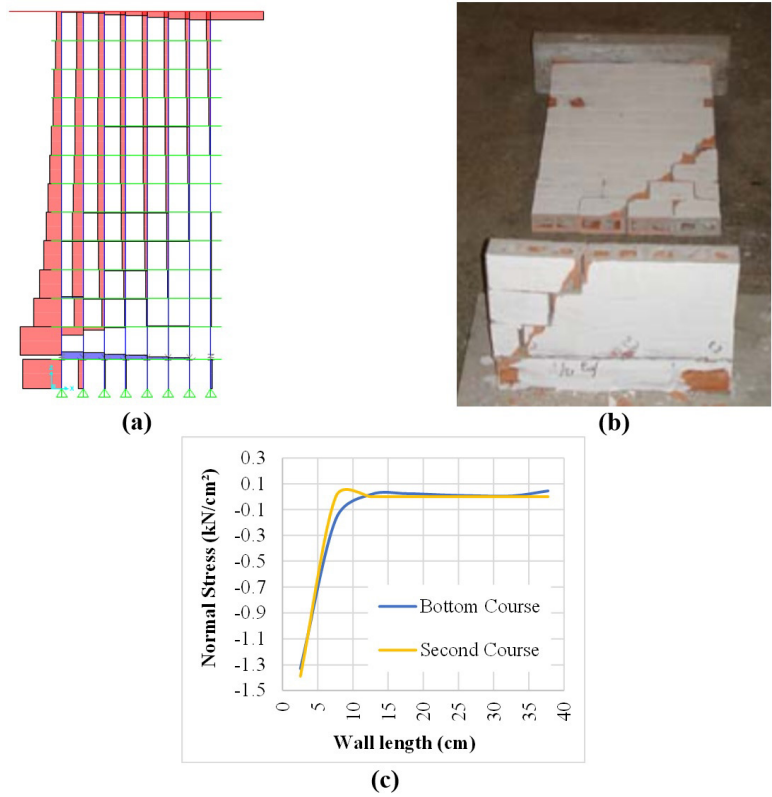
**Figure 10.** Normal stress distribution in Model 1: (a) Computational Modeling; (b) Experimental Test; (c) Normal stress distribution in the base cross sections.



**(a)**

**(b)**



**(c)**
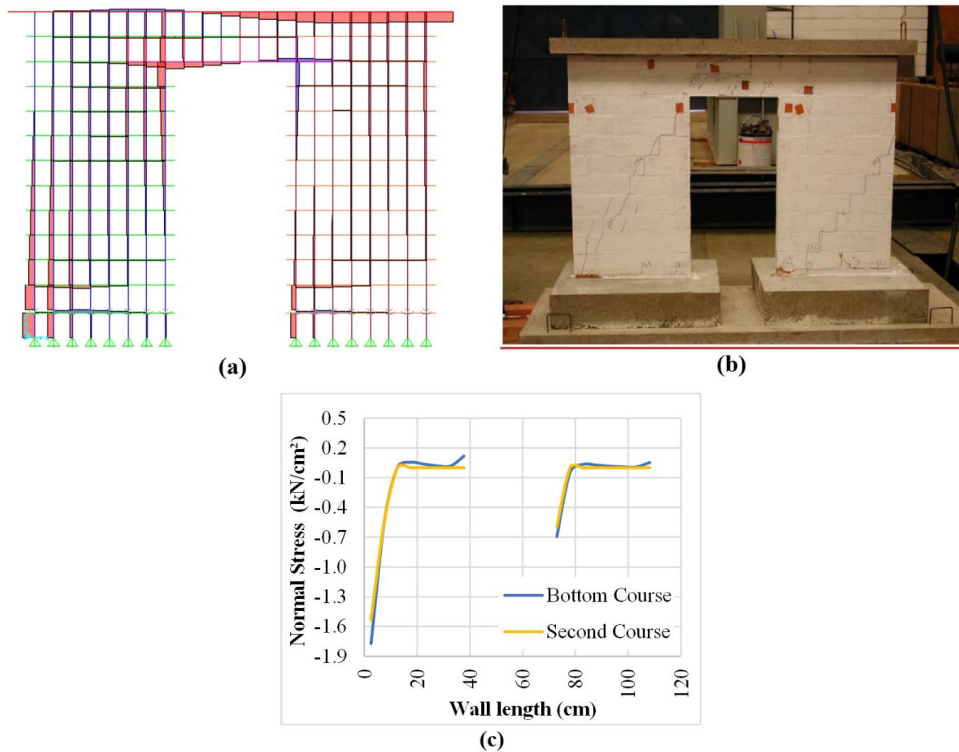
**Figure 11.** Normal stress distribution in Model 3: (a) Computacional Modeling; (b) Experimental Test; (c) Normal stress distribution in the base cross sections.

Rev. IBRACON Estrut. Mater., vol. 16, no. 4, e16410, 2023

12/15

#### 4.2.2 Models 2 and 4

The results exhibited below refer to the horizontal force caused by the failure of the experimental models, namely 10.5 kN in PICG1 and 25.5 kN in PPCG1. A comparison between Figure 12a-12b and the corresponding for PISG1 (Figure 9a-9b) reveals similar behavior, except for the occurrence of tensile stresses over the entire right edge of the wall, resulting from the vertical reinforcement. The beneficial effect of reinforcement in controlling cracking and thereby increasing wall stiffness is evident in the tensile stress peaks of Figure 12c, reaching yield stress in the cross-section of the second course, with continuous reduction in the tensile stress in the courses immediately above. The peaks are so high that the compressive stresses associated with the masonry become imperceptible, even in the cross-section region with vertical grouting. These stresses are only seen in Figure 12d, where stress in reinforcement was omitted. This figure also shows the occurrence of a stress-free region in cross-section, which declines with the addition of courses, associated with the occurrence of probable cracking. It is noteworthy that cracking was detected up to the third course in the wall test. The occurrence of short stress-free region in cross-sections beyond the third course is fully acceptable, since the reinforcement controls cracking, making it imperceptible. Regarding the region of cross-sections submitted to compressive stresses, in the base cross-section their extension is smaller, and the maximum intensity is higher. This tendency may be due to the greater bending moment intensity at the base, resulting in greater compressive and tensile stresses, thereby increasing maximum compressive stress and the stress-free region in cross-section, associated with crack extension in the mortar joint.

The results of Model 4 demonstrate the same trend of diagonal strut mobilization in both regions of the wall, as that observed in Model 2. The vertical reinforcement mobilization illustrated in Figure 13 shows that the reinforcement subjected to the greatest tension was in the wall region to the right of the opening, corroborating the occurrence of more intense cracking in this region. Nevertheless, yield stress was not characterized. In relation to compression reinforcement, a relevant stress intensity of 40 kN/cm$^2$ was detected in Model 2. It is important to note that the tests conducted by Camacho et al. [25] investigated prisms submitted to simple compression, which differs significantly from the axial compression with flexure applied to the walls studied here. Thus, it is necessary to reassess the effect of compressed reinforcement under stress distribution like that exhibited by the shear walls studied. It should also be noted that the modeling without compression reinforcement was evaluated and no substantial changes in stiffness were detected.
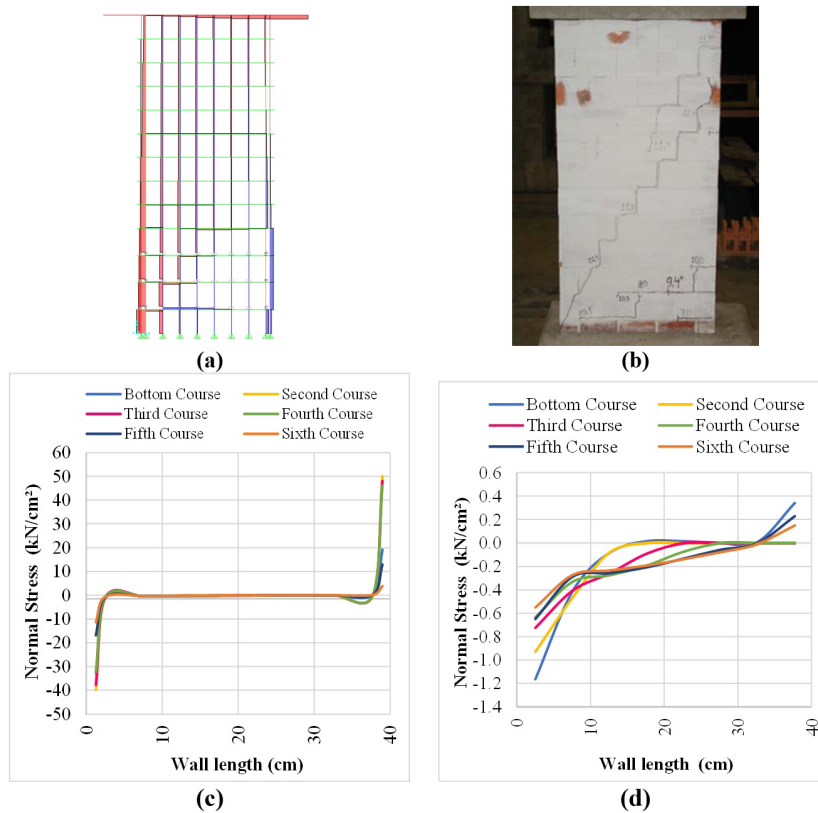


**Figure 12.** Normal stress distribution in Model 2: (a) Modeling; (b) Experimental test. Normal stress distribution in the base cross-sections: (c) with stress in reinforcement; (d) without stress in reinforcement
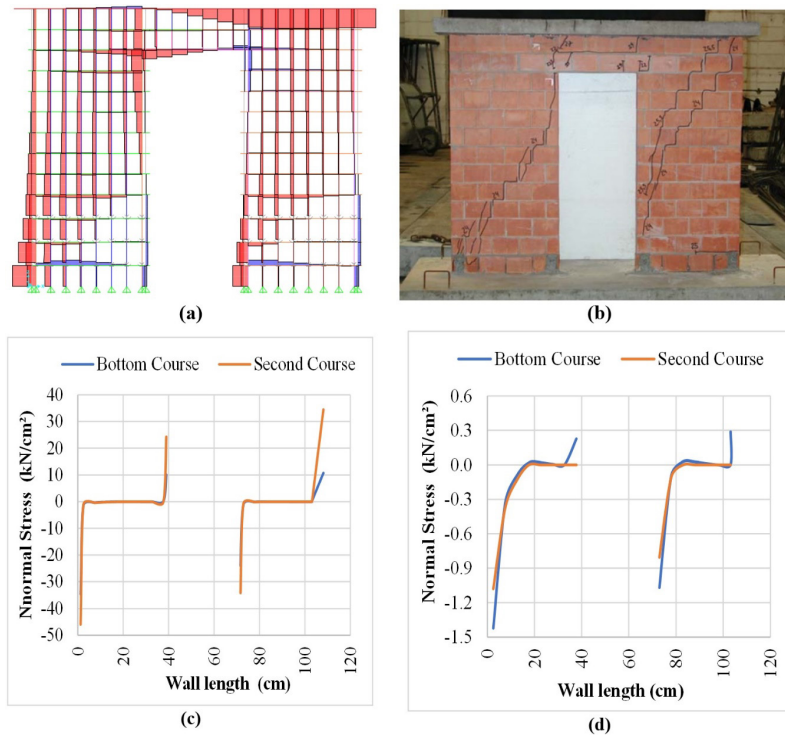
**Figure 13.** Normal stress distribution in Model 4: (a) Modeling; (b) Experimental test. Normal stress distribution in the base cross-sections: (c) with stress in reinforcement; (d) without stress in reinforcement.

## 5 CONCLUSIONS

The analyses proposed in this study consisted of using an improved equivalent frame method (EqFM) to computationally simulate the behavior of masonry shear walls subjected to horizontal and vertical loads in their own plane. The main objective was to determine the model's capacity to represent the walls stiffness degradation caused by cracking in the horizontal mortar joints. Based on the results obtained, the following conclusions could be drawn:

- The use of simple link elements that allow complete separation between the courses of the shear wall when tensile stresses occur was sufficient to simulate the initialization and propagation of cracks;
- In the shear wall without vertical reinforcement, the use of link elements associated with the first horizontal mortar joint is sufficient to represent the behavior observed, since the main cracking occurs in this joint before the wall fails;
- In the shear wall with grouting and vertical reinforcement at the ends, it is necessary to use link elements in the first three courses. Including compressive reinforcement in the modeling did not lead to significant changes in shear wall stiffness. However, its participation in stress distribution and resistance of the cross section submitted to axial compression and flexure load requires further investigation;
- The computational models developed proved to be efficient in simulating the stiffness degradation caused by cracking in the horizontal mortar joints. The numerical curves yield strong similarity with those obtained in the tests, and the computational models were always slightly more flexible and thus favor safety;
- In addition to the change in behavior between reinforced and non-reinforced shear walls, analysis of normal stress distribution in different cross-sections of the walls also indicated the efficiency of reinforcement in transferring tensile stresses between the cracks.

## REFERENCES

[1] J. A. Nascimento No., K.A.S. Medeiros, and F. Quim, "Nova modelagem para análise da interação entre painéis de alvenaria e estrutura de suporte," *Rev. Prisma.*, vol. 3, no. 52, pp. 39–48, Maio 2014.

[2] J. A. Nascimento No., "Estudo de painéis com abertura constituídos por alvenaria estrutural de blocos," Doctoral dissertation, Esc. Eng. São Carlos, Univ. São Paulo, São Carlos, SP, Brazil, 2003.

[3] G. A. Parsekian, A. A. Hamid, and R. G. Drysdale, *Comportamento e Dimensionamento de Alvenaria Estrutural*, 2nd ed. São Carlos, SP, Brazil: EdUFSCar, 2013.

[4] M. S. Paes, "Interação entre edifício de alvenaria estrutural e pavimento em concreto armado considerando-se o efeito arco com a atuação de cargas verticais e ações horizontais," Master thesis, Esc. Eng. São Carlos, Univ. São Paulo, São Carlos, SP, Brazil, 2008.

[5] R. C. Mata, "Análise experimental e numérica do comportamento de juntas em painéis de contraventamento de alvenaria estrutural," Doctoral dissertation, Esc. Eng. São Carlos, Univ. São Paulo, São Carlos, SP, Brazil, 2011.

[6] J. A. Nascimento No., "Investigação das solicitações de cisalhamento em edifícios de alvenaria estrutural submetidos a ações horizontais," Master thesis, Esc. Eng. São Carlos, Univ. São Paulo, São Carlos, SP, Brazil, 1999.

[7] D. I. S. Gomes, "Análise não-linear física simplificada de estruturas de contraventamento de edifícios de alvenaria estrutural," Master thesis, Esc. Eng. São Carlos, Univ. São Paulo, São Carlos, SP, Brazil, 2010.

[8] S. C. Peleteiro, "Contribuições à modelagem numérica de alvenaria estrutural," Doctoral dissertation, Esc. Eng. São Carlos, Univ. São Paulo, São Carlos, SP, Brazil, 2002.

[9] U. Andreaus, "Failure criteria for masonry panels under in-plane loading," *J. Struct. Eng.*, vol. 122, no. 1, pp. 37–46, Jan. 1996, http://dx.doi.org/10.1061/(ASCE)0733-9445(1996)122:1(37).

[10] G. P. A. G. van Zijl, "Modeling masonry shear-compression: role of dilatancy highlighted," *J. Eng. Mech.*, vol. 130, no. 11, pp. 1289–1296, Nov. 2004.

[11] A. Gabor, E. Ferrier, E. Jacquelin, and P. Hamelin, "Analysis and modelling of the in-plane shear behaviour of hollow brick masonry panels," *Constr. Build. Mater.*, vol. 20, pp. 308–321, Mar. 2005, http://dx.doi.org/10.1016/j.conbuildmat.2005.01.032.

[12] A. Zucchini and P. B. Lourenço, "A micro-mechanical homogenisation model for masonry: application to shear walls," *Int. J. Solids Struct.*, vol. 46, pp. 871–886, Oct. 2008, http://dx.doi.org/10.1016/j.ijsolstr.2008.09.034.

[13] K. A. S. Medeiros, "Modelagem computacional para avaliação da interação entre painéis de alvenaria e estrutura de suporte em concreto armado," Master thesis, Prog. Pós-grad. Eng. Civil, Univ. Fed. Rio Grande do Norte, Natal, RN, Brazil, 2015.

[14] A. C. S. Lopes, "Aperfeiçoamento de modelagem computacional para análise da interação entre painéis de alvenaria e estrutura de suporte em concreto armado," Undergraduate thesis, Dept. Eng. Civil, Univ. Fed. Rio Grande do Norte, Natal, RN, Brazil, 2016.

[15] Y. Belmouden and P. Lestuzzi, "An equivalent frame model for seismic analysis of masonry and reinforced concrete buildings," *Constr. Build. Mater.*, vol. 23, no. 1, pp. 40–53, Jan. 2009, http://dx.doi.org/10.1016/j.conbuildmat.2007.10.023.

[16] K. C. Voon and J. M. Ingham, "Experimental in-plane strength investigation of reinforced concrete masonry walls with openings," *J. Struct. Eng.*, vol. 134, no. 5, pp. 758–768, May 2008.

[17] H. Pirsaheb, P. Wang, M. J. Moradi, and G. Milani, "A Multi-Pier-Macro MPM method for the progressive failure analysis of perforated masonry walls in-plane loaded," *Eng. Fail. Anal.*, vol. 127, p. 105528, Sep. 2021.

[18] H. Pirsaheb, P. Wang, M. J. Moradi, and G. Milani, "A Multi-Pier MP procedure for the non-linear analysis of in-plane loaded masonry walls," *Eng. Struct.*, vol. 212, p. 110534, Jun. 2020.

[19] M. P. Barbosa, "Estudo da interação entre grupos de paredes na distribuição das cargas verticais em edifícios de alvenaria estrutural," Undergraduate thesis, Dept. Eng. Civil, Univ. Fed. Rio Grande do Norte, Natal, RN, Brazil, 2017.

[20] I. C. Guerrante, "Análise numérica de vigas de concreto armado reforçadas por encamisamento parcial," Master thesis, Prog. Eng. Civil, COPPE, Univ. Fed. Rio de Janeiro, Rio de Janeiro, RJ, Brazil, 2013.

[21] M. L. F. Simões, "Reforço à flexão de vigas de concreto armado por encamisamento parcial," Master thesis, Prog. Eng. Civil, COPPE, Univ. Fed. Rio de Janeiro, Rio de Janeiro, RJ, Brazil, 2007.

[22] N. N. S. Oliveira, "Análise de paredes de contraventamento de alvenaria estrutural de blocos de concreto considerando os efeitos da fissuração," Master thesis, Prog. Pós-grad. Eng. Civil, Univ. Fed. Rio Grande do Norte, Natal, RN, Brazil, 2021.

[23] Canadian Standards Association, *Design of Masonry Structures, CSA S304-14*, 2014.

[24] R. D. Pasquantonio, G. A. Parsekian, F. S. Fonseca, and N. G. Shrive, "Experimental and numerical characterization of the interface between concrete masonry block and mortar," *Rev. IBRACON Estrut. Mater.*, vol. 13, no. 3, pp. 578–592, Jun. 2020, http://dx.doi.org/10.1590/S1983-41952020000300008.

[25] J. S. Camacho, B. G. Logullo, G. A. Parsekian, and P. R. N. Soudais, "Influência do graute e da taxa de armadura no comportamento à compressão da alvenaria de blocos de concreto," *Rev. IBRACON Estrut. Mater.*, vol. 8, no. 3, pp. 341–364, Jun. 2015, http://dx.doi.org/10.1590/S1983-41952015000300006.

Rev. IBRACON Estrut. Mater., vol. 16, no. 4, e16410, 2023

15/15